

Theo yêu cầu của khách hàng, trong một năm qua, chúng tôi đã dịch qua 16 môn học, 34 cuốn sách, 43 bài báo, 5 sổ tay (chưa tính các tài liệu từ năm 2010 trở về trước) Xem ở đây

**DỊCH VỤ
DỊCH
TIẾNG
ANH
CHUYÊN
NGÀNH
NHANH
NHẤT VÀ
CHÍNH
XÁC
NHẤT**

Chỉ sau một lần liên lạc, việc dịch được tiến hành

Giá cả: có thể giảm đến 10 nghìn/1 trang

Chất lượng: Tao dựng niềm tin cho khách hàng bằng công nghệ 1. Bạn thấy được toàn bộ bản dịch; 2. Bạn đánh giá chất lượng. 3. Bạn quyết định thanh toán.

Tài liệu này được dịch sang tiếng việt bởi:

www.mientayvn.com

Tìm bản gốc tại thư mục này (copy link và dán hoặc nhấn Ctrl+Click):

<https://drive.google.com/folderview?id=0B4rAPqlxIMRDSFE2RXQ2N3FtdDA&usp=sharing>

Liên hệ để mua:

thanhlam1910_2006@yahoo.com hoặc frbwrthes@gmail.com hoặc số 0168 8557 403 (gặp Lâm)

Giá tiền: 1 nghìn /trang đơn (trang không chia cột); 500 VND/trang song ngữ

Dịch tài liệu của bạn: http://www.mientayvn.com/dich_tiang_anh_chuyen_nghanh.html

The UTD solutions have also been applied to convex corrugated surfaces (James, 1980). A GTD result for radiation from sources on a perfectly conducting circular cylinder, with an impedance patch on it, has been obtained by Pathak (1977).

In the case of electrically large right circular cylinders and circular cones, UTD predictions were shown to match excellently with experimental results (Pathak và các cộng sự., 1980). Pathak và các cộng sự (1981) analyzed the torsioned rays and determined the far-field pattern for a slot on a large cone, which agrees reasonably well with the measured patterns. In contrast, very few analytical results are available for EM scattering by finite length cylinders (Kinoshita & Sekiguchi, 1981; Huang and Pathak 1982). Kinoshita and Sekiguchi have obtained an exact solution for scattering of a plane EM wave (TM wave), by an infinitely thin-walled, perfectly conducting, finite, hollow cylinder. Huang and Pathak (1982) have analyzed the scattering of an EM wave by a finite length, perfectly conducting, hollow circular cylinder employing the ray technique, in conjunction with

Người ta cũng đã áp dụng các nghiệm Utd cho các bề mặt lồi gợn sóng (James, 1980). Pathak (1977) cũng đã tính được GTD của bức xạ từ các nguồn trên một hình trụ tròn dẫn hoàn hảo, cùng với một miếng trở kháng trên nó.

Trong trường hợp vật hình trụ tròn phải và hình nón tròn lớn về kích thước điện, người ta thấy các dự đoán UTD khớp rất tốt với các kết quả thực nghiệm (Pathak và các cộng sự., 1980). Pathak và các cộng sự (1981) đã phân tích các tia xoắn và đã xác định biên dạng trường xa của một khe trên nón lớn, chúng phù hợp khá tốt với các biên dạng đo được. Trong khi đó, kết quả phân tích về tán xạ EM của các hình trụ chiều dài hữu hạn còn ít (Kinoshita & Sekiguchi, 1981, Huang và Pathak 1982). Kinoshita và Sekiguchi đã tìm được nghiệm chính xác của quá trình tán xạ sóng phẳng EM (sóng TM) do một hình trụ rỗng vách cực mỏng, dẫn hoàn toàn, hữu hạn. Huang và Pathak (1982) đã phân tích sự tán xạ của sóng EM bởi một hình trụ tròn rỗng, dẫn hoàn toàn, chiều dài xác định bằng kỹ thuật tia,

a self-consistent multiple scattering method(MSM).

Keller (1960), Ryan (1968), and Burnside and Peters (1972) have considered finite cones for GTD analysis. Vafiadis and Sahalos (1983) have analyzed the problem of EM diffraction by a perfectly conducting elliptic cone. They have obtained the exact solution in the form of a dyadic Green's function which is the most general form of solution.

At its simplest, a missile may be visualized as a long but finite circular cylinder which is capped by a finite cone in the fore and with several symmetrically placed fins at the aft. The RCS for such a conically capped cylinder has been computed by Ryan and Peters (1969, 1970).

Two recent results are of interest in the context of RCS studies. The RCS prediction for the flat-winged aircraft has turned out to be considerably different than the curved-winged aircraft(Ricgger và các cộng sự., 1992). This

kết hợp với phương pháp đa tán xạ tự hợp (MSM).

Keller (1960), Ryan (1968), và Burnside và Peters (1972) đã nghiên cứu các nón hữu hạn bằng GTD. Vafiadis và Sahalos (1983) đã phân tích bài toán nhiễu xạ EM bởi một nón elip dẫn hoàn toàn. Họ đã tìm được nghiệm chính xác dưới dạng hàm Green dyadic, đó cũng chính là dạng tổng quát của nghiệm.

Dyadic: nhị nguyên, nhóm hai, hai ngôi

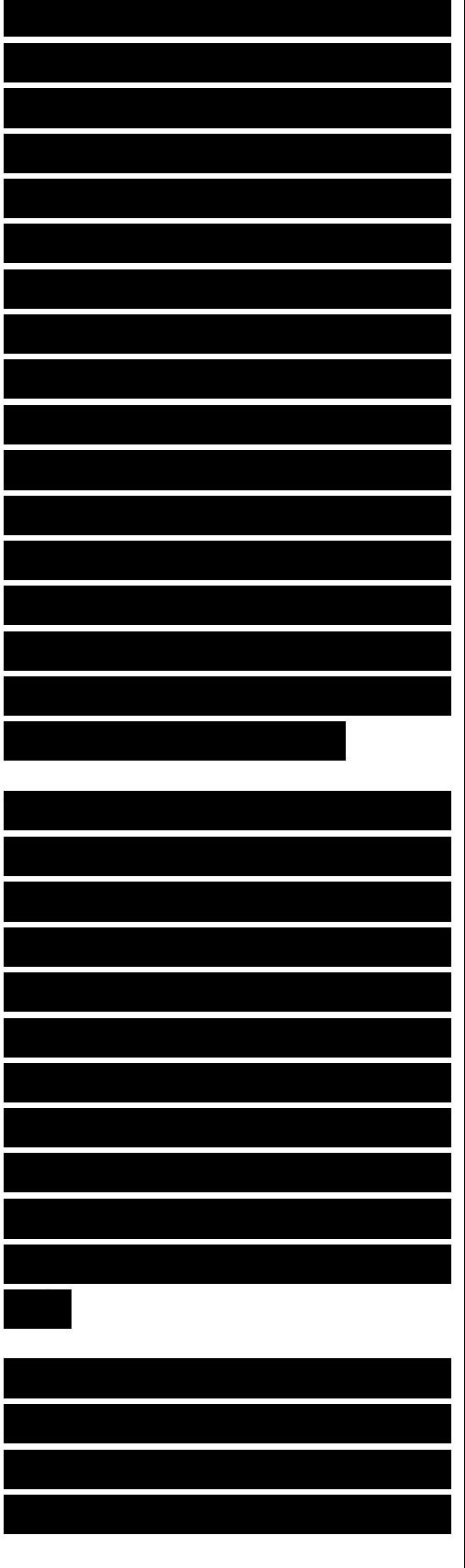
Ở mức độ đơn giản nhất, chúng ta có thể hình dung tên lửa là một vật hình trụ tròn dài nhưng hữu hạn được chụp ở phần đầu bằng một hình nón hữu hạn và có một số lá tản nhiệt đặt đối xứng ở phía sau. Ryan và Peter (1969, 1970) đã tính toán RCS cho một hình trụ có đầu dạng nón như thế.



difference has been attributed to quasi-ellipsoidal shape of the wing, so that the edge-diffraction contributions alone appear to be inadequate. A second result drawing similar conclusions is by Choi và các cộng sự (1990a) where it is suggested that omission of the creeping wave contribution in the case of the cone leads to poorer agreement of the UTD results with measured data. Such surface diffraction contributions are carefully accounted for in the subsequent conical hybrids (Choi và các cộng sự.. 1990b).

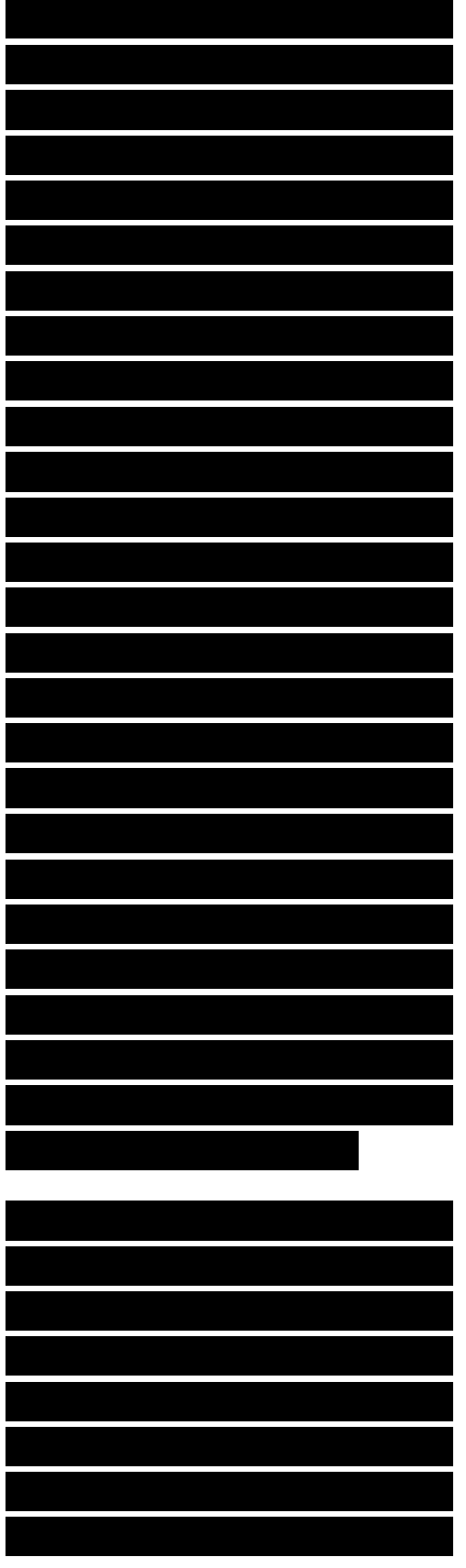
It is thus apparent that surface diffraction mechanism cannot be ignored in the scattering computations. This is consistent with the general observation made earlier in the text that surface diffraction components are usually the strongest. Further, on a closed surface such as the sphere or the ellipsoid of revolution, surface diffraction is the only mechanism of scattering.

One of the main reasons for excluding surface-diffraction from EM scattering considerations has been the immense difficulty hitherto



faced in three-dimensional ray tracing over doubly-curved surfaces. This has now been overcome by the geodesic constant method (Jha & NViesbeck, 1995) which yields all the ray parameters required for UTD (or any other asymptotic ray-theoretic method) diffraction coefficients in the closed form. Analytical expressions have been presented for all the geometric ray-parameters for the complete class of quadric cylinders and surfaces of revolution in the closed form. Individual analysis have been also presented for the general paraboloid of revolution (Jha và các cộng sự., 1989a), ellipsoid of revolution (Choudhury & Jha, 1995) and general hyperboloid of revolution (Jha và các cộng sự., 1991a), which are readily applicable to the canonical RCS computations.

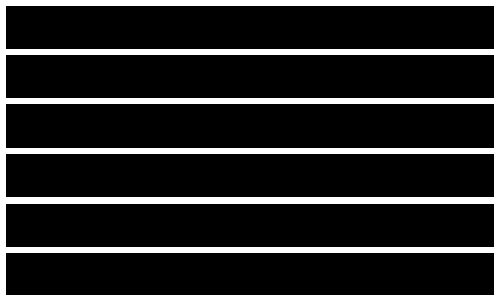
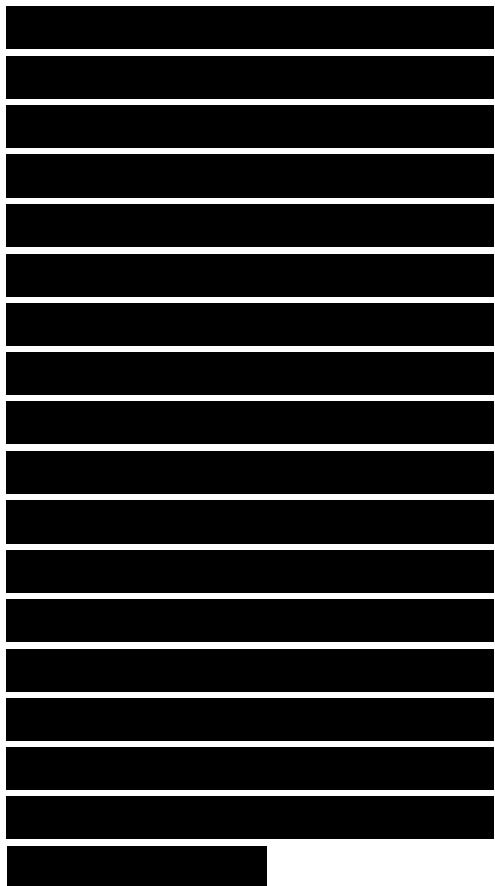
In the case of the ellipsoid of revolution and the general hyperboloid of revolution, the ray parameters require the determination of the incomplete elliptic integrals of the first, second and third kind. Since, closed form expressions do not exist for the evaluation



of these integrals, asymptotic series expansions are employed which are extremely computationally intensive (Jha và các cộng sự., 1991b). This tends to make UTD rather unattractive for RCS computations of these comparatively complex doubly- curved scatterers.

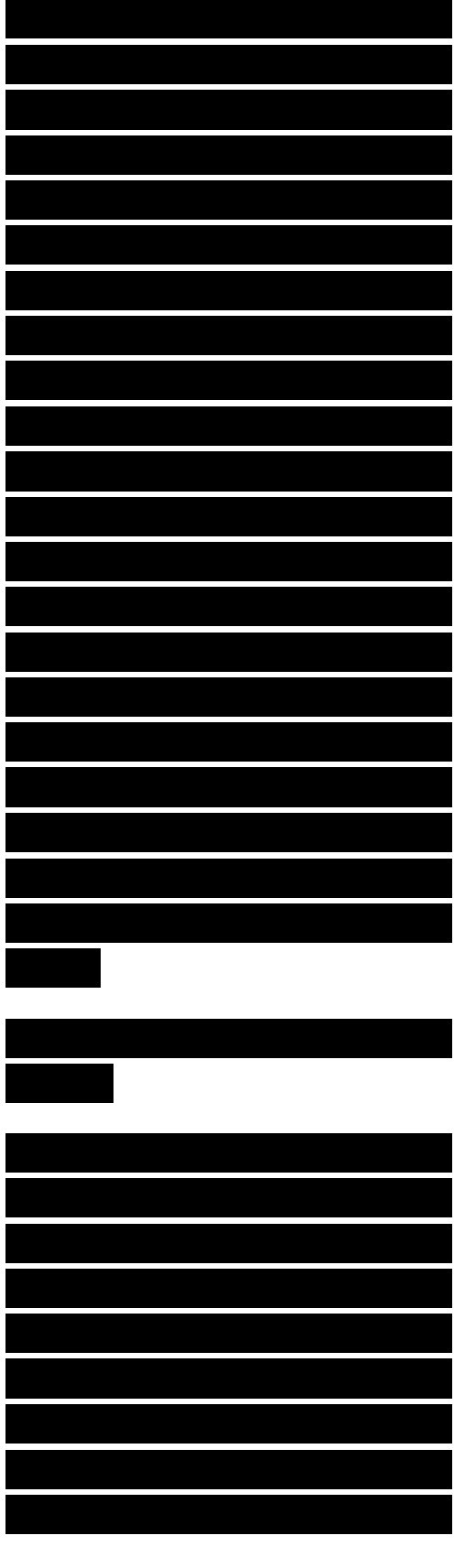
An ogive is a surface generated by the rotation of the off-section arc of the circle. It is observed that the ogive is intrinsically a surface of low RCS. GTD has been employed to determine these low RCS characteristics of the ogive using a numerical ray tracing approach (Lai & Burnside, 1987). It has been shown that the geodesic constant method in principle provides the analytical ray' tracing algorithm in the case of the ogive and ogival sections (Jha và các cộng sự., 1989b).

In contrast to the curved surface, much of the diffraction contribution of plane faced surfaces is due to the edges. Thus the semi-infinite flat plate, the dihedral and the trihedral constitute the



canonical surfaces of edge diffraction which have been extensively studied in the context of RCS. Such surfaces often require that the higher-order interactions be taken into account for increasing accuracy of diffraction contribution over wide scattering angles (Akhter & Marhefka, 1992). These higher-order interactions can also be modified and extended to the bi-conical and top hat structures for RCS computations. The edge-wave formulation has also been extended (Ivrissimtzis & Marhefka, 1990) to the tip-diffraction contributions of a trihedron. The radiation integral which is truncated and evaluated asymptotically, results in predictions which match excellently with the MoM benchmarks and measurements.

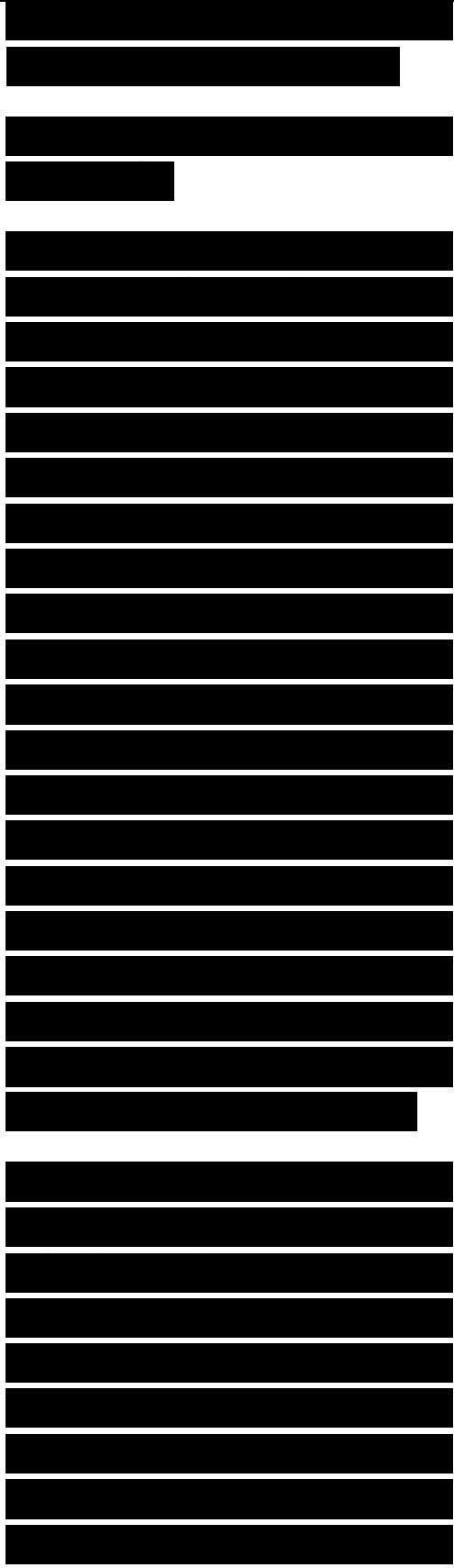
The hypothesis of multiple interactions is further strengthened in the case of flat plate geometries (Fuchs và các cộng sự., 1989), and the cube. Ray-theoretic formulations have also been extended to the polygonal plates (Pelosi và các cộng sự., 1990) and circular disc geometries to study the boresight caustics and far-angle sidelobes (Duan và các cộng



su.,
1991).

Although the UTD formulation is based on the premise that the scatterer is electrically large, smooth conducting and convex, it has been successfully applied to other variants as well. For example, the UTD analysis for a wedge with two impedance faces has been successfully analyzed to predict the optimal thickness of the RAM on a flat plate for RCS reduction applications (Bhattacharyya, 1989). The analysis of thin RAM coatings on the flat plate (Balanis & Polka, 1993) once again demonstrates the need to consider the higher-order interactions in UTD analysis to increase the accuracy of the predicted RCS results.

Pyramids comprising both lossless dielectrics and lossy absorbers have been analyzed by the UTD corner diffraction formulation (Tyson, 1991). The results are sufficiently accurate for angles away from the nose-on incidence, whereas for the nose-on incidence, the internal inhomogeneities provide the



main scattering mechanism so that the UTD predictions are least accurate for small acute angles. Comparison of UTD computation with measurement also shows the accuracy to be dependent on the incident polarization.

GTD clearly suffers from several difficulties. For practical scatterers, finding all the rays from the source point to the observation point is a formidable task; the canonical problems in contrast are somewhat simpler since they often predict only a few ray paths.

3.4.3 Physical Optics

As mentioned earlier, GO breaks down at the shadow boundaries. It predicts a zero field in the shadow region and results in discontinuity between illuminated and transition region fields. This is contrary to the observations. Further, GO fails to predict fields away from the specular direction. These shortcomings can in principle be overcome by physical optics (PO) which accounts for the wave nature of propagation. PO is essentially based upon Huygen's principle which states that each point on the wavefront (called the primary wavefront) gives rise to secondary wavefronts.

[REDACTED]

[REDACTED]

[REDACTED]

[REDACTED]

Hence a spherical wavefront, as it propagates, gives rise to secondary spherical wavelets. This provides a mechanism for the bending of waves and accounts for the diffraction phenomenon in the shadow region.

PO essentially assumes the scatterer to be electrically large, but unlike as in GO, it is assumed to be of finite size. It is therefore possible to distinguish between the phases of two incoming rays. The PO results thus depend on the wave number p associated with the propagating wave: in contrast GO assumes $p \rightarrow \infty$.

In practice the method of PO is that of induced currents. The field due to the radiating source is assumed to exist independently of the scatterer. Thus finite fields exist in both the illuminated and shadow regions and obviously must also be continuous at the shadow boundary. The effect of the scatterer manifests as a field due to the source induced current on the scatterer, known as the PO current. The total field at any point exterior to the scatterer can be symbolically denoted as

$$E/O = \hat{d}incl + E \text{ induced} \quad (3.91)$$

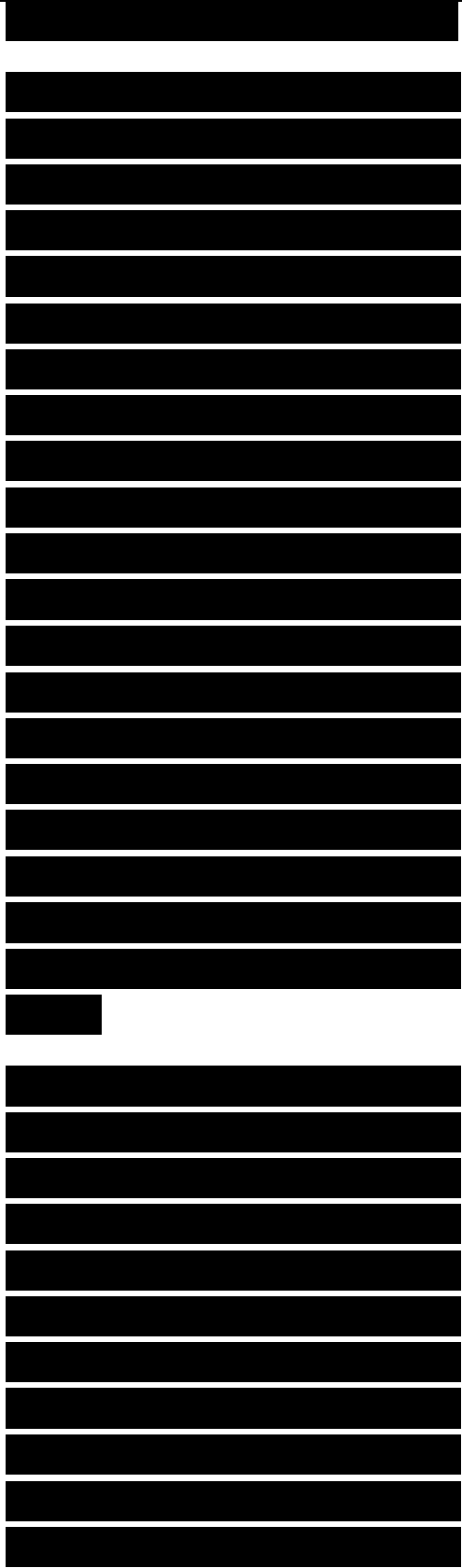
[REDACTED]

[REDACTED]

[REDACTED]

A classical solution obtained by the PO method is that of a uniformly plane wave incident on a conducting half-plane (Kraus, 1988) where the electric field upon transformation can be shown as a sum of the Fresnel sine and cosine integrals. The Fresnel sine vs. cosine integrals can be expressed with respect to the points in the shadow of the conducting half-plane as a Cornu spiral. One implication of this form of representation is prediction of a finite oscillatory field in the shadow region as well as a smooth transition from the IR. This is in contrast with GO which predicts a zero field in the shadow region.

It is often convenient to utilize GO induced fields as approximations for PO induced currents on a scatterer. This offers a simplification of the PO solutions and has been used to effectively treat the two-dimensional field problem for a perfectly conducting scatterer (Pathak, 1994). The GO induced fields yield elegant results in terms of the Hankel functions which can be readily

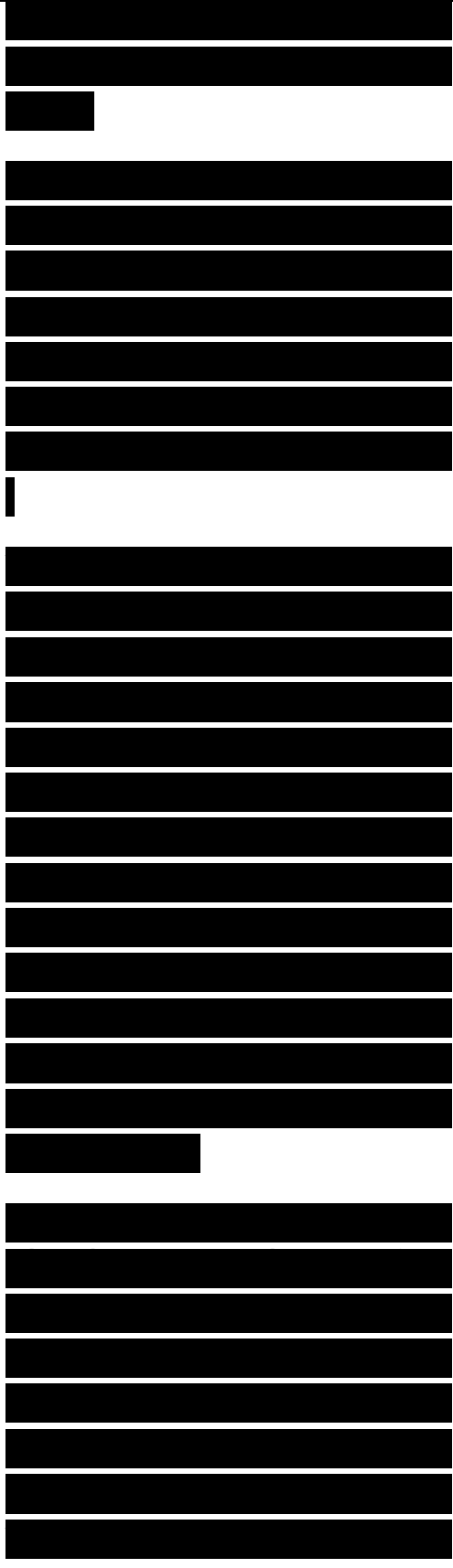


evaluated (Abramowitz & Stegun, 1964).

A closed-form PO approximation for segmented surfaces of revolution has been developed by Gordon and Bilow (1991), who have compared the nose-on PO backscatter RCS of a paraboloid of revolution with the MoM predictions.

A novel shooting and bouncing ray (SBR) method, used in conjunction with GTD techniques has also been successfully applied in a PO formulation for the analysis of the backscatter RCS from a partially open cavity (Ling và các cộng sự., 1989). This recourse to SBR has the advantage of not only treating concavities of arbitrary cross sections and material loading, but also being promising in terms of low computational requirements.

The PO method nonetheless is strongly associated with planar surfaces. Hence relatively more complicated scattering shapes are modeled as hybrids of flat panels (Klement và các cộng sự., 1988). Such panels could be multilayered and need not be perfectly conducting.



Computations have been successfully carried out for cubes shadowed by extended flat plates.

The concept of curvanire can nevertheless be introduced for PO backscatter RCS computations by employing the so-called NURBS surfaces (Perez & Catedra. 1994). This offers an attractive method of modeling curved surfaces in general since the typical computational requirements are rather low.

PO nevertheless requires that the radiation integral be evaluated numerically, which is often quite cumbersome. Furthermore PO is incapable of treating multiple reflections. Although PO does predict fields in nonspecular directions, it is interesting to note that PO is nonreciprocal in these regions.

In those cases where GO currents are employed to substitute for PO currents, the predicted solution may be constrained by the inherent weaknesses of GO. For example, in regions where GO erroneously predicts low levels

[REDACTED]

[REDACTED]

[REDACTED]

[REDACTED]

of fields, the contribution due to the radiation integral of PO is also small and prone to error. This is best observed in the case of edge-diffraction.

3.4.4 Physical Theory of Diffraction

An extension of PO which improves predictions for surfaces with edges was proposed by Ufimtsev (1962). His fringe theory is now known as the physical theory of diffraction (PTD). The basic assumption inherent in PTD is that the PO induced current is but a part of the total induced surface currents. All other current components can be symbolically put together as a correction term for the PO based method,

.....

J^u , approximated by GO currents, is the uniform term whereas J^s , represents the nonuniform component and is approximated by the current near the edge of a planar wedge. Thus the total scattered field in PTD is a sum of two surface integrals corresponding to these uniform and nonuniform components.

[REDACTED]

[REDACTED]

[REDACTED]

[REDACTED]

[REDACTED]

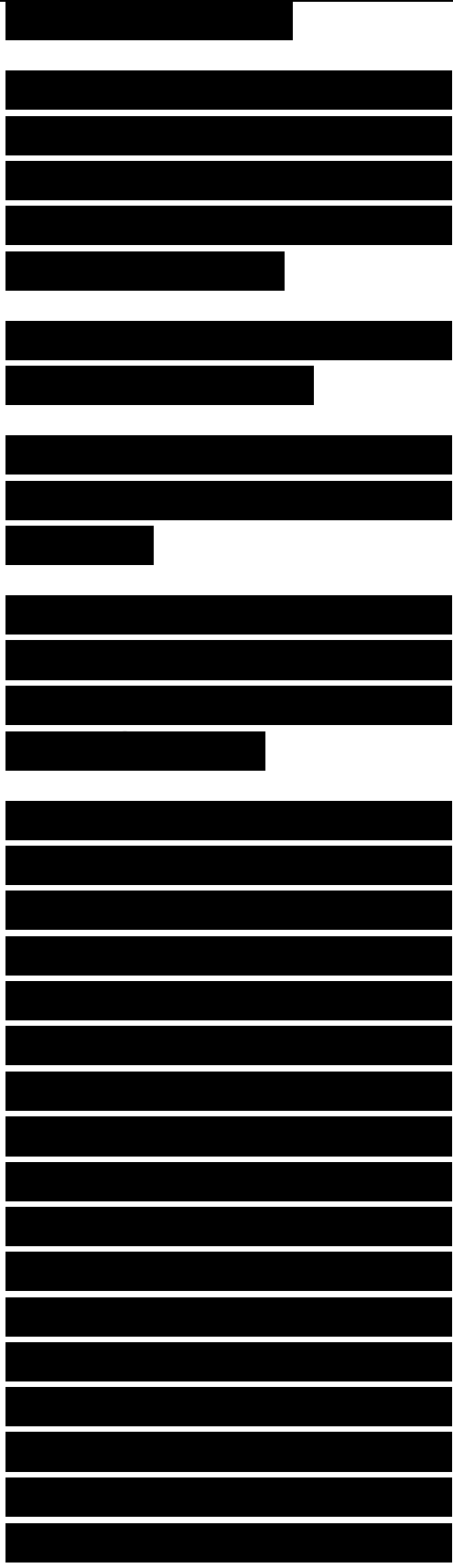
The PTD formulation is explained with respect to the incident and scattered ray angles θ_i and θ_s on the wedge (Fig. 3-15). We define θ_U and θ_D , in terms of these angles,

Let the angle exterior to the wedge be defined by θ_n . The corresponding wedge angle is given by

A diffraction related characteristic angle for the wedge α may be expressed as:

Rather than evaluating the surface nonuniform integral, PTD proposes two functions f and g as a sum of the diffraction coefficients.

Ufimtsev successfully employed PTD to account for the edge effects of conducting strips and circular disks. It was also extended to the analysis of bodies of revolution such as a right circular cylinder (Ufimtsev, 1958), cone and paraboloid (Ufimtsev, 1962), particularly for head-on illumination. In the context of the RCS of perfect electric conductor bodies, these canonical surfaces have been extensively studied by the PTD method. A comparison of various high-frequency methods including PTD for the backscatter by circular disk has



been presented by Duan và các cộng sự (1991). Yang and Bor (1992) have obtained the PTD radar backscatter of an array of rotating fans as an example of the hybrid surfacc.

The original PTD ansatz as visualized by Ufimtsev nevertheless gives rise to singularities at the caustics. Effort have been made to remove these by incorporation of equivalent edge current, a concept similar to the one used by Ryan and Peters (1969). A similar technique of including equivalent currents to account

Figure 3.15 the phenomenon of diffraction on a wedge. θ , and θ_S are the angles of incident and scattered rays The external angle of the wedge is $\pi - \alpha$.

for multiple diffractions in PTD formulation has yielded excellent accuracy for circular disks of diameter greater than 10λ (Ando, 1985; Ando và các cộng sự., 1989). In contrast, Mitzner (1974) has suggested an extremely powerful method in terms of incremental length diffraction coefficient (ILDC) which yields the PTD corrected field as a function of the observation



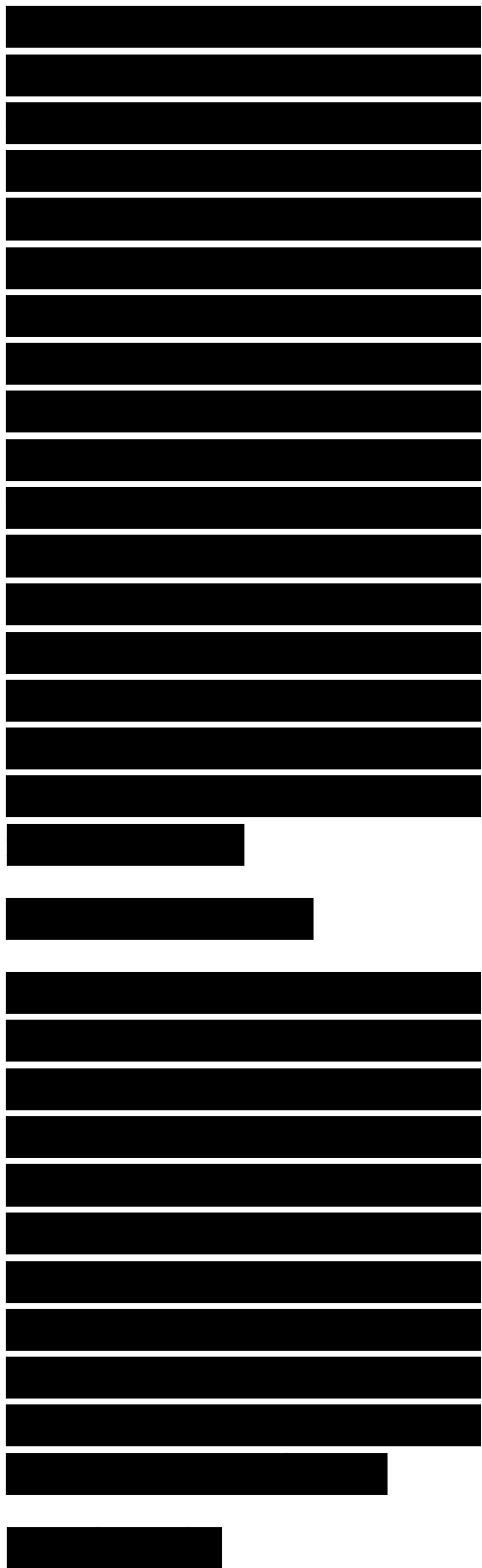
angles.

Yet another modification of PTD is by Michaeli (1984) who obtained the GTD equivalent edge currents via the diffraction coefficients. It can however be shown that Michaeli diffraction coefficients upon subtracting the PO terms are identical to the ILDC of Mitzner. An analog of diffraction by the edges of a surface is implemented for the generalization of PO currents to model a loaded dihedral comer (Corona và các cộng sự., 1987). This generalized approach, besides being uniform, improves the accuracy of the solution.

We close this section by pointing out that a very powerful technique for treating a specific scatterer is by a combination of methods described in this chapter. Relevant references of the application of such hybrid methods are listed in Suggestions for Further Reading at the end of the book.

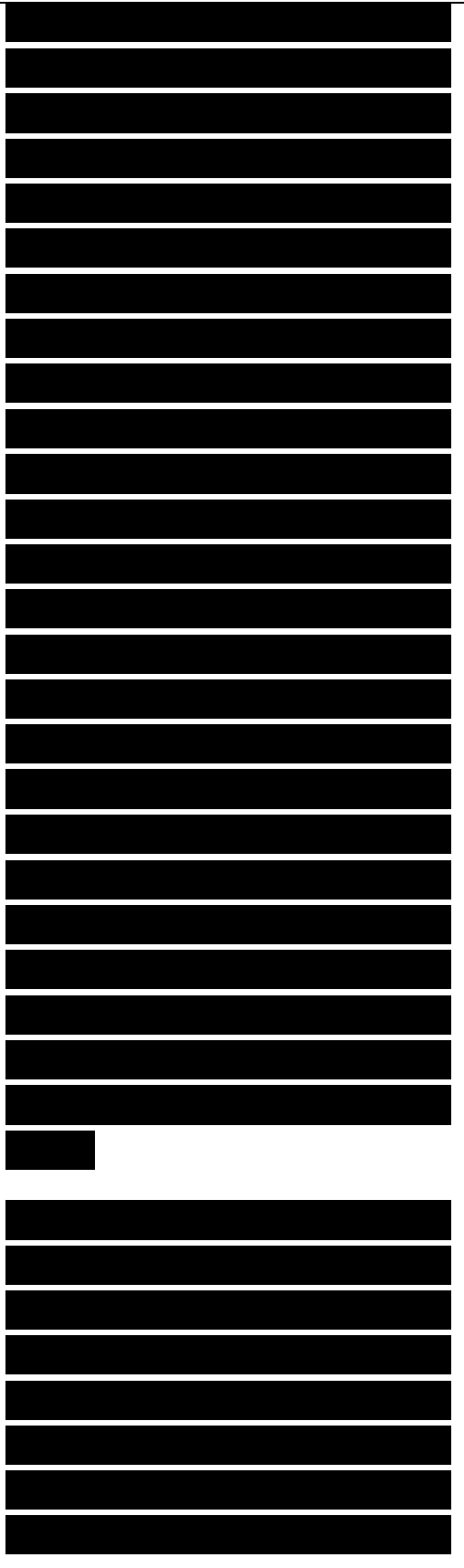
3.5 SUMMARY

The analysis of RAM involves



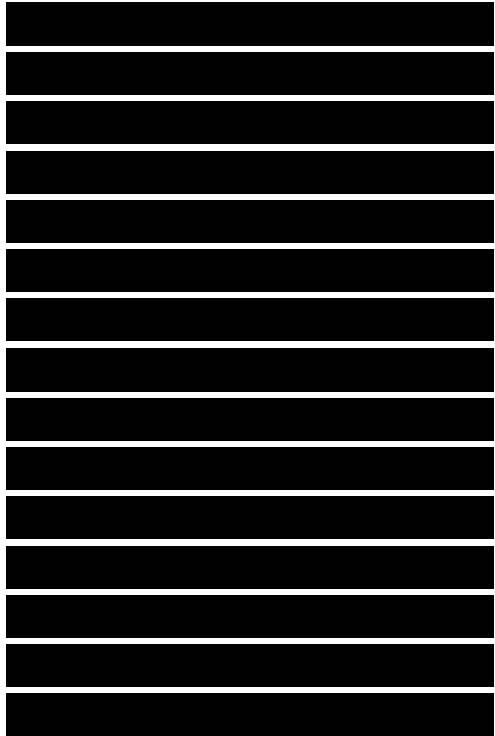
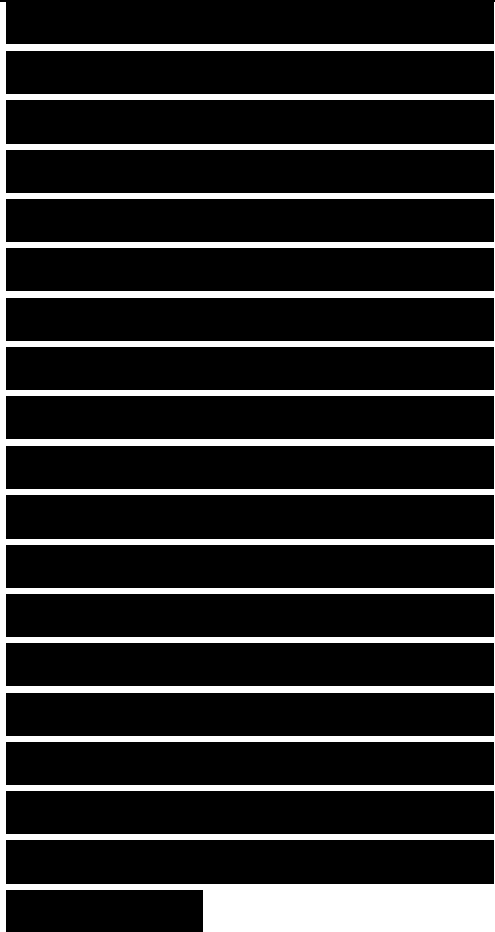
determination of the backscatter RCS, usually expressed by the reflection coefficient. The electromagnetic reflections for normal incidence at a planar RAM-free space interface may be considered as the simplest case. The reflection coefficients are derived from the boundary conditions, and the condition for zero-reflection of a metal backed RAM is obtained using the transmission line approach. For the general case of oblique incidence, both the perpendicular and parallel polarization reflection coefficients follow from the basic principles. These derivations also form the basis for the backscatter analysis of multilayered RAM structures, where the expressions are of recursive form. It is also apparent from this EM analysis that such RAM configurations are frequency dependent.

The analysis of RAM coated curved surfaces is relatively more complex. For the class of scatterers which exhibit a four-fold symmetry, conditions can be obtained for eliminating the backscatter completely. Shapes whose cross section is square, regular octagon, and so on,



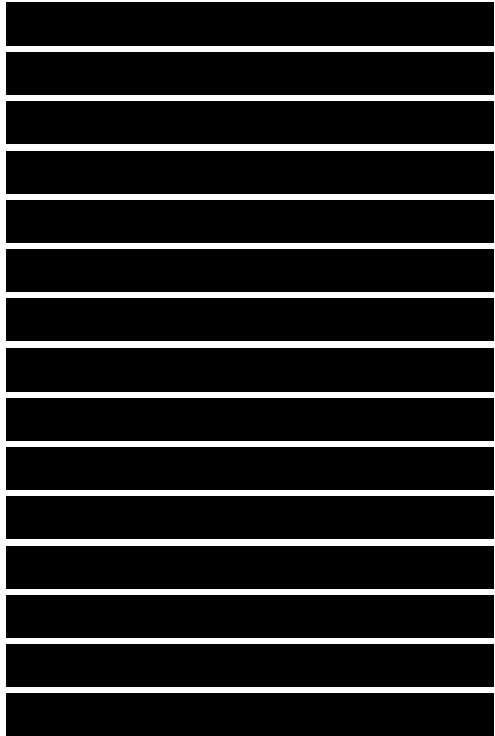
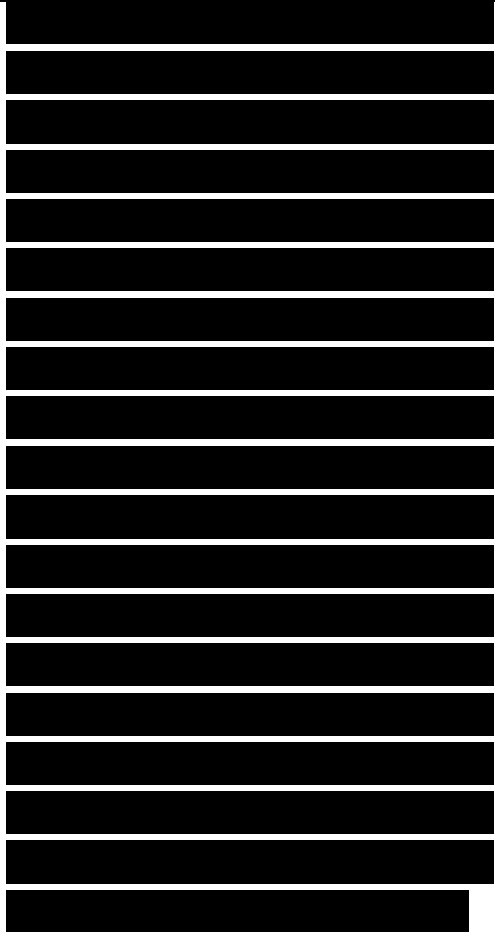
with the circle as the limit, are examples of such scatterers. Hence square cylinders, and surfaces of revolution such as sphere, cone, paraboloid of revolution, and ogive which are extremely important in aerospace engineering, may be considered for such an application. The coating itself must obey the condition that either the relative permittivity and permeability be equal, or that the lossy part of the permittivity and permeability be large. This important result is independent of frequency, and thus applicable to scatterers of all sizes.

It is often required to analyze RAM profiles on highly complex aerospace shapes which may not offer convenient symmetries. In the low frequency domain, the analysis for these is carried out by grid-based methods such as the method of moments (MoM) and the finite difference time domain (FDTD) method. MoM involves choice of suitable basis and testing functions, eventually requiring inversion of a matrix. It has been extensively applied to RAM analysis of arbitrarily shaped



scatterers and anechoic chamber designs. FDTD assumes the scatterer to be embedded in a space lattice and adapts the Maxwell equations in the finite difference form, resulting in recurrence relations. FDTD has a clear edge over MoM in treating comparatively larger scatterers. Since FDTD algorithms can be readily parallelized, this method has the potential of handling extremely complex RAM designs.

Geometrical optics (GO) assumes infinitely small wavelengths so that the scatterer appears to be infinitely large. Analysis of such a scatterer involves reflection and refraction dyads. For objects which are electrically large but finite, diffraction is incorporated into GO thus resulting in the geometrical theory of diffraction (GTD). Although these theories require the scatterer to be smooth, conducting and convex, they have nevertheless been



design goals are to be achieved. Therefore, a knowledge of the design and application of radar absorbing materials is vital to the engineer whose task is to minimize the radar signature of a vehicle.

As discussed in Chapter 6, basic scattering phenomena may be broken down into specular and nonspecular mechanisms. As might be expected, RAM design must also be approached with consideration for the scattering mechanism of interest. Accordingly, in this chapter, RAM design and performance will first be discussed with reference to specular reflections. Then, the design performance of nonspecular RAM will be considered.

The electromagnetic aspects of RAM design focus principally on the synthesis of an arrangement of dielectric or magnetic materials that provide a specified impedance profile to an incident wave. A study of the evolution of RAM design is a study of the materials and techniques employed to achieve desirable impedance properties (and, hence, good absorptive qualities) over ever increasing bandwidths. In

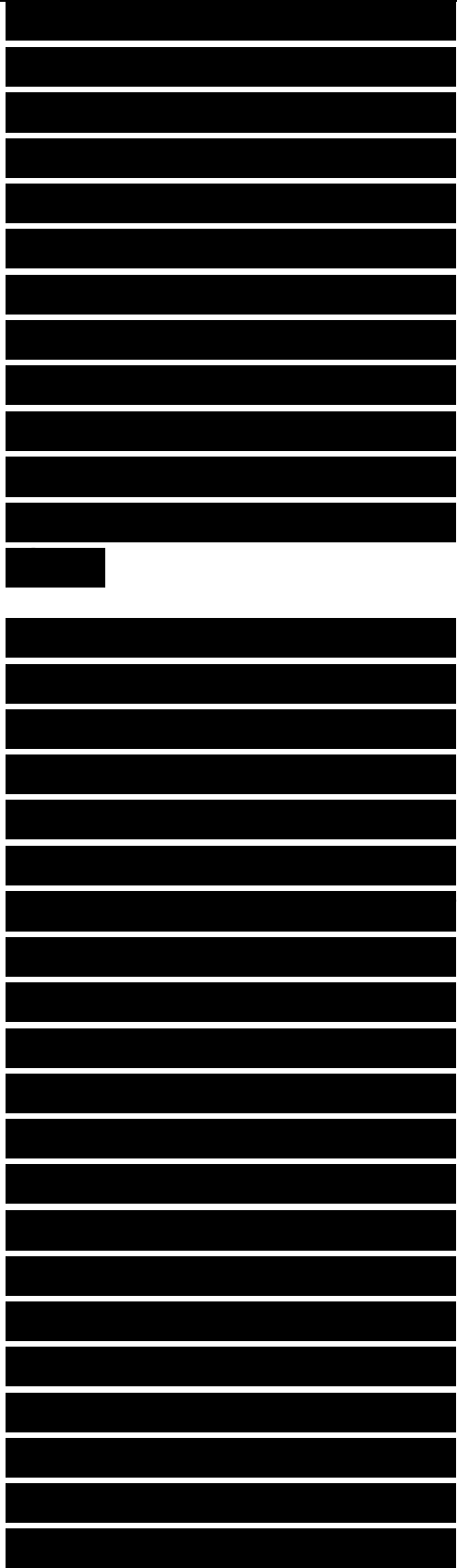
[REDACTED]

[REDACTED]

[REDACTED]

organizing the chapter, the basic theory underlying specular RAM design is first considered, and analytical design methods are presented. Then, the design methods are used to illustrate the types of structures typical of current RAM implementations and the performance that can be achieved in those implementations.

A study of the physics of electromagnetic wave absorption should begin with the microscopic or quantum theory of materials, but we will instead approach this topic with a macroscopic view of electromagnetics. Although the loss mechanisms through which RAM operates are microscopic in nature (i.e., on the atomic and crystal lattice levels), the analysis of specular RAM is most easily handled by taking a classical transmission line approach to model the reflection and transmission properties of absorbers. Similarly, successful theoretical analyses of nonspecular RAM performance have often been based on dielectric waveguide theory. In effect, the design of RAM is simply the design of a lossy



distributed network that matches the impedance of free space to that of a conducting body to be shielded.

Section 8.2 discusses loss mechanisms and relates them to the macroscopic electrical and magnetic properties of materials. The concept of terminating impedance is introduced and defined for semi-infinite slabs and for conductor-backed single layers of material. The formula for the reflection coefficient is provided, and its implication for the selection of desirable material properties is considered. Section 8.3 discusses specular reflection from flat dielectric multilayers for both the simple case of normal incidence and for the general case of off-normal incidence. An alternative approach to scattering calculations using a wave matrix formulation is then presented, and its application in light of current materials metrology techniques is discussed. Section 8.4 catalogs available types of dielectric absorber and discusses their design and level of performance. Section 8.5 provides information on circuit analog absorbers and frequency selective surfaces. Section

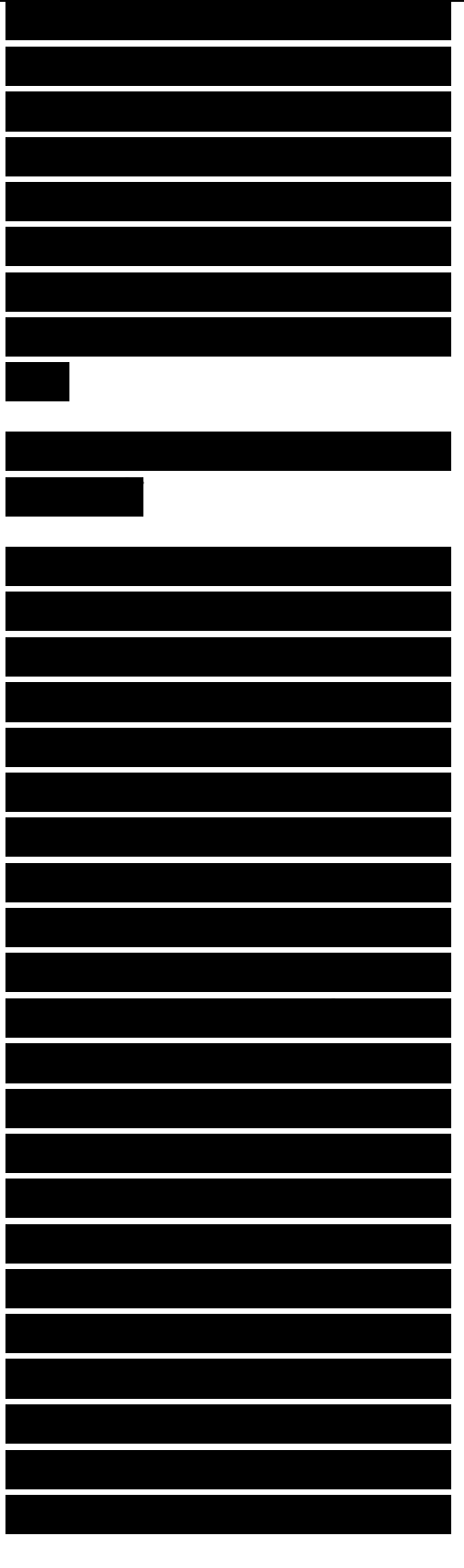
[REDACTED]

[REDACTED]

8.6 discusses magnetic RAM and its application to specular absorbers, and Section 8.7 briefly discusses hybrid RAM and radar absorbing structures. Section 8.8 considers the important topic of nonspecular RAM design and performance.

8.2 ELECTROMAGNETIC LOSS MECHANISMS

Radar absorbing materials are based on the fact that some substances absorb energy from electromagnetic fields passing through them. Such materials have indices of refraction that are complex numbers. In the index of refraction, which includes magnetic as well as electric effects, the imaginary component accounts for the loss in a material. The term loss refers to the dissipation of power or energy, quite analogous to the way energy is consumed by a resistor when electrical current passes through it. The loss is actually the conversion of electrical energy into heat, and although most absorbers do not dissipate enough energy to get detectably warm when illuminated by a radar, this is nevertheless the mechanism by which they operate. At



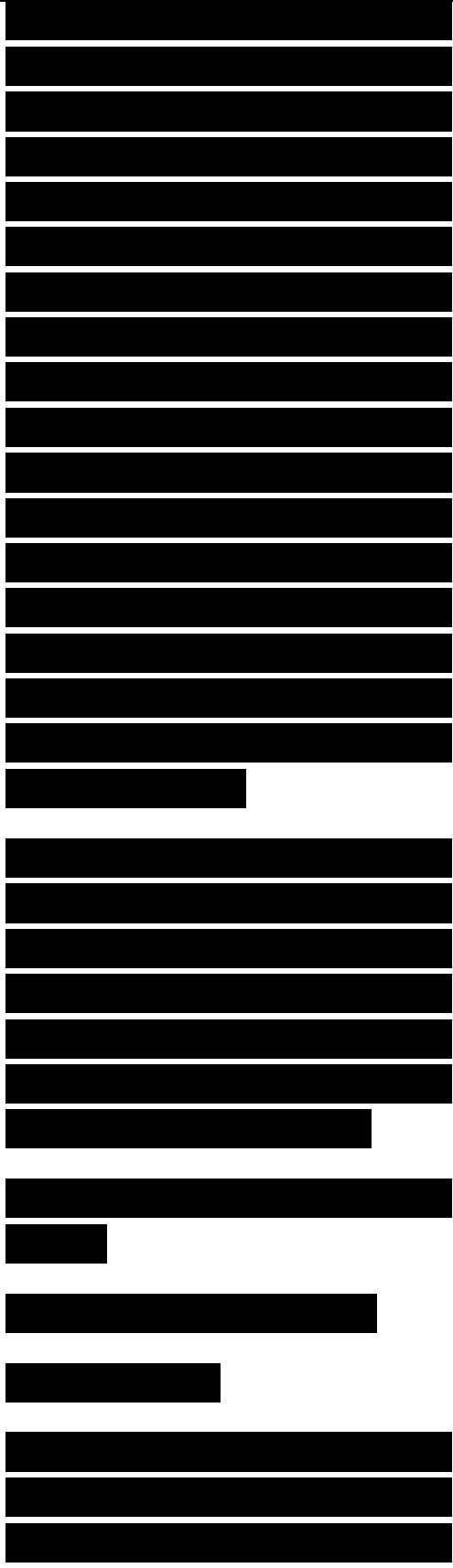
microwave frequencies, the loss is due to a number of effects on the atomic and molecular level. However, for most practical electric absorbers a majority of the loss is due to the finite conductivity of the material, whereas for most magnetic absorbers at microwave frequencies, magnetization rotation within the domains is the principal loss mechanism. In any event, it is customary to group the effects of all loss mechanisms into the permittivity (ϵ) and permeability (μ) of the material because the engineer is usually interested only in the cumulative effect.

Several common usages exist for expressing the complex permittivity and permeability. Generally, we shall deal with the relative permittivity, ϵ_r , and relative permeability, μ_r , which are normalized by the free-space values, ϵ_0 and μ_0 .

The complex notation for ϵ_r and μ_r , is normally given as

$$\epsilon_r = \epsilon_r' + i \epsilon_r'' \quad (8.1)$$
$$\mu_r = \mu_r' + i \mu_r''$$

where the real (energy storage) part of each parameter is denoted by a prime and the



imaginary (loss) part is denoted by a double prime. Because the conductivity σ of electric absorbers is often the major loss mechanism, it is convenient to express the effect of the conductivity in terms of ϵ'' . For that case, ϵ'' and σ are related by

$$\epsilon'' = \sigma / \omega \epsilon_0 \quad (8.2)$$

where ω is the radian frequency. Equivalently, in polar notation,

$$\epsilon_r = |\epsilon_r| e^{i\delta}$$

$$\mu_r = |\mu_r| e^{i\delta_m}$$

where δ and δ_m are the electric and magnetic loss tangents given by

$$\tan \delta = \sigma / \omega \epsilon_r \quad (8.4)$$

$$\tan \delta_m = \omega \mu_0 \mu_r \sigma_m$$

The index of refraction n is the ratio of the wavenumber describing wave propagation within the material to the free-space wavenumber and is to the geometric mean of the relative permittivity and permeability

$$n = k/k_0 = \sqrt{\epsilon_r \mu_r} \quad (8.5)$$

where k is the wavenumber in the material, and $k_0 = \omega \sqrt{\epsilon_0 \mu_0}$ is the free-space wavenumber. Similarly, μ_r and ϵ_r also define the intrinsic impedance, Z , of the material:

$$Z = Z_0 \sqrt{\epsilon_r} \quad (8.6)$$

where Z_0 is the impedance of free space, 120π , which is approximately 377 Ω .

The intrinsic impedance is the impedance value seen by a normally incident wave on a semiinfinite slab of a material. In practical applications, a layer of dielectric will often be backed by a conducting surface. For that case a transmission line analysis can be performed to find the effective input impedance at the front face of the layer.

For a flat metallic surface coated with a layer of dielectric material, the normalized input impedance Z_{in} is given by

$$Z_{in} = Z_0 \tanh(-jk_0 d \sqrt{\epsilon_r}) \quad (8.7)$$

where d is the thickness of the dielectric layer. This formula applies to a wave striking the surface at normal incidence, and it becomes more complicated when the wave arrives at oblique angles. The normalized impedance can be used to calculate the reflection coefficient R :

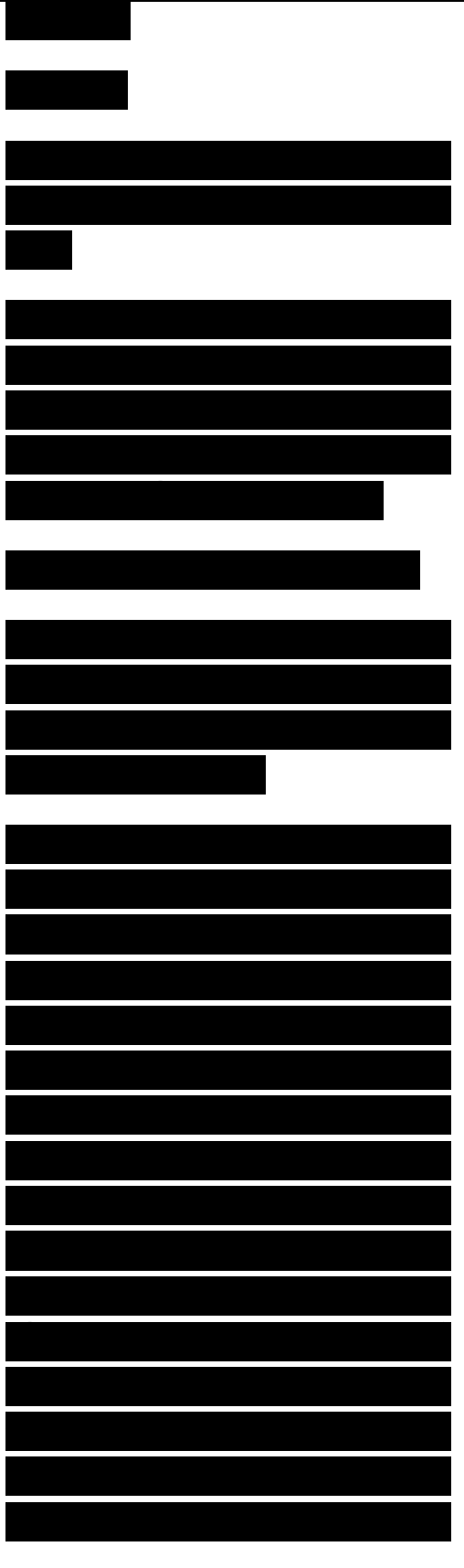
$$R = \frac{Z_{in} - Z_0}{Z_{in} + Z_0} \quad (8.8)$$

R, like t), is a complex number, but has a magnitude between 0 and 1.

In discussing reflection coefficients, it is customary to ignore the phase angle and to refer only to the “voltage” amplitude $|r|$, so that the power reflection in decibels is $R \text{ (dB)} = 20 \log_{10}|r|$ (8.9)

In the discussion that follows, the terms reflection coefficient and reflectivity will be used essentially interchangeably.

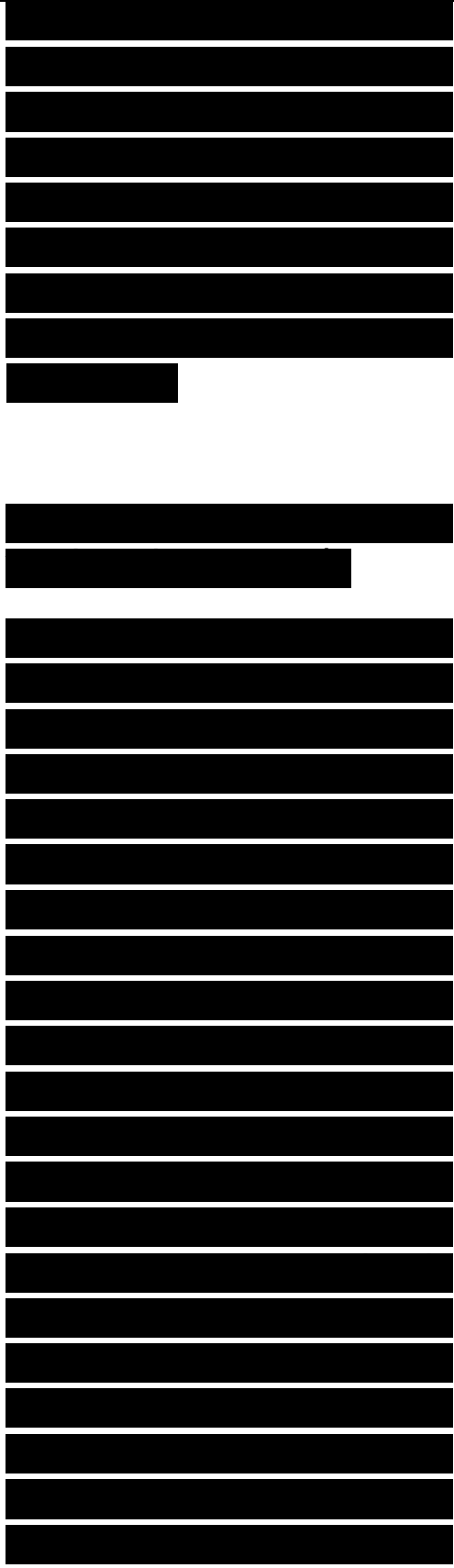
The objective of RAM design is to produce a material for which $|r|$ remains as small as possible over as wide a frequency range as possible. It should be noted that unless the material has some loss, the amplitude of the reflection coefficient will be controlled entirely by the phase and amplitude relationship between the portion of the incident wave reflected at the front surface and the portion returning via reflections at the backing surface. In some cases, we may take advantage of the phase shift on reflection to provide resonant energy



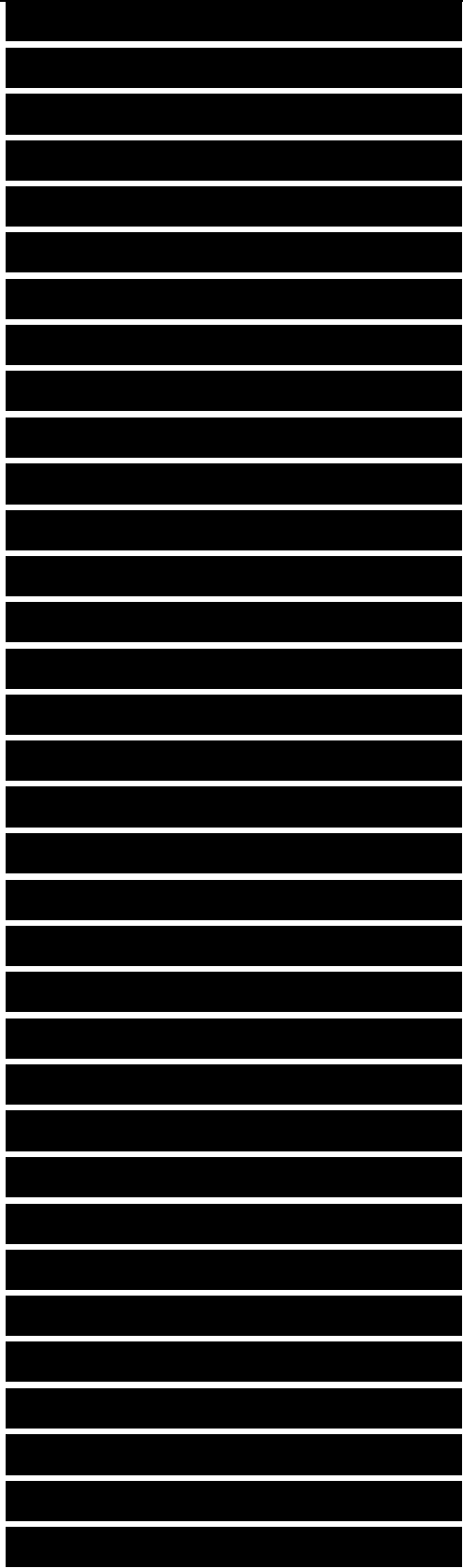
cancellation. This is inherently a narrowband RCSR technique. However, it is also often taken advantage of with lossy materials to provide improved performance at certain frequencies. The Dallenbach layer, which is discussed in detail in Section 8.4, is an example of an absorber that makes use of a combination of loss and resonant cancellation.

8.3 SPECULAR SCATTERING FROM DIELECTRIC MULTILAYERS

In RAM design, two questions concerning the electromagnetic properties of materials must be answered if absorption performance objectives are to be met (also, a host of other questions must be answered concerning physical and thermal properties of the RAM, but this discussion focuses on electromagnetic requirements). The first question to be answered is, "How do I get incident electromagnetic energy into the RAM?" As can be noted from (8.8), that question deals with the impedance mismatch seen by the wave as it enters the absorber. The second question to be answered is, "How do I absorb electromagnetic energy, once I have gotten the EM wave to enter the RAM?" That



question deals with the mechanisms available for attenuating waves within materials. However, the two questions are coupled. Note that raising the value of ϵ'' or μ'' to increase loss also raises the value of the complex permittivity or permeability, thus affecting the reflection coefficient. For example, if we were able to design a nonmagnetic material with an ϵ' value of 1, and an ϵ'' of 10, the amplitude of the reflection for a wave normally incident on a semiinfinite slab would be $|r| = 0.63$, which is only 4 dB down from the reflection from a perfectly conducting surface. Even if ϵ'' were reduced to a value of 1, $|r| = 0.21$, just over 13 dB below the reflection from a perfect conductor. To reduce the front-face reflection to -20 dB would require $\epsilon'' < 0.41$ (even for the unlikely situation of $\epsilon' = 1$). For the $\epsilon'' = 10$ case, the attenuation of the EM energy within the material would be 116 dB per free-space wavelength traveled. For $\epsilon'' = 1$, the attenuation would drop to 25 dB/X., and for $\epsilon'' = 0.41$, the attenuation is only 11 dB/X.. Therefore, adding loss to the material affects both the reflection coefficient and the achievable loss in a given material thickness, so that



RAM design is always a trade-off between the requirements raised in the two questions discussed earlier.

In practice, the problem of getting energy into the RAM and then absorbing it is normally handled by changing the electrical properties of the absorber as a function of the distance the wave travels into the material. The theory required to analyze such behavior is relatively simple for the case of plane wave incidence on flat surfaces, where discrete layers of homogeneous (within the layer) isotropic material are used. The inclusion of very thin layers of resistive material (or impedance sheets) adds very little complication to the theory. Two equivalent forms of the general theory are provided in Sections 8.3.3 and 8.3.4.

8.3.1 Thin-Sheet

Characterization Using Ohms per Square

A number of specular and nonspecular RAM designs employ thin resistive sheets to provide the loss mechanism. The characteristics of such

[REDACTED]

[REDACTED]

[REDACTED]

[REDACTED]

sheets are usually described in terms of their resistance or impedance in “ohms per square” (often denoted $\Omega/\text{sq.}$ or Ω/D). Because that electrical unit is likely not familiar to many readers, it is worthwhile at this point to define it. If a block of material with a resistivity ρ in $\Omega\text{-m}$, as shown in Figure 8.1(a), is used to make a resistor, the resistance between two opposite faces of the block is given by

Figure 8.1. Origin of the ohms-per-square notation: (a) a block of resistive material, (b) ohms-per-square resistance measurement.

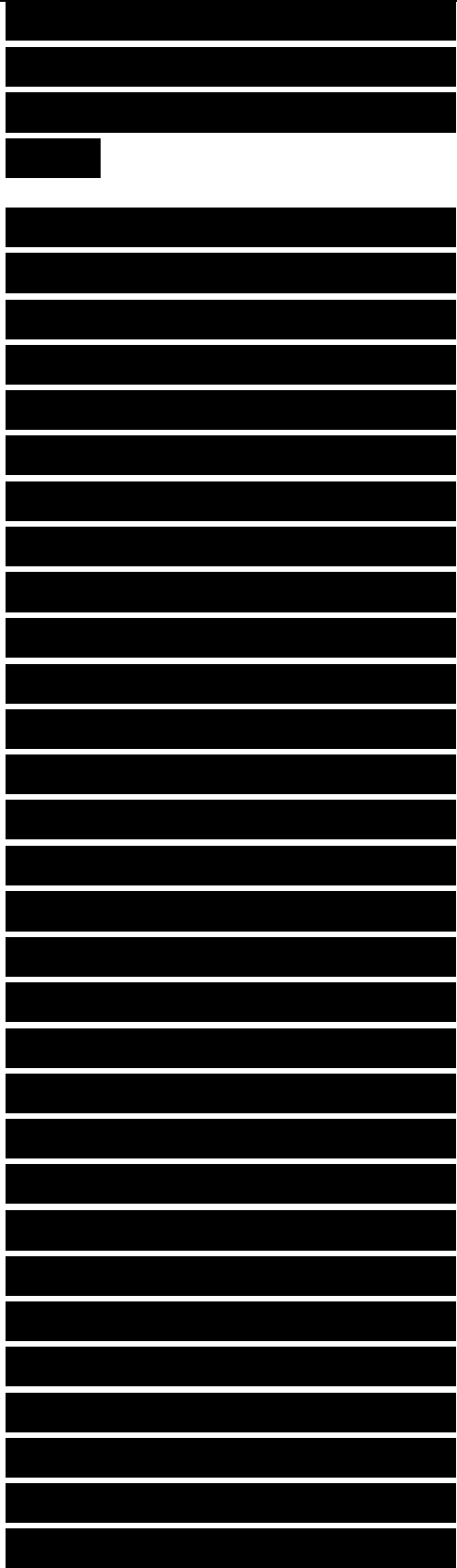
where L is the length of the block between the two faces, and the product of the width, W , and thickness, T , define the cross-sectional area, A , of the block of material.

If we take a sheet of material, place conductive bars across the width dimension, as shown in Figure 8.1(b), and measure the resistance between two bars a distance W apart, (8.10) becomes $R = \rho L/T = \rho L/A$ (the length and width, being equal, cancel). If we measure the resistance across any square piece of the material using the procedure just indicated, the



result will be the same, regardless of the size of the square. Thus arises the nomenclature ohms per square.

In modeling electromagnetic performance, the concept of an infinitesimally thin impedance sheet is valid only if the sheet is much less than an electrical wavelength thick. For example, the theoretical Salisbury screen absorber (see Section 8.4.1) is made of an infinitesimally thin 377 Ω /sq. resistive sheet in front of a conducting plate. At frequencies where the sheet spacing from the plate is an odd number of quarter-wavelengths, a zero reflection coefficient is achieved at normal incidence. For a stand-off distance of 7.5 mm ($\lambda/4$ at 10 GHz), if a 0.1 mm thick resistive sheet with an $\epsilon_r = 5$ is used, the maximum RCSR achieved is 31.6 dB at a frequency of 9.6 GHz, rather than infinite RCSR at 10 GHz. Use of a 1 mm thick, $\epsilon_r = 5$ sheet would result in a maximum RCSR of 13.4 dB at 6.9 GHz. Note that both the real and imaginary parts of ϵ_r will affect the shift in the resonant frequency, and the maximum RCSR obtained. Thick resistive sheets (like those discussed as illustration) can be modeled as layers of

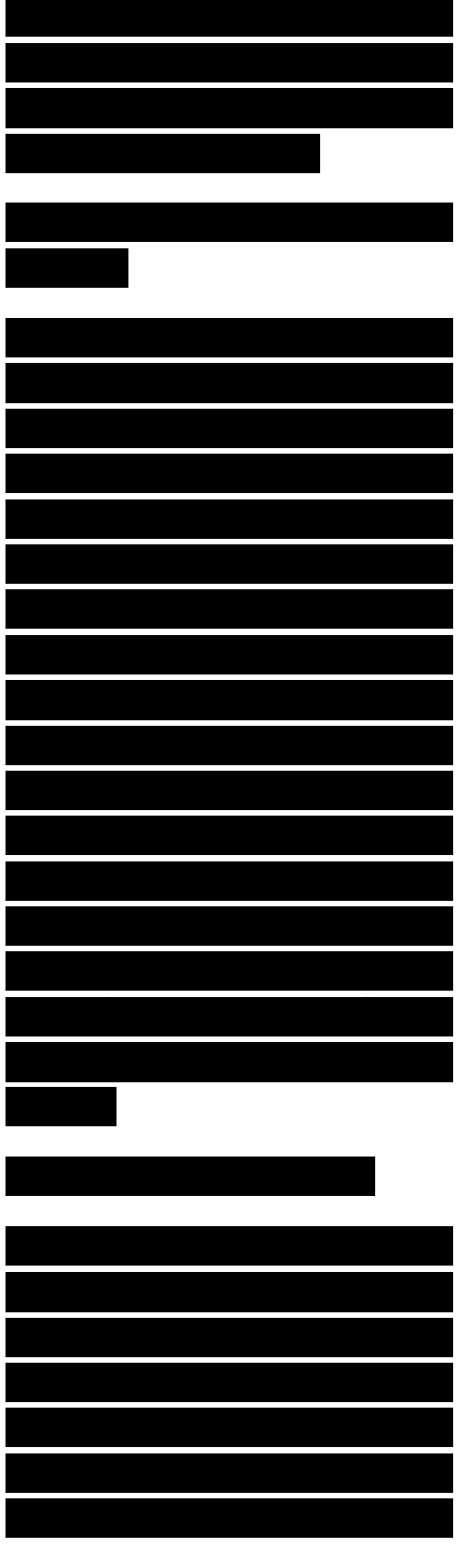


finite thickness whose ϵ_r is typically dominated by the base material, and whose lossy component is given by $\epsilon_r = \epsilon_0 - j\sigma/\omega$.

In the next two subsections, the equations for normal incidence and then arbitrary incidence of an EM wave on a flat dielectric multilayer are developed. The problem is then approached from the wave matrix point of view, and the relationship between the scattering matrix and cascade matrix is provided. Finally, an approximate procedure for determining the reflection coefficient of complicated multilayers is discussed. This approximation is particularly helpful in providing a starting point for absorber codes that use optimizers to iterate a design.

8.3.2 Normal Incidence Scattering

Calculation of the reflection of a normally incident plane wave from an infinite flat multilayer structure is a straightforward problem involving application of boundary conditions derived from Maxwell's equations to the general solution for the electric and magnetic fields in



each layer. The functional form of the fields, complex exponentials, and the stepping procedure required for multilayers make implementation of the equations on a computer (or programmable calculator) desirable. Note that existing transmission line design computer programs can often be used for absorber design, either as they are or with slight modifications.

The basic geometry to be considered is that of a finite number of dielectric layers stacked against a metallic backing plate, as shown in Figure 8.2. The layer properties may differ from one layer to the next, or they may be the same. It is assumed that impedance sheets of zero thickness may be sandwiched between layers, as suggested in Figure 8.3. The sheets can be characterized by a resistance value R in ohms per square, or by a conductance, G mhos per square, where

G

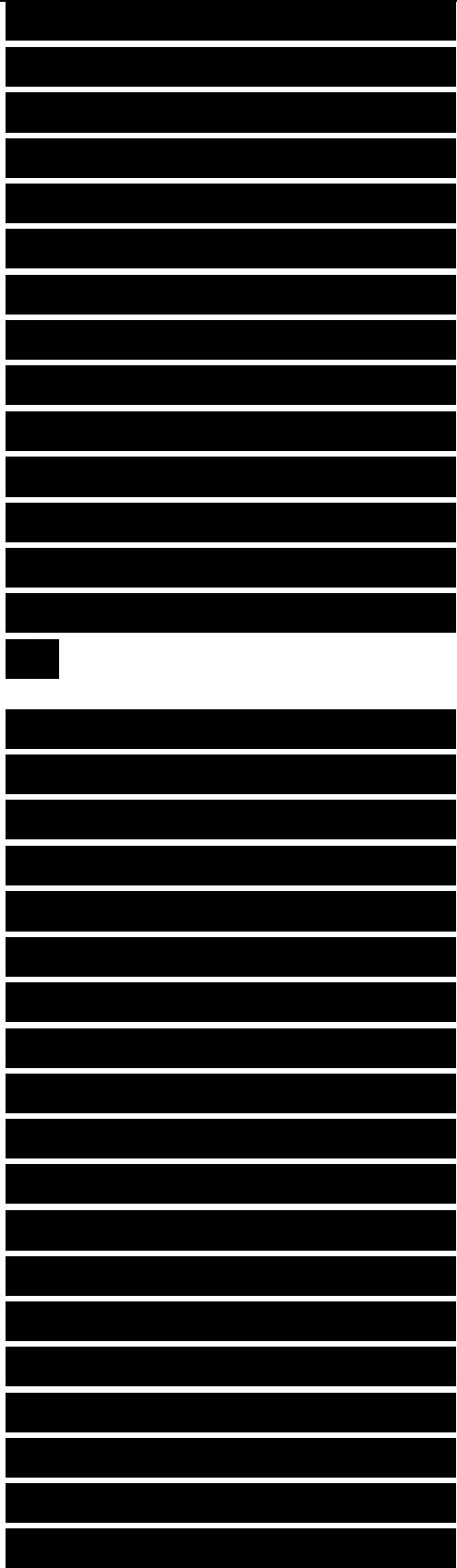
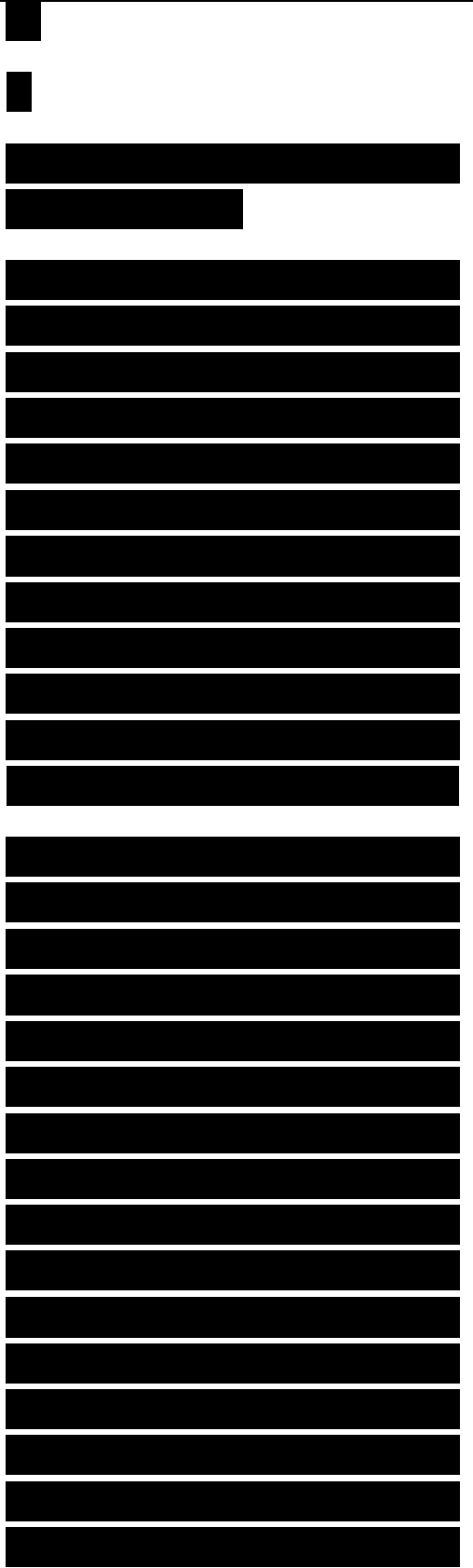


Figure 8.3. Resistive sheet sandwiched between two dielectric layers.

$G = R^{-1}$. For cases such as circuit analog absorbers, where the sheets can provide a complex impedance, the resistance R may be directly replaced by the impedance Z or the conductance G by the admittance Y . To minimize confusion in notation in the following analysis, G will be used for the sheet admittance to differentiate from the dielectric layer intrinsic admittance, which is denoted Y .

The approach used to analyze the scattering is to postulate the form of the electric and magnetic fields in the dielectric layers on either side of the resistive sheet and to specify the boundary conditions these fields must satisfy. This allows the coefficients of the field representation on one side of the sheet to be related to those on the other side. Because the layers in Figure 8.2 are numbered outward from the backing plane, it is convenient to have x increasing to the left. Thus, the positive traveling wave will be associated with



the B coefficients in Figure 8.3.

The electric and magnetic field structure in a given layer is taken to be

$$E = A e^{-ikx} + B e^{ikx} \quad (8.11)$$

$$H = Y(A e^{-ikx} - B e^{ikx}) \quad (8.12)$$

where A and B represent the amplitudes of forward and backward propagating waves, and Y is the layer intrinsic admittance. The boundary conditions to be satisfied at the interface are

$$E_+ = E_- = J \quad (8.13)$$

$$H_+ - H_- = /$$

where the plus and minus superscripts denote the fields on opposite sides of the sheet, and J is the current flowing in the sheet.

If the resistive sheet location or the boundary between two layers is represented by x_n , and subscripts per Figure 8.2 are appended to the quantities in (8.11) and (8.12) to identify the two media, then the application of (8.13) yields two equations:

$$A_m e^{-k_m x_n} + B_m e^{i k_m x_n} = A_n e^{-k_n x_n} + B_n e^{i k_n x_n} \quad (8.14)$$

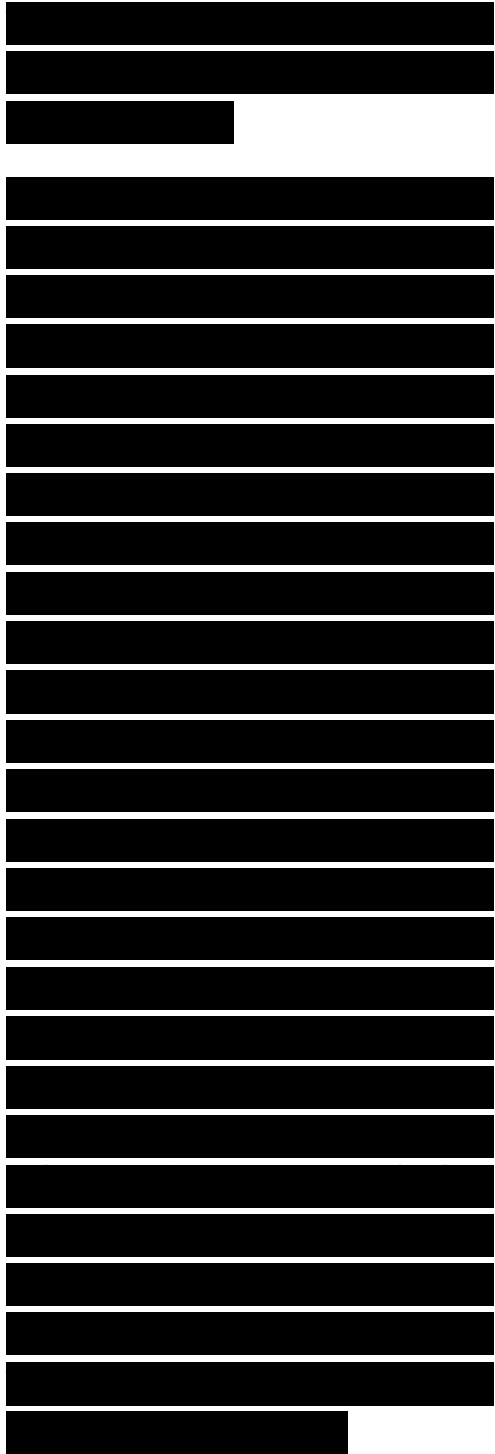
$$Y_m (A_m e^{-k_m x_n} - B_m e^{i k_m x_n}) - Y_n (A_n e^{-k_n x_n} - B_n e^{i k_n x_n}) = J$$

$$e^{ik_m x_n} = (G + Y_n) A_n$$

$$e^{-ik_m x} + (G - Y_n) B_n = Q e^{ik_m x}$$

These equations may be used to find A_m and B_m in terms of A_n and B_n :

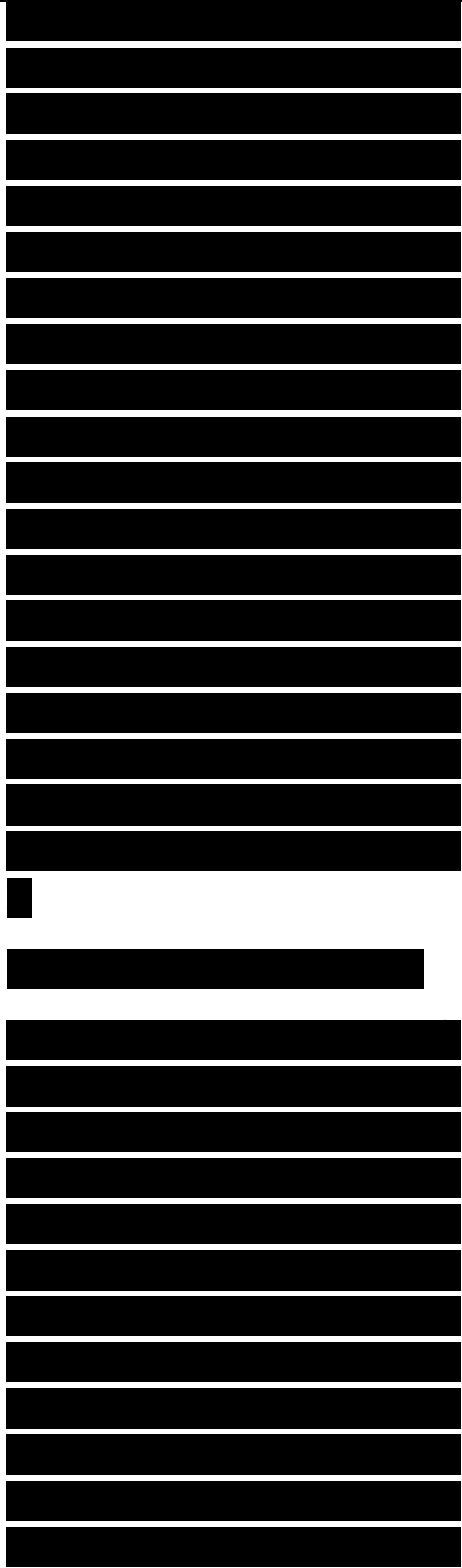
The stepping procedure begins with the assignment of arbitrary values to A_i and B_i , the coefficients of the fields in the first layer, which is adjacent to the metal sheet. For a metallic backing, the total electrical field must vanish on the sheet, therefore by (8.11), at $x = 0$, $B_i = -A_i$. The arbitrary assignment $A_i = 1$, $B_i = -1$ satisfies this particular condition. If there is no metallic backing (i.e., if the backing is free space), no wave will be traveling to the left, hence $B_i = 0$ at $x = 0$. Next, the transformer relations (8.15) are used at the first interface located at $x = x_i$, and A_2 and B_2 are calculated. (In a computer code, a pair of variables may be replaced by updated values representing the change as a boundary is traversed.) The sequence is iterated until the $N + 1$ layer is reached, which is free space outside the structure.



Because the stepping is initiated by using arbitrary values for A_{\backslash} and B_{\backslash} , the final results of A_{N+} and B_{N+} are in error by precisely the same amount as A_{\backslash} and B_{\backslash} , because the transformations across the boundaries are linear operations. It can be assumed without loss of generality that outside the structure the incident wave has unit amplitude, and the reflected wave has an amplitude R (for the reflection coefficient). Therefore, all the coefficients could have been corrected by normalizing with respect to A_{N+} , had it been known at the outset. Because the normalization constant is now known, the reflection coefficient R , associated with the structure, is simply

8.3.3 Oblique Incidence Scattering

The preceding discussion details the simplest case of scattering from planar multilayer structures, that of normal incidence. This section generalizes to the more complex case of oblique incidence. The geometry is similar to that defined in Figures 8.2 and 8.3, except that the directions of the propagating waves are not necessarily normal to the layer boundaries, an example of



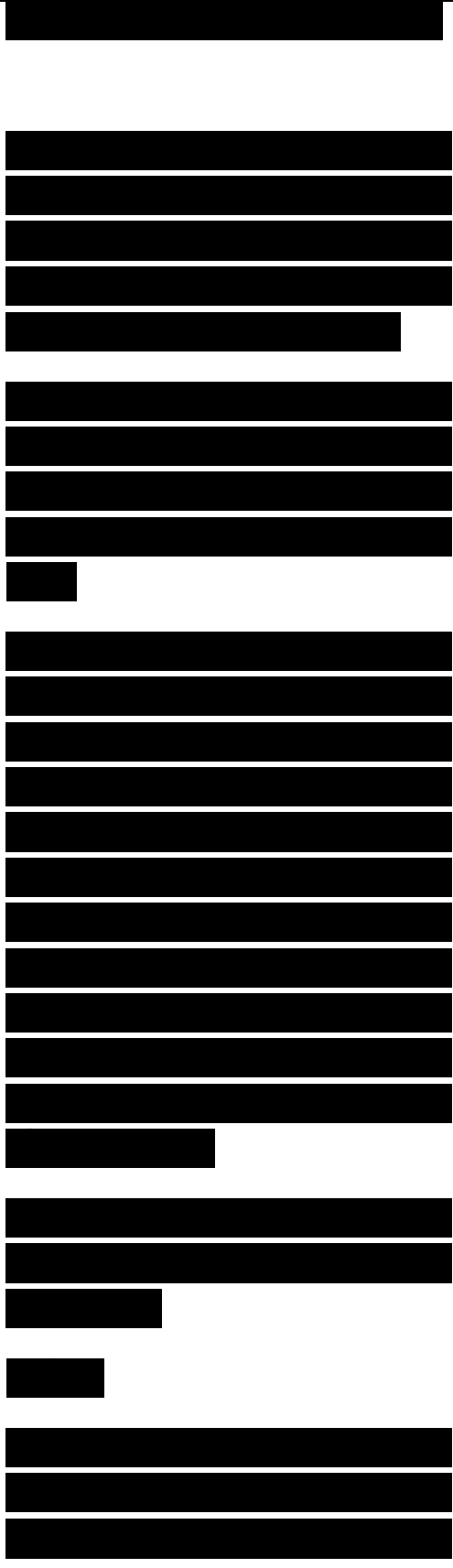
which is illustrated in Figure 8.4. For this case, the form of the wave will be where x is normal to the layer boundary and positive upward, and z is to the right in Figure 8.4. Note that (8.17) reduces exactly to (8.11) for $\theta = 0$.

Along with the previous boundary conditions on the z component of the fields, there is an additional requirement, given by Snell's law, that

Obviously, if k_m or k_n is complex, implying lossy media, the sine of the angles in general must also be complex for the equality to hold. The complex angle is a result of the fact that the planes of constant phase and planes of constant amplitude no longer coincide, and so a plane wave no longer exists [1]. Although the concept of a "complex angle" may be difficult to grasp, we may allow θ to be complex, so that

Figure 8.4. Wave propagation and reflection in a dielectric multilayer for oblique incidence.

Then The net result of having a complex angle is that the imaginary component introduces an attenuation factor

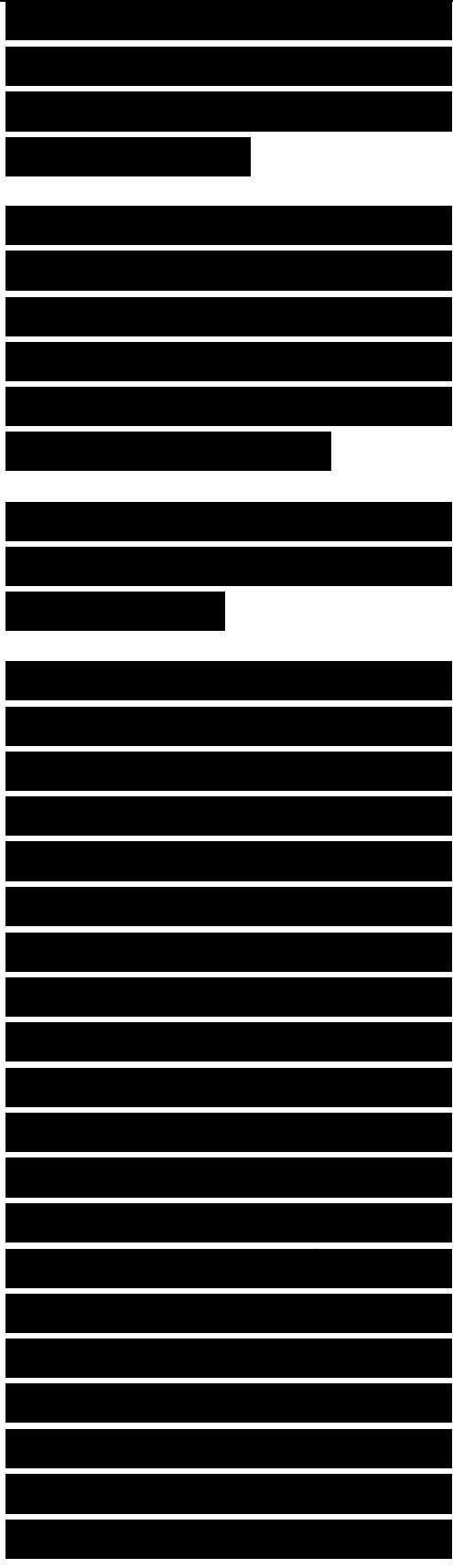


in the propagation of the transmitted wave, in addition to the usual attenuation associated with the imaginary component of the complex wavenumber.

For the case of oblique incidence two cases must be considered. The first, for the electric field parallel to the interface, provides a formula for the coefficients of

The second case is for the magnetic field parallel to the interface, for which

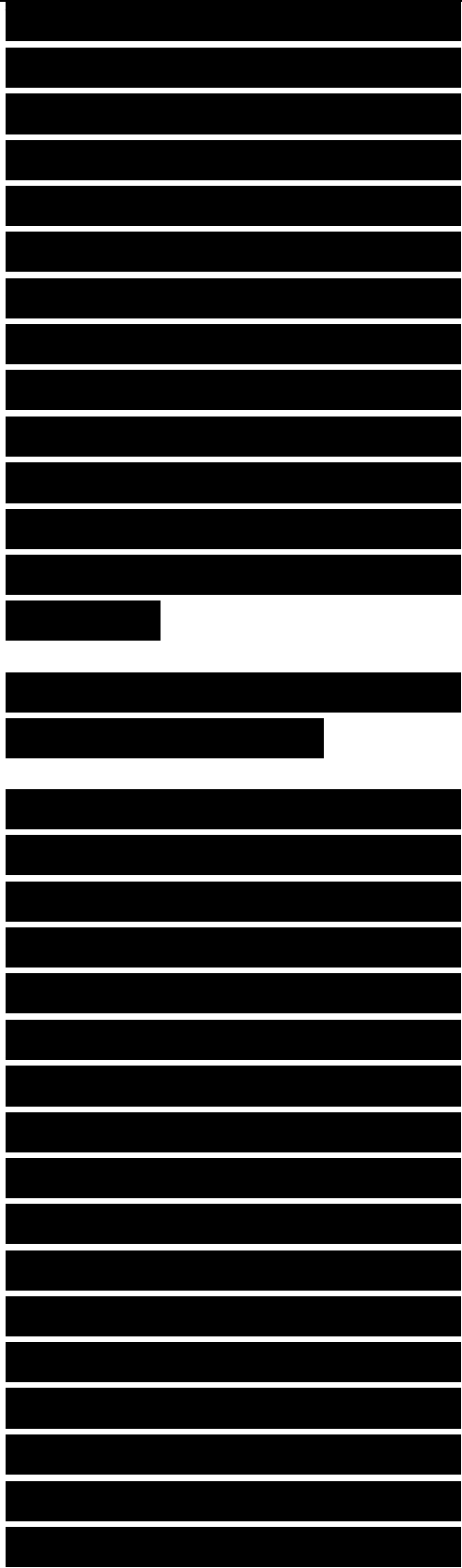
As in the case of normal incidence, a stepping procedure is used, where the boundary conditions at the innermost boundary are used to determine the relationship between A_i and S_i . Each successive layer is then stepped through until free space is reached. However, for the case of oblique incidence, generally the incidence angle on the outermost layer is given, whereas the first angle required in the computation is that in the innermost layer. Therefore, a double stepping procedure is required, where we must begin at layer $N + 1$ (free space) and step inward, calculating the value of each θ_i by using Snell's law. These values can be stored and then recalled, as needed, when the program



steps out from the inner layer outward to calculate the values of A and B. As before, the reflection coefficient is given by (8.16). Note from Figure 8.4 that this procedure calculates the specular reflection coefficient, not the backscatter reflection coefficient. Only in the case of normal incidence will the two coincide.

8.3.4 The Wave Matrix Approach to Scattering

An equivalent approach to calculation of scattering from flat multilayer dielectrics is the wave matrix approach. The basic analysis can be conducted in terms of either cascade matrices, relating the output side of a two-port to its input side, or in terms of scattering matrices, which relate the incident and reflected scattering coefficients. Collin [2] gives an excellent treatment of the cascade matrix approach in terms of reflection and transmission coefficients. The description given here utilizes the scattering matrix parameters because those are generally the most easily

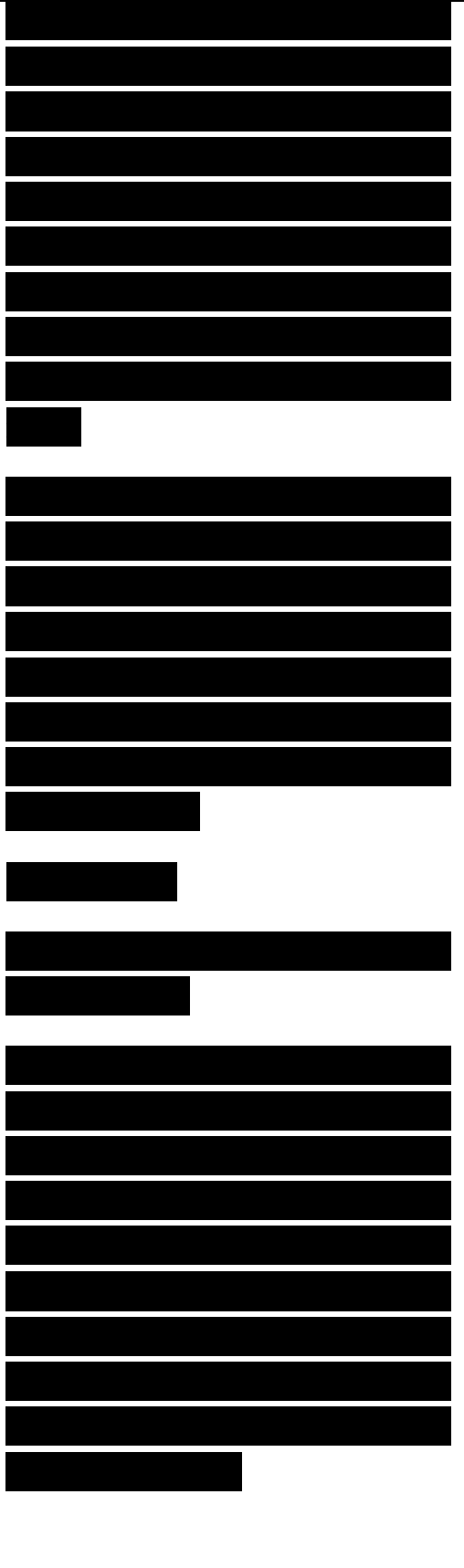


measured characteristics of a two-port network. This treatment follows Kerns and Beatty [3], and it should be noted that Collin's matrix notation and Kern's and Beatty's differ.

The shunt element circuit of Figure 8.5 might represent a circuit analog sheet or a resistive sheet in an absorber layup. The reflected waves (b_1 , b_2) at each side of its two ports are related to the incident values (a_1 , a_2) by the scattering matrix [5], where

Figure 8.5. Shunt equivalent circuit element.

In terms of reflection and transmission coefficients, S_{11} is the reflection coefficient seen by a wave incident at port 1 with port 2 having a matched termination, similarly S_{22} is the reflection coefficient seen from port 2, and S_{21} and S_{12} are the transmission coefficients from ports 2 to 1 and 1 to 2, respectively. For a shunt circuit with admittance Y , the scattering matrix is



The scattering matrices necessary to define the other elements of a multilayer dielectric are the interface between dielectric layers and the phase shift due to a dielectric layer. A material interface is described in terms of the admittance on the “left” (Y^-) and “right” (Y^+) sides of the interface by

where the admittances depend on the polarization and angle of incidence and are given by

$$Y_{TE}^- / Y_0 = \epsilon_r \cos \theta_i / \epsilon_r - \sin^2 \theta_0 \quad (8.26)$$

for the electric field parallel to the interface and

$$Y_{TE}^+ / Y_0 = \epsilon_r \cos \theta_i / \epsilon_r - \sin^2 \theta_0 / \epsilon_r \quad (8.27)$$

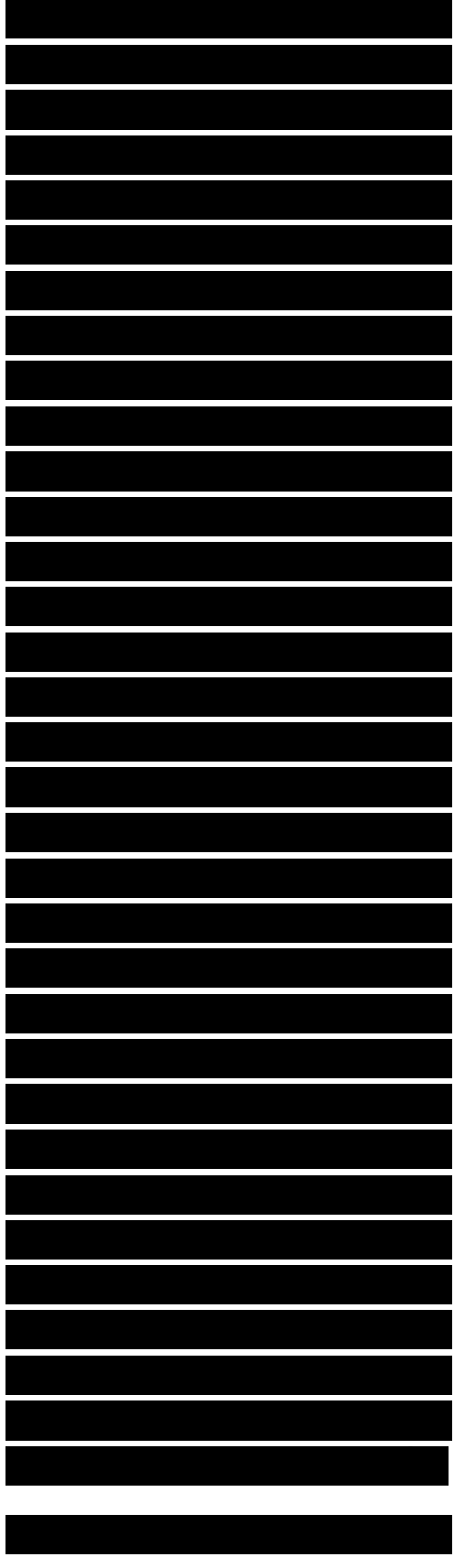
for the magnetic field parallel to the interface, where (θ_i is the angle of incidence at the left side of the interface.

A slab of dielectric of thickness d potentially introduces a phase shift and a loss, and its scattering matrix is given by where

An ability to directly use the scattering matrix components in absorber design is

particularly useful in light of current materials metrology procedures. As described in Section 9.3.2, vector network analyzers can be configured to rapidly measure the scattering matrix parameters at closely spaced frequencies over a wide bandwidth. However, the definition of the scattering matrix, which relates the reflected signals on each side of a two-port device to the incident signals (i.e., from Figure 8.5, relates b_1 and b_2 and a_1 and a_2), is not suitable for calculation of the reflection and transmission properties of a multilayer configuration. What is required, instead, is a matrix formulation that relates the inputs and outputs on one side of the two-port to those on the other side (i.e., relates a_1 and b_1 to a_2 and b_2). For this purpose, the cascade matrix, $[T]$, is normally used, because the properties of a cascade connection of shunt elements and spacers is given by a total cascade matrix $[T]_r$, which is simply the product of the component matrices:

The wave matrix approach is particularly useful in the



analysis of circuit analog (CA) designs, for which it is often desirable to use the measured properties of fabricated CA sheets to predict performance.

8.3.5 An Approximate Scattering Analysis Procedure

The analyses of the proceeding sections provide excellent tools for the evaluation of RAM performance. For use in the design stage the formulations presented can be integrated with optimization routines to provide maximum performance within a given set of constraints. However, although current RAM design efforts are usually based on computer optimization techniques, it is desirable to begin the optimization routine with a parameter set as close to optimum as practical. This generally implies that an analytical solution should be used to establish "first-cut" admittance parameters. Fortunately, RAM design practices are closely related to filter theory, and many of the tools developed for that arena can be utilized. This section briefly outlines the use of some of those tools in the design of

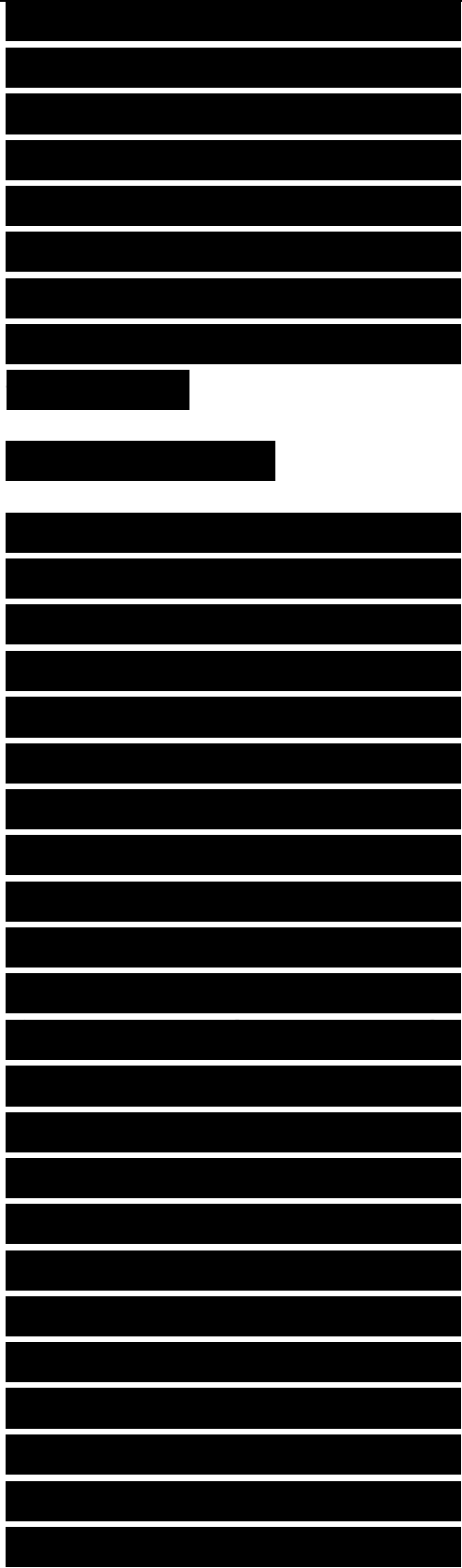
[REDACTED]

[REDACTED]

[REDACTED]

broadband absorbers using resistive sheets or circuit analog sheets separated by low-loss dielectric spacers.

Figure 8.6 illustrates the typical model assumed for this analysis. As noted in Section 8.3.3, each resistive or circuit analog sheet can be represented as an admittance shunted across the transmission line. A multielement, broadband design implies that the reflection coefficient at each shunt admittance will be small. A small reflection coefficient implies a small admittance for each shunt element. The small individual reflection coefficients allow us to assume that the total reflection coefficient is simply the sum of the reflection coefficients for each shunt element, modified by the appropriate phase shift due to line length. With this simple assumption, the characteristics of the reflection coefficient of an absorber design can be tailored to standard functions, such as a

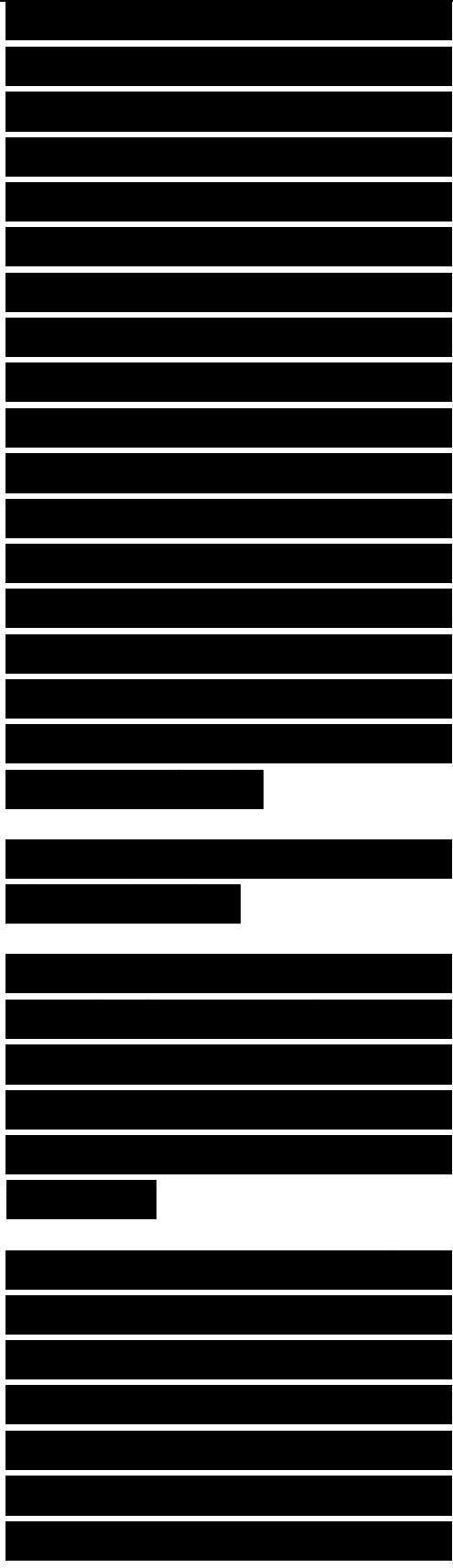


maximally flat or minimum ripple (Chebyshev) behavior with frequency. The analysis shown here is very similar to that of Collin [4], who considered the design of multilayer transformers using small reflection theory. In fact, an absorber can be considered a transformer between free space and a very small impedance. The only modification of Collin's analysis is to use shunt elements instead of transmission lines with varying characteristic impedances.

The reflection coefficient R of the absorber circuit is approximately

where multiple reflections have been neglected. The power reflection is the square of the absolute value of (8.32); and for one shunt element and two shunt element circuits it is given by

where all lines are assumed to be of equal length ($0 = kd$), the reflection coefficients are assumed to be real (to simplify the examples) and small, and the load reflection coefficient is -1 (i.e., a short circuit). The extension to $n > 2$ is



straightforward. Equation (8.33) can be written as a polynomial in powers of $\cos \theta$ by using standard identities, resulting in

A maximally flat design is achieved by setting the coefficients of all but the highest power terms to 0:

Similarly, a Chebyshev design is achieved by setting the coefficients equal to the Chebyshev polynomial coefficients:

where θ_i is evaluated at the edge of the frequency band.

Within the small reflection approximation, the reflection coefficient is related to the normalized shunt conductance via

It is interesting that this approximation provides the exact Salisbury screen result of a unity conductance for the single-layer maximally flat design. Similarly, the exact maximally flat result for the two-layer case is known to be

which is very close to the approximate result of $G_1 = 4/3$, and $G_2 = 1/3$, found by using

[REDACTED]

[REDACTED]

[REDACTED]

[REDACTED]

[REDACTED]

[REDACTED]

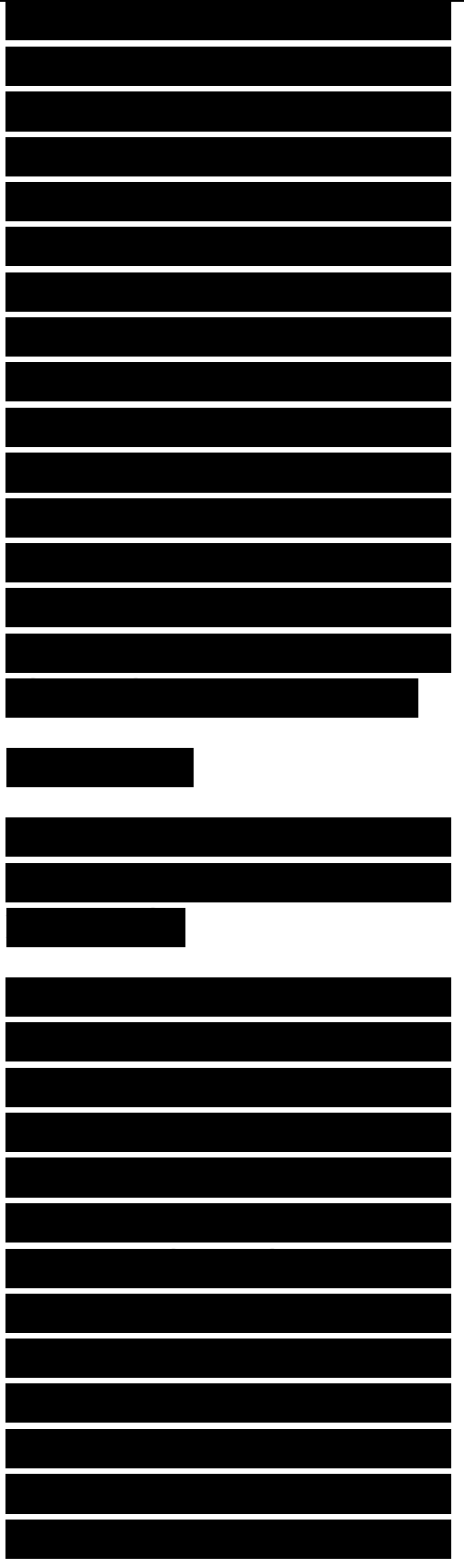
[REDACTED]

(8.35). The importance of this analysis is that it can easily be extended to complex admittances, additional layers, and other complications that render an exact analysis impossible. The approximate results can then be used as a starting point for an optimization program. Figure 8.7 illustrates the exact solution for the two-layer design given in (8.38). Also shown is the approximate result given in (8.35).

Frequency (GHz)

8.4 DIELECTRIC MULTILAYER ABSORBER DESIGN AND PERFORMANCE

The ideal radar absorber would be thin, light, durable, easily applied, inexpensive, and have broadband frequency coverage. As an alternative, we might wish to have a structural RAM that is mechanically sound and has no size, weight, or cost penalty over standard structural materials. As might be expected, neither of these ideal RAM types has yet been formulated. Nevertheless, since World War II (the Germans developed a magnetic RAM paint during the war and used it



to reduce the RCS of submarine conning towers), a significant amount of effort has been invested in the development of absorbers that are practical for military applications.

To illustrate absorber design and performance, RAM types that are in widespread use are described and their properties are analyzed. Although the emphasis is on broadband absorbers, the descriptions start with simple, narrowband, singlelayer absorbers, which form the components for multilayer broadband absorbers. An underlying assumption in the treatment provided is that RAM volume is a constraint. Therefore, little attention is given to the design of RAM for anechoic chambers and other similar applications, although those types of absorbers are briefly described as examples of geometric transition RAM and are described in more detail in Chapter 13.

8.4.1 Salisbury Screens and Dallenbach Layers

[REDACTED]

[REDACTED]

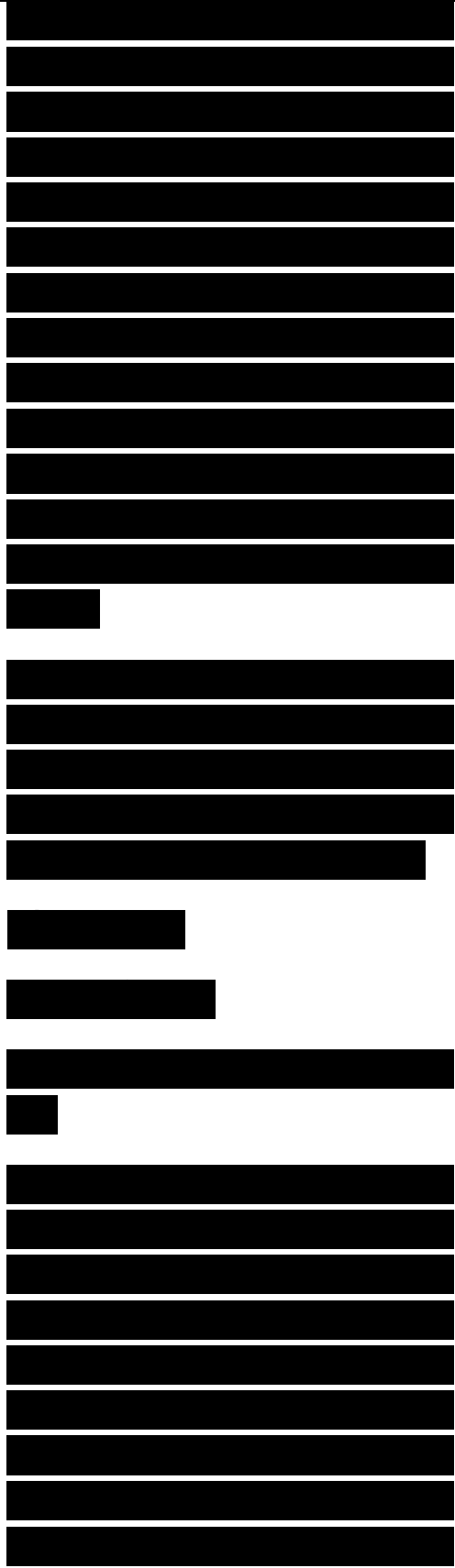
[REDACTED]

Two of the oldest and simplest types of absorbers are represented by Salisbury screens and Dallenbach layers. The Salisbury screen [5] is a resonant absorber created by placing a resistive sheet on a low dielectric constant spacer in front of a metal plate. The Dallenbach layer [6] consists of a homogeneous lossy layer backed by a metal plate. Each is analyzed in the following.

Figure 8.8 illustrates the geometry of the Salisbury screen. In the analysis of its performance, we assume that an infinitesimally thin resistive sheet of conduc-

Resistive Sheet
Incident Plane Wave

Plastic Foam or Honeycomb Spacer
tance G , normalized to free space, is placed a distance d from a metal plate. Typically, a foam or honeycomb spacer might be used, so spacer dielectric constants in the 1.03 to 1.1 range are normal. To simplify this analysis, the normalized permittivity of the spacer is assumed to be that of



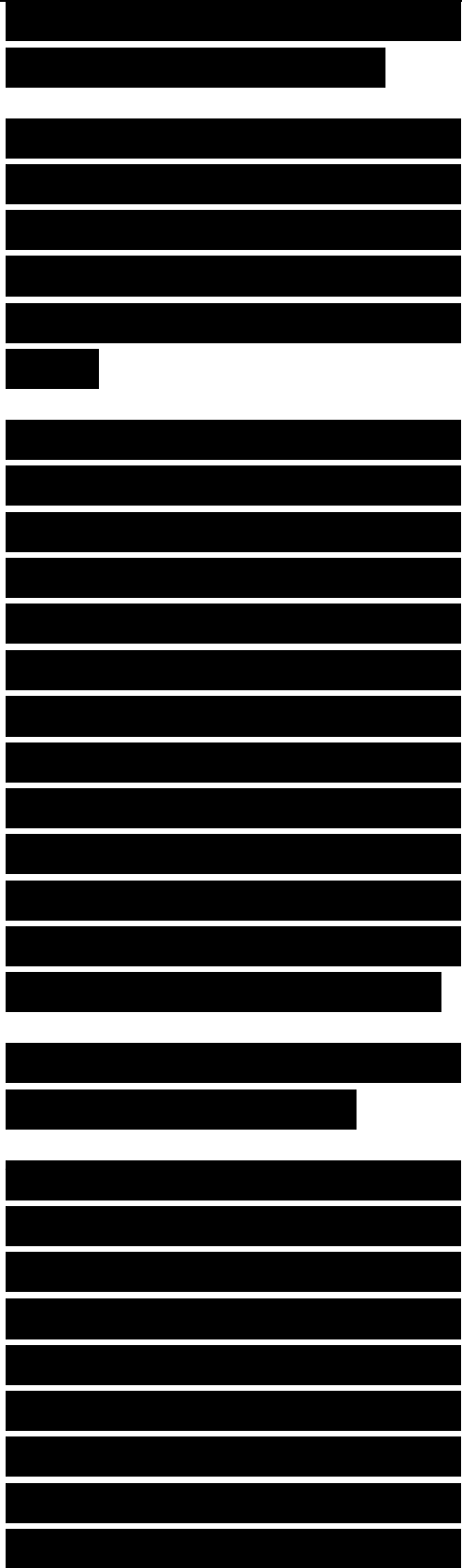
free space (i.e., $\epsilon_r = 1$).

From (8.16), the reflection coefficient for a dielectric multilayer will be 0 if B_{n+} is forced to 0. For the simple case of the Salisbury screen, substituting in (8.15),

where $Y_1 = Y_2 = 1$ (free space), and $k_2 = k_0 = 2\pi/\lambda$ (the free-space wavenumber). $B_2 = 0$ only if the quantity in brackets is 0. This requires that the magnitudes of the two exponentials in the brackets be equal and that their phase angles be opposite. The equal amplitude requirement forces G to equal 1, or equivalently, the unnormalized resistance to be $377 \text{ } \Omega/\text{sq}$. In that case, (8.39) becomes

The condition $B_2 = 0$ requires $\cos(2W/\lambda) = 0$, which implies that

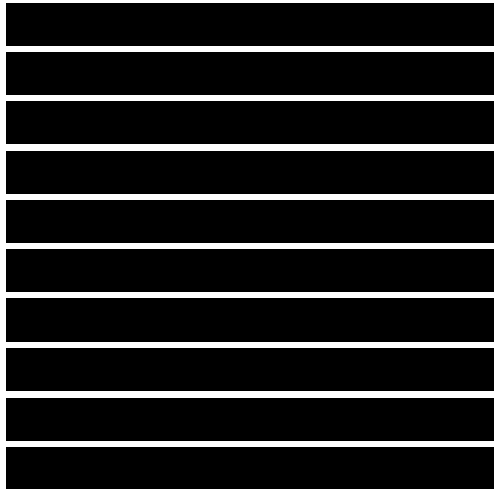
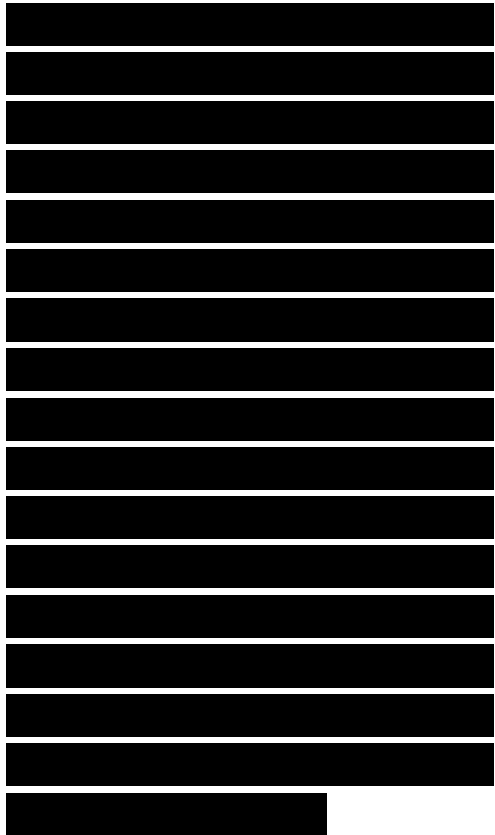
Thus, for zero reflectivity, a Salisbury screen requires a $377 \text{ } \Omega/\text{sq}$ resistance sheet set at an odd multiple of an electrical quarter-wavelength in front of a perfectly reflective backing. Higher dielectric constant spacers may be used and still satisfy (8.40), but with a consequent reduction in bandwidth, because k for that



case will be larger than k_0 , and thus a given frequency change will cause a larger change in B_2 than for the $\epsilon_r = 1$ spacer.

Another way to think of the Salisbury screen is in transmission line terms. A quarter-wavelength transmission line transforms the short circuit at the metal plate into an open circuit ($G = 0$) at the resistive sheet. The sum of the sheet and open circuit admittances, which is the value seen by the impinging wave, is just that of the sheet, $1/377$ mho, and thus a matched load is provided and no reflection occurs. By the same token, at multiple half-wavelength spacings, a short circuit is again seen and perfect reflection is obtained.

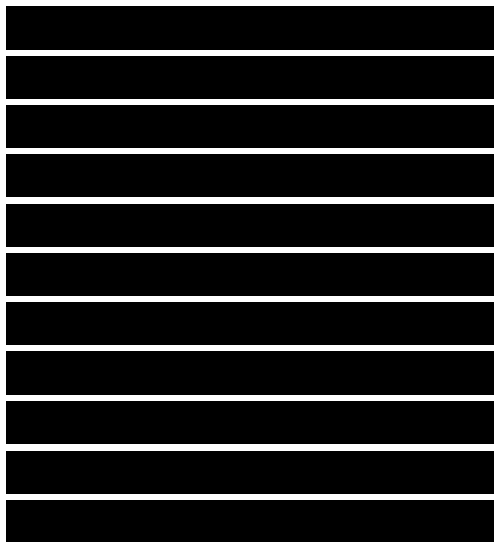
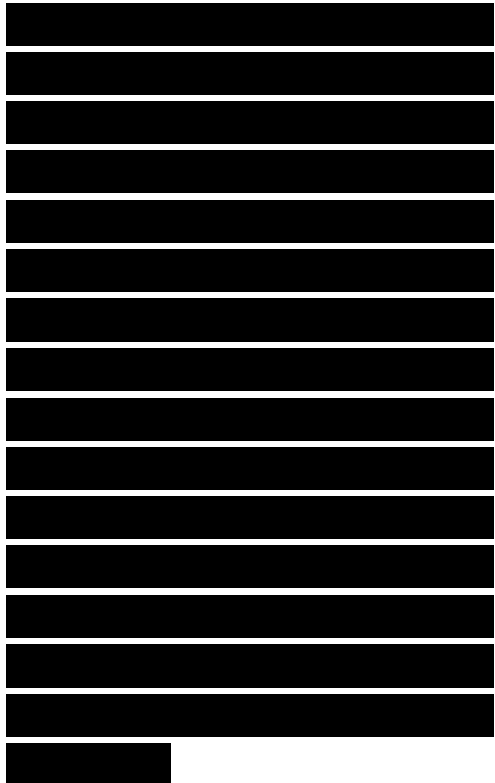
The screen performance for a 1.27 cm spacing is shown in Figure 8.9. Note that the reflection coefficient reaches its minimum value at a frequency of 5.9 GHz ($\lambda = 5.08$ cm). The best performance is obtained for a resistivity of 377 fl/sq, but the performance is still a respectable -18 dB for a resistivity 20% lower (300 fl/sq). However, a resistivity of



2000/sq yields barely a -10 dB reflectivity level at the design spacing. The fractional bandwidth for the 377H/sq screen at a - 20 dB reflectivity level is about 25%.

To achieve similar performance at a lower frequency, the spacing must be increased because the wavelength becomes longer. This effect is shown in Figure 8.10, and it will be observed that a pair of nulls now exist, one at three times the frequency of the other. The minimum reflectivity levels are the same as those in Figure 8.9. The nulls will occur at odd integral multiples of the lowest frequency due to the fact that the design spacing can be any odd multiple of a quarter-wavelength.

The Salisbury screen has been used in varying degrees in commercial absorbing materials. However, the rapid oscillations for large spacings would render it ineffective over a wide frequency range. For increased mechanical rigidity, plastics, honeycomb, or higher density foams may be used as spacers. To maintain the electrical spacing, the resistive sheet would be mounted over a dielectric layer trimmed to be



an electrical quarter-wavelength in thickness. As noted before, the gains in mechanical rigidity and decreased thickness obtained by using a higher dielectric constant spacer are paid for in reduced absorber bandwidth.

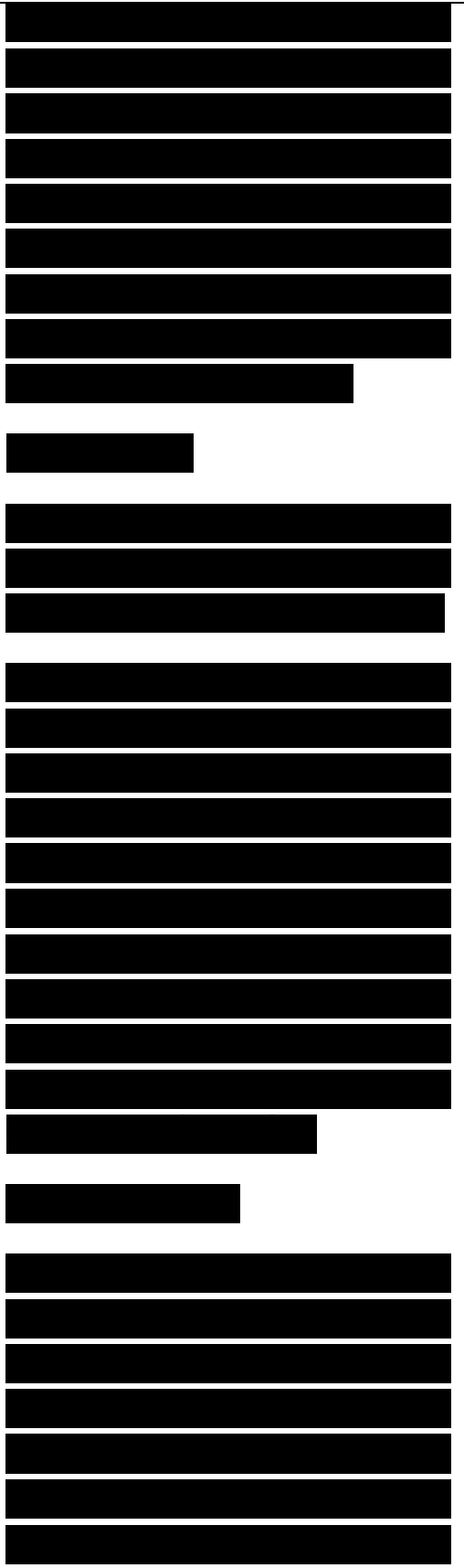
Frequency (GHz)

Figure 8.10. Theoretical performance of a Salisbury screen for a stand-off distance of 2.54 cm.

The preceding analysis assumed normal incidence of a plane wave on the absorber. It is interesting to explore the specular performance of the Salisbury screen at off-normal angles. It can be shown [6] that the magnitude of the reflection coefficients for both parallel and perpendicular polarizations are given approximately by

$$w-w-fr^K \quad (8-42)$$

where θ is the angle off-normal. Equation (8.42) is plotted in Figure 8.11. Note that performance is better than 20 dB (i.e., $|R| < 0.1$) for angles up to 35° . A more exact analysis of general RAM performance as a function of



incidence angle can be found in [7], but the error (8.42), is no worse than 5 dB, and therefore it is useful as a rough estimate of Salisbury screen behavior with angle.

Another simple resonant absorber, the Dallenbach layer, is constructed of a homogeneous lossy layer backed by a metallic plate. The reflection at the surface of a material is due to the impedance change seen by the wave at the interface between the two media. Therefore, if a material can be found whose impedance relative to free space equals 1 (i.e., $\sqrt{\epsilon_r} = \sqrt{\mu_r}$), there will be no reflection at the surface. In this case the attenuation will depend on the loss properties of the material (ϵ''/ϵ' and μ''/μ') and the electrical thickness.

Unfortunately, materials with the appropriate dielectric and magnetic properties to act as a matched RAM over any appreciable frequency range are difficult to find, and so the question becomes one of optimizing the loss at a given frequency using available materials. For a single material layer backed by a conducting plate, the reflection coefficient is given by substituting (8.7)

[REDACTED]

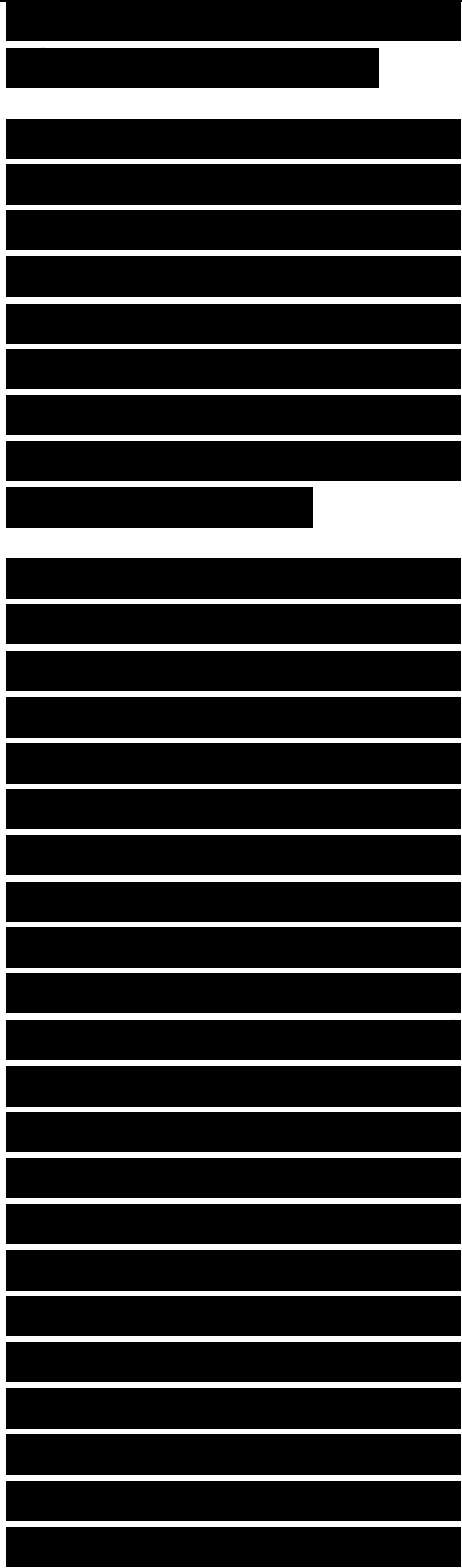
[REDACTED]

[REDACTED]

into (8.8) to provide

where d is the thickness of the layer. Figures 8.12 and 8.13 from [8] provide curves of reflection as a function of material thickness in wavelengths for several hypothetical materials. The permittivity and permeability are written in polar form per (8.3).

Several things should be noted from the plots. First, for nonmagnetic materials ($\mu_r = 1$), the best RCSR performance occurs when the material is near a quarter-wavelength thick electrically. The solid curve of Figure 8.12 illustrates this point. However, adding magnetic loss shifts the optimum electrical thickness to larger values because of the +1 reflection coefficient for the magnetic field at the conducting back plane. A pure magnetic absorber, if it were available, would have an optimum thickness near an electrical half-wavelength, as illustrated in Figure 8.13. Note on both figures that a hypothetical material with $\mu_r = \epsilon_r$, indicated by the diagonal traces, simply provides a linearly increasing loss in dB with increasing thickness in



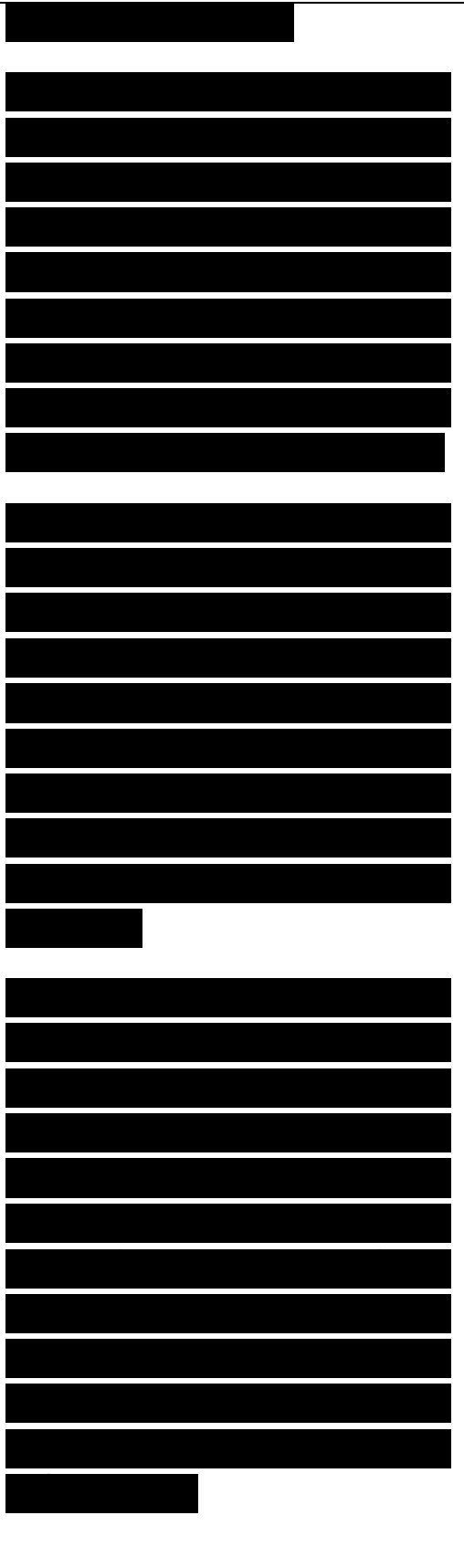
wavelengths.

Figure 8.13. Reflectivity curves for dominantly magnetic materials. Solid trace is for $|er| = 1$, $|tr| = 16$, $\theta = 0^\circ$, and $\theta = 10^\circ$. Dashed trace is for $|er| = 16$, $|jur| = 25$, $\theta = 20^\circ$, and $\theta = 30^\circ$. Diagonal trace is for $|er| = |ur| = 4$, $\theta = \theta = 15^\circ$.

For off-normal incidence, the behavior of a homogeneous layer is similar to that for Salisbury screens [6]. For the case where the index of refraction of the layer is much greater than 1, (8.42) provides a much better approximation to the angular performance for the Dallenbach layer than it does for the Salisbury screen.

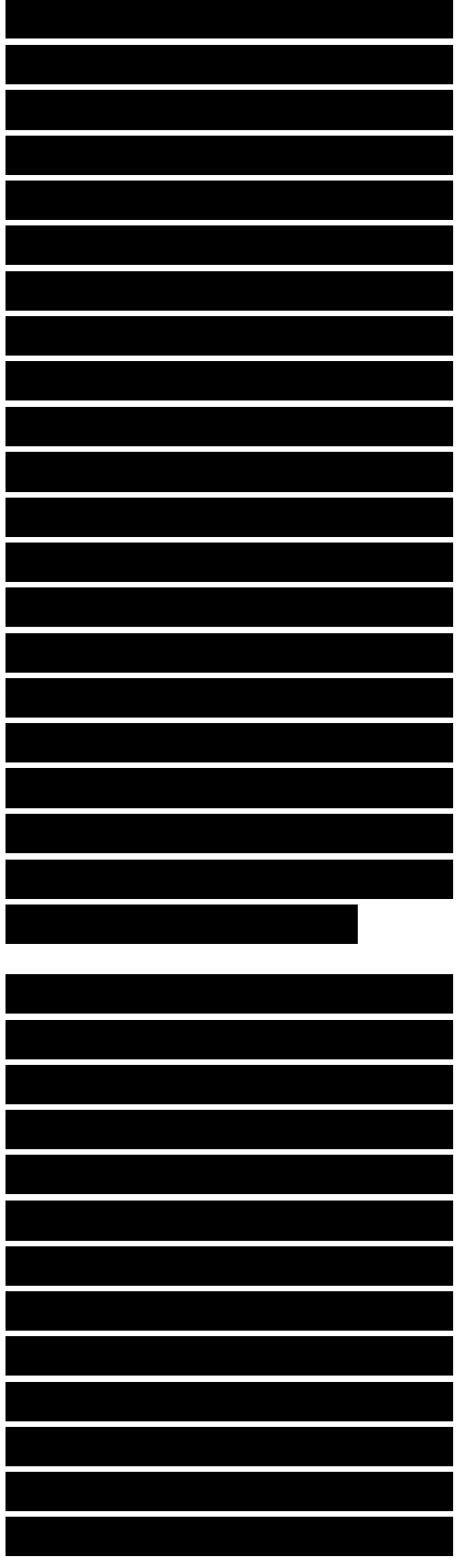
An additional question concerns the fractional bandwidth that can be achieved with the Dallenbach type absorber. Ruck [6] presents an analysis giving an approximate bandwidth for an ideal Dallenbach layer, assuming that the fractional bandwidth B is much less than 1, in terms of the material properties, the material thickness, and the wavelength at maximum RCSR performance, λ_0 , for a given reflection level R as

Figure 8.14 provides plots of



bandwidth for 20 dB RCSR versus thickness for single layers with only electric or magnetic losses. Note that a material with purely dielectric loss has a fractional bandwidth around 20% for a material thickness close to $X/4$, which is somewhat less bandwidth than for the Salisbury screen. For magnetic materials, the bandwidth increases as the material becomes thinner. The values plotted are not accurate for small electrical thicknesses because a large bandwidth violates an initial assumption. However, in the limit, the infinitesimally thin magnetic lossy layer is equivalent to a magnetic Salisbury screen that, in theory, has infinite bandwidth [6].

Another single layer absorber has been postulated and analyzed by Gauss at the Ballistic Research Laboratory [9]. It is based on mixing filaments of radar absorbing chaff (RAC) in a solid binder of near unity dielectric constant. Attenuation of the incident wave is provided by resistive dissipation in the filaments, which are metallic strands with length to diameter ratios of about 1000, and diameters of about 500 A.

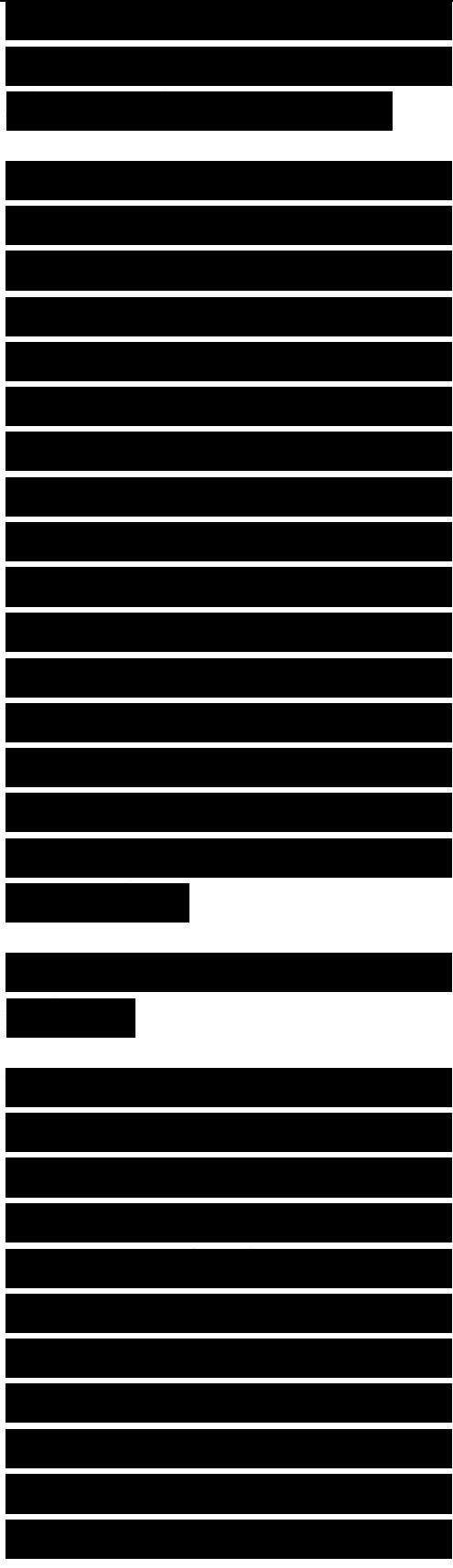


Filament separations in the binder are one-half to one-third the filament length.

An analysis is provided in [9] for two cases; the first is a regular array of filaments in the matrix and the second is for filaments with random orientation. Calculated RCSR for a 2 cm thick application using a regular array of filaments exceeds 30 dB from 10 GHz through 100 GHz. For the random filament orientation, RCSR is 13 dB at 10 GHz, and greater than 30 dB from 30 GHz through 100 GHz. It should be noted that the RCSR values quoted are theoretical and are not based on measurements of fabricated samples.

8.4.2 Multilayer Dielectric Absorbers

As noted in Section 8.4.1, it is difficult to achieve the wide bandwidths generally desired of radar absorbers by using a thin single-layer absorber. Therefore, much work has been done in extending the bandwidth of absorbers through the use of multiple layers. The approach employed is the same as that for pyramidal and other geometric transition absorbers—slowly

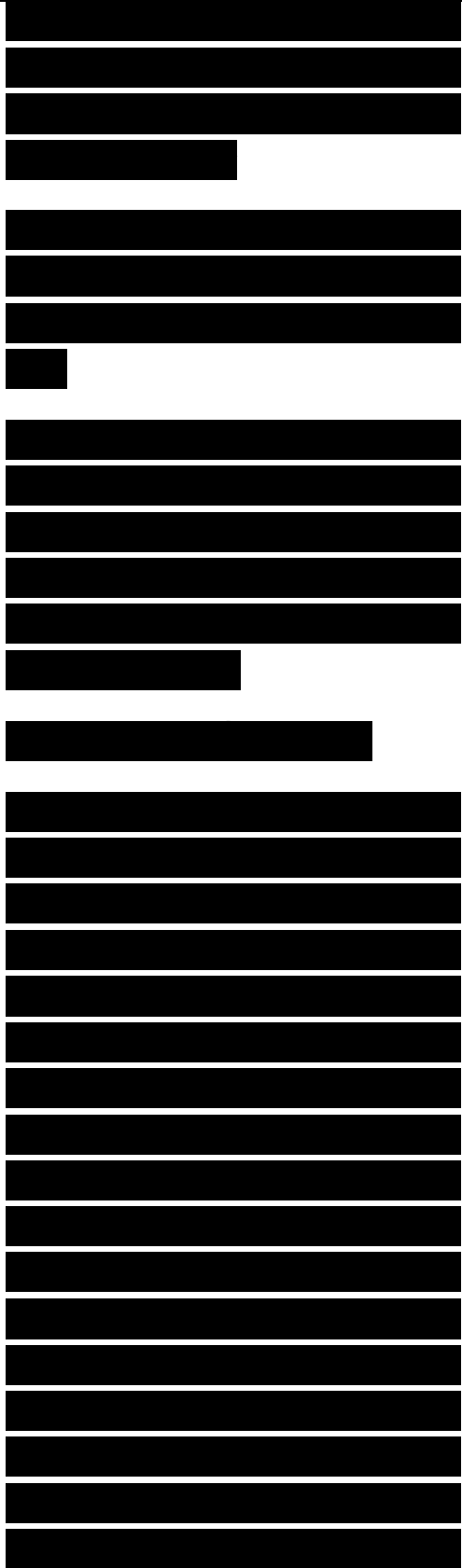


changing the effective impedance

Figure 8.14. Bandwidths of thin homogeneous (a) electric or (b) magnetic layers as a function of layer thickness (from [6]).

with distance into the material to minimize reflections. Two important types of multilayer absorbers will be discussed, Jaumann absorbers and graded dielectric absorbers.

The bandwidth of a Salisbury screen can be improved by adding additional resistive sheets and spacers to form a Jaumann absorber. To provide maximum performance, the resistivity of the sheets should vary from a high value for the front sheet to a low value for the back. The bandwidth is dependent on the number of sheets used, as illustrated in Figure 8.15 and Table 8.1. For this illustration, the spacing between sheets was fixed at 7.5 mm (a quarter-wavelength at 10 GHz) and a quadratic resistance taper was used. The fractional bandwidth for slightly less than 20 dB



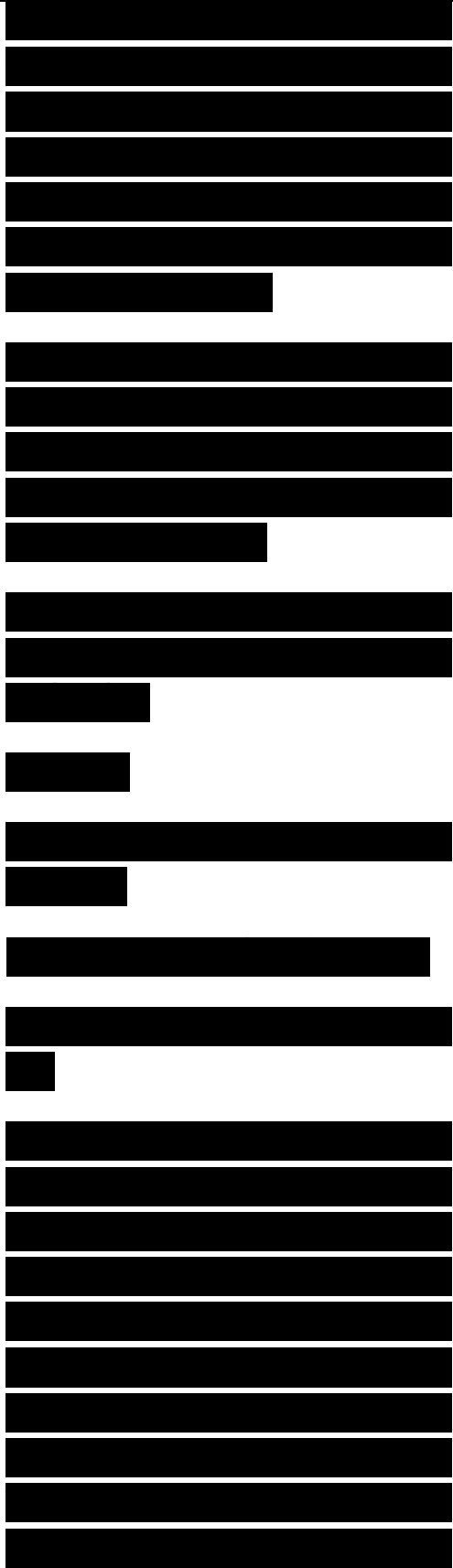
performance is shown in the table. Note that a four-sheet structure has about four times the fractional bandwidth of a single layer, but is four times as thick (3 cm versus 7.5 mm).

Even better performance is available for Jaumann absorbers with more sheets, as illustrated by a six-layer RAM in [10]. A 3.56 mm spacing between

Figure 8.15. Predicted performance of multiple-sheet Jaumann absorbers.

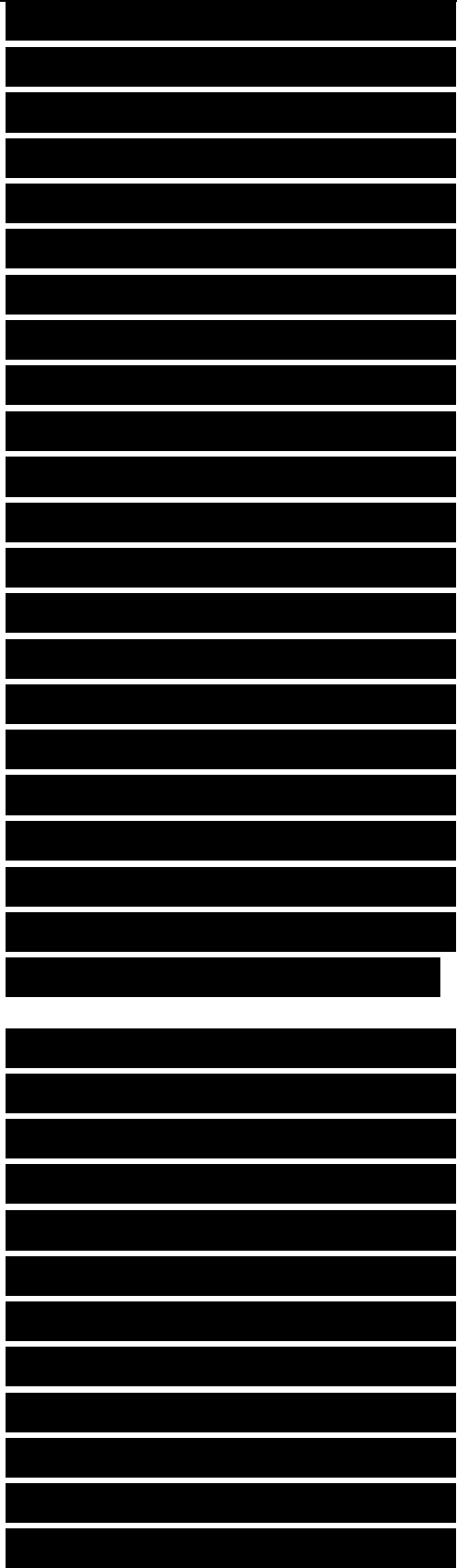
Table 8.1
Bandwidth of Jaumann Absorbers
Fractional Total
Number of sheets bandwidth
thickness (cm)

layers with a spacer $\epsilon_r = 1.03$ (probably styrofoam) was used. Table 8.2 provides resistivity values for the lossy sheets, and Figure 8.16 provides a plot of the predicted RCSR performance. Note the large change in resistivity from front to back provided by the approximate quadratic taper used. An average RCSR of 30 dB was measured for this



A more successful and useful approach has been to assume a model for ϵ and J_L as a function of the distance z into the absorber, and then to solve for the resulting reflection coefficient. A number of models have been used for the taper including linear, exponential, and one (Jacobs) making the fractional rate of change in ϵ_r per wavelength in the material a small constant. Table 8.3, extracted from [6], lists a half-dozen versions of tapers, along with the thickness required at the lowest frequency for 20 dB RCSR. Note that the minimum thickness is on the order of 0.3λ , implying that even in the ideal case, an absorber nearly 5 cm thick would be required for 20 dB performance down to 2 GHz.

Typically, practical graded dielectric RAMs are constructed of discrete layers, with properties changing from layer to layer. One commercial example is the AN series of graded dielectric absorbers made by Emerson and Cuming. AN-74, a three-layer foam absorber about 3 cm thick, is advertised to provide 20 dB RCSR down to 3.5 GHz. Dipped honeycombs, with successive dippings to lesser



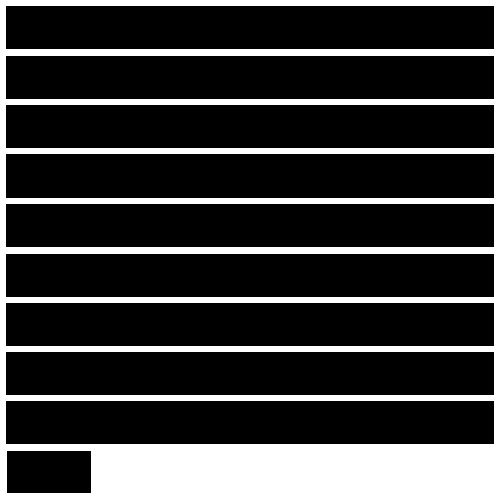
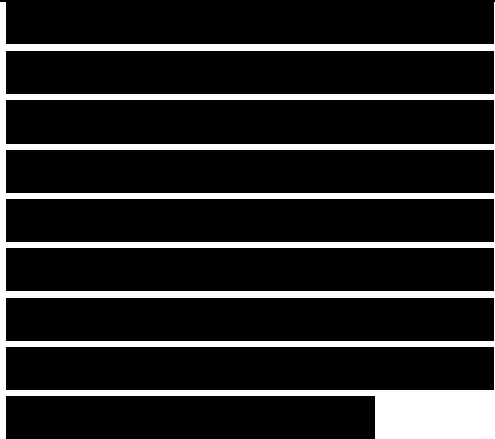
depths, have also been used to provide the conductivity gradient required for a graded dielectric absorber. Figure 8.17 provides measured reflectivity data for a commercial three-layer graded dielectric absorber about 1 cm thick.

Several other RAM types exist that are, in effect, graded dielectric absorbers. The first type appears to be a homogeneous single-layer absorber, but, due to its method of production, is actually a graded dielectric. The second type uses a geometric transition to provide an effective dielectric gradient.

A technique for reducing the reflection from the front face of a flat absorber is to produce a material whose intrinsic impedance is very close to unity. Two

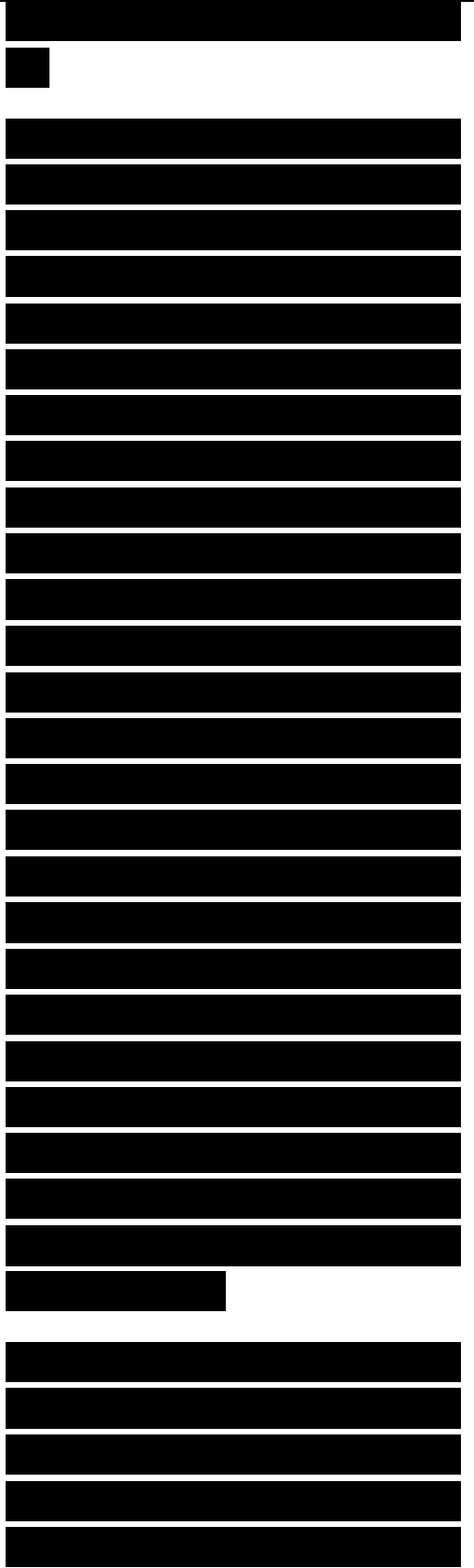
Table 8.3

Several Graded Dielectric RAM Designs [6] common examples of absorbers employing such a technique are the hair-type and the carbon-loaded low-density foam absorbers. However, both types employ a conductivity gradient to some degree.



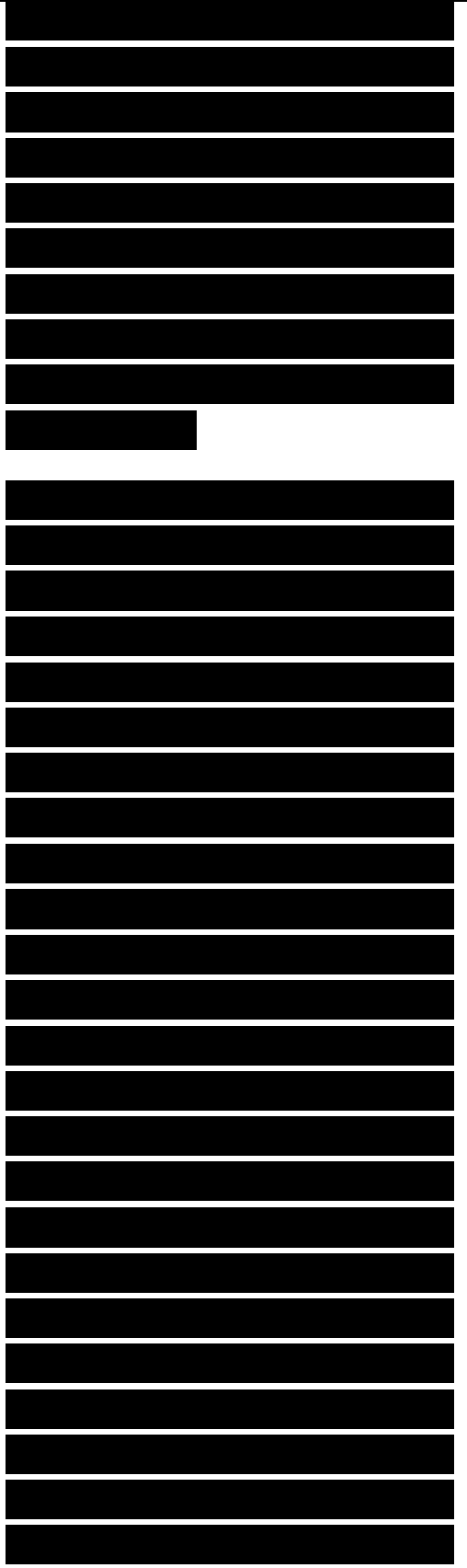
The original hair-type absorber was developed by NRL in the late 1940s for an anechoic chamber used to cover from 2.5 to 25 GHz [11]. The material is constructed by impregnating mats of curled animal hair with a mixture of conducting carbon black in neoprene. Because the mats normally are laid flat to dry after dipping, gravity tends to provide a dielectric gradient, as more of the conductive mixture ends up toward the back of the mat. Currently available commercial versions of hair-type absorbers require approximately a half-wavelength material thickness for 20 dB of RCSR [12]. Because of its poor structural properties and poor RCSR performance compared to pyramidal absorbers and graded dielectrics, hair-type absorbers tend to be used less than they once were.

A more recent version of the “hair mat” absorber is a netting absorber produced by the Plessey Corporation. A 1.2 cm thick plastic netting is provided with a conductive coating. Again, there is a variation in



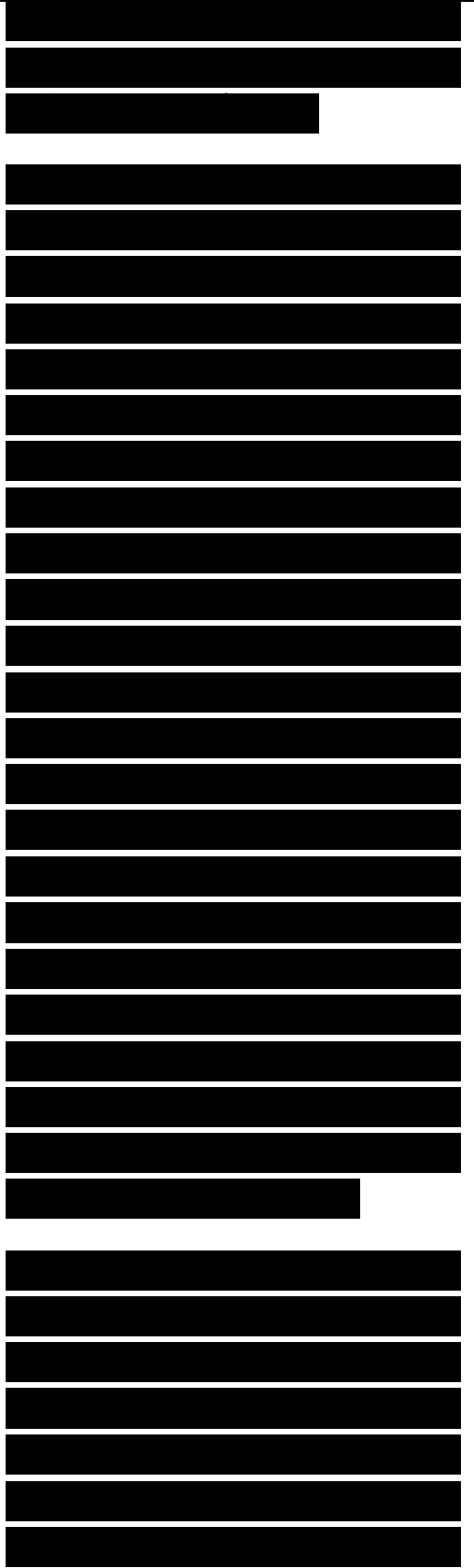
the amount of conductive material from front to rear, providing a dielectric gradient. Advertised RCSR performance of the netting is better than 10 dB from 6 GHz through 100 GHz, with better than 15 dB performance over an 8 to 14 GHz band [13].

Another class of single-layer absorber (and the one most commonly used in anechoic chambers) depends upon carbon-loaded foam to provide loss, but also uses a geometric transition from free space to the highly lossy medium to provide a dielectric gradient and thereby reduce reflections. The most common form used in anechoic chambers is the pyramidal absorber illustrated in Figure 8.18. Other common shapes include an aggregate sine wave (convoluted) front, conical shapes, and off-normal angle wedges. These types of absorbers can provide reflectivity reductions in excess of 50 dB, but may require thicknesses in excess of 10λ to do so [14]. Figure 8.19 provides an indication of the RAM thickness needed for a given level of RCSR versus frequency, and of the performance of the RAM at angles far off-normal [15].



As requirements on sensitivity have increased for indoor ranges, significantly more effort has gone into the analysis of the performance of geometric transition absorbers [16,17]. Reference [17] provides an interesting comparison of the reflection coefficient for several shapes that might be used for anechoic chamber absorber. Compared are rectangular, sinusoidal, and triangular profiles. In all cases the analysis assumes that the basic material composing the absorber extends an infinite distance behind the front profile. The triangular profile is found to provide significantly better performance than the other two, because of the more gradual taper of the spatially averaged impedance seen by the incoming wave.

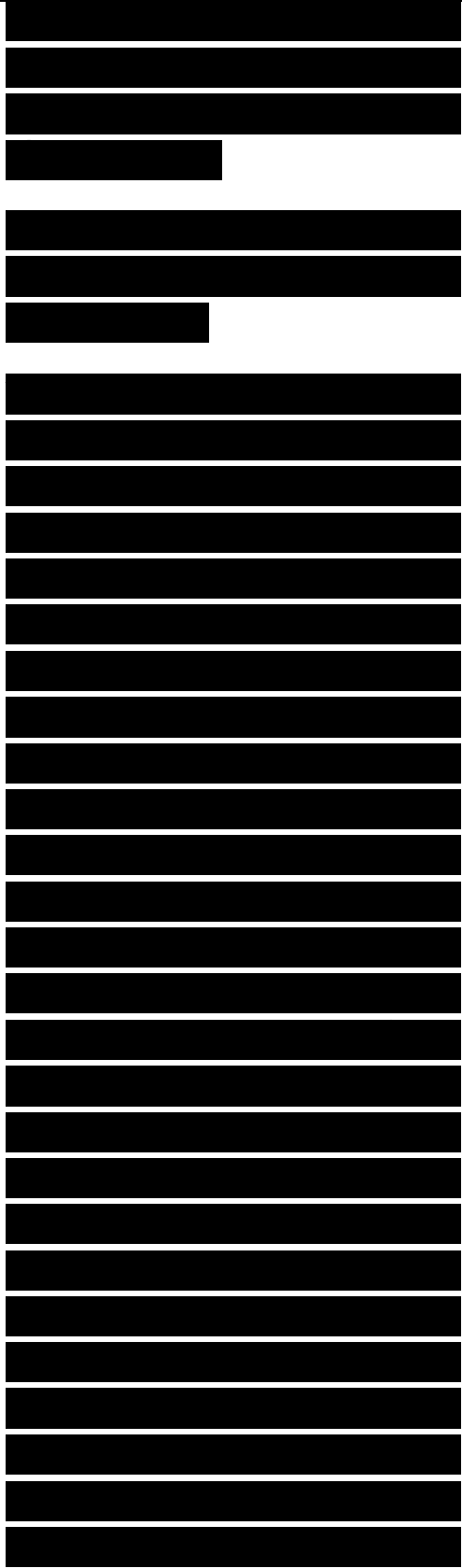
Figure 8.20, from [17], provides a plot of reflection coefficient for a IX deep version of a triangular profile and a variant of a triangular profile. Note that the variant provides almost 10 dB better performance at normal incidence than does the



triangular profile, because of the better taper at the top and the inclusion of more absorptive material toward the bottom of the profile.

8.5 CIRCUIT ANALOG RAM AND FREQUENCY-SELECTIVE SURFACES

As pointed out previously, the design of specular RAM is equivalent to a transmission line matching problem, where the goal is to limit the reflection seen at the input caused by a short-circuit termination. The Salisbury screen and Jaumann absorbers use resistive sheets, which have only a real part to their admittance, as the matching elements. Significant flexibility can be gained in the design process if the sheets can have a susceptance as well as a conductance. This imaginary part of the admittance can be obtained by replacing the continuous resistive sheet with one whose conducting material has been deposited in appropriate geometrical patterns (e.g., dipoles, crosses, triangles), such as those shown in Figure 8.21. The significantly better performance than the other two, because of the more gradual taper of the spatially averaged impedance seen by



the incoming wave.

Figure 8.20, from [17], provides a plot of reflection coefficient for a IX deep version of a triangular profile and a variant of a triangular profile. Note that the variant provides almost 10 dB better performance at normal incidence than does the triangular profile, because of the better taper at the top and the inclusion of more absorptive material toward the bottom of the profile.

8.5 CIRCUIT ANALOG RAM AND FREQUENCY-SELECTIVE SURFACES

As pointed out previously, the design of specular RAM is equivalent to a transmission line matching problem, where the goal is to limit the reflection seen at the input caused by a short-circuit termination. The Salisbury screen and Jaumann absorbers use resistive sheets, which have only a real part to their admittance, as the matching elements. Significant flexibility can be gained in the design process if the sheets can have a susceptance as well as a conductance. This imaginary part of the admittance can be obtained by replacing the continuous resistive sheet with

~~one whose conducting material has been deposited in appropriate geometrical patterns (e.g., dipoles, crosses, triangles), such as those shown in Figure 8.21. The~~

Angle From Normal (Deg.)

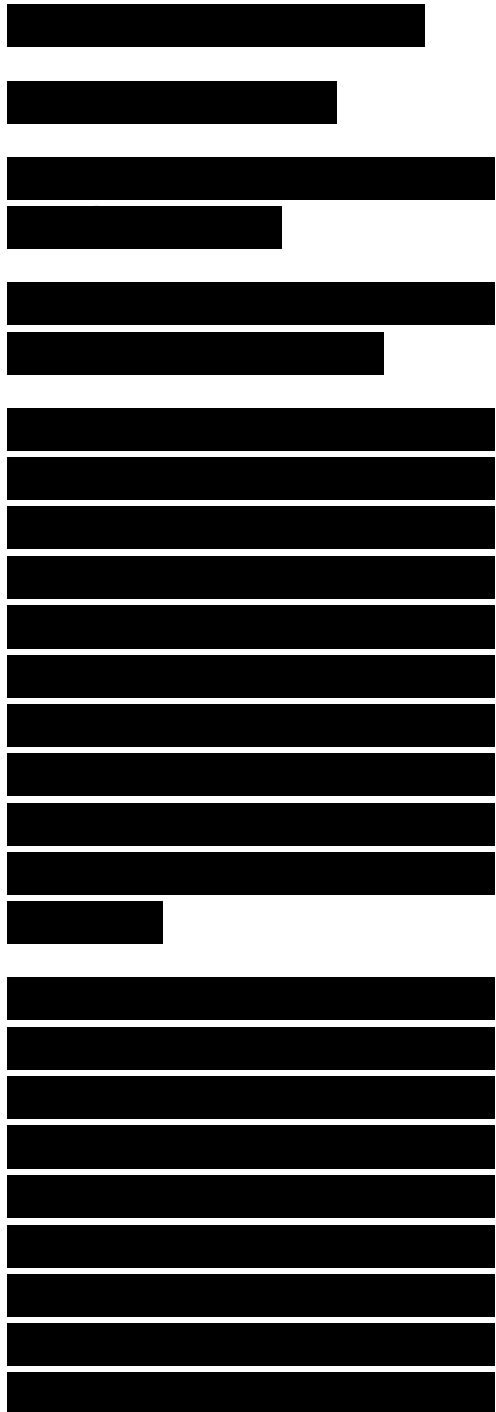
(b) Intersecting Wires

(d) Crossed Dipoles (e) Dual Period Strips

Figure 8.21. Typical circuit analog element geometries.

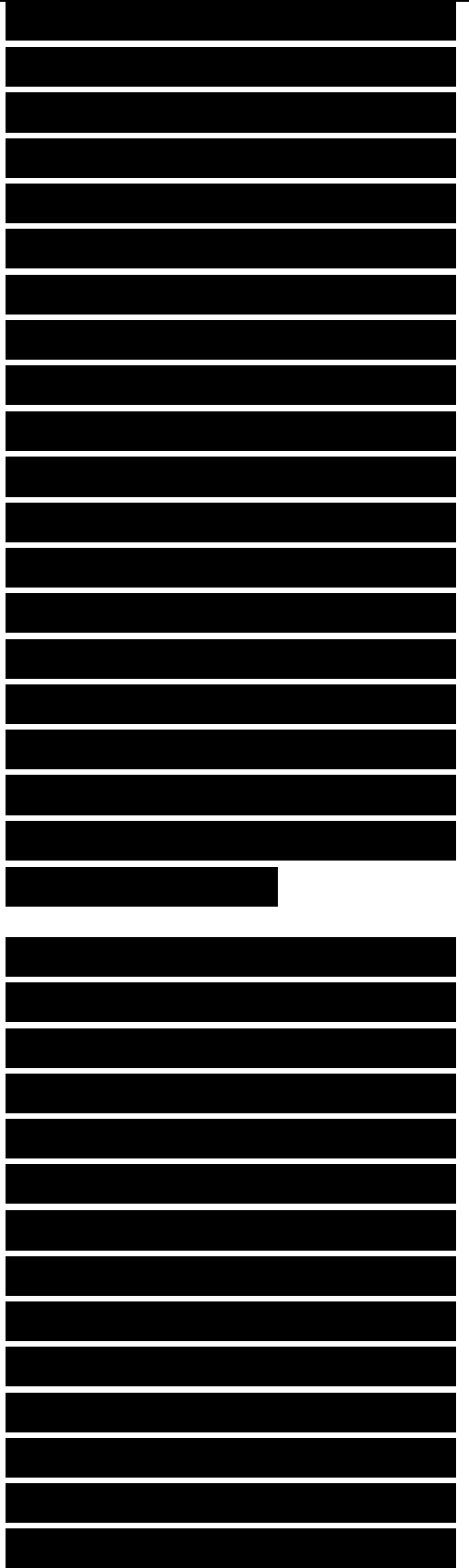
term circuit analog (CA) for such absorbers is derived from the fact that the geometrical patterns are often defined in terms of their effective resistance, ca-pacitance, and inductance; and then equivalent circuit techniques are used in the subsequent analysis and design of the resulting absorber.

A design problem closely related to that of circuit analog sheets is that of bandstop or bandpass surfaces. However, in contrast to CA RAM, such frequency- selective surfaces (FSS) do not absorb RF energy. Rather, an FSS is a frequency filter that might be employed, for example, as a bandpass radome in front of a radar



antenna or as a diplexer for a dual-frequency antenna. Figure 8.22 illustrates typical geometries used for bandpass applications. Duals of those geometries are often used as bandstop filters. In FSS applications, a highly conductive pattern is used because no absorption is desired. Thus, the impedance of the sheet is purely imaginary, and the design relies on changes in reactance with frequency to provide appropriate bandpass or bandstop characteristics.

Because so much more can be done to tailor the admittance properties of a circuit analog design than with Salisbury screens or Jaumann absorbers, better performance can be achieved within the same space constraints. However, optimization of the variables controlling the admittance properties is also more complicated. Thus, current CA design practice typically relies on rather sophisticated, and usually time-consuming, computer programs, often with internal optimization routines.

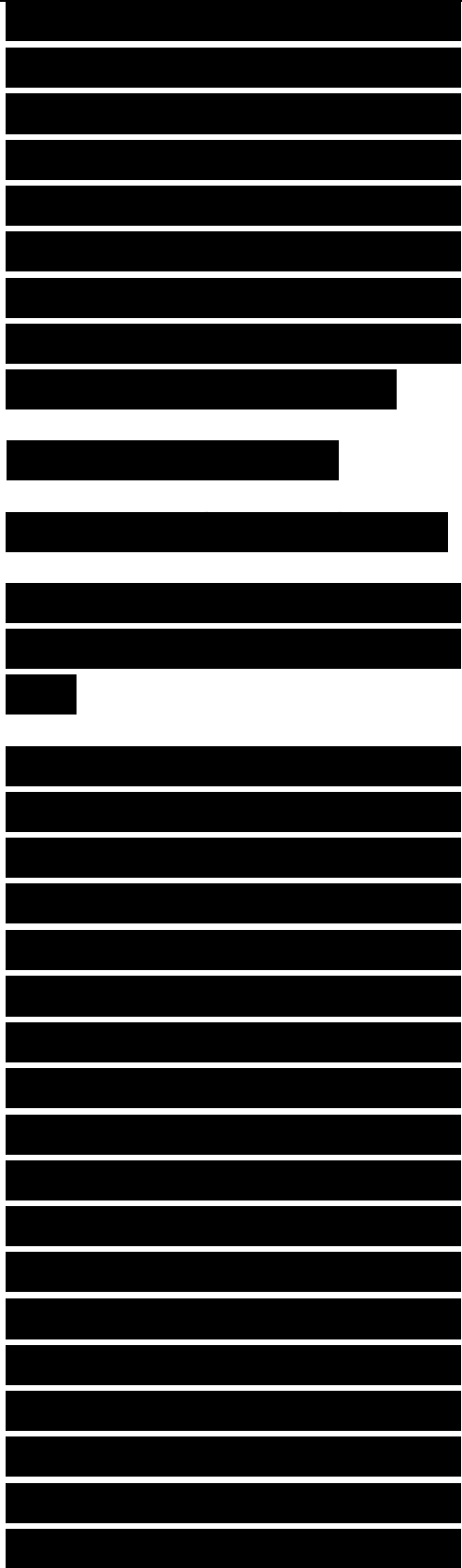


Nevertheless, an understanding of the design techniques used does not depend on the details of the computer implementation, and it is in that area that the following discussion focuses.

(b) Circular Slot, Circular Hole
(e) Four-Legged Symmetrically Loaded Slot

Figure 8.22. Typical frequency selective surface element geometries.

Assuming that a minimum level of performance over some frequency range is required, and that a maximum thickness is specified, four steps are to be completed in the design process for a CA absorber. The first step of the design process is to arrive at admittance characteristics for each CA layer as a function of frequency. The number of CA sheets to be used is a function of the RCSR required and the desired bandwidth, as with the Jaumann designs. As a rule of thumb, a broadband CA design can typically be implemented with one or two fewer sheets than would be possible using resistive sheets in a Jaumann

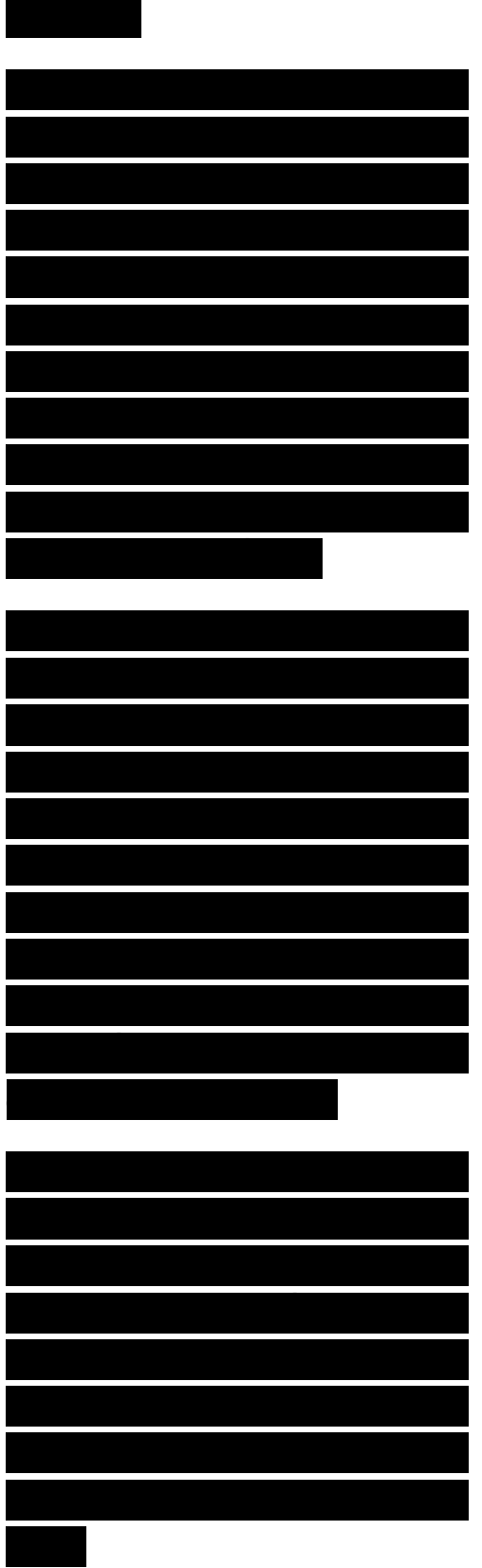


absorber.

The second step of the design process is to find realizable geometry and conductance combinations that match as closely as possible the desired admittance characteristics for each sheet. Typically, the geometry to be used (e.g., dipoles, Jerusalem crosses) will be specified, and the geometry variations will involve the size and spacing of the elements.

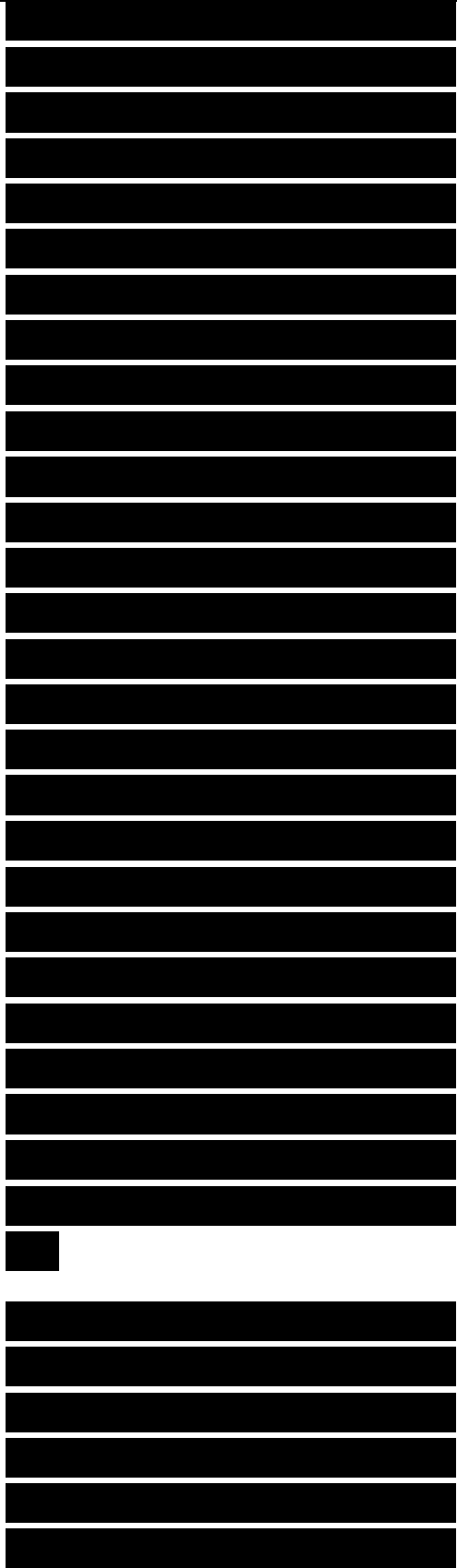
Because it is unlikely that, on detailed analysis, any realizable design will exactly meet the desired admittance characteristics, the third step is to calculate performance of the design based on the achievable admittance properties. In this step, performance characteristics as a function of polarization and incidence angle may also be calculated.

The final step is to iterate the design until an achievable and acceptable combination is found. Given specifications and appropriate constraints, a computer program or series of programs will often be used to perform all four steps.



Nevertheless, because most optimization programs work much more efficiently if they are given a “nearly correct” answer as a starting point, it is very useful to be able to make approximate performance calculations. For an initial estimate of the optimum admittance characteristics, an extension of the approximate reflection analysis of Section 8.3.5 to include complex admittance is helpful. Those initial admittance parameters can serve as input to an optimization program utilizing either the wave matrix or stepping procedure approach to calculate exact admittance parameters. The remainder of this section discusses equivalent circuit and integral equation techniques that can be used to translate admittance characteristics to CA geometries. Much of the following material has been drawn from notes prepared by Dr. J. P. Montgomery of Electromagnetic Sciences, Inc.

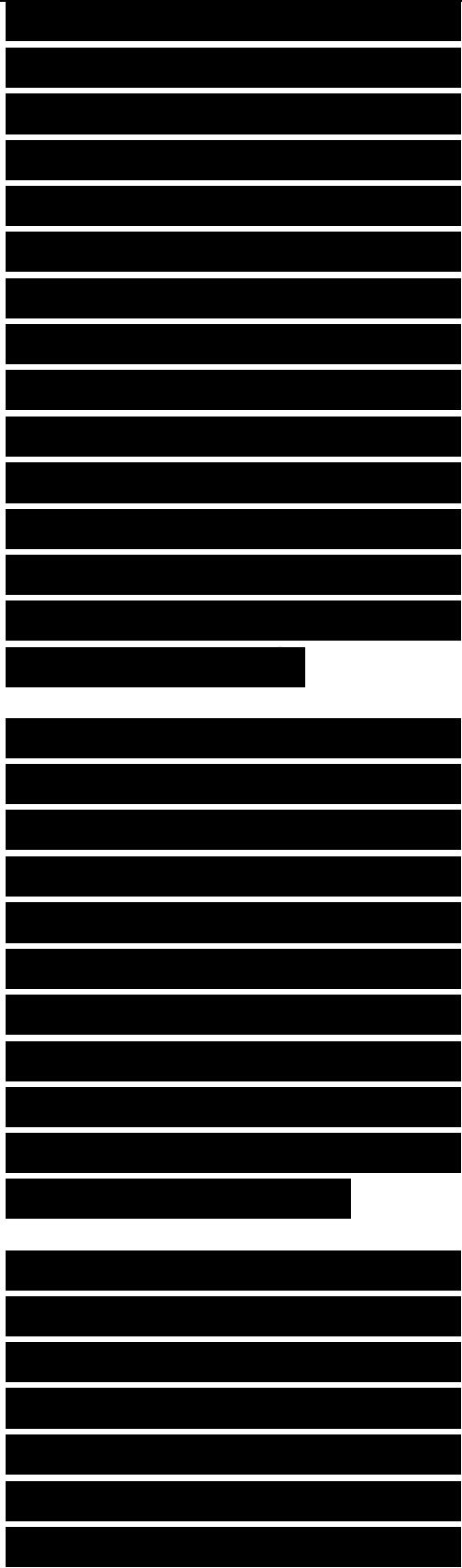
Once the desired admittances have been derived, either analytically or through numerical techniques, those values must be translated into a geometric design. Several methods may be used to



perform this translation. The earliest technique, and one still useful in design, is to draw on equivalent circuit analyses originally intended for waveguide filter design. Marcuvitz [18] provides the equivalent circuits for many configurations that can be used for CA or FSS design. More complex geometries can often be modeled with combinations of circuit components for which characteristics are known.

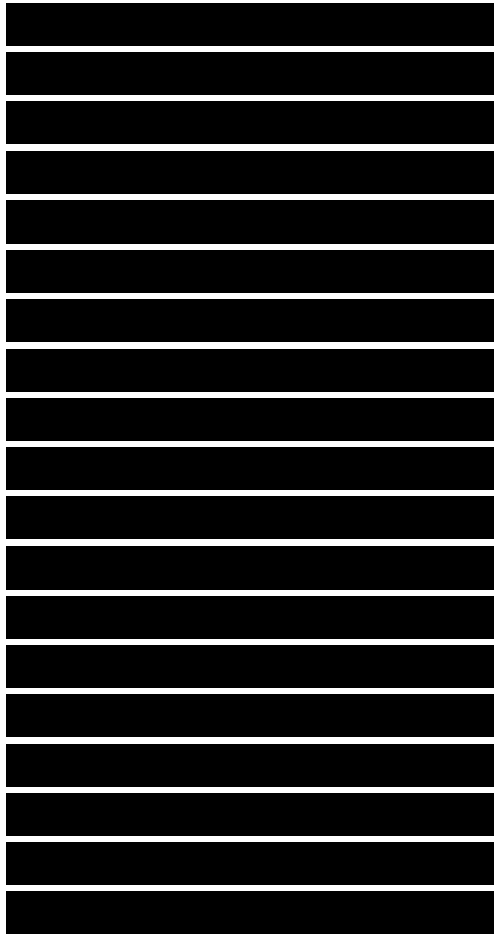
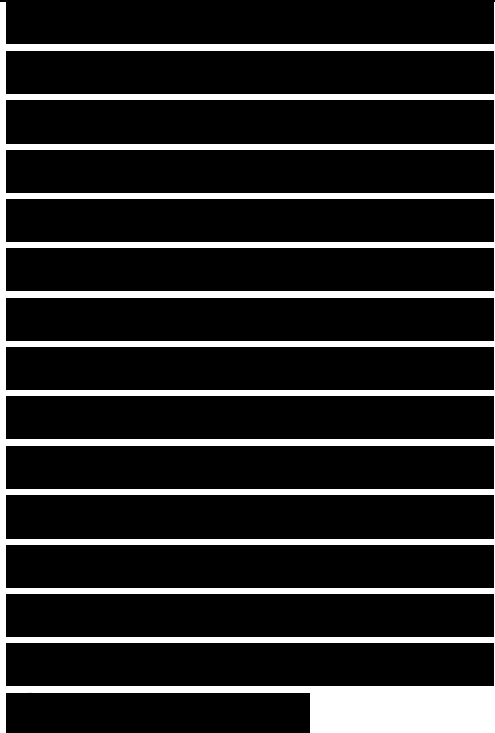
The alternative to a closed form solution using equivalent circuits is to seek a numerical solution. Because the equivalent circuit analyses often provide only a first-order solution, ignoring higher-order modes, numerical techniques are often used to refine equivalent circuit results for the final circuit realization.

Typically, CA and FSS designs consist of elements, such as dipoles or slots, that are on the order of a half-wavelength long. A periodic structure is used to ensure a uniform surface. In analysis of circuit analog sheets, the Floquet theorem [19] allows us to



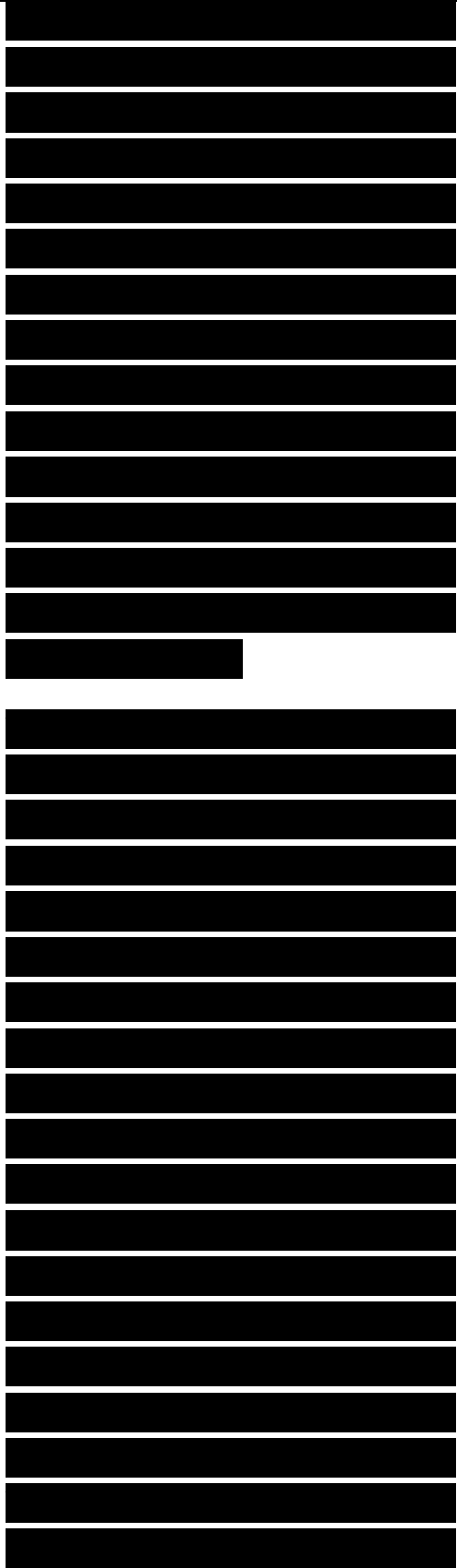
confine attention to a single cell in the periodic structure. In essence, it is assumed that the structure is infinite and illuminated by an infinite plane wave. This being the case, the result for a single cell applies to all cells in the surface. In practice, the structure is finite, and some differences must be expected because the cell-to-cell coupling for cells near the center of the array is different from that of those near its edges.

For circuit analog RAM that is planar and thin along the direction normal to the surface, the tangential electric field will be continuous across the sheet, and the magnetic field will exhibit a discontinuity directly related to the current on the surface. It follows that any equivalent circuit chosen to represent the CA sheet must have these same properties. The analytical procedures presented in Section 8.3 recognized the transmission line analogy to RAM design, and Figure 8.5 pointed out that the equivalent circuit of a thin sheet can be modeled as an admittance shunted across the transmission line. The exact nature of the



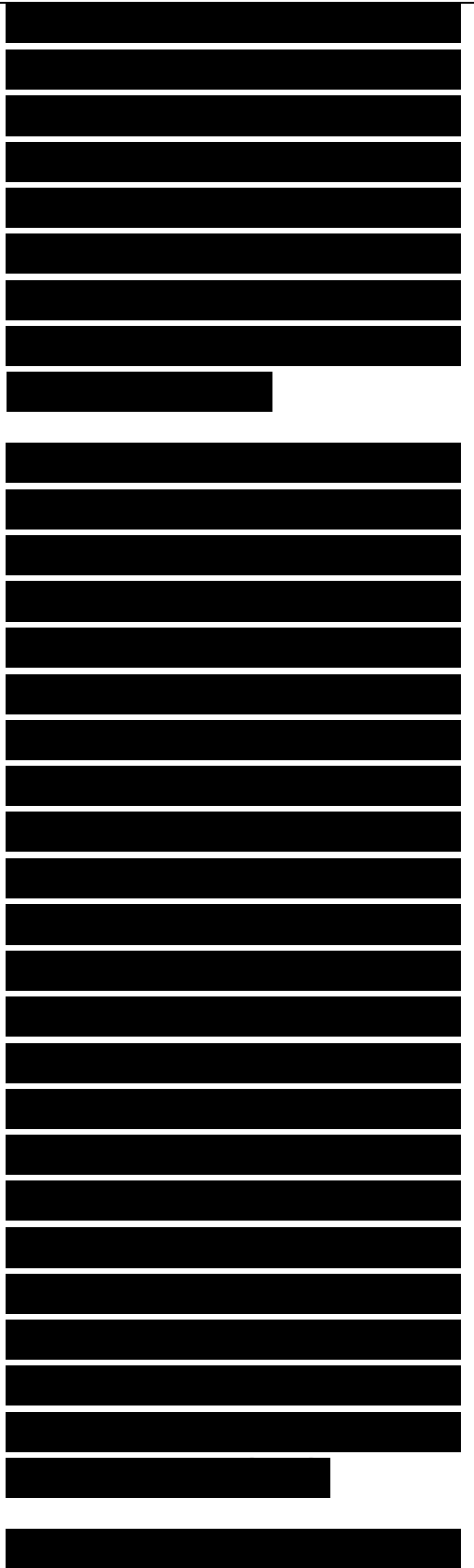
admittance depends on the geometry of the periodic surface. A common example is a dipole array, for which the simplest equivalent circuit is a series RLC network shunted across the line. However, that equivalent circuit is valid only near the first resonance. In general, the broadband equivalent circuit will take the form of multiple, parallel, shunt RLC circuits, each with different loss, resonant frequency, and bandwidth characteristics.

Numerical analysis of periodic planar surfaces has been the subject of many research papers (e.g., [20-24]). The majority of the techniques explored are based on an application of the method of moments to solve a vector integral equation by using a finite matrix approximation, where either the transverse electric field or the surface current in the periodic cell is the unknown, depending on the geometry. If the periodic cell consists of apertures, the electric field is a natural unknown, because a convenient modal series may be available if the aperture is rectangular, circular, or some other elementary shape. If the

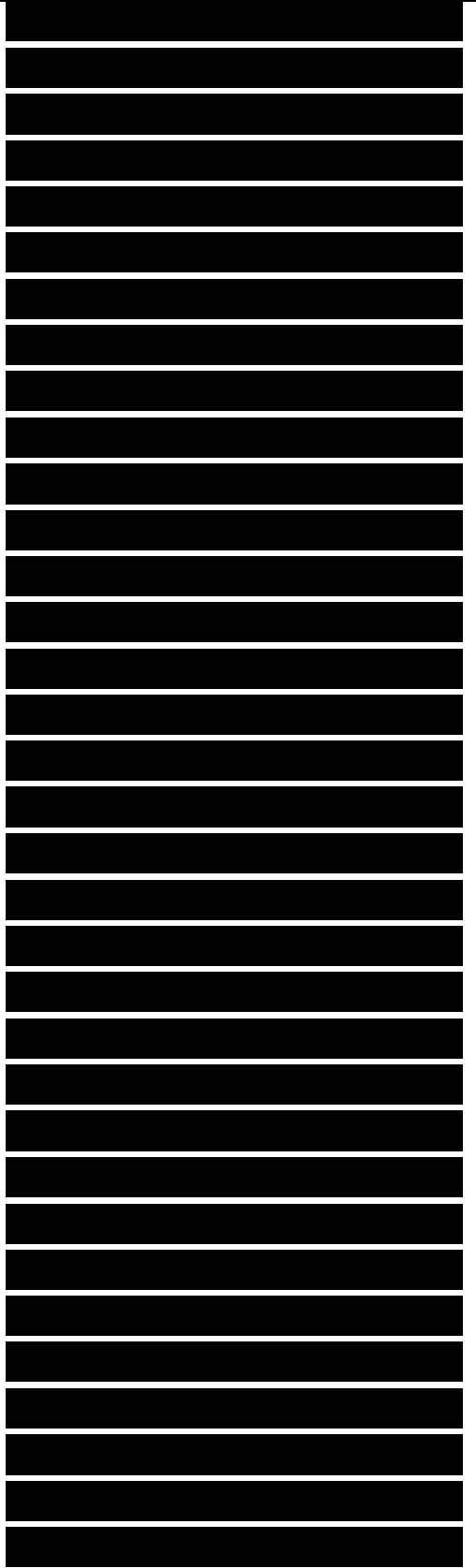


periodic cell consists of conductors of simple shape (such as dipoles or intersecting wires), the current on these wires is a convenient unknown because of similar logic. Some authors have used a universal expansion such as the Floquet series, but have generally met with limited success because of the large number of unknowns. The analysis of a single-layer circuit excited by a single plane wave is generally sufficient for design work when using scattering matrix techniques. Some authors have examined multilayer circuits by solving for the circuit parameters simultaneously [25, 26]. However, the single-layer technique can be extended to heavily coupled circuits by using the generalized scattering matrix that includes higher-order modes [27]. This, of course, requires the use of multiport scattering matrices. When excess coupling is suspected, the analysis of a two-layer circuit can be implemented by adding a magnetic and electric ground plane to the geometry. The admittance of the circuit with and without the adjacent circuit can then be examined.

The method of moments is quick and accurate for most



shunt circuits. However, there are practical difficulties. The geometry must generally have some elementary shape for a modal solution. For example, for a thin linear dipole, a simple Fourier series whose terms are zero at the ends of the dipole will be complete. For a flat dipole, the dual of the rectangular waveguide modes can be used [20]. Similar dual expansions can be used for circular elements [28]. Often, approximate modal expansions can be used if the wire is thin. As an example, consider a bent dipole geometry, for which an approximate modal expansion is a Fourier series in the local coordinate of the dipole. This technique has been used extensively [29] to analyze the three- and four-legged slot geometry used by Pelton for metallic radomes [30]. More complex geometries can be modeled by using a pulse basis expansion. However, the expansion must be complete to ensure an accurate solution. If the expansion does not include critical current terms, an inaccurate solution may result.

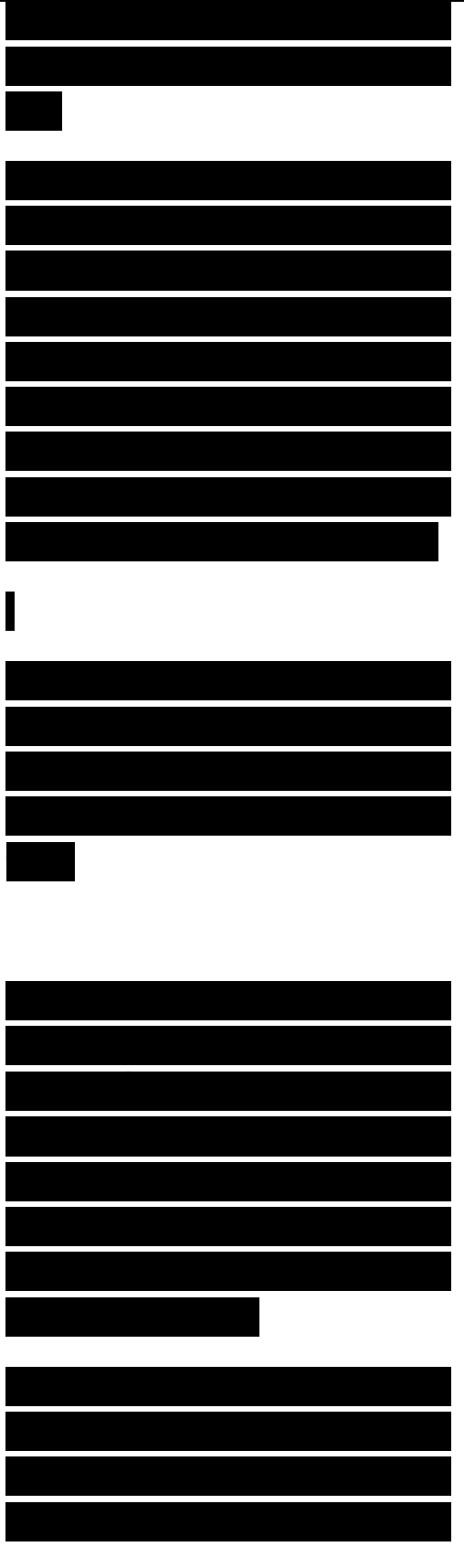


In any event, the reason for employing circuit analog sheets rather than simple resistive sheets in an absorber layup is to provide increased bandwidth through increased control of the impedance properties of the lossy material. Figure 8.23 illustrates the improved performance possible for a simple single-layer Salisbury

Figure 8.23. Single-layer dipole circuit analog screen optimized for maximum percentage bandwidth for three minimum performance constraints.

screen where the resistive sheet has been replaced by a dipole CA screen. Note that the predictions are for the polarization parallel to the dipoles. The perpendicular polarization case would show much different (and generally much worse) RCSR performance.

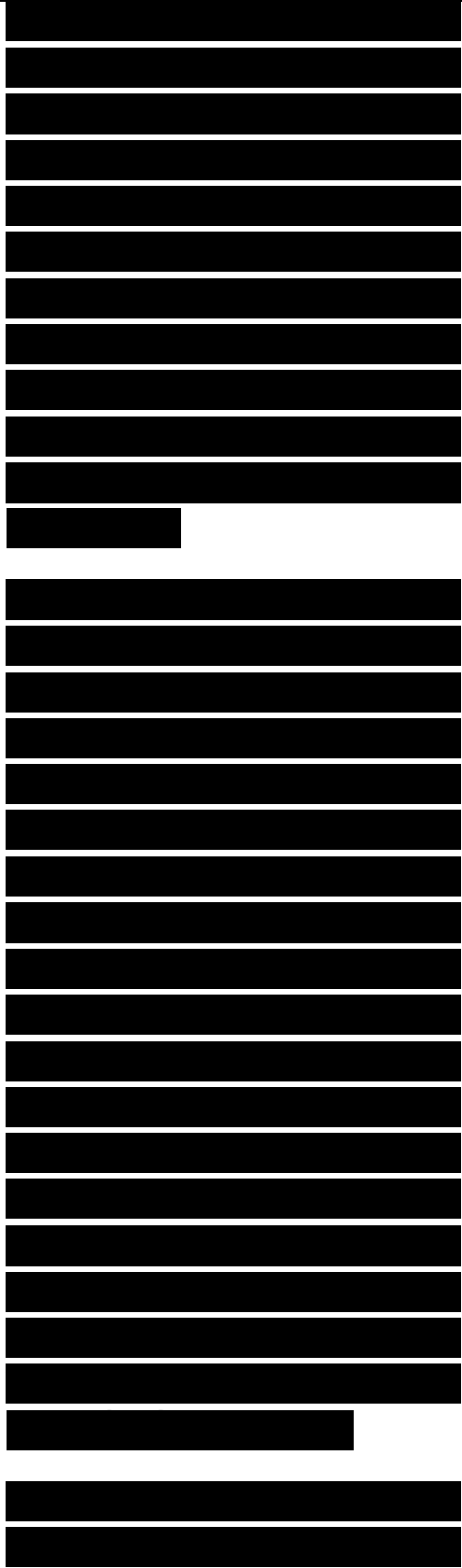
Three curves are plotted. For the first case, a CA design code with an optimizer has been constrained to provide infinite RCSR at the design center



frequency of 10 GHz and a maximum bandwidth commensurate with the infinite RCSR constraint. We noted earlier that a standard Salisbury screen has a percentage bandwidth of about 25% at the -20 dB point. By using the dipole screen, the bandwidth has been increased to 55% without any penalty in maximum performance.

The other two cases illustrate one of the trade-offs available in CA design. If the decision is made to constrain the RCSR so that it is no less than 20 dB over as wide a band as possible, the second curve is obtained. For that case, the percentage bandwidth has increased to 75%, because in the design of the CA sheet geometry and loss characteristics peak performance has been traded for bandwidth. The third curve is a further illustration of the same point, where now the RCSR is constrained to be no less than 10 dB. The optimized design provides a 120% bandwidth, compared to the 75% bandwidth at the -10 dB level provided by the resistive sheet design.

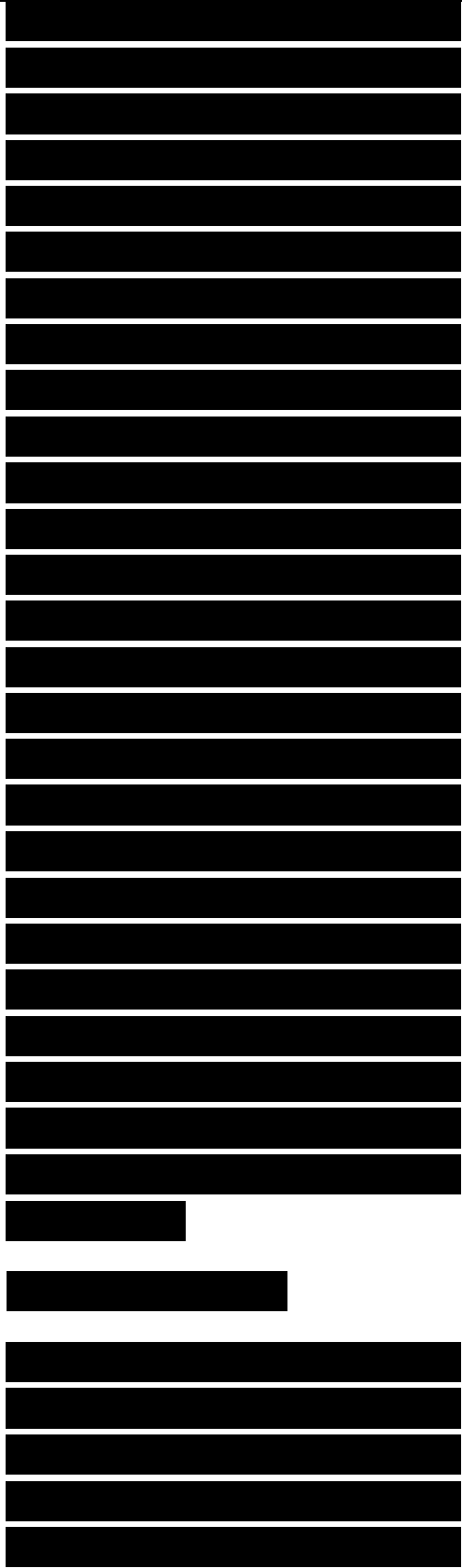
Note that there is one additional difference between



the CA absorber and the conventional Salisbury screen. The RCSR pattern for the CA absorber no longer shows the periodic nulls characteristic of the Salisbury screen. That is because the imaginary part of the sheet impedance is dependent on the size of the pattern elements relative to the radar wavelength. Thus, although the real part of the CA sheet impedance is such that nulls would be expected, there will be a large imaginary component to the impedance at the higher frequencies that will result in a large reflection coefficient. For example, the three designs shown provide RCSR values between 3 and 7 dB at 30 GHz, where the second Salisbury screen null would be expected. However, this is not generally a particularly severe disadvantage, and it is clear that circuit analog is able to provide significantly better performance than conventional Salisbury screens or Jaumann absorbers, given the same thickness constraints.

8.6 MAGNETIC RAM

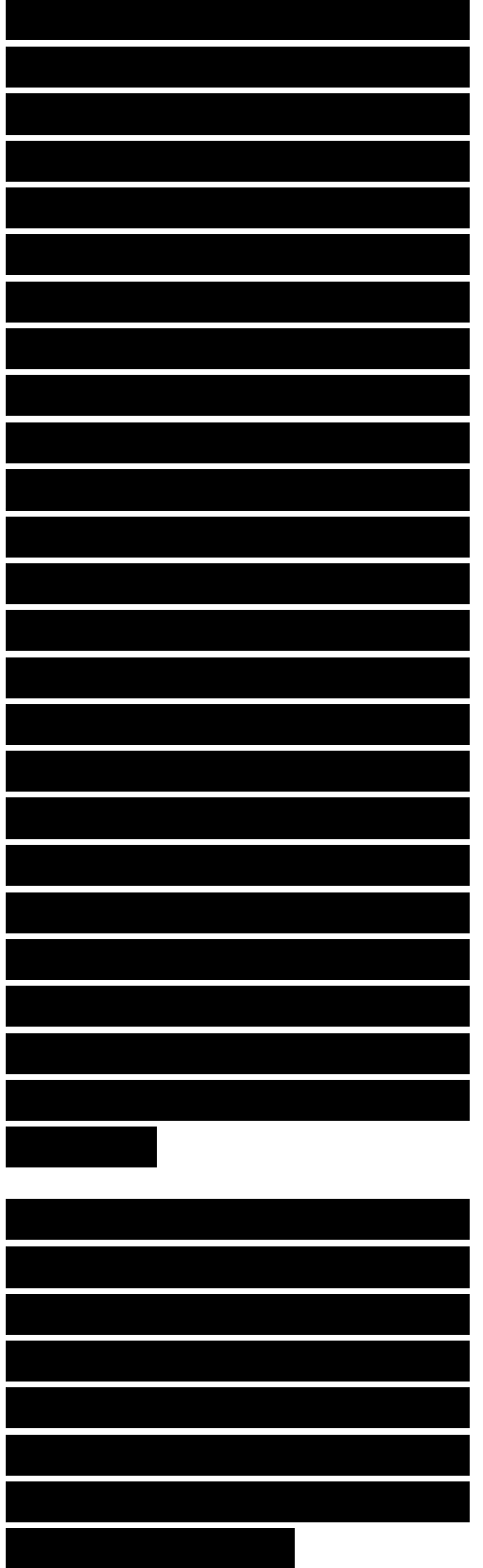
So far in discussing RAM design we have limited ourselves to materials whose relative complex permeability is $U_j = 1 + i0$. For that case, the intrinsic impedance of the



material is simply $377/\sqrt{\epsilon_r}$, and the index of refraction is $\sqrt{\epsilon_r}$. Magnetic materials are those whose relative permeabilities are different than that of free space. Clearly, the presence of permeability values greater than 1 gives us significantly more freedom in tailoring the intrinsic impedance and index of refraction of a material to meet our needs for absorber performance. However, although we will focus in this section on the magnetic properties of materials, the magnetic materials available for use in RAM generally have relative permittivities higher than their relative permeabilities. Therefore, in practice we do not deal with purely magnetic absorbers, that is, those with $\epsilon_r = 1 + i0$, but with materials that contain both magnetic and electric loss properties.

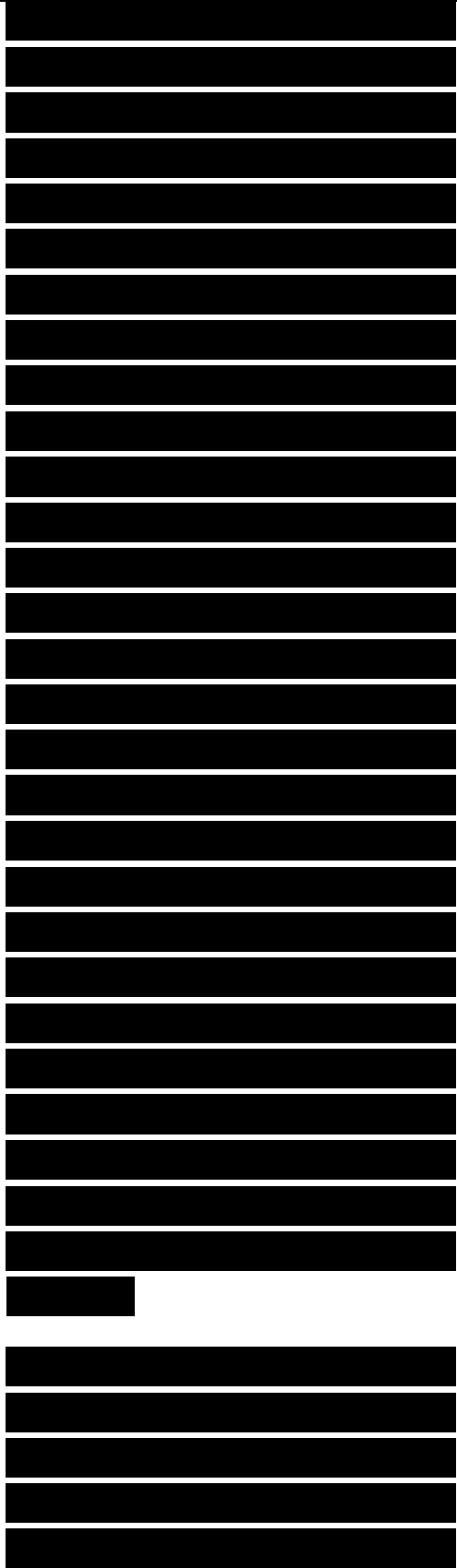
The catalog of materials available for use as magnetic absorbers at microwave frequencies is large, but iron or compounds of iron are most often exploited. The two most common magnetic materials employed in RAM are carbonyl iron and ferrites.

Carbonyl iron is a pure iron



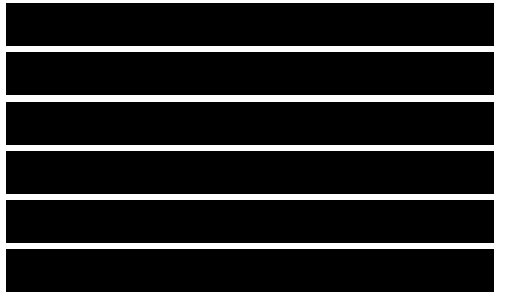
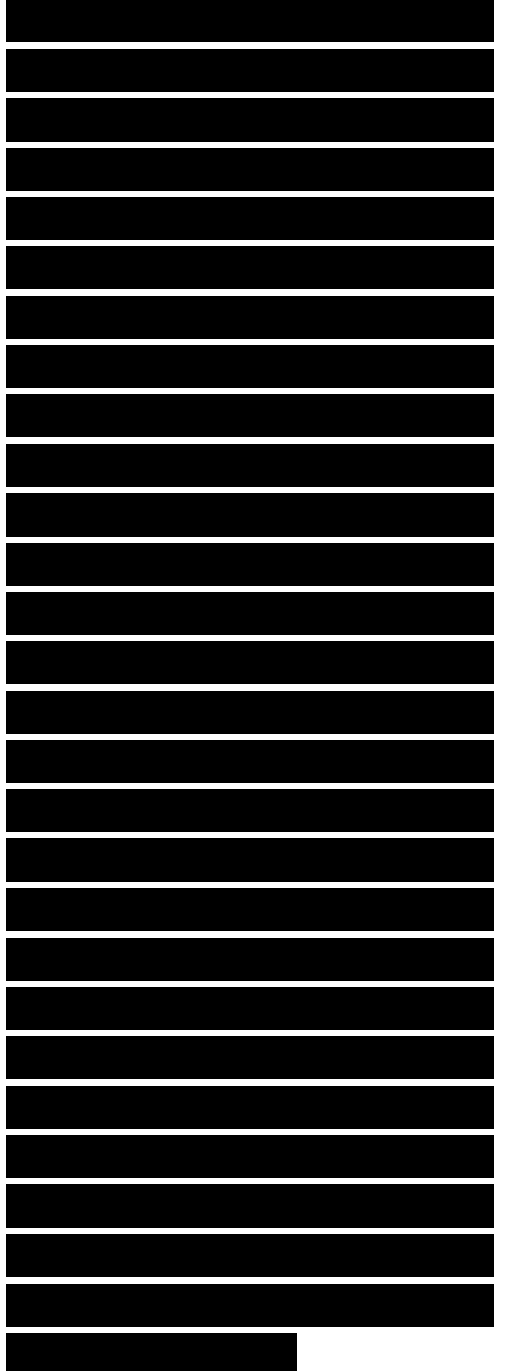
powder (the carbonyl term relates to how it is produced), with particle diameters ranging from a few micrometers to tens of micrometers. RAM performance is a function of particle size, and in the ideal situation individual particles contain a sufficient number of magnetic domains that they are isotropic, but small enough that self-shielding is not a problem (the observation that iron bars do not make particularly good radar absorbers leads us to conclude that particle sizes should be a small fraction of a skin depth in size and long conduction paths should not be available, if good absorption rather than reflection, is to occur). Therefore, our ability to pack conducting particles into a nonconducting matrix for use as RAM is limited by the packing density we can achieve before particles begin to touch (percolation) and long current paths appear.

Ferrites are ferrimagnetic substances composed of iron oxides and other metallic oxides. Because they are nonconducting, ferrites naturally provide a high



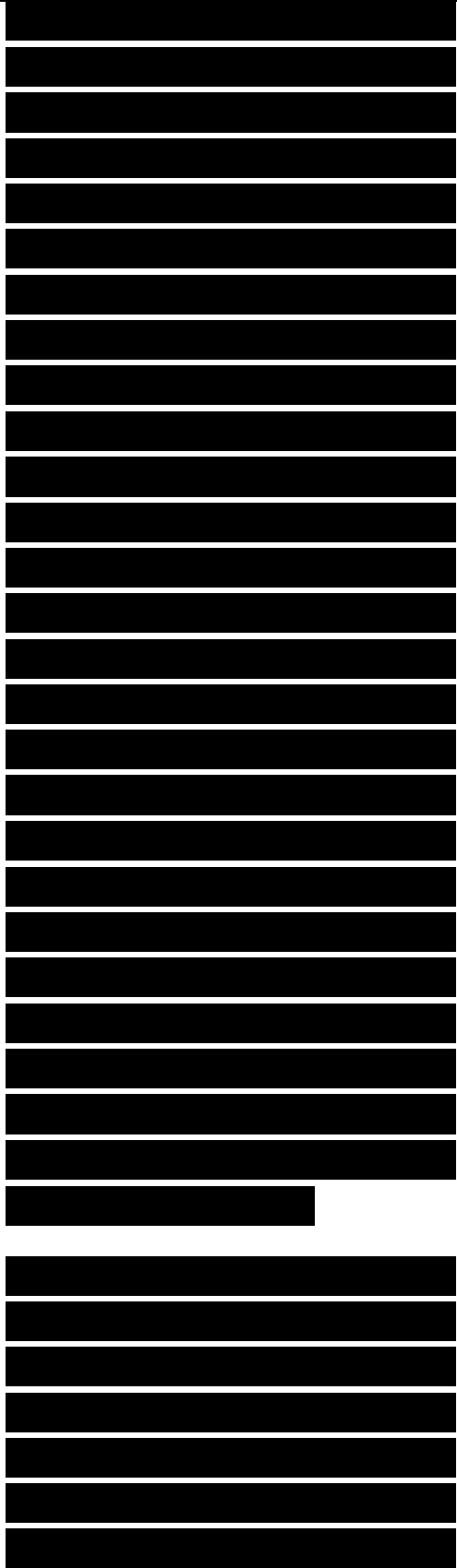
packing density of magnetic material. Also, because the lattice structure and the metallic elements used to dope ferrites can be controlled and varied, the electromagnetic properties of ferrites can be better tailored to meet specific requirements than those of iron or other metallic magnetic substances. However, one disadvantage of ferrites is that their saturation magnetization is low compared with iron, and the loss-bandwidth product of the material is proportional to the value of the saturation magnetization. Because the basic lattice structure of ferrites consists of two sets of magnetic dipoles aligned in opposition, the resulting magnetic moment per molecule will be lower than for the pure magnetic metals [31]. However, the ability to obtain high packing densities, to resist oxidation to a nonmagnetic form, and to allow synthesis of properties through appropriate doping make ferrites widely used in magnetic RAM.

Magnetic RAMs are found in a number of forms. Ferrite materials are often sintered in the form of small, rigid tiles, and application to a surface requires careful consideration of bonding techniques. Another



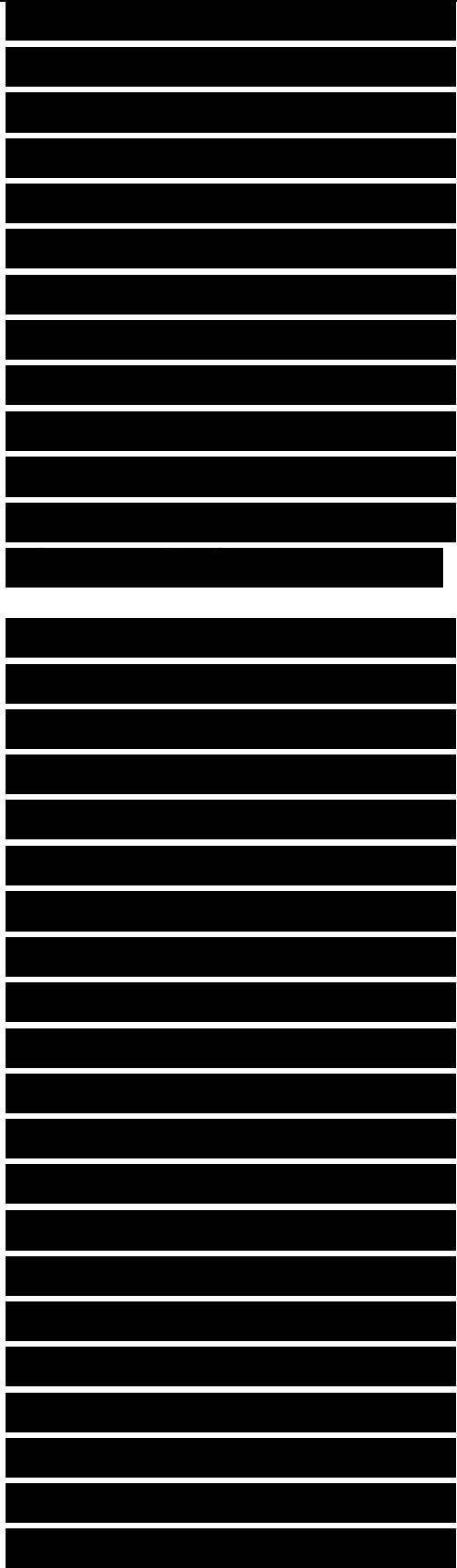
method of manufacturing involves embedding the magnetic materials in a flexible matrix of natural or synthetic rubber, which can then be glued to the surface to be shielded. Again the bonding method requires attention. Several firms have developed spray-on materials in which the magnetic "dust" is suspended in an epoxy vehicle. Because the solid particles are heavy, they tend to settle at the bottom of the container used for spraying, and constant agitation is required. The lossy coating is built up to the desired thickness by the deposition of several thin layers. Uniform thickness, and therefore uniform properties, are difficult to achieve unless skilled operators are available or can be trained for the task. The material can also be brushed on. Such materials are often used to reduce traveling and creeping waves, thus providing nonspecular RCSR.

The spray-on RAM, also referred to as iron paint, has the advantage that irregular surfaces can be covered more easily than with the flexible sheets, although singly curved surfaces (cylinders, cones) are amenable to the use of the sheets. For both forms of



material, adequate surface preparation is required or else the absorbing layer may peel off. Because these materials all contain iron in one form or another, they tend to streak rust in an oxidizing environment. At high temperatures, oxidation of carbonyl iron to nonmagnetic Fe_2O_3 is a severe problem because the oxidation causes a permanent loss of absorbing properties.

Although magnetic RAM tends to be heavy, its virtue lies in the ability to provide extended low-frequency performances with reasonable material thicknesses. Where an ordinary dielectric absorber would have to be many inches thick to achieve low-frequency coverage down to 100 MHz, the magnetic materials can often be much less than a tenth as thick to achieve comparable performance. The reason for this is that the magnetic losses can be tailored for low frequencies, as sketched diagrammatically in Figure 8.24. Because the losses tend to increase for the lower frequencies via increasing μ_r , and the electrical thickness of the material tends to “keep in step” with the frequency, performance persists at lower



frequencies. At the higher frequencies, the magnetic properties no longer contribute much to the performance, and the dielectric properties (ϵ_r) now account for whatever loss occurs. Table 8.4 graphically illustrates these traits for a nickel-zinc ferrite

Frequency (GHz)

Figure 8.24. Schematic illustration of the frequency behavior of ferrites.

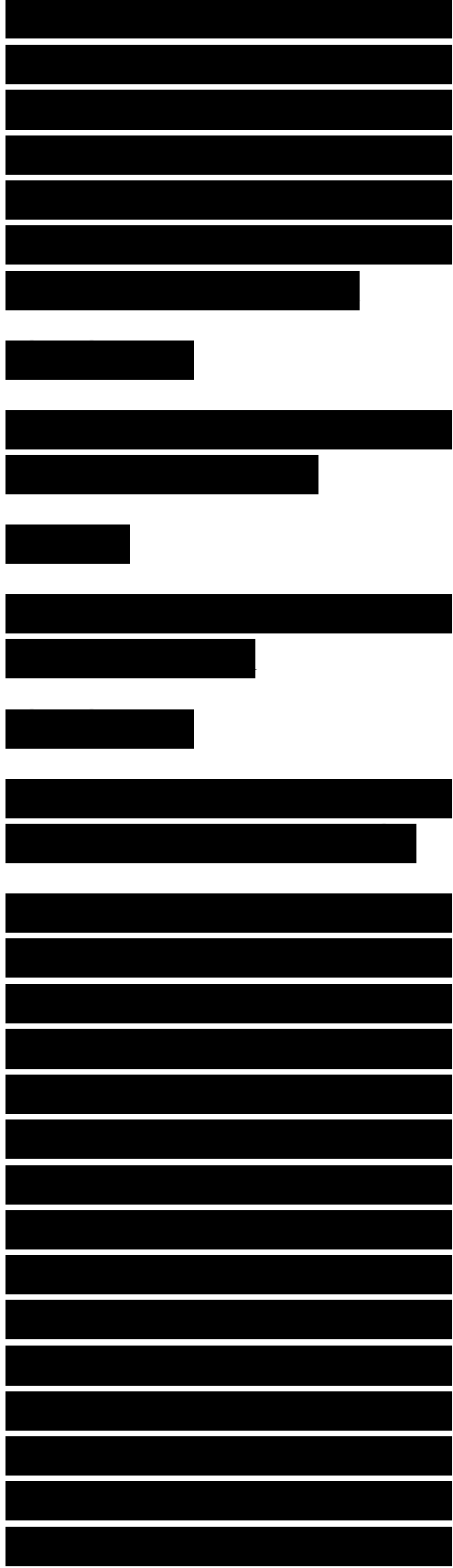
Table 8.4

Electrical Properties Sintered Nickel Zinc Ferrite

Frequency (GHz)

Note: (v and ϵ_r values were provided by William R. Cuming.

for which the electrical properties, index of refraction, and front-face reflection coefficient are listed. Note that at 100 MHz the ferrite's electrical thickness will be more than 50 times its physical thickness and, because $\sqrt{\epsilon_r} \sim \epsilon_r$, the front-face reflection will be more than 20 dB below the incident level. Thus, most of the return will be that portion of the wave not attenuated during its two-way path through the ferrite. In contrast, at 10 GHz, the ferrite's electrical thickness is only 2.3



times its physical thickness, and there is a high front-face reflection that can be cancelled only by use of resonant techniques.

Besides the essentially "single-layer" magnetic materials, multiple-layer magnetic materials can also be used. These are designed to take advantage of the fact that different magnetic materials will have permeability curves that peak at different frequencies. The remainder of this section considers single-layer magnetic materials and then briefly surveys some recent efforts in multilayer magnetic RAMs.

The analysis of an electric Salisbury screen showed that a resistive sheet should be placed at the maximum of the electric field, offset $X/4$ from the surface. By analogy, a magnetic Salisbury screen would require a magnetic lossy layer at the peak of the magnetic field, which is immediately on the metal sheet [32]. With the assumption that $\mu \gg \mu_0$ and ϵ_r , reference [6] provides an analysis for which $R = 0$ when $\cos \beta d = Z_0$ (8.45)

Note that meeting the requirements of (8.45) for practical peak values of βd en-

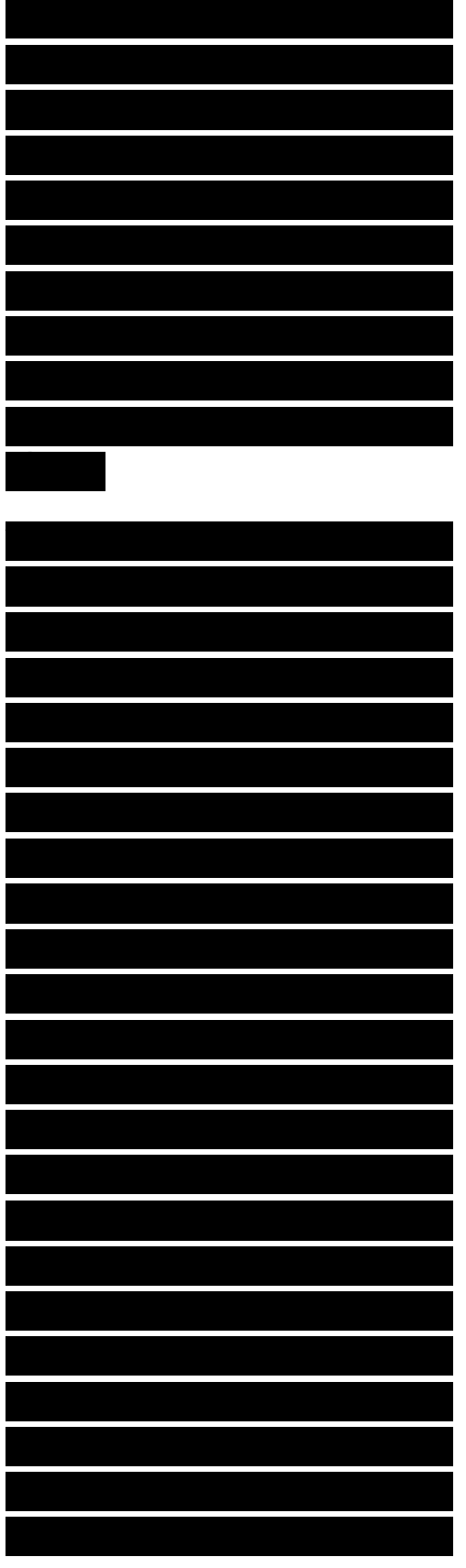
[REDACTED]

[REDACTED]

[REDACTED]

countered in magnetic materials would permit a very thin absorber to be used at microwave frequencies. However, finding materials that meet the conditions on μ and ϵ required of a magnetic Salisbury screen is extremely difficult, although some of the ferrites have properties resembling those required over small frequency ranges.

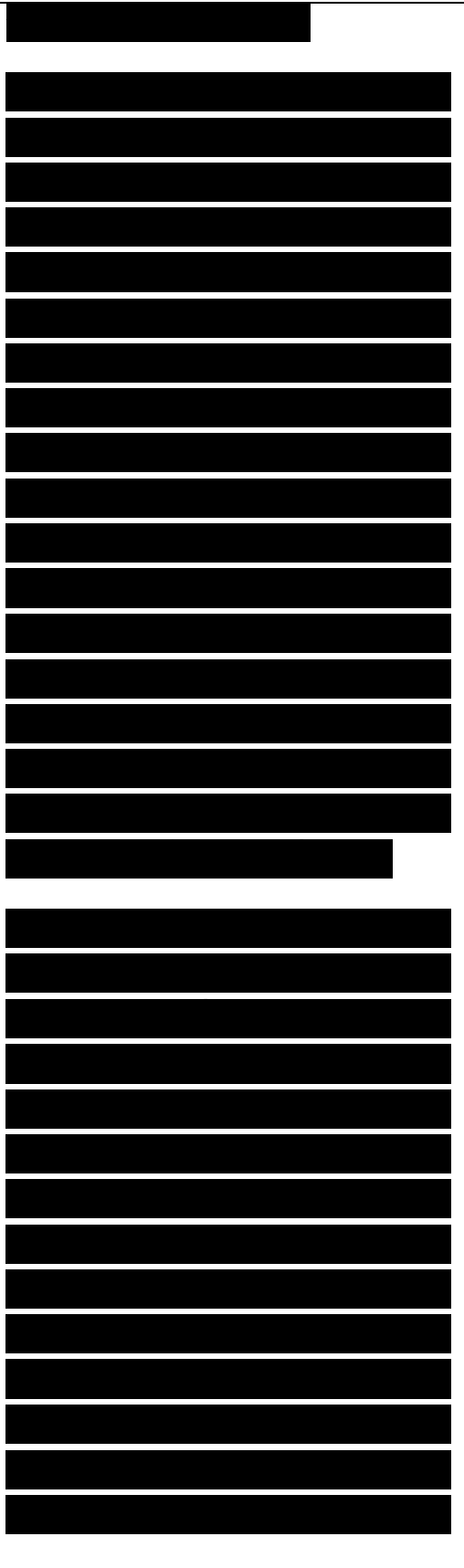
The difficulty in finding materials with properties suitable for magnetic Salisbury screens means that most single-layer magnetic absorbers are not designed in accordance with (8.45). However, an attempt is often made to adjust material properties so that the intrinsic impedance is as near that of free space as can be obtained, over as wide a frequency range as possible. For iron or ferrite powder loaded into a dielectric matrix such as rubber or neoprene, this can be done by control of the percentage loading of the magnetic material. An additional technique useful with magnetic materials is to form a magnetic Dallenbach layer. The guidelines of [8] can be used in that case to determine optimum thickness as a function of material



properties.

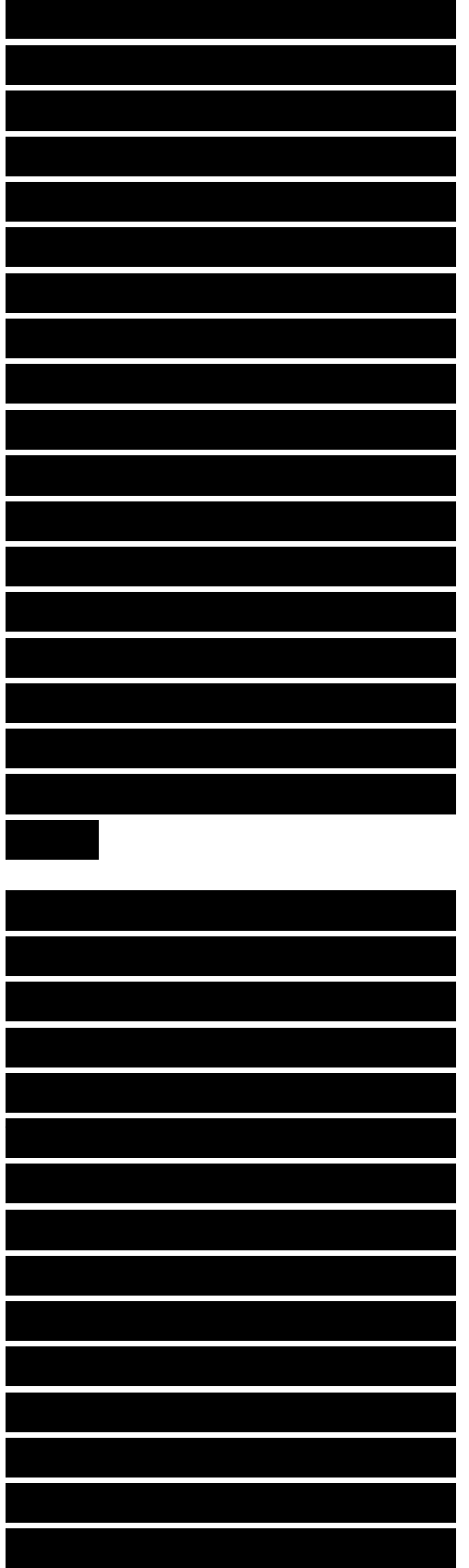
Magnetic absorbers, particularly those made of sintered ferrites, have the advantage of being useful at high temperature. However, although their physical properties may hold to above 1000°C, Curie temperatures, above which the magnetic properties essentially disappear, are typically much lower. For example, cubic spinel ferrites have Curie temperatures below 600°C, and hexagonal ferrites below 500°C. Ferromagnetic materials can be constructed with Curie temperatures in the 500° to 1000°C range, but they present serious problems of chemical stability [33],

Figure 8.25 provides plots of RCSR for four commercially available sintered ferrite absorbers. Their thicknesses vary from about 6 mm to about 8.5 mm, and they are relatively heavy (about 34 kg/m²) and very brittle. However, note that all provide some RCSR at 100 MHz (three better than 10 dB), and the frequencies at which they show peak performances range from 250 MHz to 700 MHz. At 250 MHz, the free-space wavelength is 1.2 m. An electric Salisbury screen at that



frequency would be 30 cm thick. These magnetic absorbers provide good RCSR performance in thicknesses typically less than 5% of the value required of dielectric absorbers. Again, as was noted from Table 8.4, such performance is possible because of the combination of an intrinsic impedance close to that of free space and an index of refraction much greater than 1, providing an electrical thickness much greater than the mechanical thickness. Therefore, for low-frequency performance where space is a problem, magnetic absorbers have significant advantages in spite of their weight and mechanical properties.

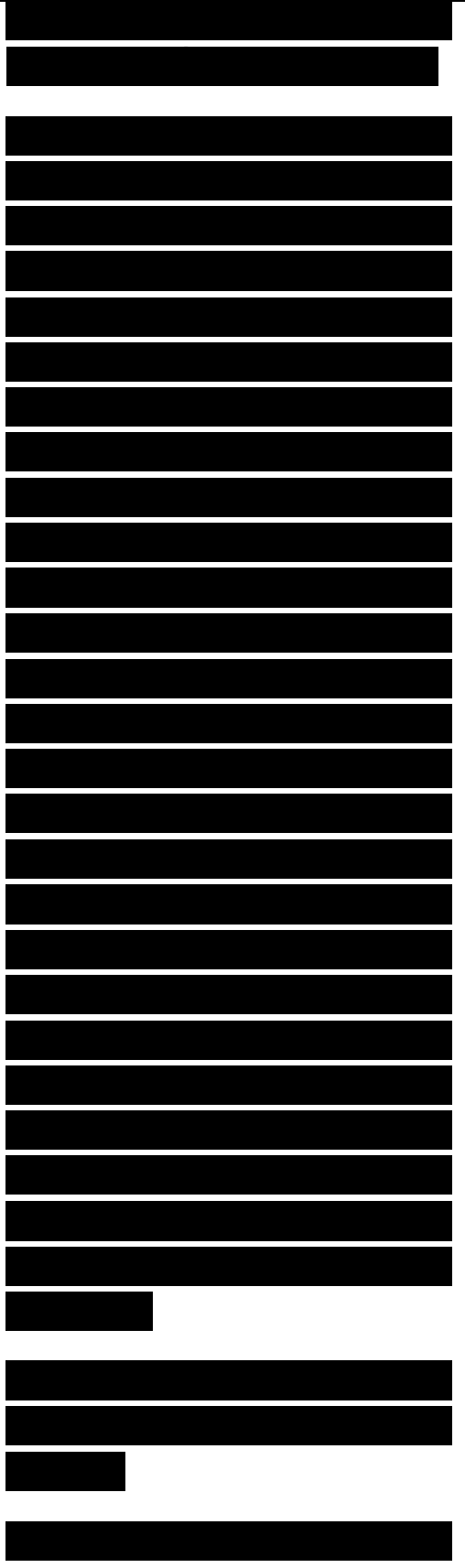
As in the case of dielectric materials, magnetic materials may be layered to take advantage of changes in properties between layers to enhance performance. Several methods can be used. For materials such as hexagonal ferrites in which the frequency at which $\lambda/4$ peaks can be controlled by doping, matched layers over different frequency ranges can be produced. Alternatively, different magnetic materials can be layered to optimize use of the properties of each.



The natural ferrimagnetic resonant frequency of a hexagonal ferrite can be controlled by replacement of a portion of the Fe+3 ions in the lattice by divalent and tetravalent metal ions such as Co+2 and Ti+4 . Therefore, magnetic materials can be constructed with properties similar to those of Figure 8.26, with different layers exhibiting different magnetic resonance frequencies [35]. Figure 8.27 illustrates one design of an optimized four-layer absorber, which required minimum reflectivity over a 1 to 15 GHz range, subject to a maximum absorber thickness of 7.5 mm. Table 8.5 provides the relative permeabilities at the resonant frequencies, where layer 1 is the outer layer and layer 4 is against a reflecting plate. Note that, on the average, better than 10 dB of RCSR is predicted from below 2 GHz up to 20 GHz, and this is obtained from a RAM less than 0.3 in. thick.

8.7 HYBRID RAM AND RADAR ABSORBING STRUCTURES

Historically, absorbers have been materials added to a



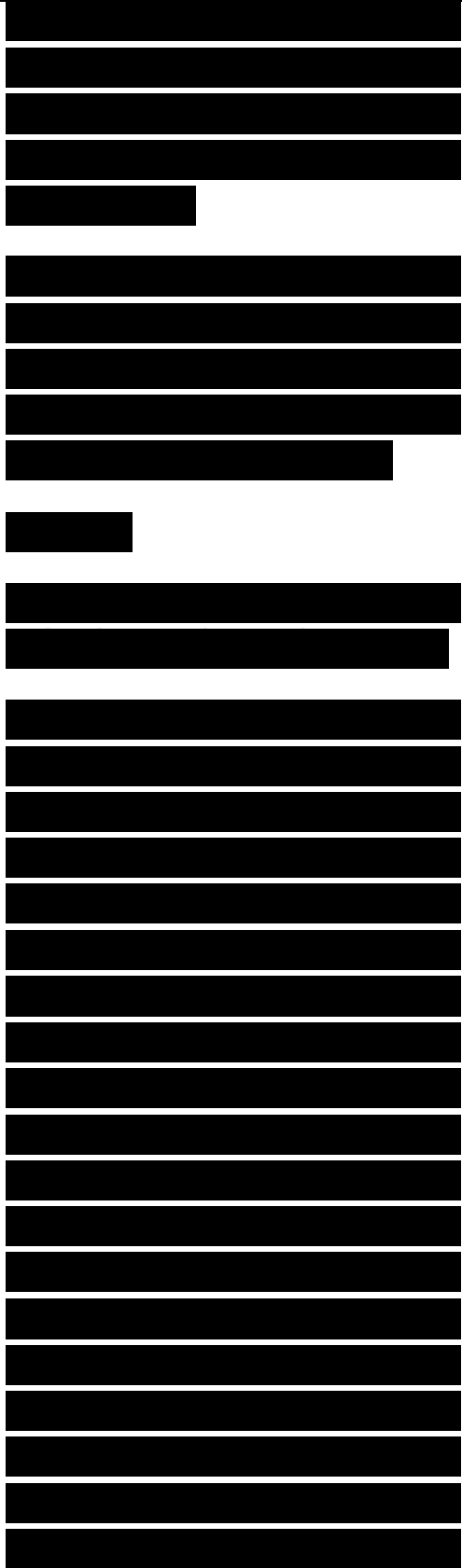
structure after the mechanical design was sized to carry the required loads, with the absorber included

Figure 8.27. Reflection loss characteristics of an optimized absorber composed of four layers of hex-agonal ferrites specified in Table 8.5 (from [35]).

Table 8.5

Ferrite Properties for a Four-Layer Optimized Absorber [35]

as a parasitic element. The underlying assumption was that the RAM would have no significant structural properties of its own. The spreading use of composites as structural materials in a number of types of platforms has increased the interest in the design of RAM as an integral part of the structure or, in some cases, as the primary load-bearing member. Particularly in the aviation community, the move toward composites as structural materials has not been driven by RCS requirements. Instead, composites (both metallic and nonmetallic) have generally been employed where they offer weight savings over conventional structures. Therefore, it is of interest to



consider how radar absorbing properties might be integrated into composite structures.

Concurrently, work has been done in combining RAM types (e.g., magnetic and circuit analog, or Jaumann and graded dielectric) to provide broader bandwidths in thinner packages or improved performance within the same band for the same RAM thickness. Materials that combine two or more of the basic absorber designs are called hybrid RAMs. Although not all of the work on hybrid RAM is related to radar absorbing structures (RAS), the two areas have been closely enough related that they can be logically grouped for discussion.

The major thrust in RAM for military applications has been toward the development of thin, broadband absorbers. In particular, as the radar community has widened the bands in which threats appear and as the drive to low RCS

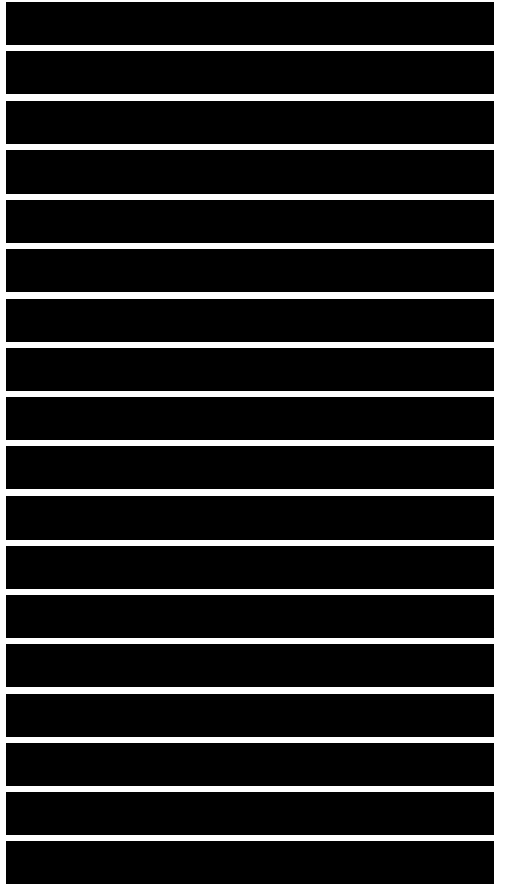
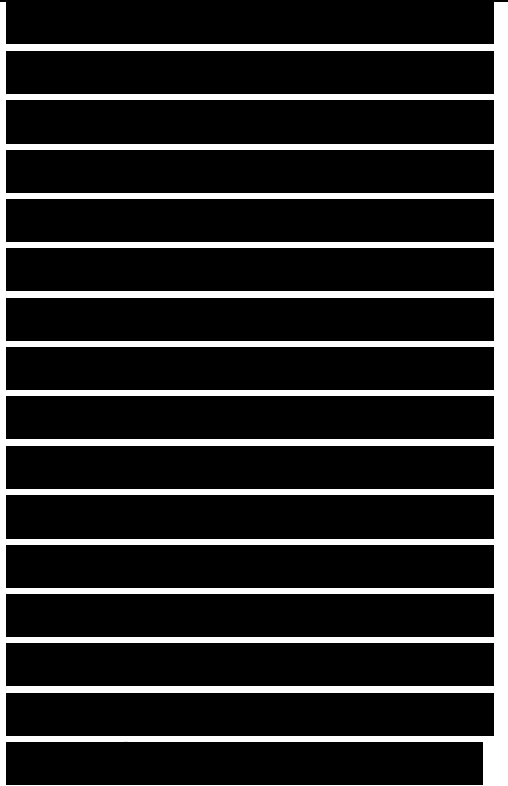
[REDACTED]

[REDACTED]

[REDACTED]

shapes has led to platforms whose RCS is proportional to the square of the radar wavelength, the need for low-frequency absorbers has increased. From the earlier discussion on dielectric RAM, it is clear that an absorber employing only electric loss will require a substantial thickness if it is to operate down to the VHF region. In fact, for wideband operation, such a RAM might be expected to be nearly a meter thick. It would be rare for such a large amount of real estate to be available solely for RAM application.

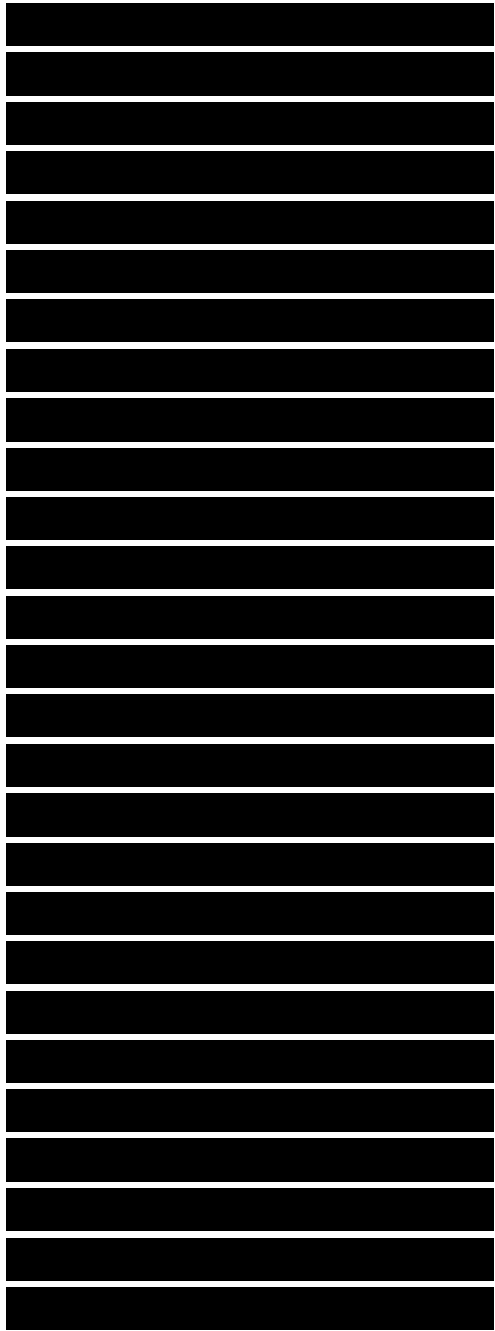
Sintered ferrite magnetic RAM, on the other hand, as shown in Figure 8.25, can provide significant RCSR in the VHF and UHF bands with thicknesses of only 5 mm to 10 mm, and such material operates best when next to a conducting surface where the magnetic field is a maximum. Therefore, a hybrid RAM for wideband operation that includes low frequencies might employ a back layer of magnetic material, with front layers of Jaumann absorbers, CA sheets, or graded dielectric. If properly designed, the dielectric absorber will be essentially transparent to the low-



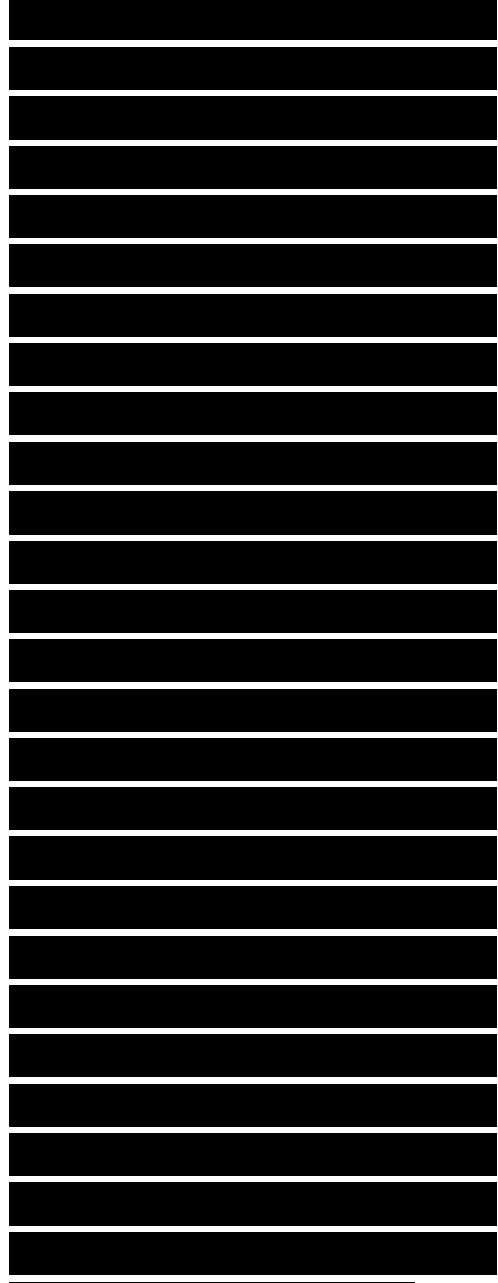
frequency waves, which will pass through and be absorbed in the magnetic back layer. At microwave frequencies, where the magnetic absorber would show poor performance if used alone, the front layers of dielectric RAM would provide the attenuation.

Other types of hybrid designs blend two dielectric RAM techniques to give improved performance over the microwave band within the same thickness used for either of the techniques alone. Figure 8.28 provides predicted data for a three-layer Jaumann absorber, a four-layer graded dielectric absorber (dipped core honeycomb, for example), and a hybrid formed by combining a Jaumann with a graded dielectric. Each layer is 7.5 mm thick, so the total RAM thickness is 3 cm. No front-face material has been modeled for these predictions. Note that the use of the combined techniques provides both improved low-frequency performance and good performance through K_a band.

One of the major problems in implementing RAM in low dielectric materials such as honeycomb is providing a front face for the RAM that meets mechanical requirement but permits the incident EM wave



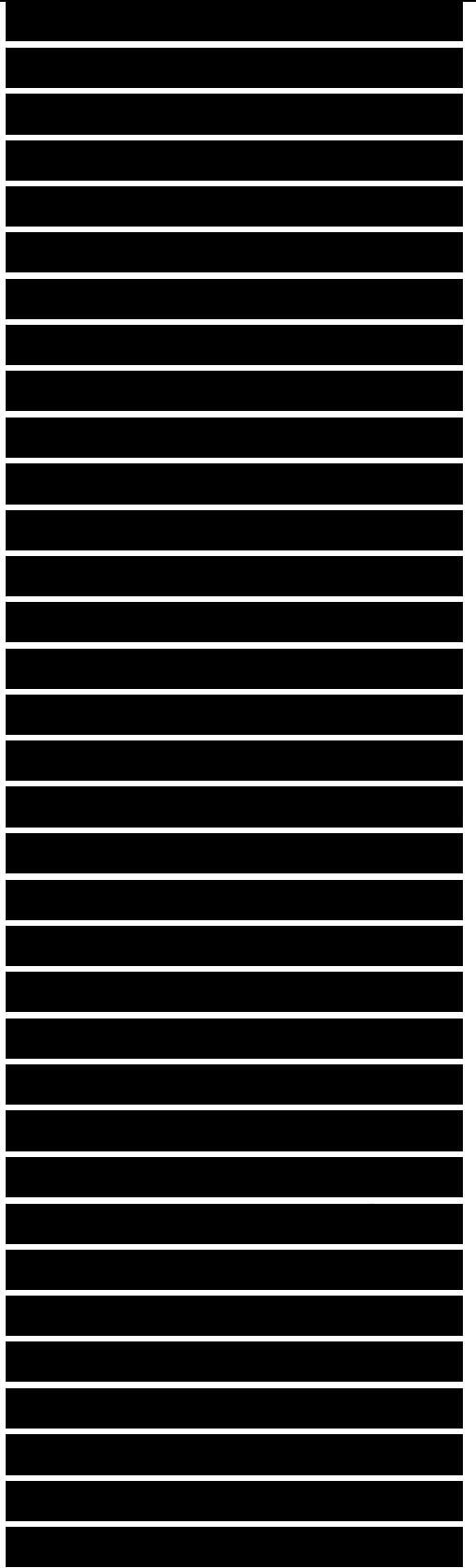
to enter the RAM where it can be absorbed. Figure 8.29 provides predictions for the hybrid RAM of Figure 8.28, along with plots of predicted performance when a front-face sheet is added to the RAM. Face sheets of $\epsilon_r = 3.0$ material are assumed (on the low end for dielectric constants of available structurally sound material [36]), and the plots provided are for sheet thicknesses of 0.5 mm and 1.0 mm. The addition of the front face does not degrade performance at the lowest frequencies, because the electrical thickness of the facing is so small it has little effect on wave reflection. However, as frequency increases, the front face provides an increasingly poor match to the incoming wave, and performance degrades. Even though the basic null structure of the unfaced hybrid is still evident, the frequency of the nulls has been shifted and their depth significantly decreased. Based on the thickness of the front face required to meet mechanical specifications, the hybrid design parameters could be iterated to produce best performance within the constraints levied by the front-face requirements, but



Dựa vào độ dày của mặt trước theo các yêu cầu của thông số cơ học, các thông số thiết kế lai hóa có thể được lặp để cho hiệu suất tốt nhất trong các ràng buộc do các yêu cầu mặt trước, nhưng việc đưa vào mặt trước

inclusion of a front face will always bring with it performance penalties.	sẽ luôn luôn ảnh hưởng xấu đến hiệu suất.

Absorbing primary structures can also be implemented by using the design techniques discussed earlier. Primary structures are often constructed from solid laminates with resistive or CA sheets as the absorber mechanism, as loading the resin with conducting material can unduly reduce the strength of the final laminate. Figure 8.30 provides predictions for a laminated structure consisting of four layers of $\epsilon_r = 3.0$ material separated by three resistive sheets having a quadratic resistance taper (94, 377, and 848 ft/sq). Each laminate layer is 4.81 mm thick (chosen for resonant performance at 9 GHz using $t = \sqrt{\lambda V \sim \epsilon_r}$), for a total thickness of just under 2 cm. Although the level of performance is not nearly as impressive as that achieved by the low dielectric constant hybrid, RCSR values in excess of 10 dB are predicted from below 3 GHz to above 16 GHz. Nulls in the design are placed to provide good performance in the S, X, and Ku threat bands. In addition to having reasonable RCSR performance, such a panel would be very strong and might be suitable as a primary load-bearing structure.



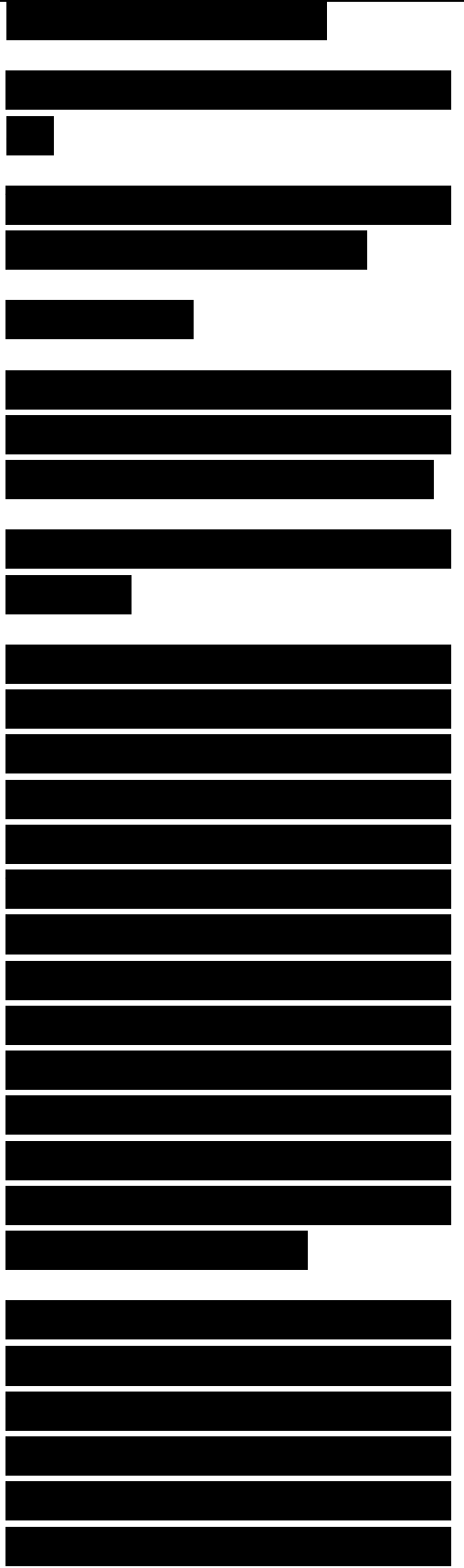
Frequency (GHz)

Figure 8.30. Reflection coefficient as a function of frequency for a solid laminate RAS absorber.

8.8 NONSPECULAR RAM

The discussion of RAM to this point has concentrated on the reduction of specular, or mirrorlike, radar returns. As has been noted in all of the earlier chapters that discuss design guidelines, the first tool to be employed in RCSR is shaping, and the goal of shaping is to eliminate all specular returns in the primary threat sectors.

Obviously, if that goal can be accomplished, specular RAM has a very small role in RCSR design, and the reduction of nonspecular returns requires the focus of our attention. However, although significant



progress is being made in the application of nonspecular absorbers, the theory necessary to support a design methodology is not nearly as well understood as for the specular case.

Nonspecular returns arise from surface traveling waves, edge waves, and creeping waves. In addition, the returns from gaps and cracks and edge diffraction are also often classed as nonspecular returns. The characteristic that distinguishes most of the mechanisms of interest in nonspecular scattering is that they are due to surface currents along the direction of propagation and are therefore spatially extended effects. For this reason, the optics formalisms that apply to specular RAM design are, in general, not appropriate for nonspecular RAM design.

In this section two different areas of nonspecular RAM design are explored. The first discusses the use of magnetic or dielectric surface coatings to reduce surface currents and

[REDACTED]

[REDACTED]

[REDACTED]

[REDACTED]

hence reduce traveling and creeping wave returns. The second area concerns the use of tapered resistive strips (and, by extension, bulk edges) to both attenuate edge diffraction returns and control the sidelobes of the specular returns from surfaces.

[REDACTED]

[REDACTED]

8.8.1 Magnetic and Dielectric Coatings for Surface Wave Control

[REDACTED]

As was noted in Section 8.6, magnetic RAM is employed most effectively in close contact with a perfectly conducting surface where the magnetic field has its highest value. It has long been known that a thin coating of magnetic RAM could effectively reduce traveling and creeping wave returns; however, until recently the analytical tools available for use in the design of such coatings were limited to canonical problems such as scattering from small spheres [6]. Though not generally as effective (on a dB attenuation per wavelength of coating basis), lossy dielectrics can also be employed to reduce surface currents. Clearly, the

[REDACTED]

mechanisms that control the loss must be understood if intelligent designs are to be formulated. The remainder of this section describes an analytical development that leads to an approach for the design of surface coatings to reduce nonspecular scattering.

An initial approach to the calculation of the effects of a surface coating on traveling wave amplitude was provided by Strattan [37], based on an analysis by Collin treating surface waves along dielectric slabs [38]. In that analysis, an assumption is made that the slab is electrically thin enough that only the lowest order mode propagates. Reference [39] provides a numerical analysis of surface wave propagation on lossy ferrite slabs, which includes the effects of higher-order modes. The treatment here will consider only the simpler case of lowest order mode propagation.

In his development of surface wave propagation along dielectric slab waveguides, Collin notes that a surface with an inductive component to its impedance can support a bound wave only for the polarization

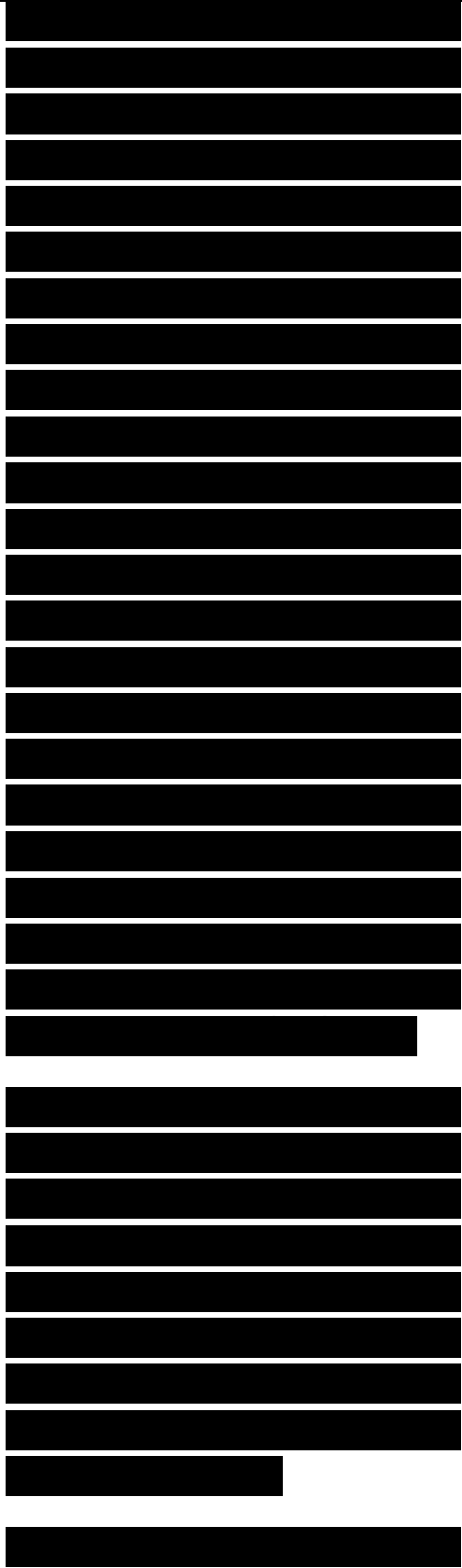
[REDACTED]

[REDACTED]

[REDACTED]

for which the magnetic field is parallel to the surface. In fact, we see traveling wave effects on RCS because a metallic surface has a surface inductance equal to its surface resistance. However, as the resistance of metals is low, the attenuation is negligible. In his development, Stratton considers the requirements for a surface coating that will support a traveling wave, yet provide significant attenuation. Thus, in nonspecular RAM design, the same two questions arise as in specular design: How do I couple energy into the absorbing medium? How do I provide attenuation once the wave is in the absorber?

Figure 8.31 illustrates the problem to be solved, which involves a perfectly conducting plane coated with a thin layer of homogeneous material with properties ϵ_i and f_X . The incident wave has an electric field in the x-z plane, and the associated magnetic field in free space is given by

$$H_{y0} = H \exp[i(\Delta)Z - k(x)] \quad (8.46)$$


with propagation constants β_0 and β_1 such that

$$\beta_0 \cos \beta_1 h = \beta_1 \cos \beta_0 h \quad (8.47)$$

where λ_0 is the free-space wavelength. A similar set of equations holds for the magnetic field inside the layer, with the values of β_0 , h , and β_1 depending on the thickness of the layer and the electrical properties of the coating (i.e., $\beta_1 = \beta_0 \sqrt{\epsilon_r - \sin^2 \theta}$). For the guided wave case, the impedance at the boundary must match for the two waves (the free-space wave and the one in the coating layer). A matched condition occurs with $Z_{ox} = Z_{\lambda x} = Z_s$, where Z_{ox} is 377Ω , and Z_s is the surface (or input) impedance of the coating. Matching impedances and solving for the equivalent of (8.46) in the material gives $h = \lambda_0 Z_s / 377$. The value of h can then be substituted into (8.47) to find p .

The parameter of interest is the attenuation of the z-traveling wave provided by the coating,

and that is given by the imaginary part of 3, where

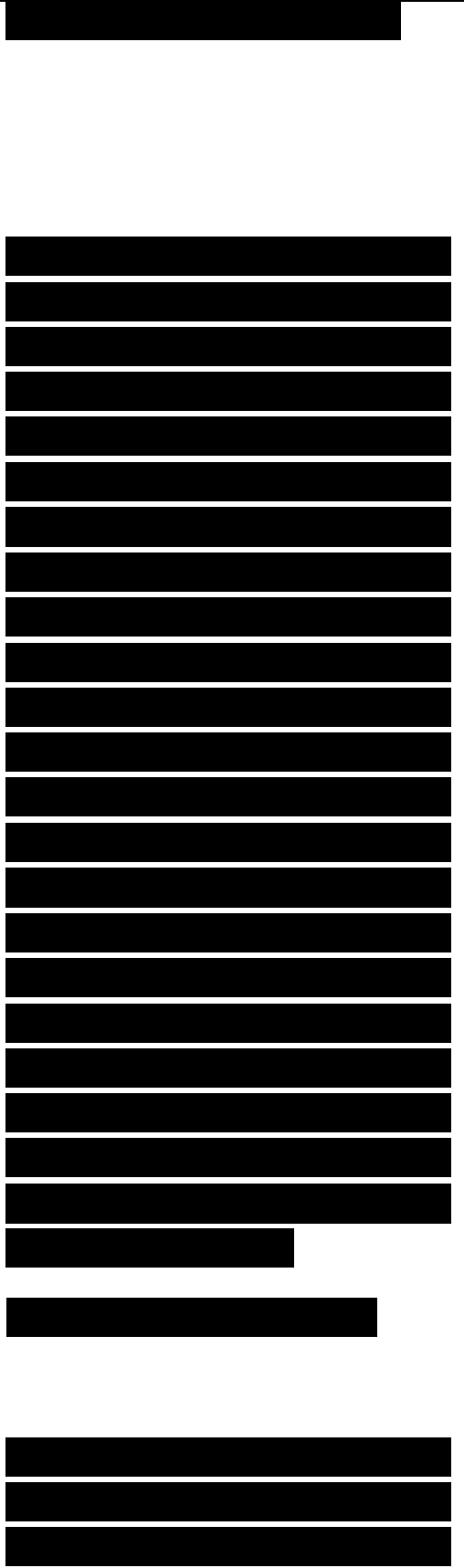
$$P = (2ir/A_0)(1 - Z_f/3772)^{1/2} \quad (8.48)$$

The surface impedance of the layer will depend on the angle of incidence of the incoming wave. However, for large ϵ and μ , values, the direction of the refracted ray in the material layer will be very close to normal, regardless of the incidence angle. For example, typical properties for a ferrite-loaded neoprene coating at 1 GHz might be $\epsilon_r = 14 + i2.38$ and $\mu_r = 2.5 + i1.0$ [40]. The angle of the wave refracted into a layer of such material would remain within 10° of normal for angles down to grazing. So it is a reasonable approximation to assume that the impedance is not a function of incidence angle and is given by the normal incidence formula, (8.7). The attenuation per wavelength of travel in the z-direction in the layer is then given by

$$L = 8.69 \text{Im}\{\gamma\} \text{ dB}/\lambda \quad (8.49)$$

where $\text{Im}\{\gamma\}$ indicates the imaginary part.

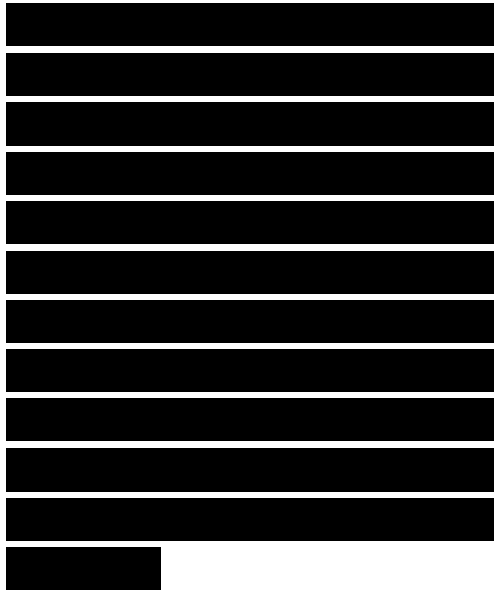
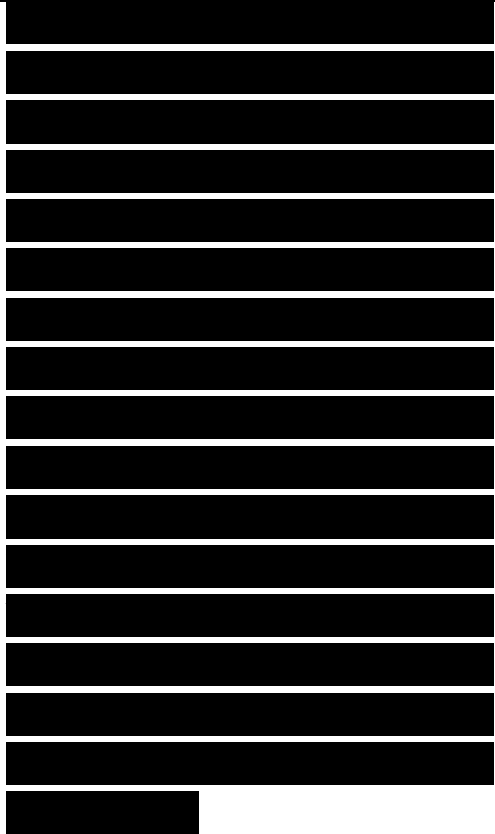
Figure 8.32 provides a plot of the loss in dB per free-space wavelength of travel for a 1 GHz wave propagating in a



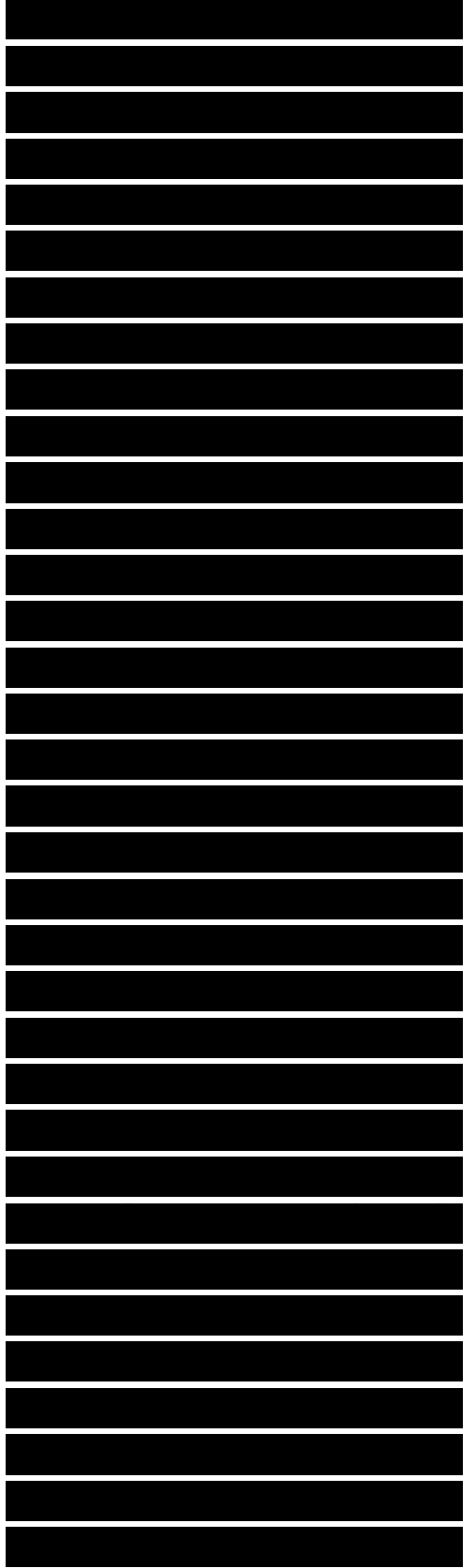
surface layer with the electrical properties given previously. Note that the attenuation rises rapidly with increasing thickness, but peaks and then begins rapidly decreasing. The decrease occurs as the surface impedance begins to go from inductive to capacitive, and the layer begins to shed, rather than trap, a surface wave. The peak loss for the material shown is about 28 dB/ X_0 and occurs for a layer thickness of about $0.037\lambda_0$, or 1 cm at 1 GHz.

Although very thin, purely dielectric surface coatings are not as efficient at attenuating traveling waves as surfaces with magnetic properties, dielectric loss can be employed for that purpose. Loaded-core honeycomb or lossy dielectric layers above a ground plane will produce loss, with the loss depending on the dielectric properties and the thickness.

Medgyesi-Mitchang and Putnam [41] provide a method-of-moments analysis that considers scattering from flat and curved strips coated with



thin dielectric layers. Figure 8.33 provides predicted results for 10A. long strips. Three cases are shown. The first, for a conducting strip, shows the expected traveling wave lobe appearing around 15° from grazing, as would be expected for the indicated polarization. The second case is for a strip coated with a lossless dielectric. Note that the traveling wave has not been suppressed, but it has moved closer to grazing due to the increased effective electrical length of the strip (because of the presence of the dielectric). Adding loss to the dielectric results in about a 10 dB decrease in the traveling wave amplitude (note that the EE convention is used, so $\epsilon_r = \epsilon' - j\epsilon''$ rather than $\epsilon' + j\epsilon''$). Equation (8.49) would predict about 0.5 dB/ X_0 attenuation of the traveling wave, so if two-way propagation (to the end of the strip and back) is assumed, results are commensurate with predictions from the simple theory presented earlier. Note, however, that the assumption of normal incidence surface impedance in the preceding analysis is not very accurate in this case. For the 15° grazing angle that produces the peak traveling wave return, the angle of the ray refracted into the



material is about 40° off normal incidence.

For a layer as thin as in Figure 8.33 ($0.057X_0$), the electric field intensity in the dissipative material is low, and hence the attenuation is also low. Increasing the thickness of the layer increases the attenuation, and results as good as those obtained for the magnetic absorber can be obtained, albeit at the expense of significantly increased thicknesses. For the earlier example, a 1 cm thick magnetic coating provided 28 dB of surface wave attenuation at 1 GHz for each wavelength of propagation. The dielectric coating with $\epsilon_r = 2 + i1$ providing the same attenuation would be about 4 cm thick. However, increasing the dielectric constant to $\epsilon_r = 8 + i4$ would give a maximum attenuation of about 25 dB/ X_0 in a layer only $0.1X_0$ thick.

8.8.2 Tapered Resistive Edge Treatments

As noted earlier, scattering arises from impedance discontinuities on a body. Those discontinuities can be due to changes in materials (e.g., transition from a metal

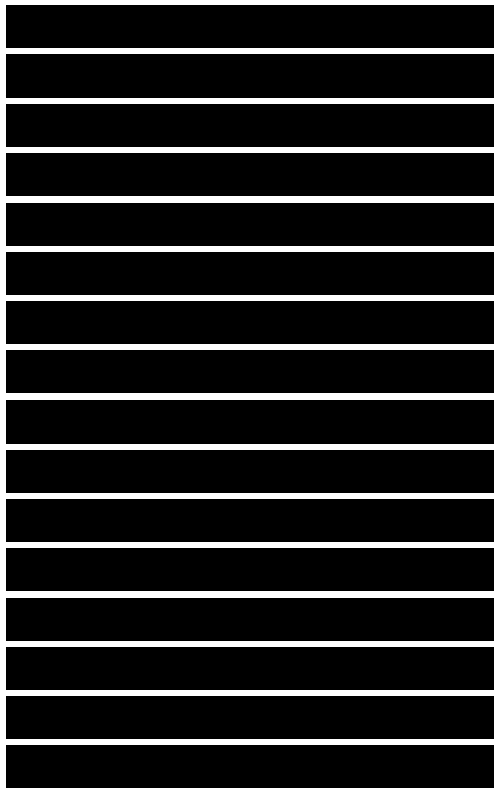
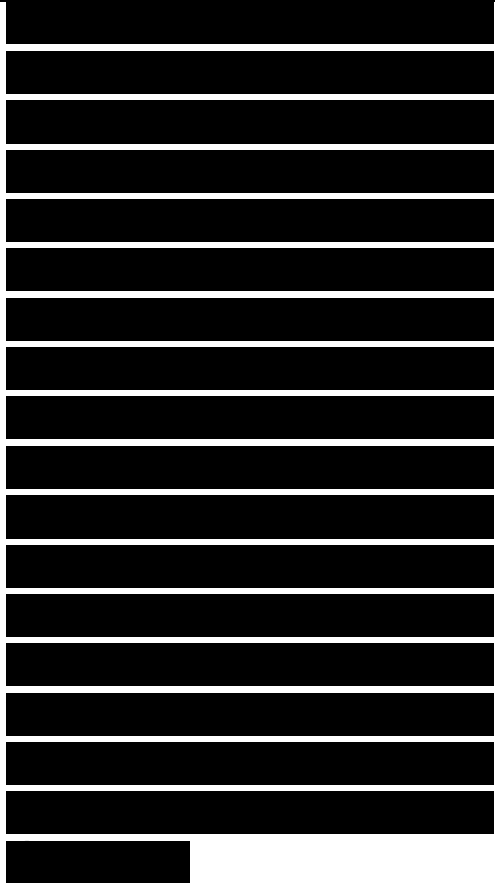
[REDACTED]

[REDACTED]

[REDACTED]

fuselage to a nonconducting canopy), or they can be geometric (a discontinuity in any derivative of the surface contour provides a theoretical opportunity for back- scatter, although discontinuities with radii of curvature greater than a wavelength can generally be ignored). Obviously, two of the most severe discontinuities achievable are sharp edges and corners, but they are also structures that often appear on vehicles designed for low RCS because of their natural occurrence in application of the shaping rules.

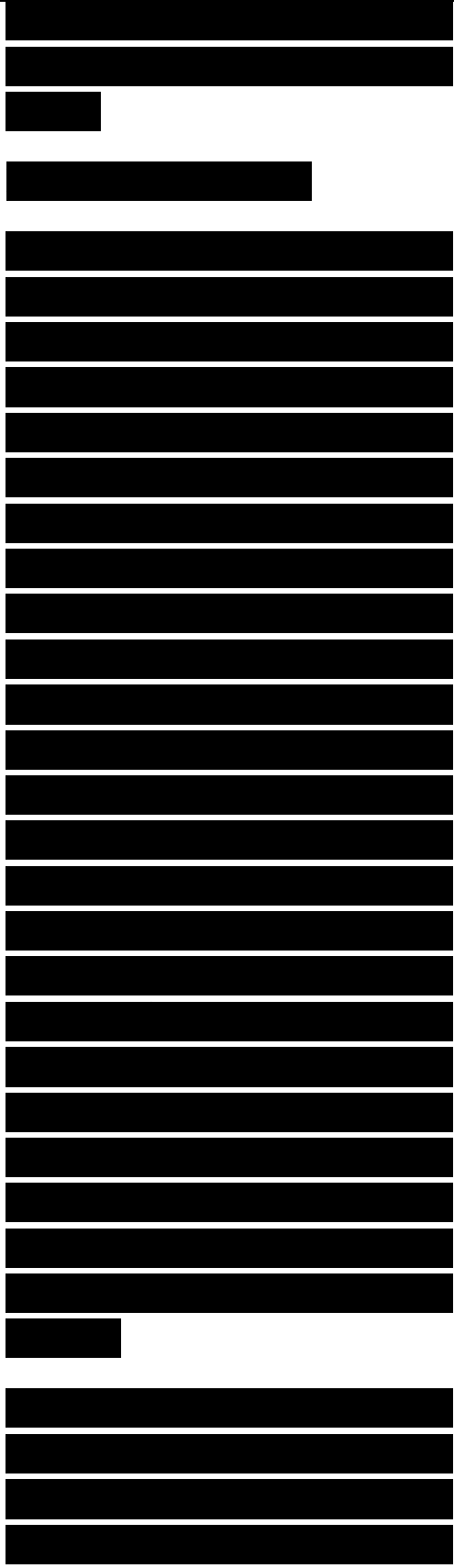
Edges and corners are important constituents in three different types of scattering. First, specular to a leading edge for parallel polarization or a trailing edge for perpendicular polarization, there is an edge diffraction return given as $\sigma = L^2/tt$, and a corner provides a lower level, but relatively isotropic, diffraction return. Next, edges and corners provide the area from which physical optics end- region returns arise. Finally, edges and corners provide discontinuities that reflect surface traveling waves and edge waves, giving the opportunity for return in the



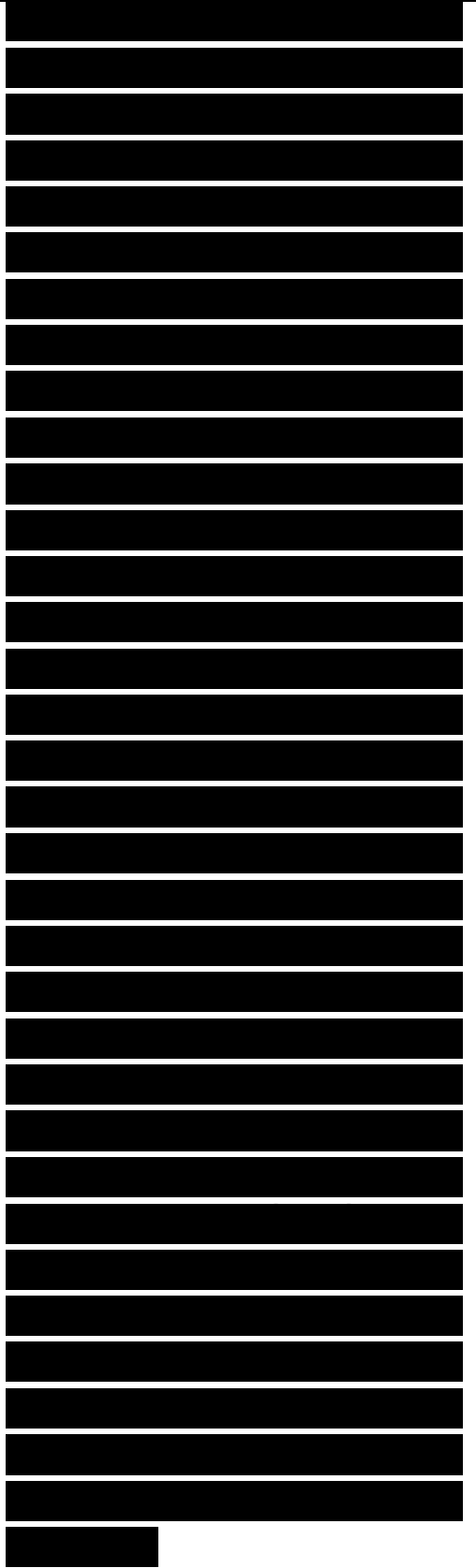
backscatter direction.

Therefore, the treatment of edges can potentially reduce threat sector RCS levels for all three of the major scattering mechanisms expected in a vehicle shaped for low RCS. As in the design of specular RAM, wideband edge treatments must provide a slowly varying impedance to taper the transition between free space and the body being treated. In treating 3D bodies, that transition is generally provided by geometrically and electrically tapered bulk edge absorbers implemented as a graded dielectric (e.g., loaded core honeycomb). In addition, tapered resistive sheets may also be used on the face of the bulk absorber to add to the performance. The geometry of a bulk edge treatment is shown in Figure 8.34(a).

Analytical tools for design of bulk edge absorbers are not nearly as well developed as tools for specular RAM design.



In fact, much of the work to date on such absorbers has been empirically based, either through actual testing of bulk edge treatments on measurement ranges or through numerical experiments using method-of-moments codes. Even the numerical experiments have not looked at the general design problem, as that would require a 3D MOM code able to model a volume (not surface) potentially many wavelengths in size in each of the three dimensions. Therefore, much of the analysis and numerical modeling has treated the simpler problem of a resistive sheet added as an edge termination to a thin, flat plate, as shown in Figure 8.34(b). Even for that case, only a 2D geometry can typically be modeled, and so the effect of corners is not included. All of the examples in this section have been produced for the 2D case, so the assumption is made that treatments that are effective for reducing edge scatter mechanisms will also be effective for the corner scatter case.

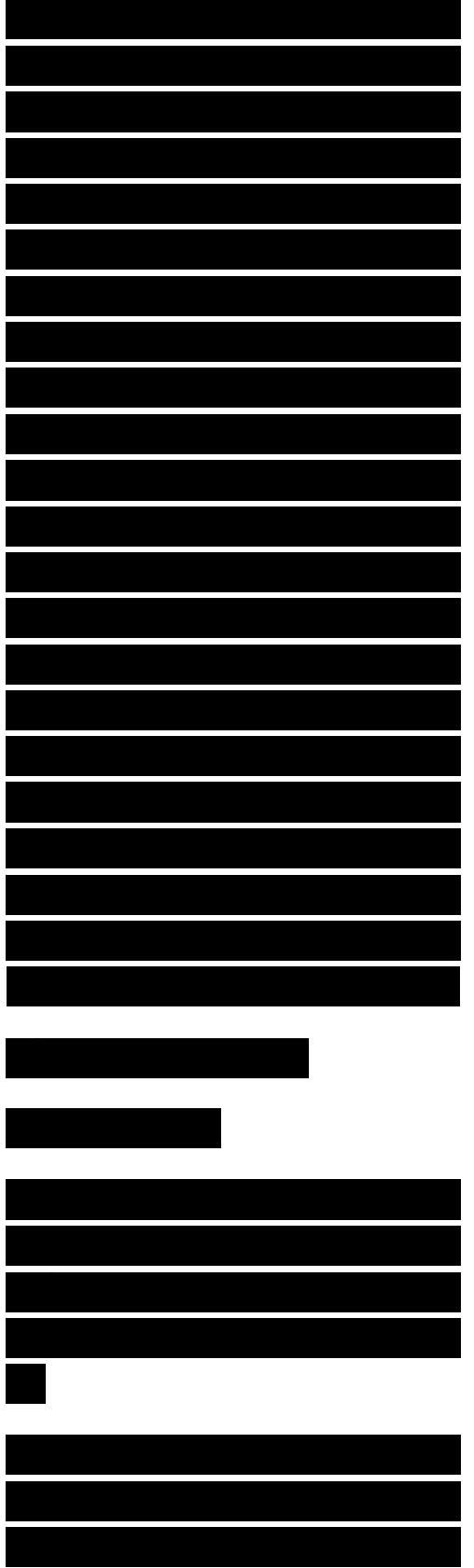


It would, of course, be nice if an analytical approach would provide design guidance based on all three of the scattering mechanisms of interest for edges. No such approach currently exists. Historically, the design of resistive tapers has postulated a taper (e.g., quadratic, exponential, parabolic) and then analyzed the resulting scattering characteristics when the taper was applied as an edge treatment. However, scattering is caused by currents, and the current taper, not the resistive taper, should be controlled. Haupt and Liepa [42] recognized the fact that the current is the quantity of interest and presented an analysis that treats control of the sidelobes of the specular return from strips based on control of the current

Conducting Plate Resistive Card
 $R \sim 0 \quad R \sim R(x)$

Figure 8.34. Edge treatment absorbers: (a) tapered bulk edge absorber, and (b) resistive edge card absorber.

taper. Numerical modeling has shown that edge treatments which adequately control



specular sidelobes also provide good reduction of the diffraction and traveling wave returns. Applications of the results of [42] and extensions to other tapers were developed by John Shaeffer for the Georgia Tech RCSR Short Course [43], and his results form the bulk of the examples that follow.

The focus of [42] is design of resistive tapers for control of the sidelobes of the specular return, what we have called end-region scattering. The contention is made (and demonstrated with numerical examples) that physical optics is sufficient to describe the scattering for angles near broadside and for highly resistive or tapered resistive strips, because for those cases the edge currents make such a small contribution to the total surface currents. With the assumption that physical optics holds, a simple relationship between the surface current and the resistive taper can be derived. For a 2D strip with a finite width in the x direction, the resistive taper in terms of the current taper $J(x)$ is given by

$$R(x) = \frac{377}{2} \left\{ \frac{e^{-kx} \cos W/J(x)}{\sin(\theta)} \right\} \quad (8.50)$$

for polarization parallel to the edge of the strip (E-polarization), and

$$R(x) = 377 \sin \theta [e^{-ikx \cos \theta} J_0(x) - 1/2] \quad (8.51)$$

for polarization perpendicular to the edge of the strip (H-polarization), where θ is the grazing angle (note that Figure 1 in [42] is not correct in its polarization definition).

Clearly, a physical resistance taper cannot be changed as a function of the incident wave direction, so for design purposes the broadside case ($\theta = 90^\circ$) is chosen for analysis. For the broadside case (8.50) and (8.51) both reduce to

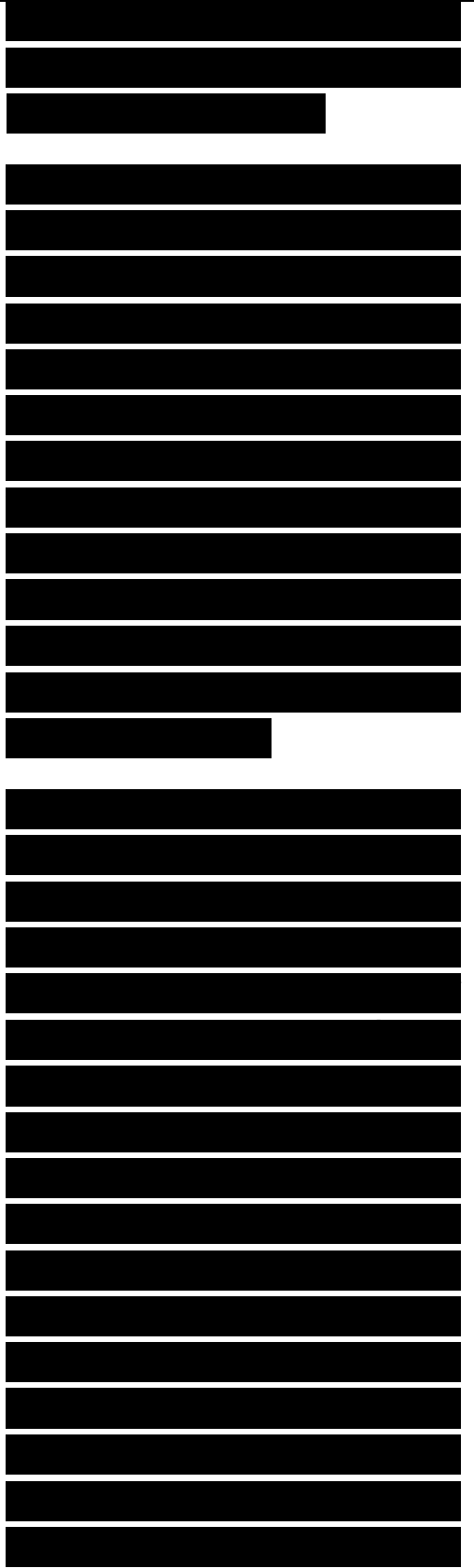
$$R(x) = 377 [J_0(x) - 1/2] \quad (8.52)$$

Obviously, use of the resistive taper given by (8.52) will result in the desired current taper only for broadside incidence. Tapers for angles other than broadside may be obtained by using (8.50) and (8.51). However, for those cases a complex impedance taper will result, rather than a simple resistive taper, so for our

examples tapers based on (8.52) are used.

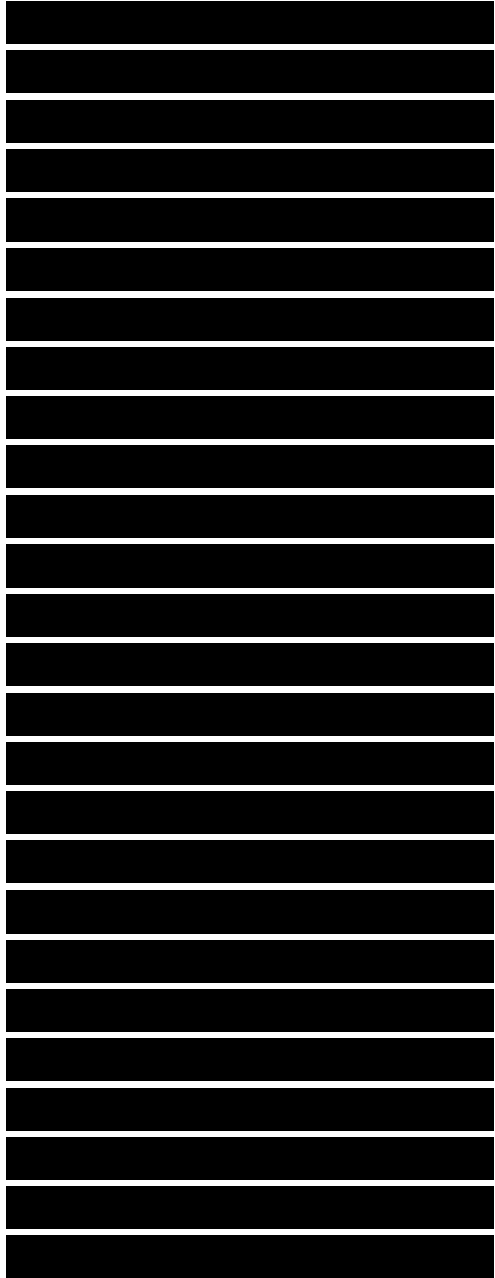
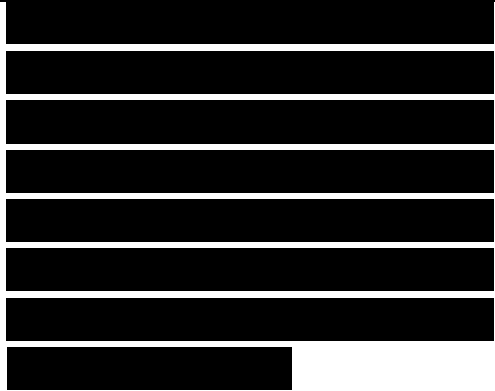
With control of the current taper on the strip, the design of resistive tapers to produce low sidelobes is similar to the problem of designing illumination tapers for low-sidelobe antennas. Also, since the farfield radiation pattern is related to the Fourier transform of the current on the strip, advantage can be taken of the work done in windowing functions for sidelobe control in spectral analysis [44],

Figure 8.35 shows five normalized current tapers typical of windowing functions used for spectral analysis. Based on results for reasonable length tapers (i.e., tapers one-half to one wavelength long) the Hanning and linear tapers have shown the best performance of those examined. The linear current taper (also called the triangle taper or Bartlett taper) has a first sidelobe 27 dB down from the peak, and a sidelobe fall-off of 12 dB/octave. That compares favorably with the uniform, or rectangular taper (no current taper), which has a -13.2 dB first sidelobe and a



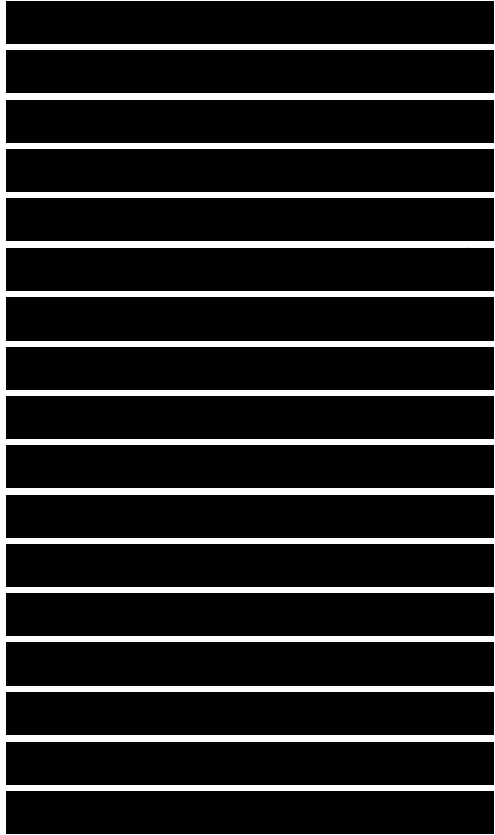
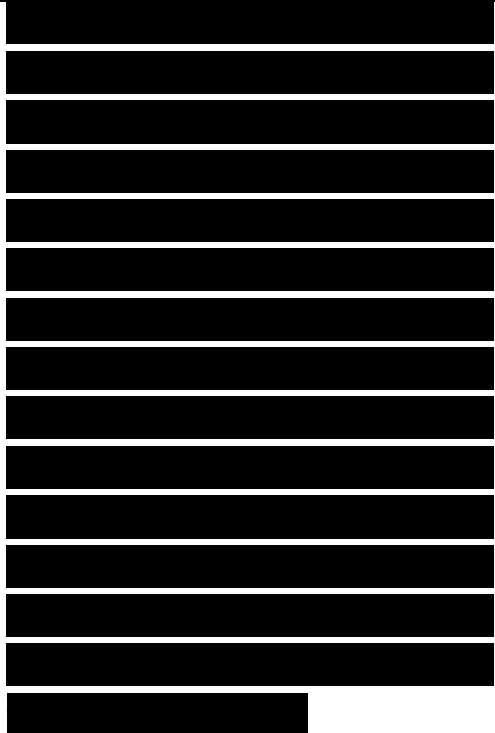
fall-off of only 6 dB/octave. The Hanning taper is a cosine-to-the-first-power taper, and it has -23 dB first sidelobes and a 12 dB/octave fall-off rate.

Given the desired current taper, (8.52) can be applied to solve for the resistive taper that provides such current. Figure 8.36 plots the resistance tapers that correspond to the current tapers in Figure 8.35. Note that all of the tapers have a zero resistance at the edge of the strip that adjoins the metallic surface and an infinite resistance at the free-space end of the strip. The two best tapers have current values at the midpoint of the resistive strip of $n_x H_i$, one-half the physical optics current for a conductor. This translates to a resistance value of $377/2 \text{ ft/sq.}$ at the midpoint of the strip. Figure 8.37 plots the surface current on a 5X long conductive strip for grazing, 45° , and broadside illumination angles for E-polarization and the resulting backscattered RCS for that case. Note the strong edge diffracted field. In Figure 8.38, the two edges of the conducting strip have been



replaced by 2X long tapered resistances designed to provide a linear current taper. Therefore, the conductive strip is IX wide. At broadside, the resistive strips have produced a current that exactly matches the desired linear profile. At 0° and 45°, the taper is not quite linear, but it still smoothly transitions the current from a maximum value to zero. Note that the sharp current singularities at the leading edge that produce the large edge diffraction return have been very effectively killed off by the resistive taper.

The backscatter pattern for the strip with tapered resistive edges clearly points out the advantages of such treatment. Most obvious is the large reduction in the edge diffraction return, which has gone from -8 dBm to about -44 dBm. In addition, the sidelobes have been lowered (which was the original intent of the design). One disadvantage of tapering the currents is that the mainlobe width is increased (for the linear taper, the percentage increase in the 3 dB beamwidth is theoretically 28% [44]); however, that is a small price to pay for the significant reduction in RCS obtained far



off specular. A similar analysis by Shaeffer of the effects of the 2X linear current taper for //polarization shows that a +3 dBm traveling wave return is reduced to -35 dBm. A IX. linear current taper reduces the traveling wave lobe by about 18 dB. Thus, a tapered resistive treatment is effective in reducing the traveling wave return as well as the edge diffraction and the specular end-region returns.

The analysis in [42] and the examples from [43] make the simplifying assumption that any resistive taper, and hence any current taper, may be obtained. There are practical limitations on the high- and low-resistance limits that may be achieved and on the precision with which a resistive taper may be manufactured. In addition, as noted, the performance falls off rapidly as the width of the resistive treatment (in wavelengths) decreases. For effective performance, at least a one-half wavelength taper is required at the lowest frequency of interest and a full wavelength is better. Nevertheless, even with the

[REDACTED]

[REDACTED]

[REDACTED]

practical problems of implementation, tapered resistive treatments provide significant capabilities for RCSR of vehicles shaped for low RCS.

Strip Position (x/λ)

(a)

Backscatter Angle (degrees)

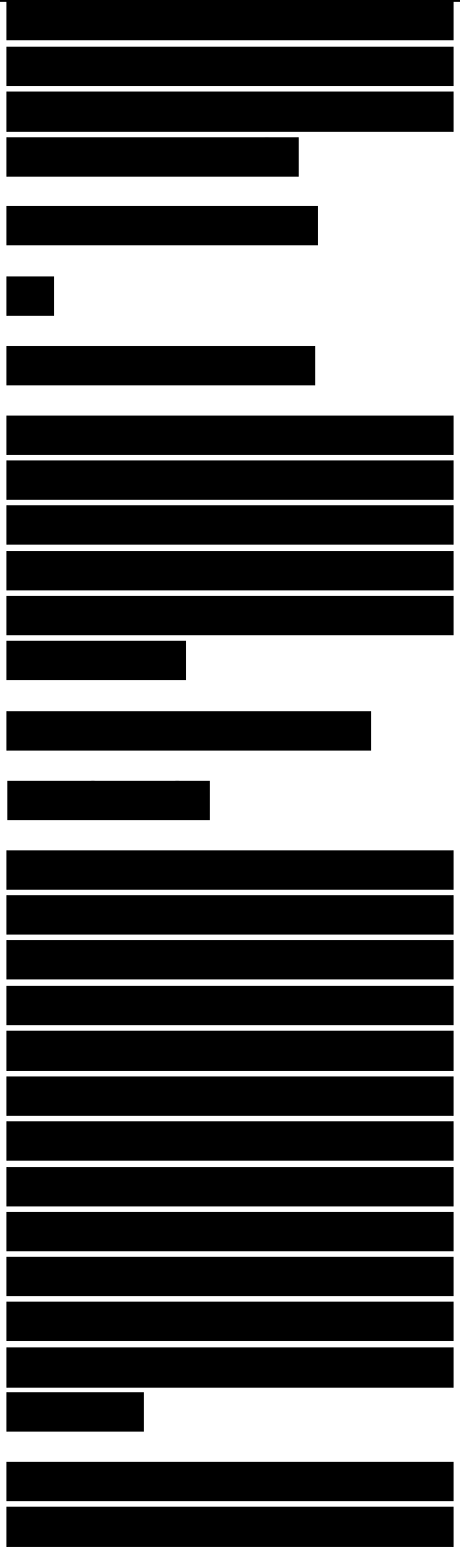
Figure 8.37. (a) Surface currents on a 5λ wide conducting strip for grazing angles of 0° , 45° , and 90° ; and (b) backscattered RCS for the 5λ strip for the electric field parallel to the edge of the strip.

Strip Position (X/λ) (a)

8.9 SUMMARY

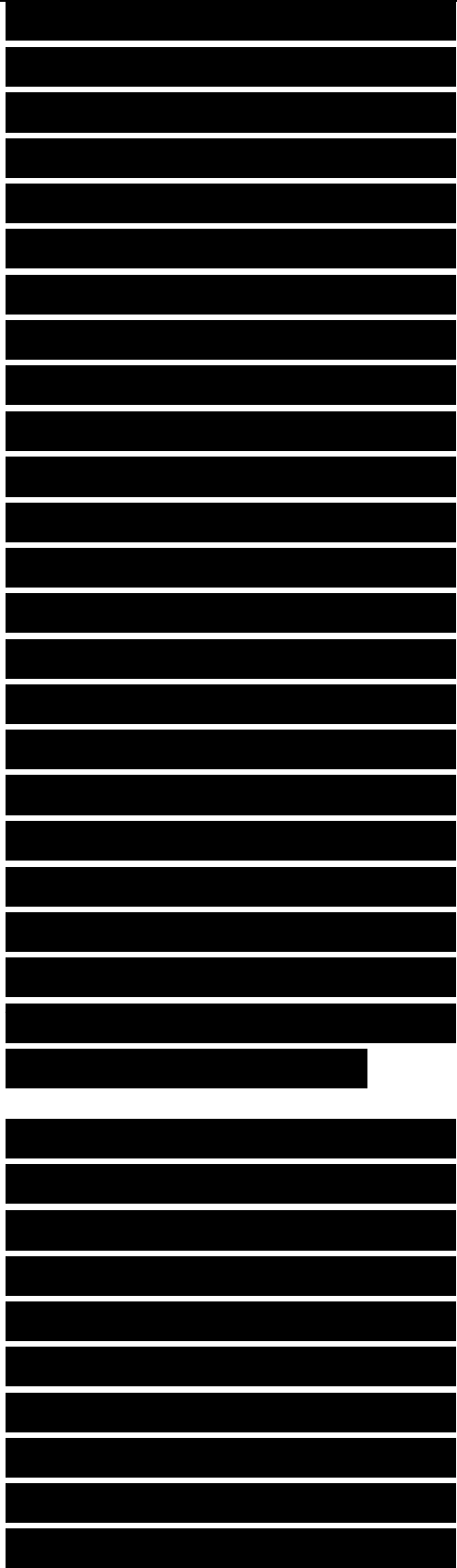
Satisfactory broadband RAM performance is predicated on getting the RF energy into the RAM and then providing sufficient loss to absorb the necessary energy within the allowed RAM thickness. These two requirements often conflict, because high-loss materials often have intrinsic impedances much different from that of free space, and thus suffer high front-face reflections.

There are two basic solutions to this dilemma, but each has its drawbacks. The first



solution is to taper the loss from the front to the back of the absorber; this method is employed in Jaumann, graded dielectric, and geometric transition absorbers. However, the increased performance obtained by tapering the admittance is accompanied by increased thickness. Typically, such absorbers will be near a half-wavelength in thickness at the lower end of the frequency band over which they provide a 20 dB or greater level of RCSR. Some reduction in thickness can be obtained through use of circuit analog sheets to replace resistive sheets, or through hybrid (e.g., CA and graded dielectric) techniques. Again, a penalty must be paid, this time in terms of design complexity and cost.

The second solution is to employ materials with both a high loss and an intrinsic impedance near that of free space, which implies a material with a high value for both μ and ϵ . Many practical magnetic materials come close to meeting those requirements, but only over a very limited frequency range because of the highly resonant nature of the permeability. Again, multilayer



techniques utilizing different magnetic materials can be used to extend the bandwidth at the cost of RAM thickness and complexity.

When very wide bandwidths are required, hybrid techniques that take advantage of the low-frequency performance of magnetic materials and the high-frequency performance of circuit analog or graded dielectric are attractive. However, although such hybrids can provide significant performance in a reasonable thickness, problems in bonding, complexity in production and maintenance, and high cost are typical of such designs.

Integration of RAM into the structure of a vehicle is an obvious advantage from a design standpoint. Therefore, RAS is a fruitful area of current research. For aerospace applications in which honeycomb is normally utilized, substitution of a circuit analog, Jaumann, or graded dielectric absorber may be relatively straightforward. Problems arise, however, in designing a front face for the honeycomb that meets mechanical requirements with

[REDACTED]

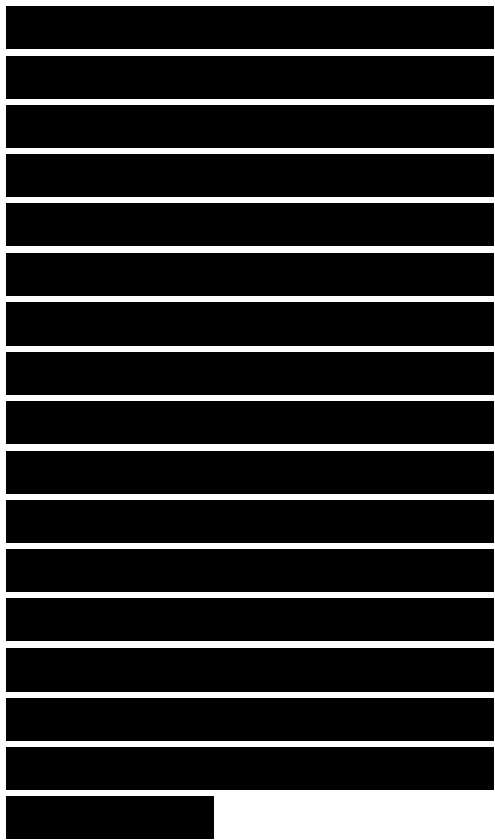
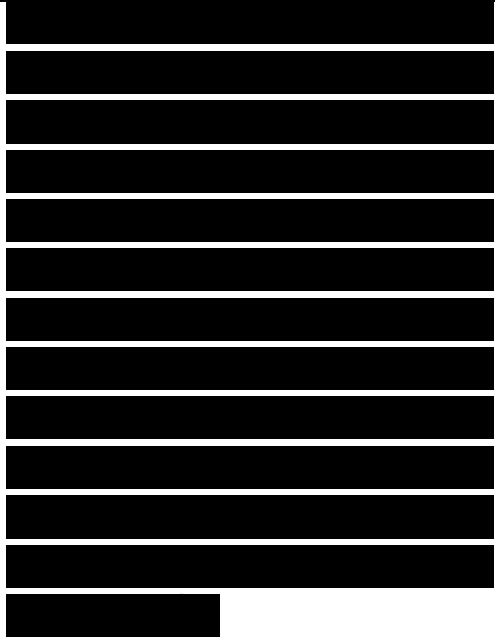
[REDACTED]

[REDACTED]

minimum reflection of the incoming RF energy. For primary structures that require significant strength, various laminates using internal resistive or CA sheets to provide loss have been studied. In general, such designs surrender RCSR performance level and bandwidth for added strength.

For applications in which a specific threat sector can be identified, every effort will normally be made to shape a vehicle to minimize the specular RCS. In such cases, attention must be paid to the return caused by traveling waves and edge diffraction. The design of absorbers to suppress these effects is much different from that for reduction of specular reflection. Analyses are available that discuss the suppression of edge diffraction, and an analysis was presented that deals with traveling wave absorption.

This chapter has cataloged typical types of RAM and discussed their performance characteristics. A wide range of

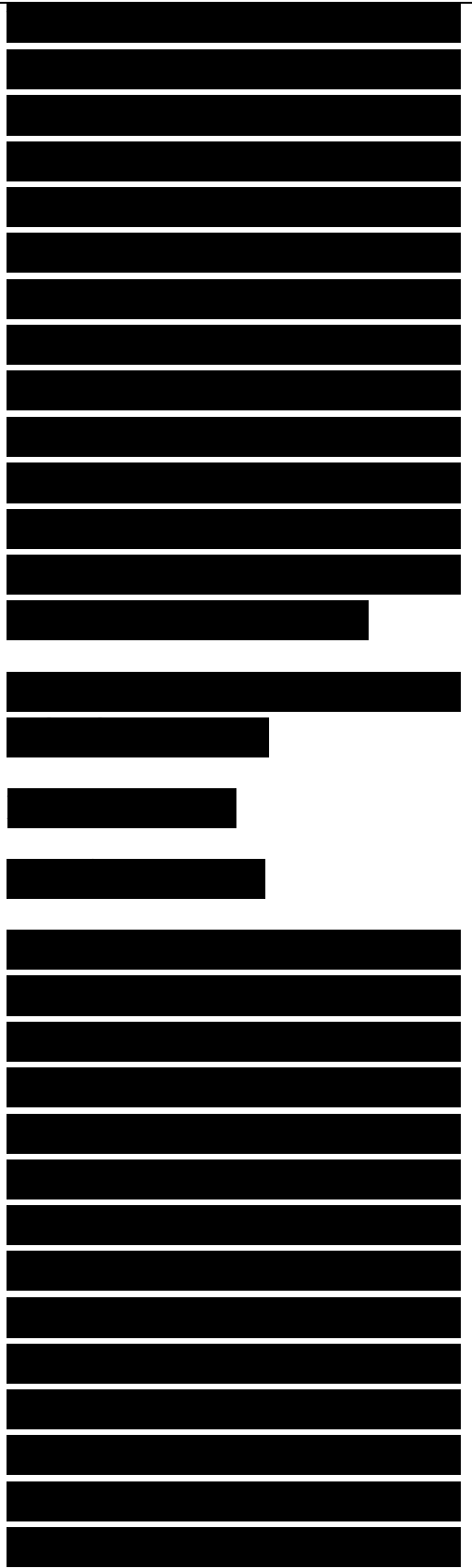


commercial material can be obtained for RCSR application. Nevertheless, whether commercially available RAM is purchased or an effort is made to tailor a new design to the specific problem, RAM application will usually involve a trade-off between performance, cost, complexity, and ease of manufacture and maintenance. Only through knowledge of RAM performance, familiarity with the types of RAM available, and good engineering judgment will the best RCSR solution to a given problem be chosen.

Chapter 9 Radar Absorber Measurement Techniques
Eugene F. Knott

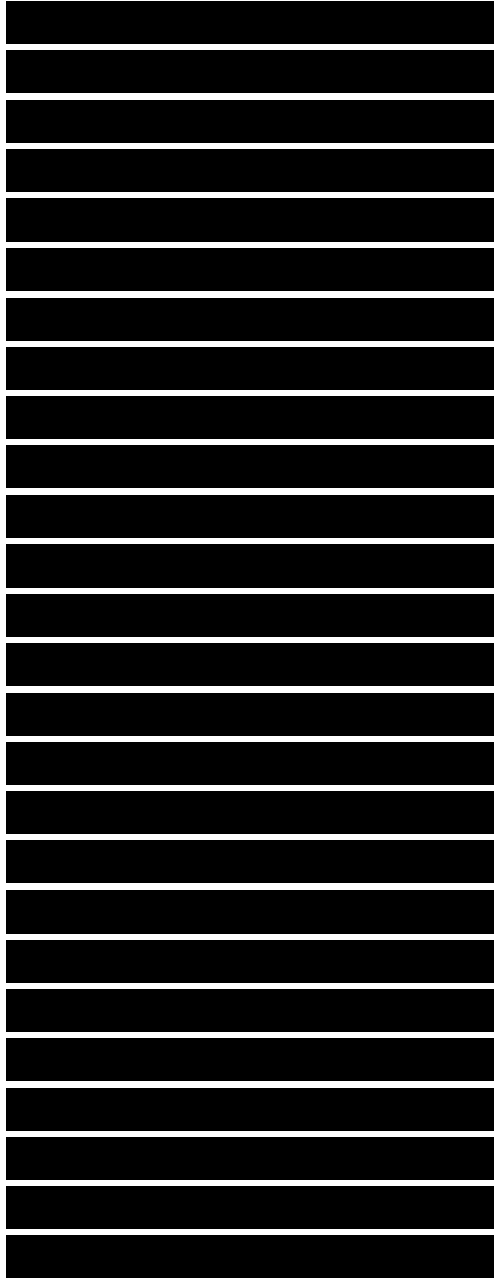
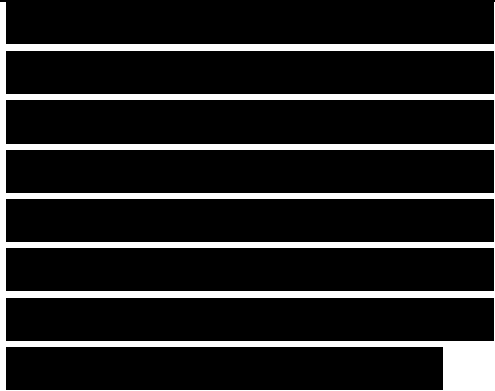
9.1 OVERVIEW

Like any other product, the design of a radar absorber depends a great deal on its intended application. The application itself, along with the properties of the materials available to fabricate the product, lead to the evolution of one or more concepts or configurations. Once we evolve a design to suit the application, whether specified or perceived, we must verify the performance of the concept. If we are successful enough to develop a product line from it,



we must assure our customer of our widely advertised performance by means of quality control. These three different requirements demand three different kinds of measurement and evaluation, as diagrammed in Figure 9.1.

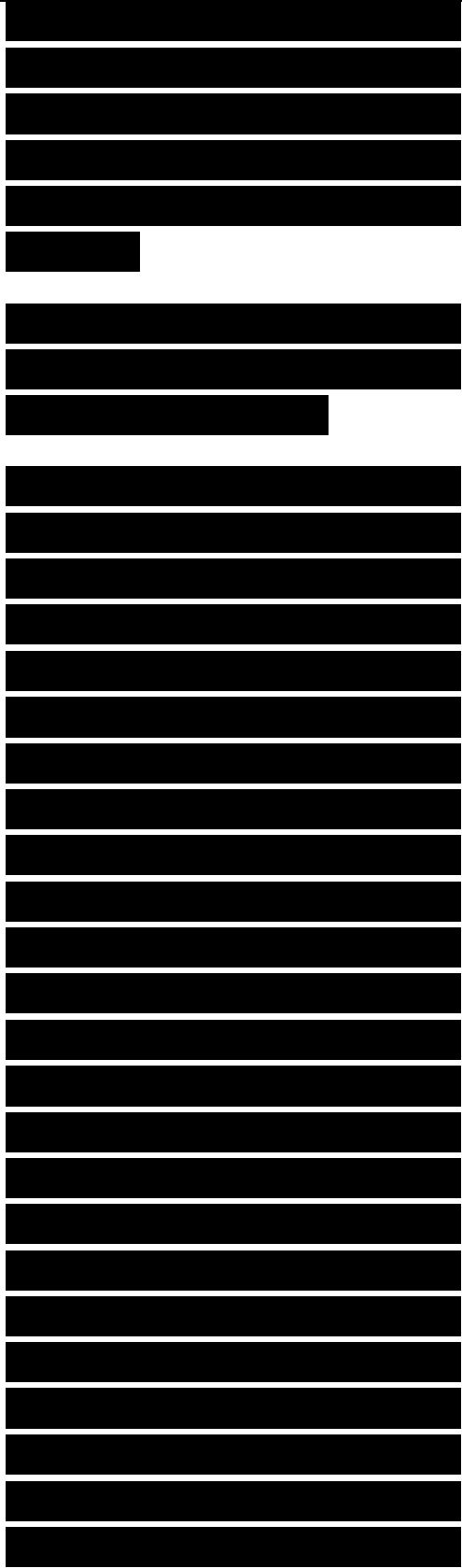
The most basic information needed in the electrical design of the absorber is the electromagnetic properties of the materials we expect to use to manufacture it. Equally basic, although not listed in the diagram, are the physical properties of those materials, such as density, tensile strength, durability, chemical stability, and compatibility with bonding systems (adhesives). Bulk materials are characterized by their relative permeabilities and permittivities, whereas thin sheets are more conveniently characterized by complex impedances. Permeability and permittivity are recognized as complex quantities, and we typically normalize these values with respect to the corresponding free-space values. The impedance of a thin sheet is also a complex quantity (a resistance and a reactance). Although the unit of sheet impedance is ohms,



measured results are typically labeled ohms per square to emphasize that a thin sheet, not a lumped element, was measured.

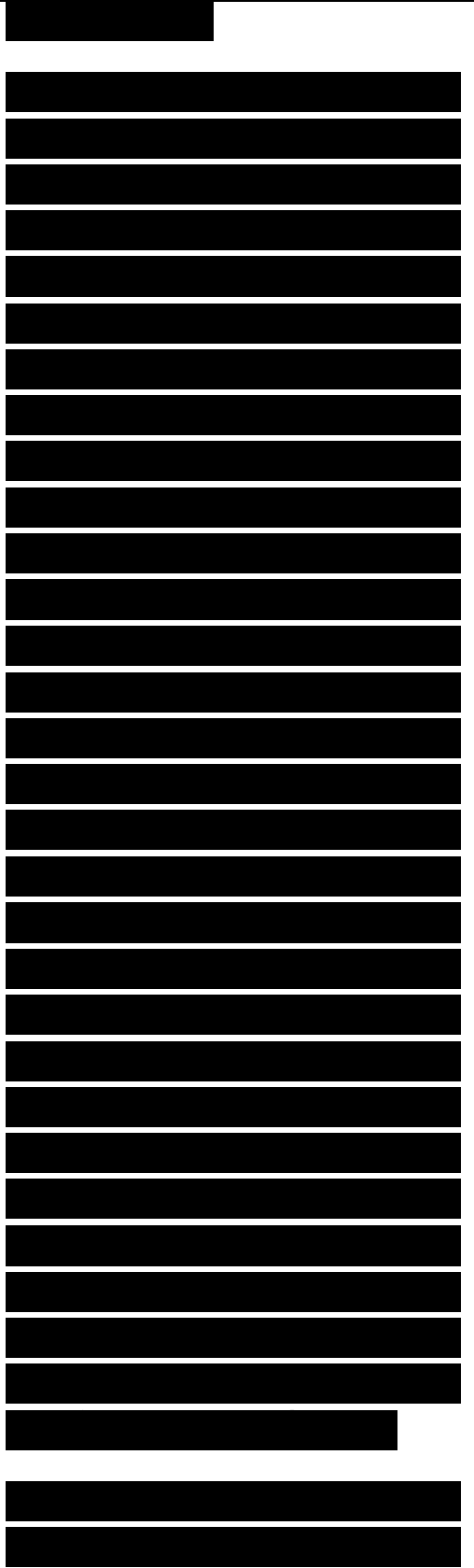
Figure 9.1. The objective of the measurement governs the equipment and test method used.

The relative permeability and permittivity of test samples are most accurately measured in small fixtures that are actually short sections of transmission lines. This minimizes the escape of energy from the system, thus reducing the risk that energy losses might be attributed to nonexistent losses within the test sample. It also allows an accurate evaluation of the material properties because of the well-documented soundness of the theory on which the measurements are based. Transmission-line measurement systems are also compact enough to fit on a laboratory bench, which makes them convenient to use and easy to operate. We present the basis of transmission-line theory in Section 9.2 and the extraction of the desired material properties from those measurements in Section 9.3.



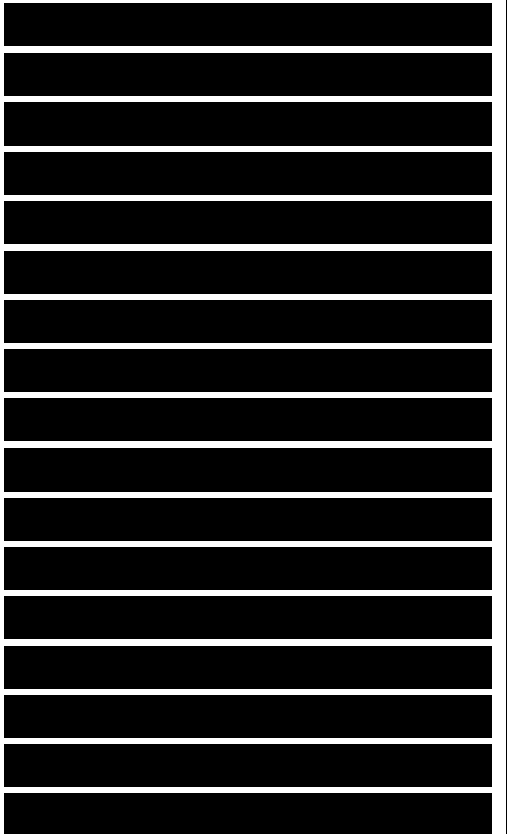
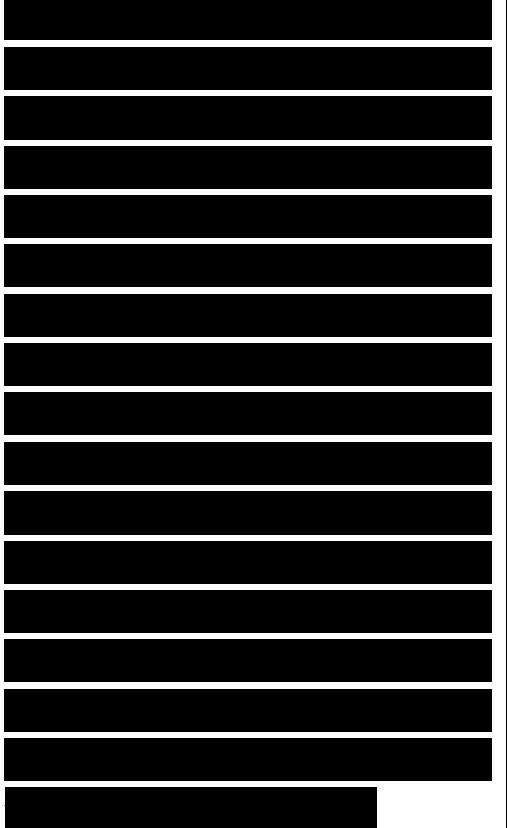
The thin sheets used in the design of some absorbers are not easily measured in transmission lines, because it is difficult to install them in the sample holders ordinarily used to measure permeability and permittivity. A device called the admittance tunnel is used instead, and much larger samples are required. The admittance tunnel is an absorber-lined box typically fitted with a small transmitting horn at one end, a small receiving horn at the other, and the test sheet installed between the two. The sheet properties are calculated from a comparison of the signals received with and without the test sheet in place. In a less familiar version of the admittance tunnel, the receiving horn is replaced by a metal backing plate, and the reflection characteristics of the plate-backed sheet are measured instead. The admittance tunnel test fixture is discussed in Section 9.5.3.

Because transmission-line measurements demand exquisitely small samples at



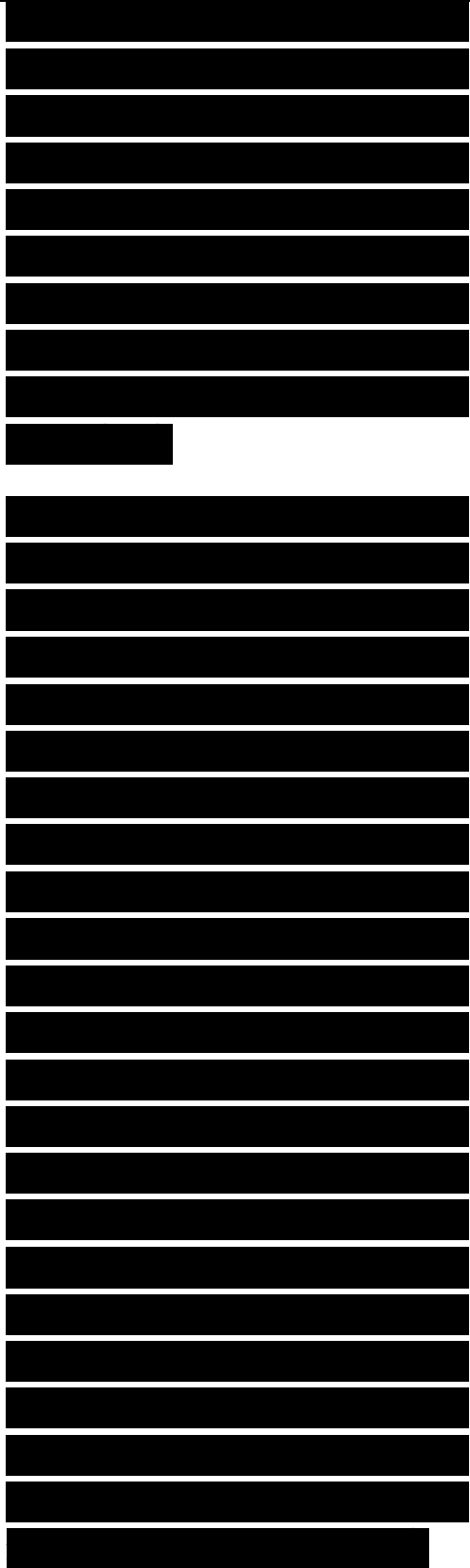
millimeter wavelengths, alternative methods must be used. One is the resonant cavity that, like the transmission line, is an enclosed system that prevents the escape of energy. The measured quantity in this case is a comparison of the Q (relative loss) and the resonant frequency of the cavity with and without a test sample packed inside. We discuss the interferometer in Section 9.5.2 as a special case of the cavity method.

We may estimate the electromagnetic performance of any absorber design by using the formulations given in Chapter 8 and the measured relative permeabilities and permittivities (or sheet impedances) described in Sections 9.3 and 9.5.3. Indeed, this estimate is one step that already should have been performed in the iterative design and optimization of the absorber. However, the estimate is subject to several sources of error, among them an inadequate knowledge of the electromagnetic properties of all the components in the absorber design, errors in the



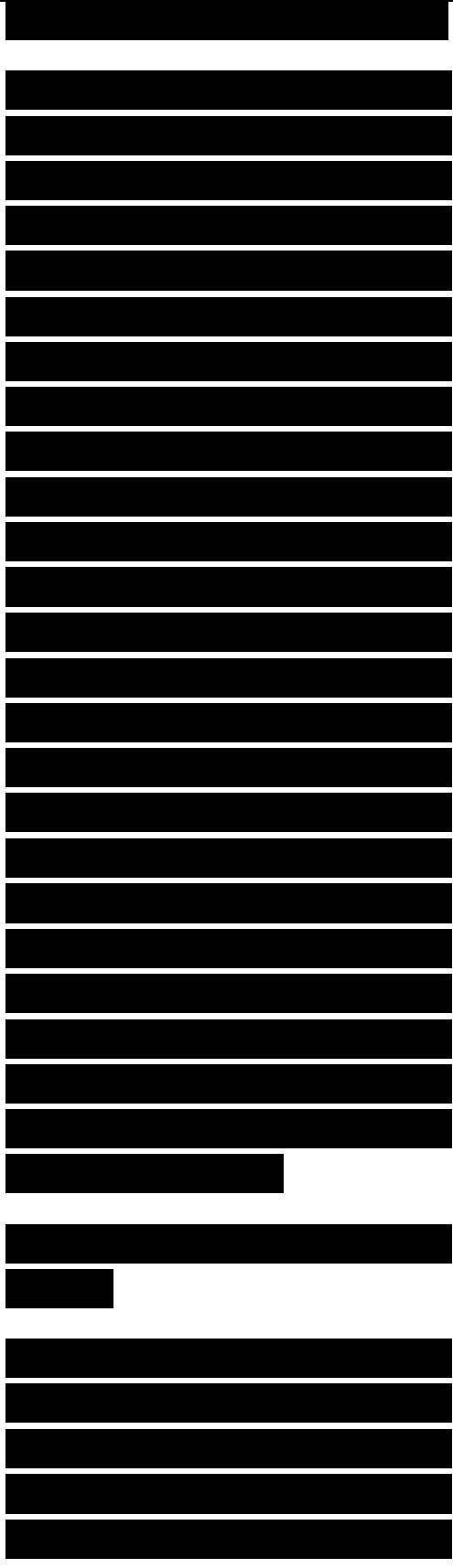
measurement of properties of individual components, and variations in manufacturing tolerances. It is therefore prudent, if not mandatory, that theoretical estimates of performance be verified by direct measurement of a test sample fabricated according to design specifications.

Because of inevitable variations in the electromagnetic properties from one point in the final product to another, and because the final product is much thicker than any of its component parts, this experimental verification of performance usually cannot be assessed in transmission-line measurements, as the individual components were. In addition, reflectivity of the fabricated test sample is of interest, not the electromagnetic parameters of the components used in its design. It is therefore more convenient, more realistic, and less costly to measure a large sample of the assembled absorber in a different kind of fixture. Figure 9.1 shows two options for such evaluations.



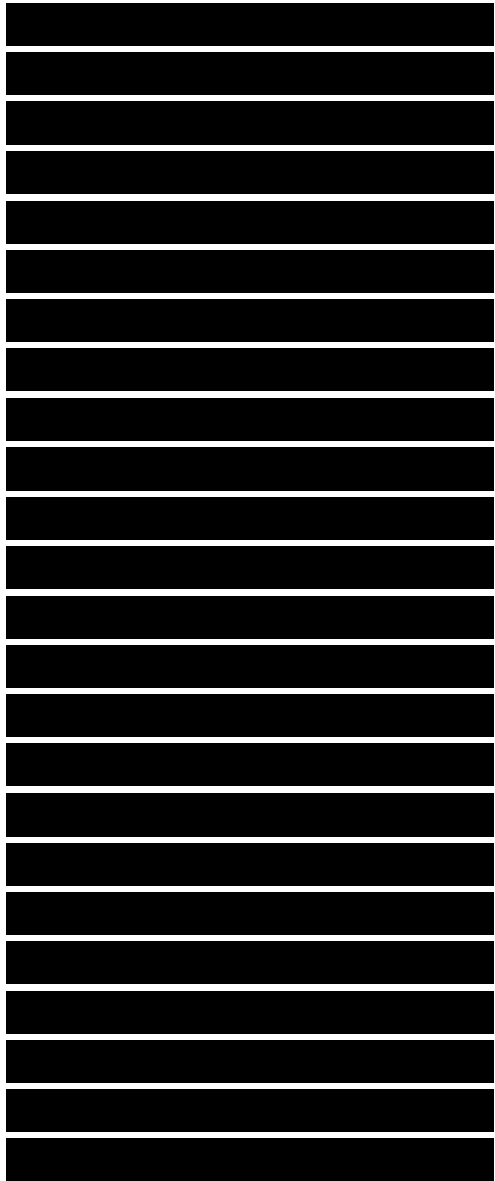
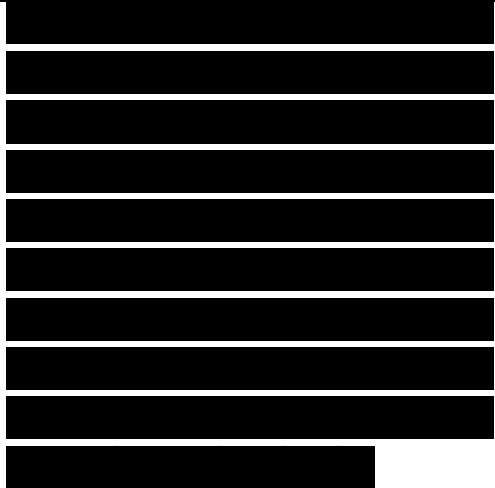
One is the classic NRL arch measurement and the other is a free-space RCS measurement of the absorber installed on a metal backing plate. We regard both as free-space methods because the test samples are not enclosed by the conductors of a transmission-line sample holder. Two differences distinguish them. In the arch setup, the bistatic reflectivity is measured, sometimes as a function of the bistatic angle, and the transmitting and receiving antennas are located within a few sample widths of the sample itself. In the free-space RCS method, the monostatic reflectivity is measured, usually as a function of the angle of arrival of the incident wave, with the sample located in the far field of the transmitting and receiving antennas. Both methods are discussed in Section 9.4.

We do not restrict our consideration of absorber measurement to stealth applications. Recognizing that pyramidal absorbers are used in test facilities and that they



demand quality control as much as any other product, we cite an unusual test fixture designed for this particular need. It is the large waveguide described in Section 9.5.1 and used primarily to evaluate chamber materials at low frequencies.

Few of the absorber evaluation techniques discussed in this chapter are new, as most of them rely on basic measurements of the reflection of energy from test samples, or the transmission of energy through them, or both. These kinds of measurements were once made at a relatively small number of test frequencies, due to limitations in equipment and the time required to set up and adjust the equipment. The development of reliable phase-locked, voltage-controlled signal sources in the 1960s and powerful microprocessors in the 1970s, and marriage of the two in the 1980s, has changed that. We now have sophisticated machines that can be programmed to collect coherent reflection and transmission data over octaves of bandwidth in a relatively short time, and the data can be stored digitally for any variety



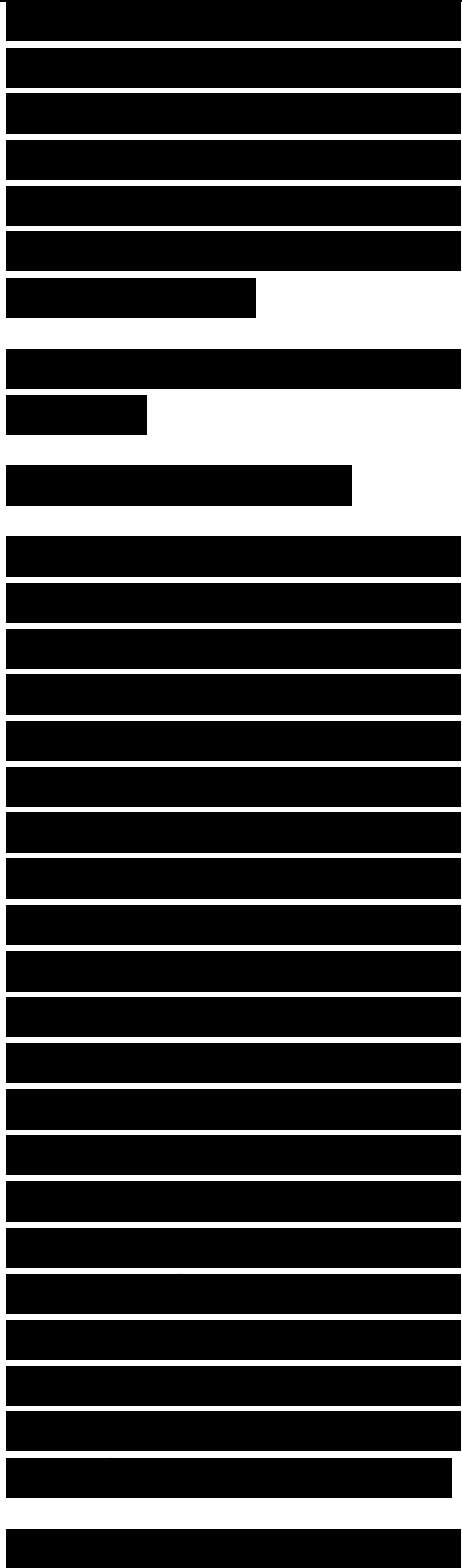
of subsequent processing. Nevertheless, we include in the chapter occasional discussions of how it used to be done.

9.2 TRANSMISSION LINE THEORY

9.2.1 Basic Relationships

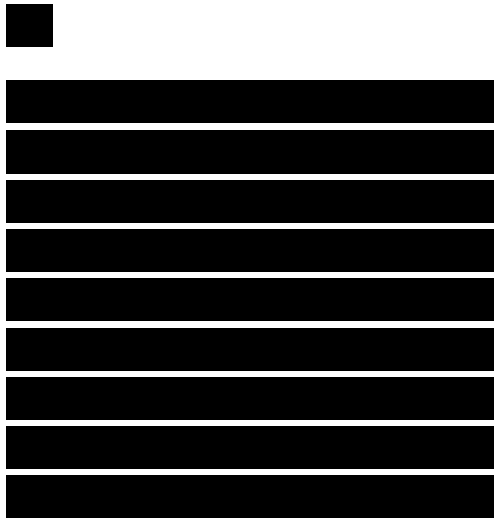
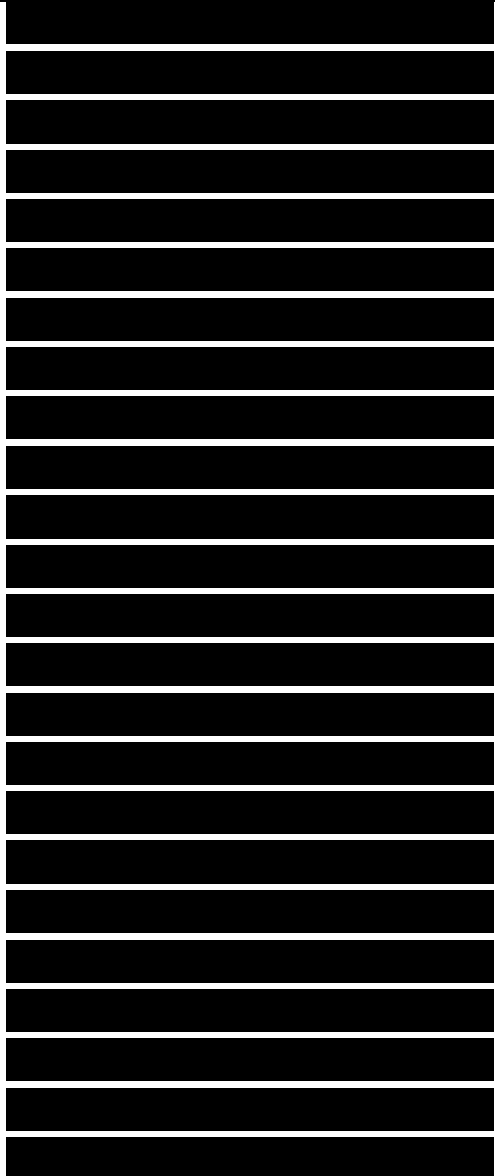
The transmission line is a basic device used to measure the electromagnetic properties of materials because the theory of wave propagation within the line is well understood and RF energy is confined within the system. A sample holder—a short section of transmission line—is loaded with a test sample machined to fit the line, and the reflection of RF energy from it, or the transmission of RF energy through it, or both, are measured. Because the dependence of the two measured quantities on the electromagnetic properties of the material in the line is known, those properties may be extracted by appropriate manipulation of the test data.

The application of the theory



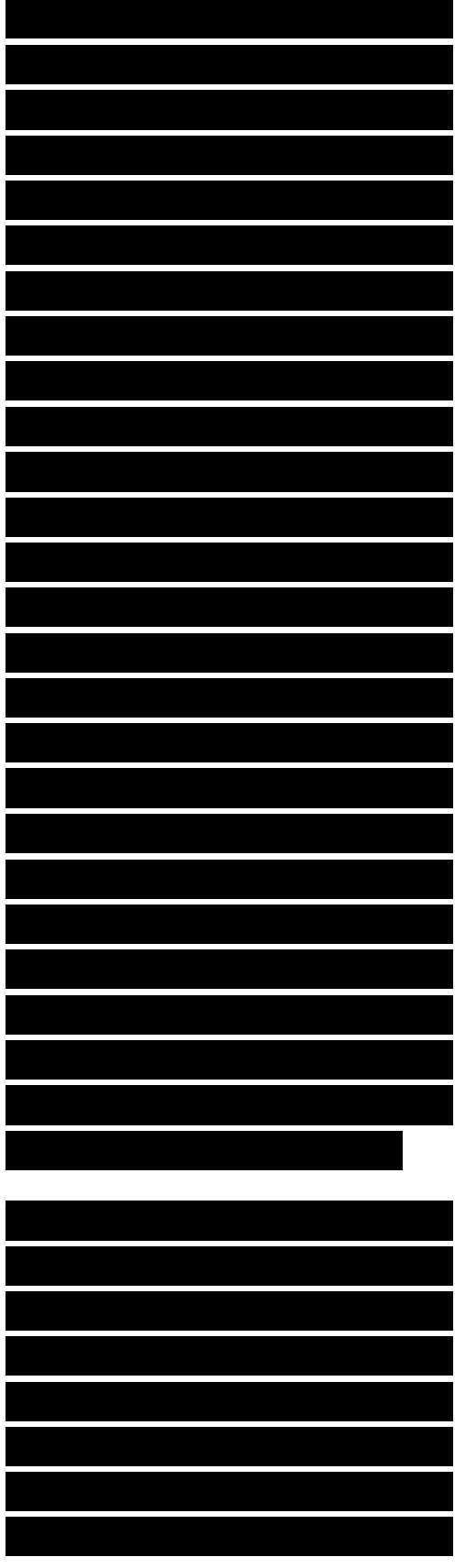
demands that the transmission-line sample holder be uniform, which is to say neither the transverse dimensions of the line nor the properties of the material in it may vary along the length of the line. Although the uniformity in dimension is not an unreasonable restriction, the demanded uniformity in material properties does restrict the kinds of materials that may be accurately measured. The dielectric properties of honeycomb spacers used in the fabrication of some absorbing materials, for example, vary from point to point in the material. Unless the period of the variation is a small fraction of the wavelength or a small fraction of the transverse dimension of the line, the properties of the sample cannot be accurately deduced from the measurements.

With this uniformity understood, we may launch a signal down the line and observe (measure) the signal at the far end. The signal is assumed to be monochromatic and characterized by a propagation factor, γ , that is, in general, a complex number. When there are no ohmic losses in the line, γ is the



imaginary number $\alpha = \gamma R/Z_0$, which describes the shift in the phase of the signal as it travels along the line; in the absence of loss, there is no change in its amplitude. In the TEM (transverse electromagnetic) lines to be discussed in a moment, k is the wavenumber discussed in Chapter 8 and λ is the wavelength of the signal as measured within the material in the line. If there are energy losses in the line, due either to the finite conductivity of the conductors of the line or losses in the material filling it, γ and k are complex quantities. In the latter event, a complete characterization of propagation in the line demands that we account for the decay in amplitude, as well as the shift in phase, with increasing distance.

As agreed in Chapter 1, we allow our signal to vary harmonically with time as $\exp(-i\omega t)$, but we suppress that variation in any mathematical expressions for fields, voltages, or currents. To account for the possibility of reflections from the receiving end of the line, we must admit the existence of



both forward- and backward-traveling waves. This being the case, the voltage at any point z along the transmission line may be represented as the sum of the voltages due to the forward and backward waves:

$$V(z) = V_i e^{-\gamma z} + V_r e^{\gamma z} \quad (9.1)$$

where V_i and V_r may be complex numbers, and the subscripts indicate the incident (forward) and reverse traveling voltage waves. The currents flowing in the conductors of the line may similarly be expressed as

$$I(z) = \frac{V_i e^{-\gamma z} - V_r e^{\gamma z}}{Z_0} \quad (9.2)$$

where Z_0 is the characteristic impedance of the line. The assumed (backward) direction of propagation in the second term in (9.1) and (9.2) is responsible for the reversal of the sign of the second term in (9.2) in comparison with that of the second term in (9.1).

We may form the ratio of (9.1) and (9.2) to determine the impedance at any point z along the line:

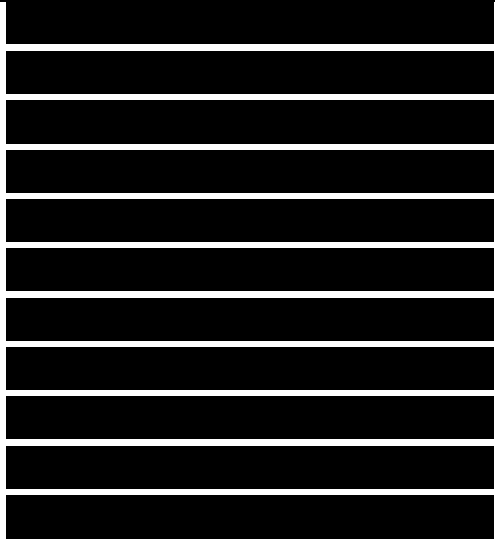
In working with transmission

lines we are almost always interested in the value of this impedance for two very specific positions along the line: at the load terminating the line and at some distance d toward the source from that load. If we denote the load impedance by Z_l , we may set $z = 0$ at the load and calculate the load voltage reflection coefficient V_r/V_i .

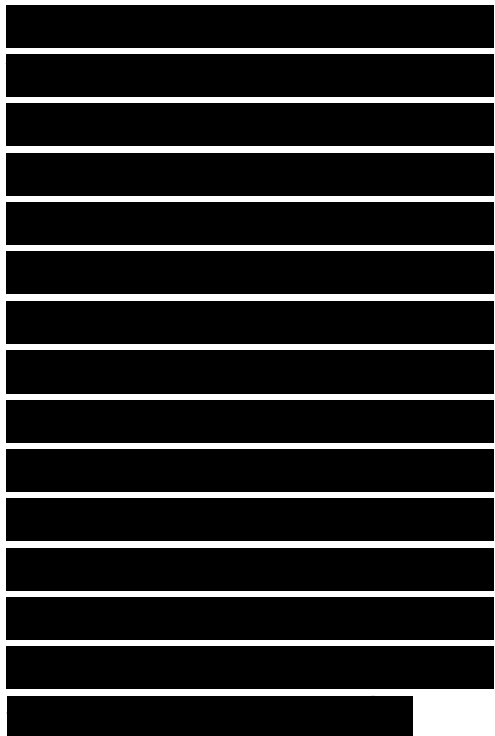
Now, by letting $z = -d$ and inserting the value of (9.4) for V_r/V_i back into (9.3), we have

where $Z(-d)$ is understood to mean $Z(-d)$. The reader may note that the signs of the second terms in both the numerator and denominator of (9.5) are the reverse of the signs found in most texts on transmission lines. This is because those texts assume the $\exp(j\omega t)$ time dependence in contrast to our $\exp(-j\omega t)$. Whatever the time convention, (9.4) and (9.5) constitute the most useful relationships at our disposal for the measurement of test samples in transmission lines.

That utility is the theoretical basis relating the impedance at the input of a line of length d to the impedance terminating its

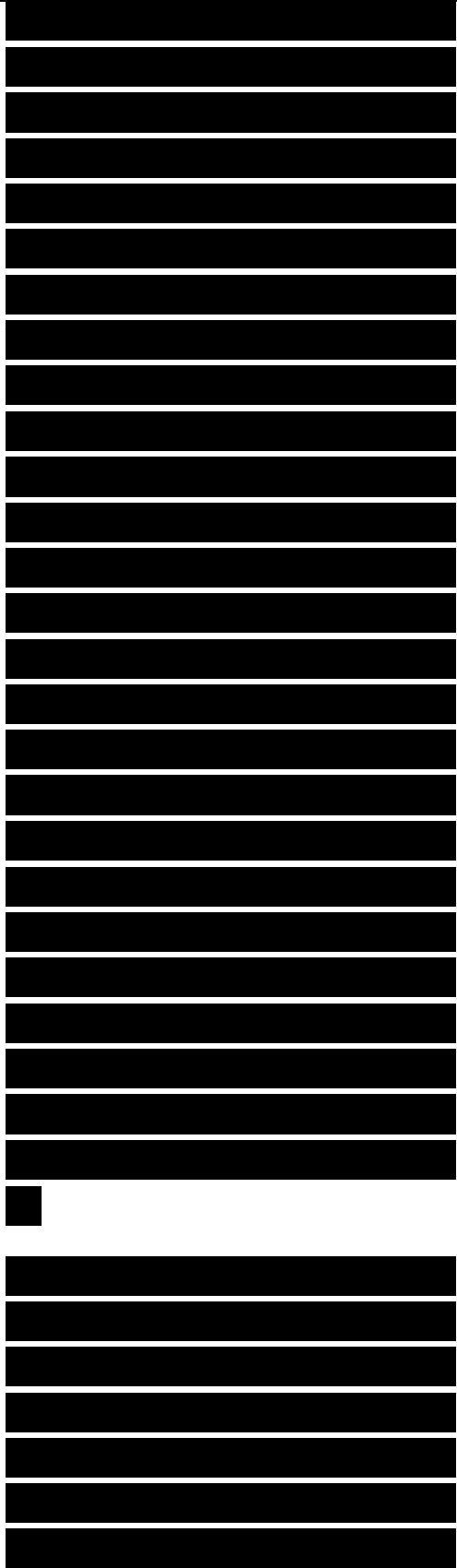


■



output end. The “terminating” impedance might well be another transmission line of quite different characteristics and might well be followed by yet another transmission line. Thus, given the characteristic impedance, propagation constant and physical length of each section of any cascaded set of transmission lines, plus the value of the terminating impedance of the last one, we may calculate the impedance and effective reflection coefficient at the junction between any pair in addition to the impedance presented at the input of the first one. Equations (9.4) and (9.5) are therefore a pair of transformer equations that may be used to generate another pair of numbers (an impedance and a reflection coefficient) associated with the input end of the transmission line section, given the nature of the load at the output.

These two powerful expressions have yet another attraction: they demand no measurement of voltages or currents at the input or output ends of transmission lines, even though their development is based on a consideration of



such quantities. Their transforming properties depend on only two comparisons: a comparison of the electrical length of the line with its physical length, and a comparison of the terminating impedance with the line's own characteristic impedance. Both comparisons can be deduced from measurements of amplitude and phase shift, and it does not matter whether we express them in terms of field strengths or voltages and currents. We will take advantage of this generality in a moment.

9.2.2 TEM Lines and Waveguides

Two kinds of transmission line are commonly used for the evaluation of bulk electromagnetic properties—the TEM line and the rectangular waveguide—but the propagation characteristics of the two are different. The electric and magnetic fields inside the TEM line are both transverse to the length of the line, as suggested in Figures 9.2 through 9.4, with the result that energy propagates within the line just as it would in an unbounded medium made of the same material filling the

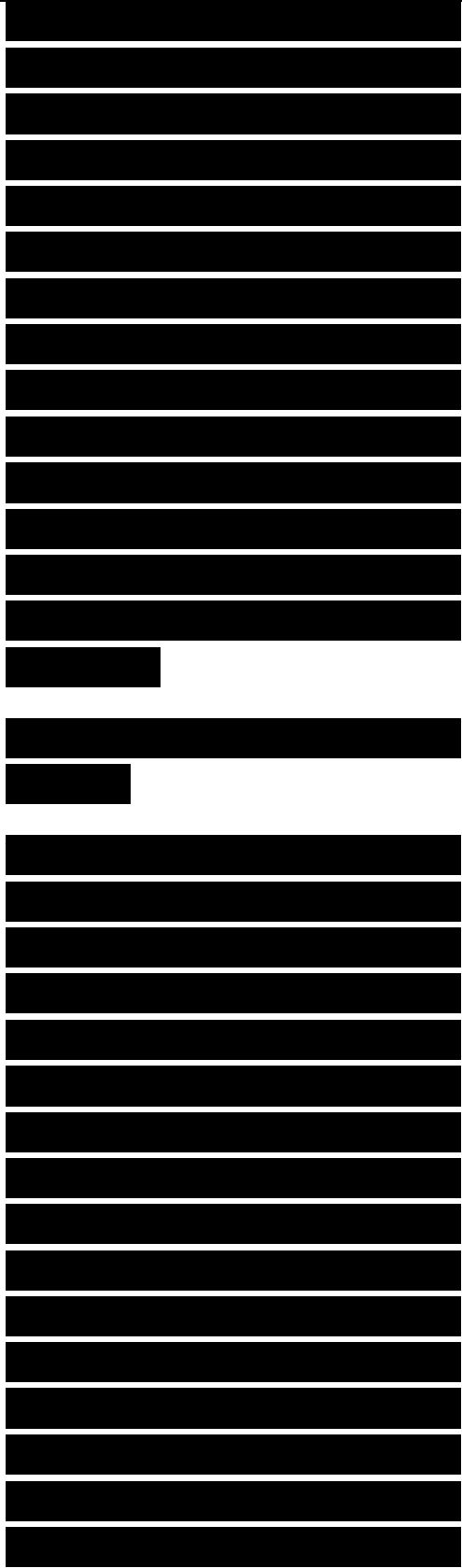
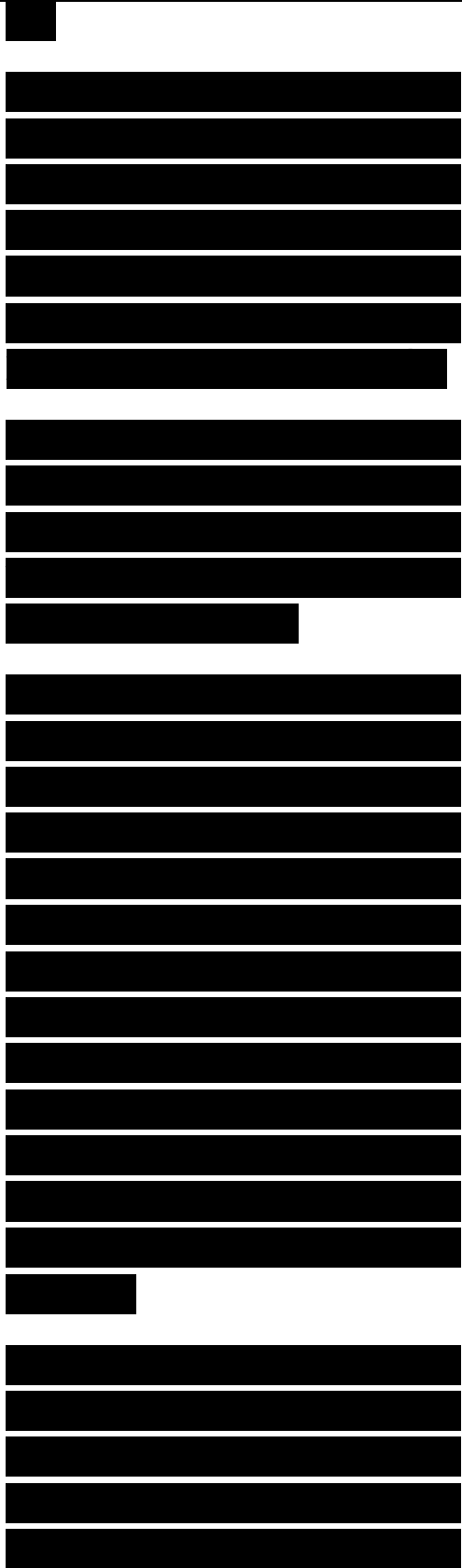


Figure 9.2. Electric field lines are radial and magnetic field lines are circumferential in the coaxial transmission line. Energy is constrained between the inner and outer conductors and does not escape the line.

Figure 9.3. Electric and magnetic field lines lie on families of circles for the twin conductor line. Energy can be radiated from this line.

TEM line. The fields in waveguides (hollow conducting pipes), by contrast, must have components along the direction of propagation as well as transverse to it, a condition due to the lack of a second conductor within the pipe. The existence of these longitudinal field components is interpreted mathematically as a pair of waves that zigzag down the guide, one zigging while the other zags, as suggested in Figure 9.5.

This is due entirely to the fact that the waveguide has only one conducting boundary, with the result that no fewer than two waves must exist to enforce the boundary condition

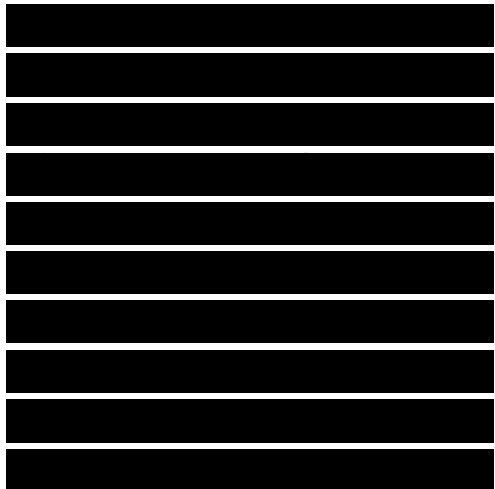
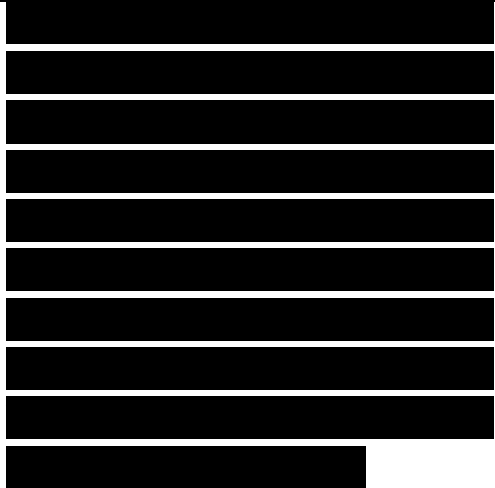


that the tangential electric field vanish at the conducting walls of the guide. A disconcerting consequence is that, when the frequency drops below well-defined cutoff values, the wave pair can no longer satisfy the electromagnetic boundary conditions and propagation virtually ceases. In essence, the waves rattle waveguide

Figure 9.5. The increased wavelength of propagation down a waveguide is due to cross-guide propagation of a pair of zigzagging waves.

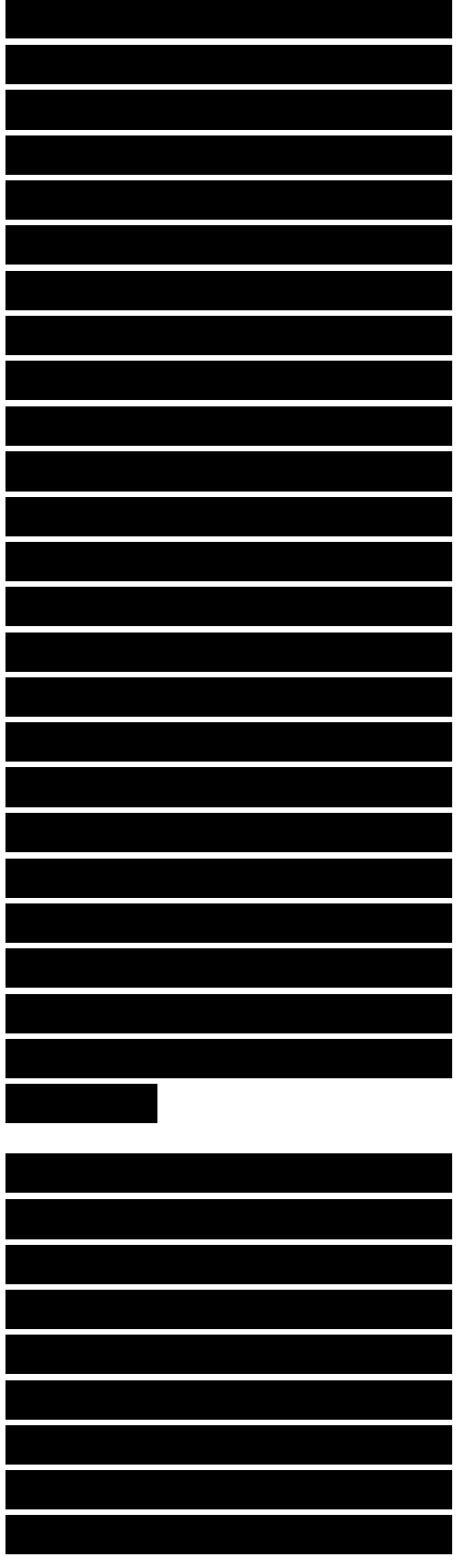
back and forth sideways between the walls of the guide instead of propagating along it, and no energy is conveyed from the input end to the output end. This restricts the bandwidth available for the measurement of the electromagnetic parameters of bulk materials in (hollow) waveguides.

A corollary of the cutoff phenomenon is that if the frequency is high enough, other zigzagging wave sets may also satisfy the boundary conditions, presenting the possibility that a waveguide may support more than one mode of propagation. Propagation modes that may exist are governed by the



electrical height and width of rectangular waveguides and by the electrical circumference of circular waveguides, as measured in the material filling the guide. The method ordinarily used to prevent higher order mode propagation is to choose the transverse waveguide dimensions so that only the dominant (lowest order) mode can exist over the intended range of operating frequencies. For example, the frequency separation between the lowest and next-lowest mode of propagation in air-filled rectangular waveguides less than half a free-space wavelength in height is precisely an octave. This is why no single microwave band (i.e., L-band, S-band, C-band) covers more than an octave of bandwidth and why each band is instrumented with waveguides whose dimensions differ from one band to the next.

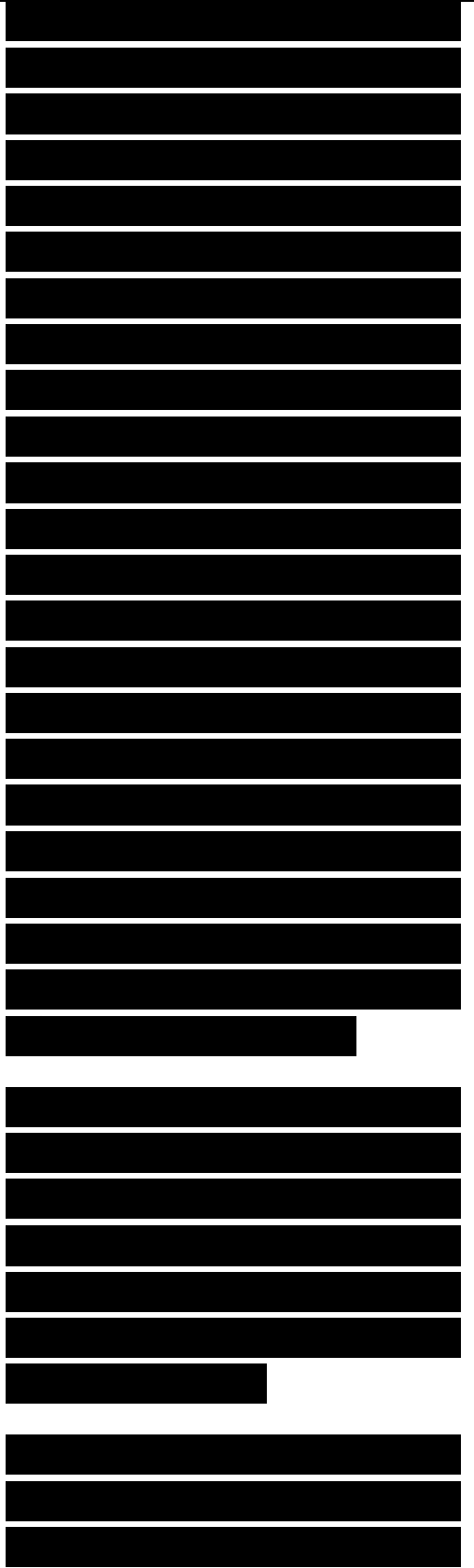
Waveguide propagation modes are grouped according to whether the electric or magnetic field is transverse to the direction of propagation, known as TE (transverse electric) and TM (transverse magnetic) modes, respectively. There is no component of electric field along the length



of the waveguide in TE modes and no component of magnetic field along the length of the waveguide in TM modes. The two kinds of mode are further classed (by subscript) according to the number of half-cosine cycles that may exist along the width and height of the waveguide. Therefore, the electric field has no longitudinal component in the TE₀ mode, no component along the wide dimension of the guide, and the intensity of the remaining field component (along the narrow dimension of the guide) varies sinusoidally from zero at one side of the guide to a central maximum at the center to zero at the other side. This variation in field intensity is suggested in Figure 9.6.

Figure 9.6. Field structure in rectangular waveguide for the TE₀ mode of propagation (from [1], Table 8.7, p. 414. Copyright John Wiley & Sons, 1984; reprinted with permission).

The lateral components of the propagation directions of the zigzag waves in a waveguide results in a phase shift along



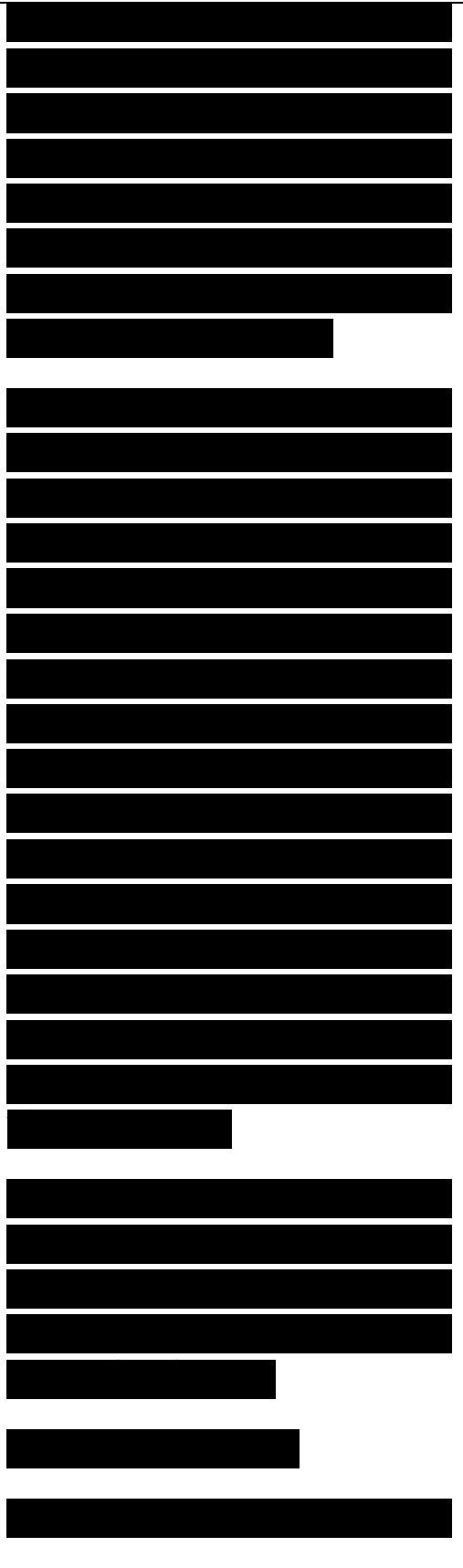
the guide that is less than in free space. The wavelength, λ_g , used to reckon the propagation constant is therefore longer in the guide than in free space. The guide wavelength for an air-filled rectangular waveguide, for example, is

where m and n are the number of half-cosinusoidal field variations along the width a and height b of the guide, respectively, and λ_0 is the free-space wavelength of the signal. The normalized guide wavelength for the TE_{10} mode ($m = 1, n = 0$) is charted in Figure 9.7 by way of example for a standard X-band, air-filled rectangular waveguide (internal height and width of 0.4 x 0.9 in.). The guide wavelength rises to infinity at the cutoff frequency, which in this case is 6.56 GHz.

Figure 9.7. Normalized guide wavelength for a waveguide 0.9 in. wide and 0.4 in. high operated in the TE_{10} mode at X-band frequencies.

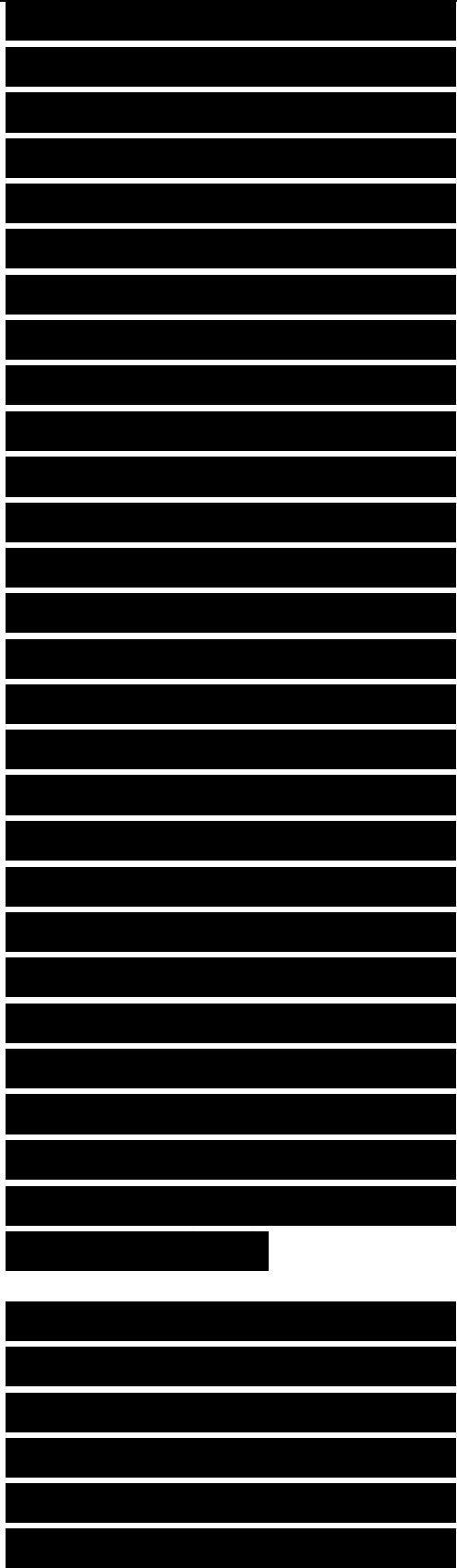
9.2.3 Sample Holders

The choice of whether to



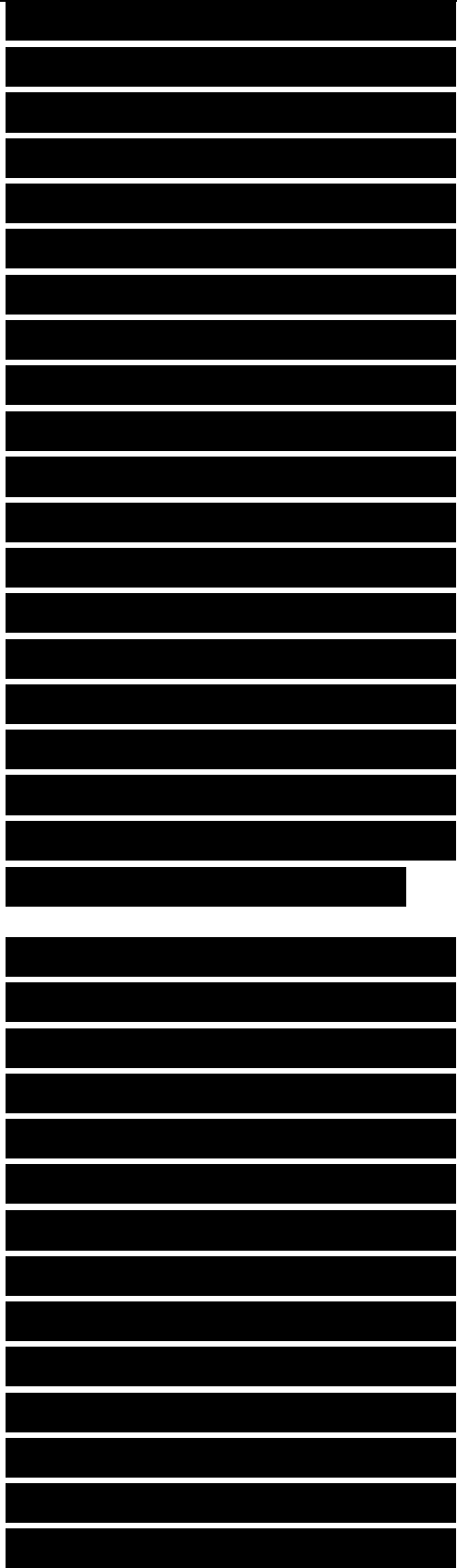
employ TEM or waveguide systems for the evaluation of material properties depends in no small measure on the equipment available, the frequencies for which such information is desired, and the physical size of any inhomogeneities that may be present in the test sample. The coaxial line (a TEM transmission line) is more convenient to use than the rectangular waveguide if the frequencies of interest cover more than an octave. This is because waves propagating in the coaxial line do not suffer the cutoff phenomenon; even direct current (zero frequency) can be transmitted down the line. A single, suitably designed coaxial sample holder, for example, can be used for material testing over the frequency decade between 1 and 10 GHz. It requires, by contrast, no fewer than four different waveguide sizes, and therefore four different sample holders and four different sets of tests, to service the same range of frequencies.

This is not to say that the TEM line cannot support higher order modes, however. When the mean circumference of the coaxial line exceeds a wavelength or so, for example, the line can support



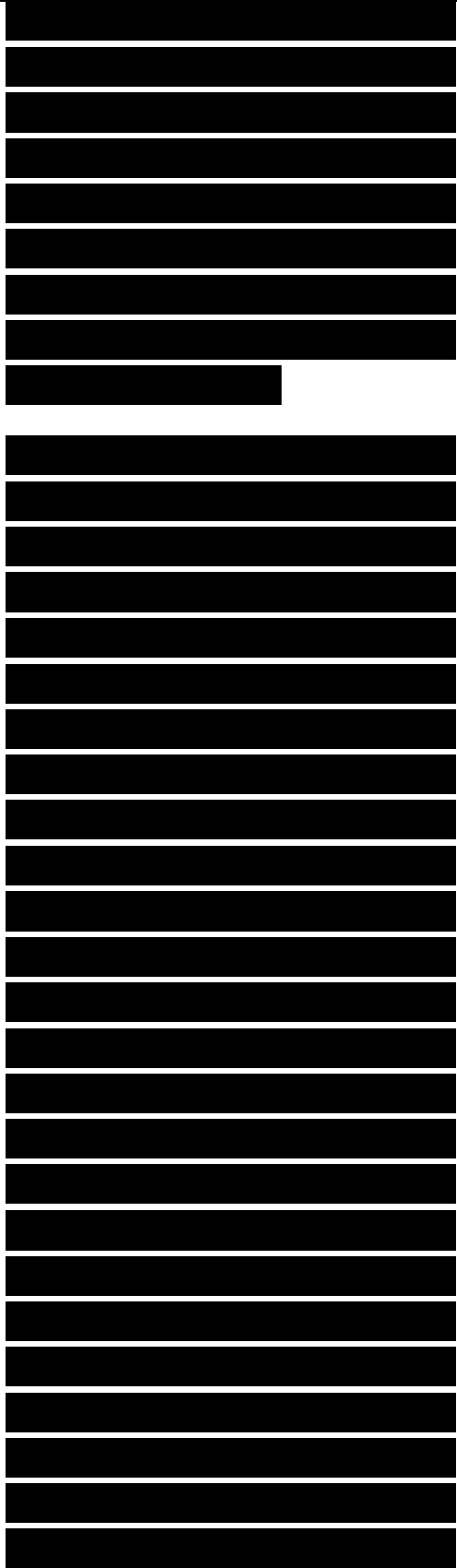
propagation modes having longitudinal field components. Because the mean circumference is governed by the size of the line, higher order modes in coaxial lines may be prevented by making the sample holder small enough. This in turn demands smaller test samples, making the fabrication of the samples as well as the sample holder more costly. Smaller lines and samples also increase the possibility that small, undetected inhomogeneities in the sample can have a greater effect on the accuracy of the test data than they would in larger samples.

Just because the line is large enough to support higher order modes does not mean that such modes will, in fact, be present. Most of the time they may be prevented simply by minimizing discontinuities in the line that can excite them. In addition to careful design and fabrication of the sample holder, one of the simplest methods of accomplishing this is to avoid bends and turns in the lines connecting the sample holder to test signal generation and detection equipment.



Because the insertion of the test sample in the sample holder increases the internal electrical dimensions of the line, these kinds of design considerations are as important for TE and TM waveguides as they are for TEM lines.

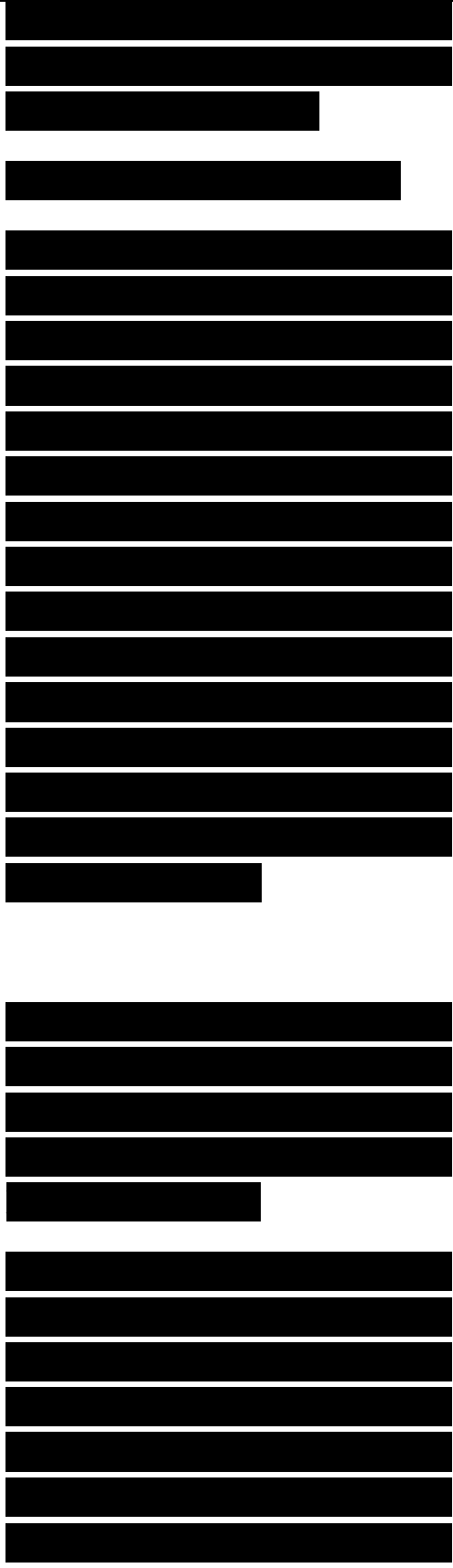
Because electromagnetic energy is confined between the conductors of the coaxial line of Figure 9.2, but can escape from the lines in Figure 9.3 and 9.4, the coaxial line is the most common TEM system used for measuring the properties of uniform test samples. The most common single-conductor line used for such tests is the rectangular waveguide. The coaxial line demands a washer-shaped test specimen whereas the test specimen needed for the rectangular waveguide is simply a slab, as illustrated in Figure 9.8. The samples may be as thick as can be conveniently handled and measured, but in many cases they are machined to a thickness of $A/8$ or less, as measured in the material, to minimize the possibility of generating undesired (unaccountable) modes within the sample.



The samples should be fabricated to fit snugly within the sample holder, making good contact with all conducting surfaces, which sometimes complicates the design of the sample holder. Good contact is generally assured if the samples fit snugly in the holder without deformation, sometimes a difficult requirement to satisfy when the test material is soft or rubbery. Almost all sample holders are designed for easy removal from the test set-up so that the samples may be inserted

Figure 9.8. Test samples for coaxial lines and rectangular waveguides should be carefully machined to close tolerances.

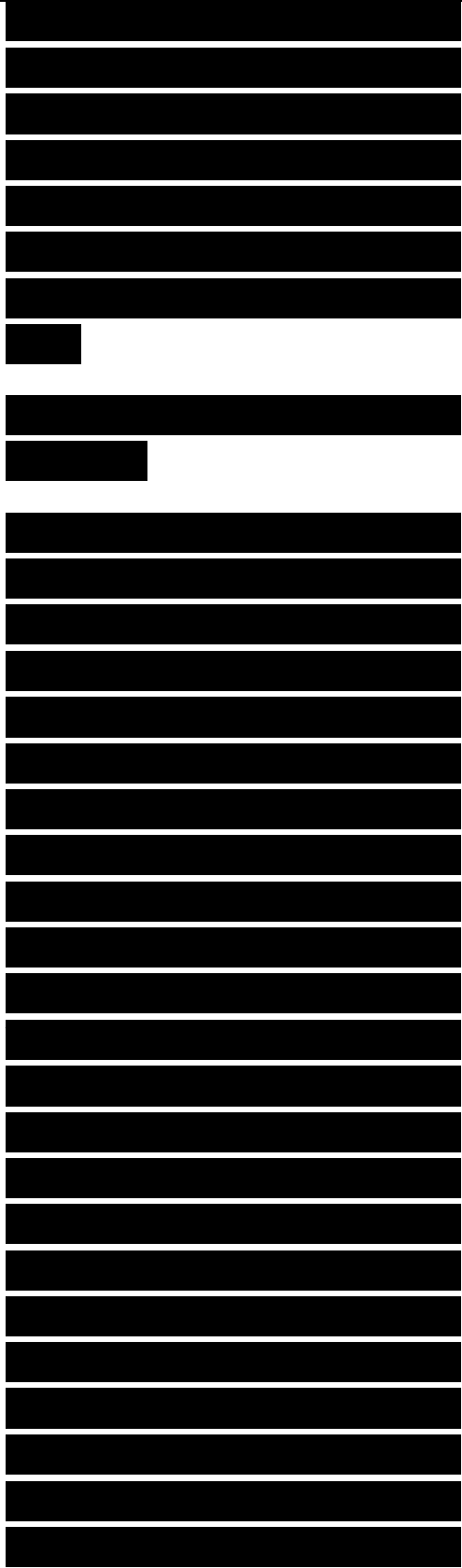
into or tapped out of the holder with minimum disturbance to the rest of the system. Because the center conductor of the coaxial sample holder must be supported in place whether or not a sample is inside it (see Section 9.3), it is more complicated to design and



handle than the rectangular waveguide sample holder. In either case it may be necessary to build a fixture for the sole purpose of inserting the sample and positioning it transverse to the guide dimensions.

9.3 TRANSMISSION LINE MEASUREMENTS

The measurement of test samples in transmission-line holders was once a laborious process because of the crudeness of the equipment available at the time. Although contemporary sample holders are no better than previous ones, we can now conduct tests at dozens of frequencies in the same time it used to take for a single frequency. Contemporary off-the-shelf instrumentation is designed for the rapid and convenient, if not accurate, measurement of the scattering matrix of any two-port device, whereas we were content then to measure only the reflections from the input end of the sample holder. To emphasize modern capabilities, we first consider how samples were typically measured before the eruption of push-button technology.



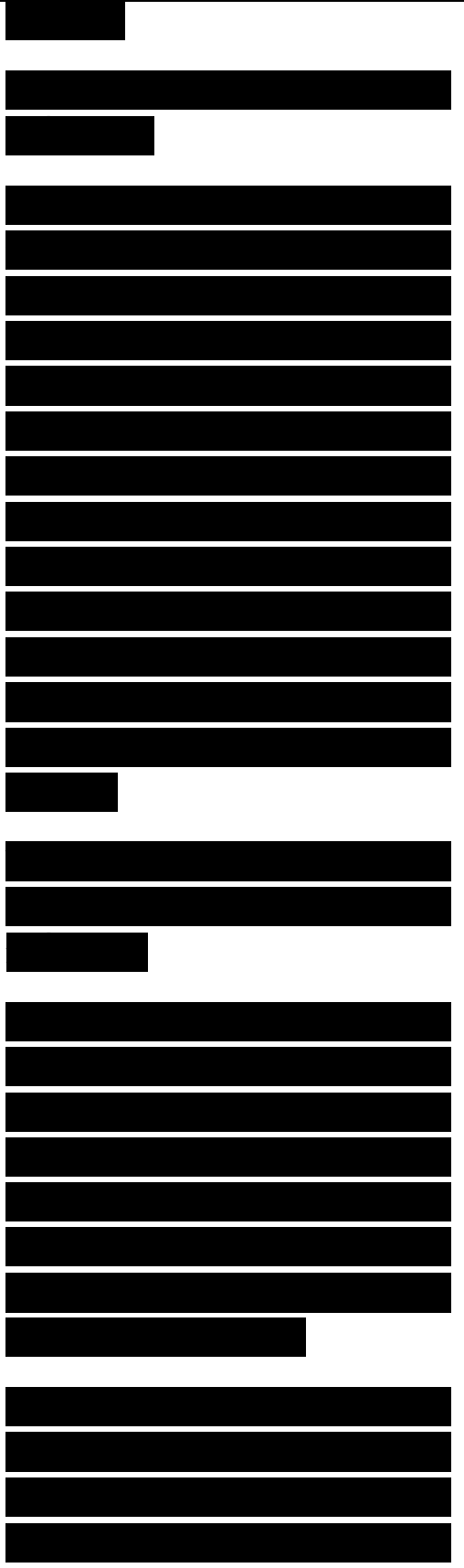
9.3.1 Open- and Short-Circuit Measurements

The elements of the typical, but archaic, test system are shown in Figure 9.9. Its five major elements were a signal source, a slotted section of waveguide or transmission line, the sample holder, a sliding short circuit, and a signal detector. Not shown in the diagram are other devices used to monitor the frequency and output power of the signal generator.

Modulated Pad Slotted Sample Sliding RF source section holder short

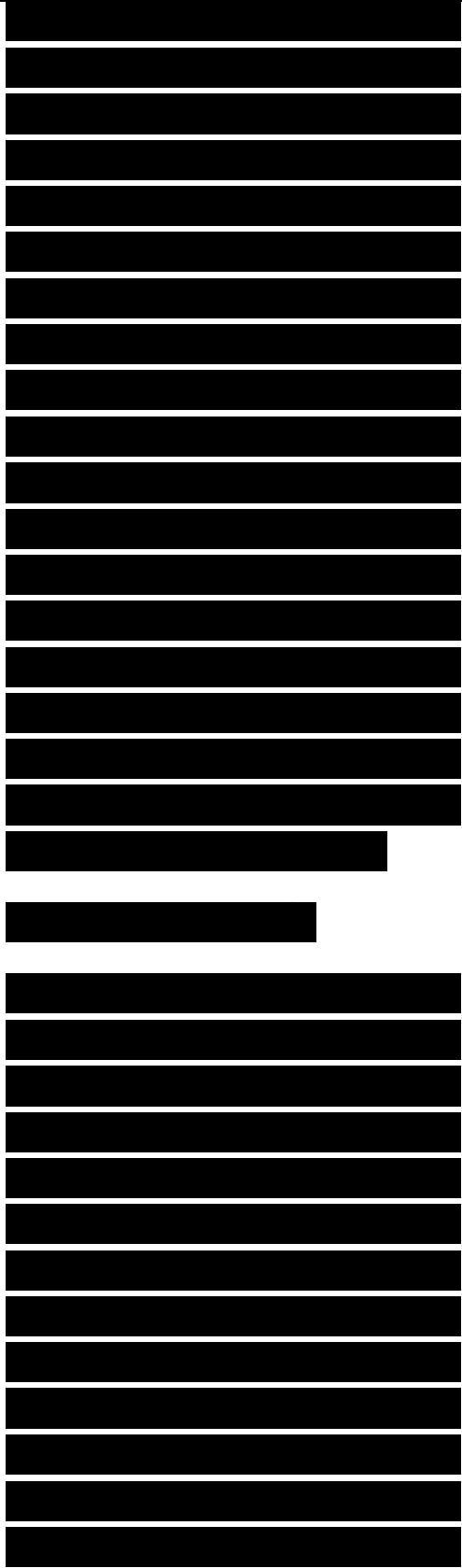
Figure 9.9. A simple bench setup uses a slotted section to sample the standing wave pattern inside the line due to reflections from the sample in the sample holder. The inset shows how a probe is inserted into the space between the conductors of the slotted section.

To protect the signal generator from the severe impedance mismatch presented by the sample and the short circuit behind it, the signal generator



typically was separated from the rest of the system with a pad, a fixed attenuator. The signal itself was modulated at an audio rate so that a simple detector and audio amplifier could be used to measure the signal sensed by the probe of the slotted section. The amplifier output was simply an accurate panel meter calibrated in decibels. The sample was typically backed by a sliding short whose position relative to the rear face of the sample could be measured, either with a dial gauge or by counting screw turns.

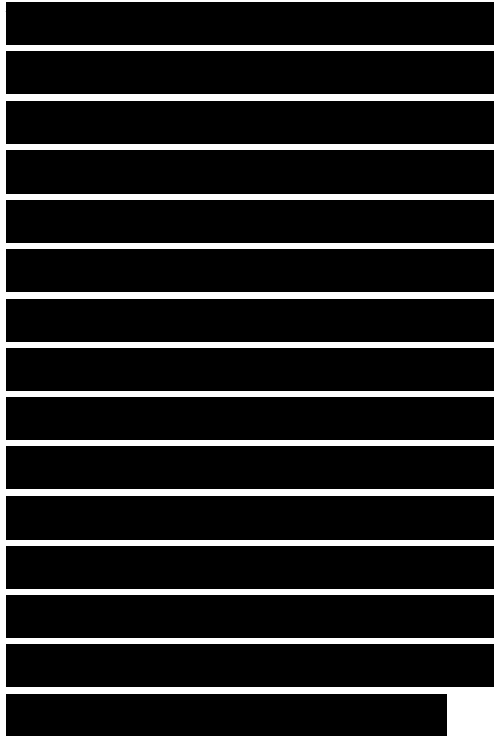
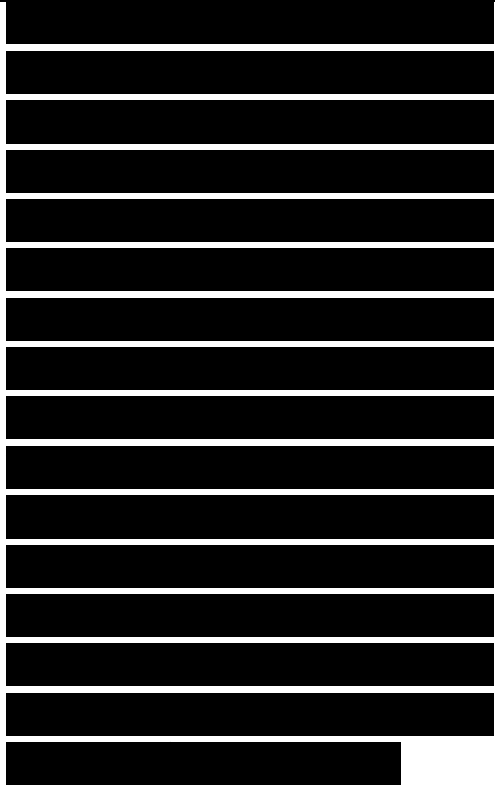
The slotted section inserted between the sample holder and the signal generator allows us to sample a standing wave pattern inside the line. The slotted section is simply a short length of transmission line with a longitudinal slot machined in it. As shown in the inset, a small probe is inserted a short distance into the line through the slot to sample the electric field inside. This probe is mounted on a sliding carriage that may be moved along the line (toward or away from the



generator), so that the standing wave pattern may be measured as a function of position from the front face of the test sample. The convenience and accuracy of the position measurement may be enhanced, particularly at higher frequencies, by a dial gauge mounted on or driven by the probe carriage. The slotted section shown in Figure 9.9 is a coaxial line, but waveguide slotted sections may also be used.

As we saw in Chapter 8, the reflection from a slab of material can be expressed in terms of the thickness and electromagnetic properties of the slab, the wavelength of the signal and the nature of the medium behind the slab. Because this is equally true of a material packed into transmission lines, we may deduce the properties of that material by measuring the reflection from it. The standing wave pattern in the slotted section was the yardstick by which the reflection from the sample was measured and interpreted.

The standing wave in the line is the sum of two waves traveling



in opposite directions, as shown in Figure 9.10. A measurement of the voltage standing wave ratio (VSWR, pronounced viswar) is sufficient to determine the strength of the backward traveling wave compared to that of the incident wave:

$$VSWR = \frac{1 + |\Gamma|}{1 - |\Gamma|} \quad (9J)$$

Under ideal conditions, this characterizes the amplitude of the reflection from the test sample, but for reasons that will become clear in a moment, the magnitude alone is not sufficient to completely characterize the sample material. We also need the phase of the reflection, which hinges on a knowledge of the relative location of peaks or nulls in the pattern as measured from the front face of the sample.

Although it might be thought that the pattern position could easily be established by the measurement of the physical dimensions of various parts of the system, it is easier and more accurate to measure the standing wave pattern in the absence of the sample. A precision short circuit (a carefully machined metal plug) is used

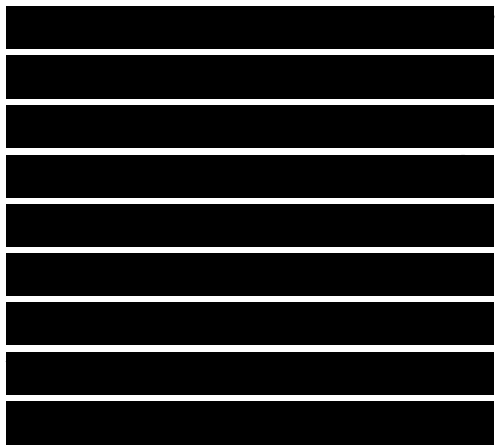
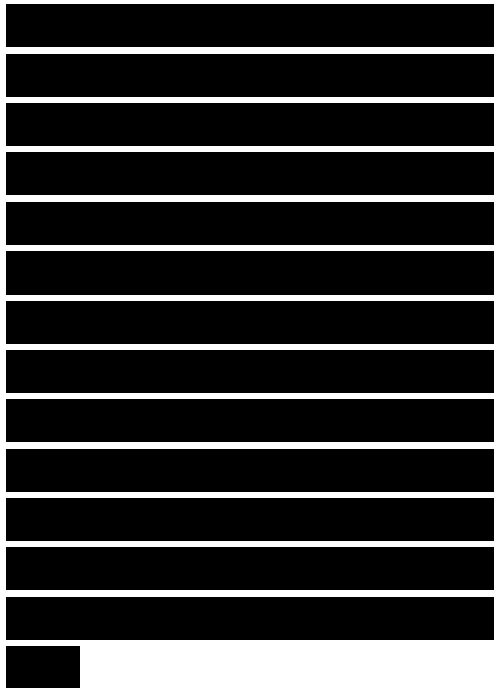
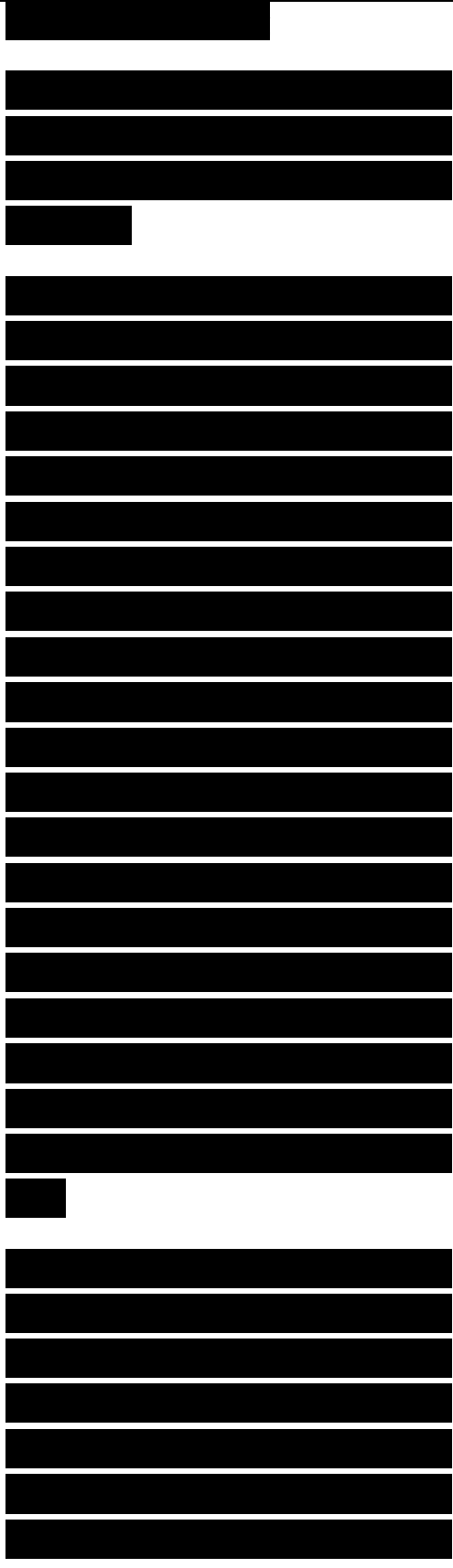


Figure 9.10. Two waves propagating in opposite directions create a standing wave with a period of precisely $\sqrt{2}$.

for this purpose. It is typically inserted in the sample holder so that the position of the front face of the plug matches that of the sample when the latter is installed. When displayed in the decibel format, the nulls are sharp and deep for this short-circuited condition, and their positions establish a reference plane (not at, but corresponding to, the location of the front face of the sample) for measurements of the test specimen. Residual losses in the system that might otherwise be assigned to losses in the sample may also be assessed in this calibration measurement and then accounted for when the complete set of test data is reduced and interpreted.

Therefore, it takes two sets of measurements to establish the phase and amplitude of the reflection from the test sample: one set with the sample installed and one set without it, the latter being essentially a calibration of the system. A



comparison of the two VSWR readings gives us the amplitude, and the distance by which the nulls shift toward or away from the generator gives us the phase. In general, however, this is insufficient to uniquely determine the four intrinsic numbers—the real and imaginary parts of the relative permeability and permittivity—that characterize the material. The determination of four unknowns demands, in one way or another, the measurement of four quantities, and thus far we have measured only two.

We may wriggle out of the requirement to measure two additional quantities when there are no magnetic constituents in the sample, for then we can usually assume that the permeability of the sample is the same as that of free space. This being the case, the two quantities measured are sufficient to determine the permittivity. Even at that, however, we usually have to perform an additional system calibration, particularly if our sample is thin, has little loss, or both.

The reason for this is that the null shift for electrically thin samples is small, and an error in determining the shift in the

[REDACTED]

[REDACTED]

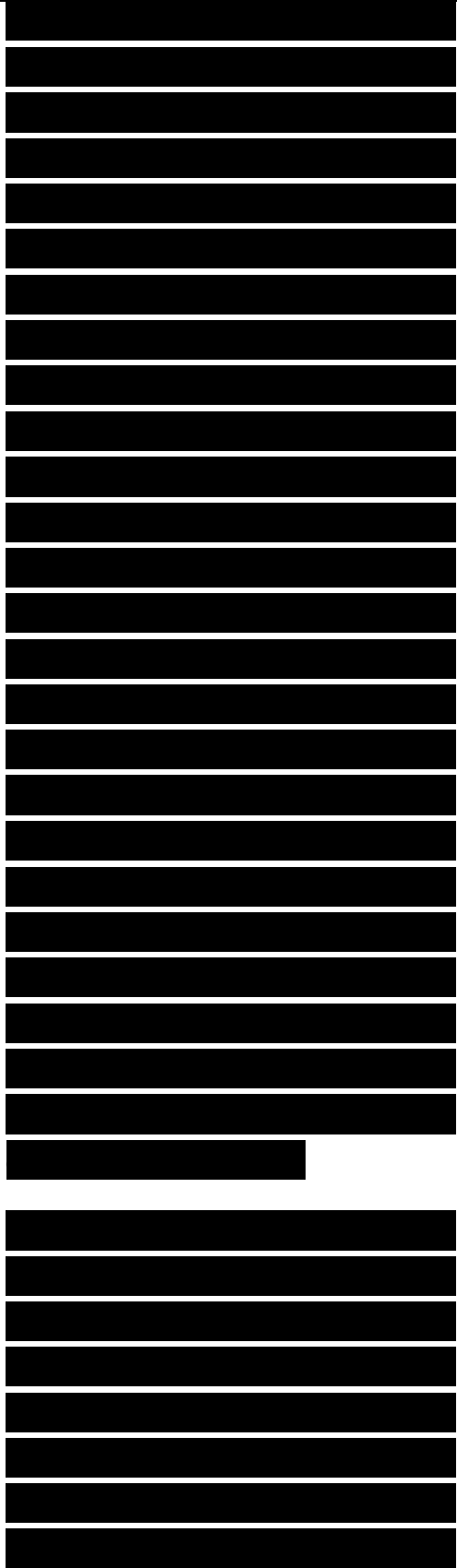
[REDACTED]

[REDACTED]

[REDACTED]

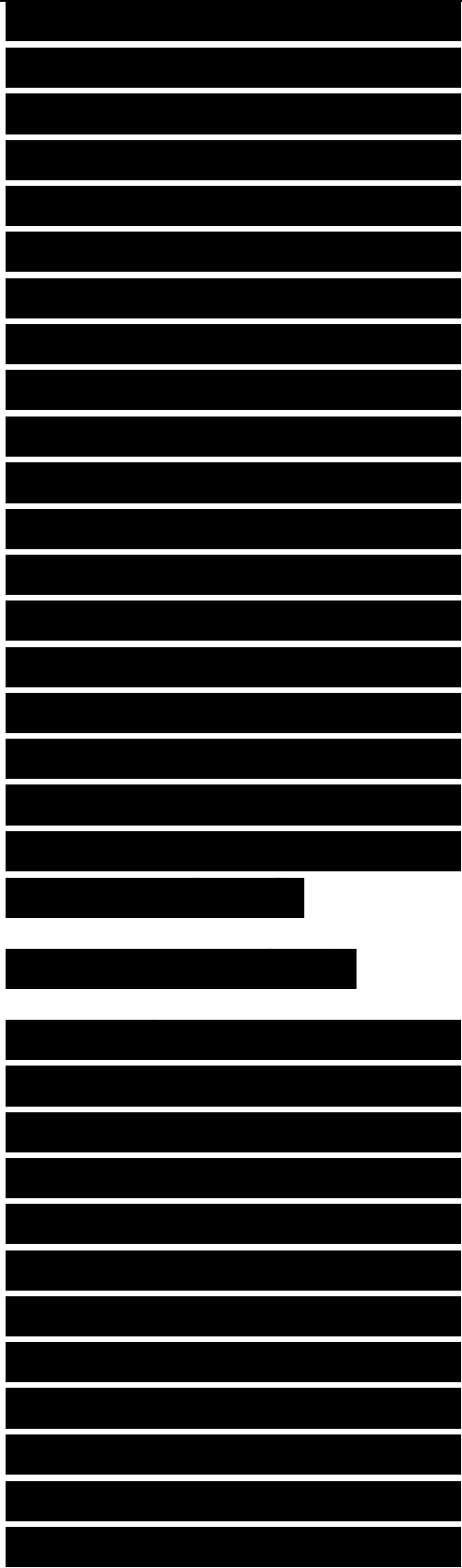
nulls of the standing wave pattern becomes larger the thinner is the sample. Similarly, small sample losses become harder to separate from system losses the thinner is the sample. The accuracy of the measurement in these cases can be improved if we contrive to fabricate the test sample to be between $A/8$ and $A/4$ thick, as measured in the material. This seems to pose a dilemma: How do we estimate the optimum electrical thickness of a test sample whose electrical properties, by definition, are unknown? (If they were known, there would be no need to measure them in the first place.) Actually, we usually have some idea of what those properties are because we will have measured similar materials at comparable frequencies in the past.

If the sample is thin, we should probably back it with an open circuit to maximize the electric field at the sample. This has the effect of enhancing the apparent loss of the sample as it influences the VSWR to be measured, and this is one reason why we include the



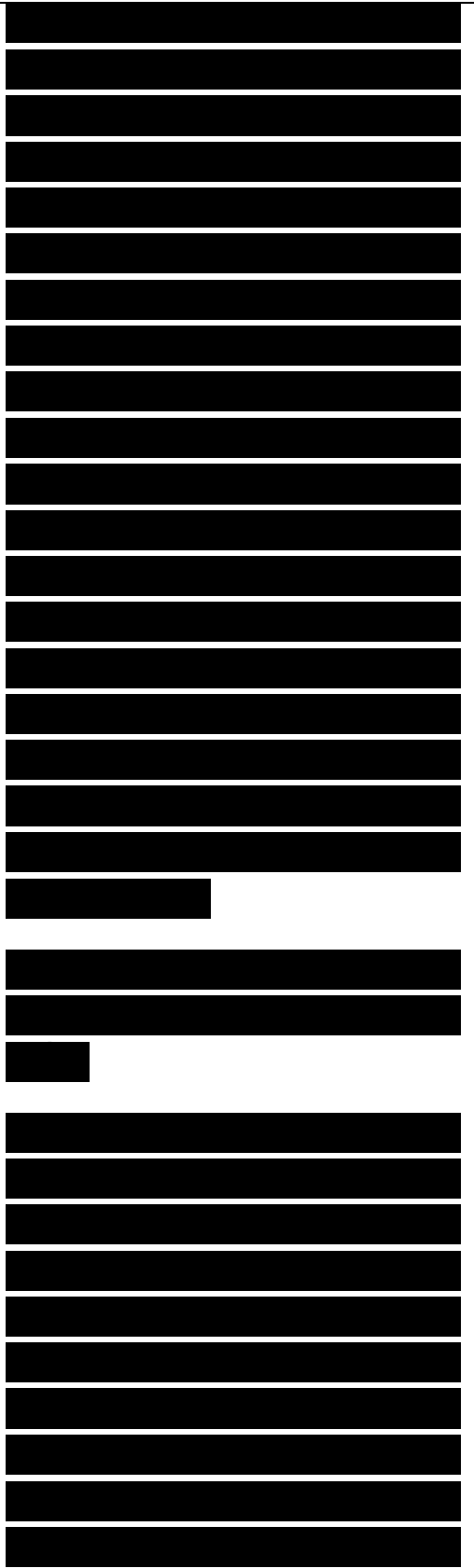
sliding short in the bench setup shown in Figure 9.9. We can create an open-circuit condition at the rear face of the sample by positioning the shorting plunger $A_0/4$ behind the sample. We will have to establish that position, however, by other measurements with the empty sample holder in place, this time with no shorting plug in it, to determine the electrical position of the plunger to create that condition, as the physical position of the plunger is not necessarily an accurate indicator of the electrical position. In the few cases when we have precision open circuits on hand to install at the rear of the sample holder, the additional calibration is not needed, of course.

The sliding short is a useful device used to alternately install open or short circuits behind the test sample when we cannot assume that the permeability of the sample is the same as that of free space. In this event we have four quantities to measure instead of two (so that we have as many measured quantities on hand as we have unknowns to determine), and we must repeat our slotted-line standing-wave



pattern measurements for two different conditions. Any two sets of measurements are theoretically useful, and one time-honored procedure was to measure the test sample when backed by a short circuit and again when backed by an open circuit. A more extensive set of data could be obtained and processed by measuring the standing wave pattern for several different short positions behind the sample, generating a locus of points on the complex plane whose analysis is likely to yield more accurate values of the four unknown quantities.

Although that may be the case, we will be content to illustrate the reduction of data collected with only short-circuit and open-circuit terminations backing the rear face of the sample. For this purpose we assume the model shown in Figure 9.11, in which t is the physical sample thickness, Z_0 and k_0 are the characteristic impedance and propagation



constants of the empty line, and Z_2 and k_2 are those of the sample-filled section of line. The latter depend on the relative permeability and relative permittivity of the material via

If we contrive to measure the reflection coefficient at the front face of the sample for short- and open-circuit terminations at the rear of the sample, we may calculate the normalized impedances at the front face from (9.3). These will be found to be

where $w = \exp(ik_2t)$ and $z_r = Z_2/Z_0$. The normalized impedances on the left sides of (9.10) and (9.11) are measured values, and z_r and w on the right sides are unknowns to be determined.

We now form the product and the ratio of (9.10) and (9.11), and inserting the values of (9.8) and (9.9), we have

We then extract the desired values of $\hat{\epsilon}$ and ϵ_r by forming the product and the ratio of (9.12) and (9.13):

The solution represented by (9.14) and (9.15) is unique so long as the sample is less than $\lambda/2$ thick (as measured in the

[REDACTED]

[REDACTED]

[REDACTED]

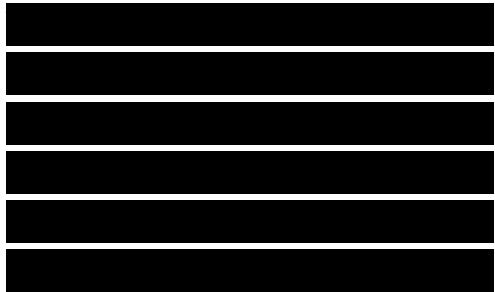
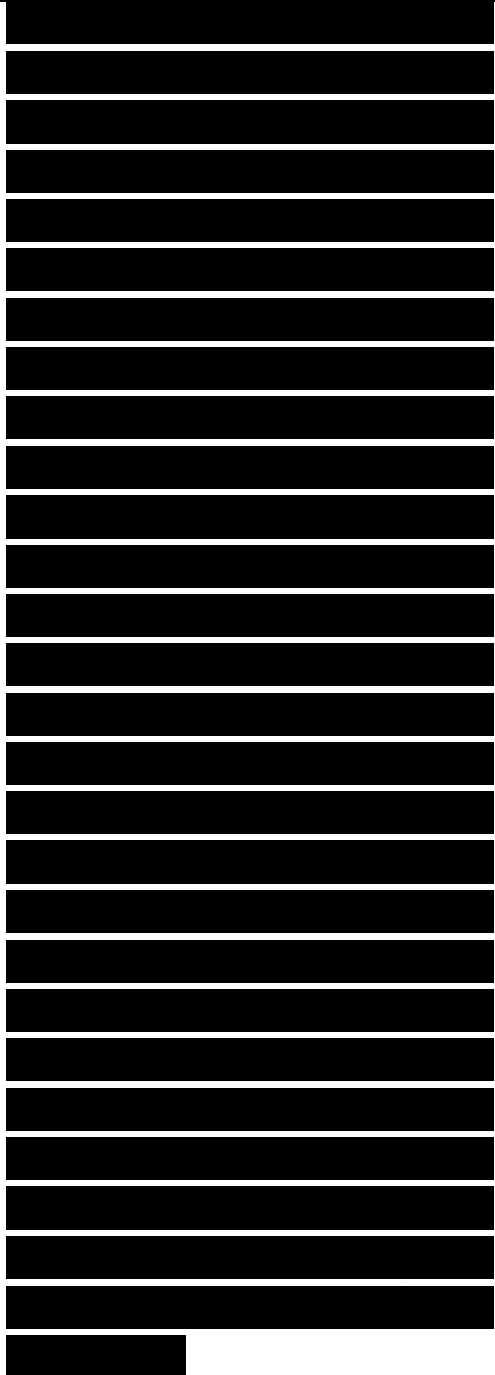
[REDACTED]

[REDACTED]

[REDACTED]

material), but is ambiguous otherwise. This is because the phase angle of w can be resolved no closer than an integral number of π rad and is the prime reason for fabricating thin test samples. Therefore we might deduce the wrong values for n ? and ϵ_r if the sample happens to be too thick. However, there are two ways to resolve the ambiguity. One is to repeat the measurements with a different sample of the same batch of material cut to a slightly different thickness, and the other is to repeat the measurements at a slightly different frequency. The assumption in the latter case is that, even if the sample properties vary with frequency, the frequency difference is chosen small enough that that dependence does not materially influence the measured quantities. The disadvantage of the two methods of resolving the ambiguity is a doubling of the time and effort invested in testing.

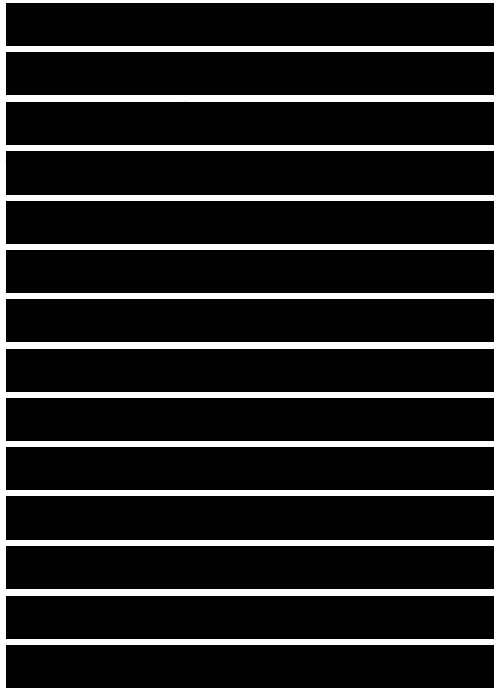
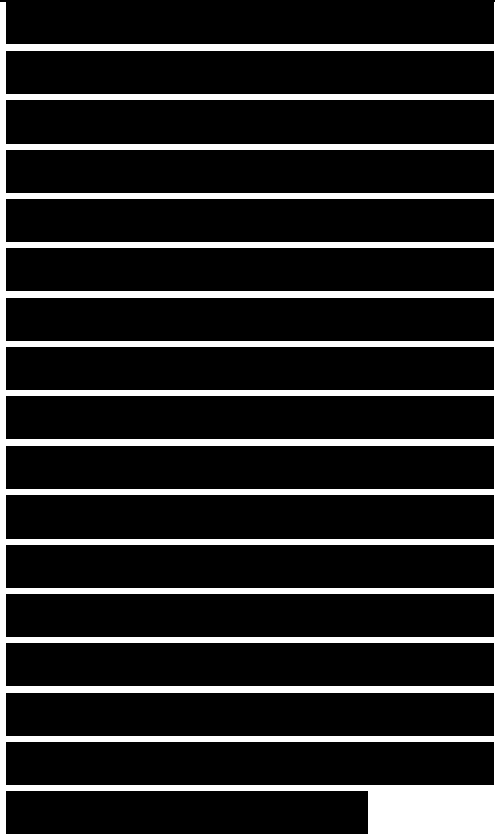
If we can assume the material to be nonmagnetic (that its permeability is sensibly that of free space), the right sides of (9.10) and (9.11) contain only one complex unknown (the complex permittivity), and the



left sides contain one complex measured value. In this event, only one complex measurement is required (either the short-circuit impedance or the open-circuit impedance at the front face of the sample). The resulting equation, either (9.10) or (9.11), then becomes a transcendental expression that may be solved graphically or by well-known mathematical techniques, such as the Newton-Raphson method. These methods of solution do not eliminate the ambiguity that results when the sample is more than $A/2$ thick, however.

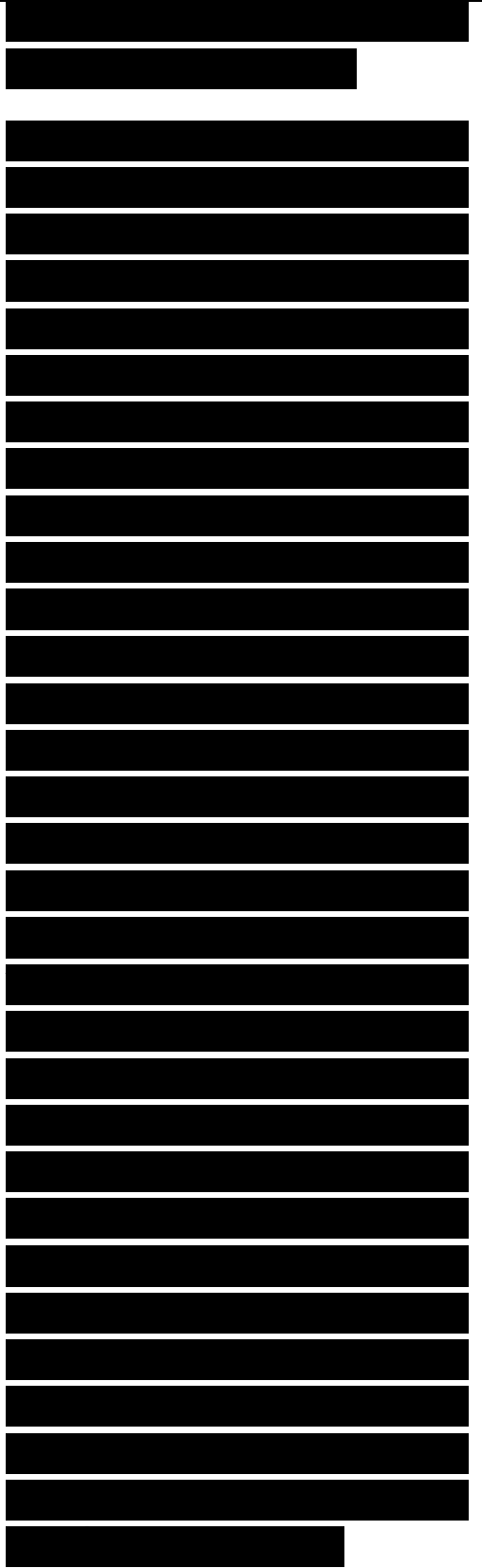
9.3.2 The Network Analyzer and the Scattering Matrix

The network analyzer has become a basic tool in the measurement of the properties of radar materials. It replaces the slotted section as a device for measuring the reflections from test samples, and it is capable of providing test data for literally dozens of frequencies at great convenience in relatively short time. Indeed, the Hewlett-Packard Company has even offered its Model 8510 series of network analyzers as basic instrumentation for RCS measurements as well as more

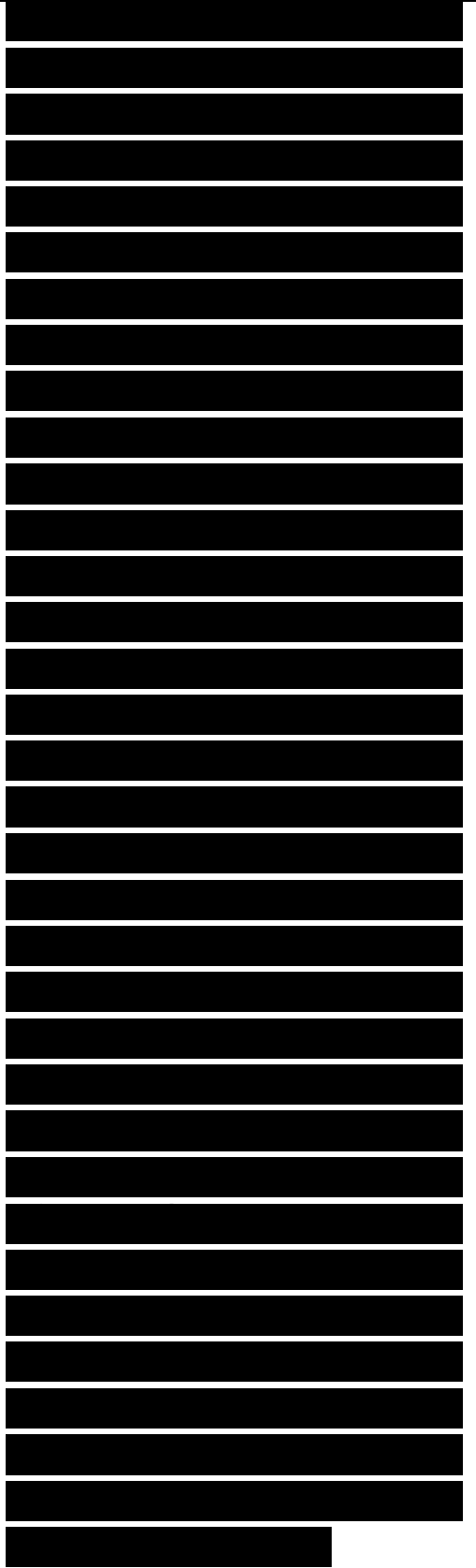


mundane bench testing [2].

The network analyzer is a coherent instrument capable of a wide variety of measurements. The basic instrument compares an unknown signal with a reference signal of the same frequency, and its output is a signal or indication, either by panel meter deflections, real-time video displays, or streams of bits, of the amplitude and phase of the unknown signal. To preserve the coherence of this indication, the analyzer demands that the reference signal be derived from the same source used to excite the device under test, usually a two-port network. The purchaser of the instrument usually has the option of ordering a package complete with a self-contained, phase-locked, voltage-controlled signal source, a small but powerful internal microprocessor, a communication bus addressable by an external computer, and any of a variety of special-purpose interfaces (sometimes called test sets) designed for specific test requirements.



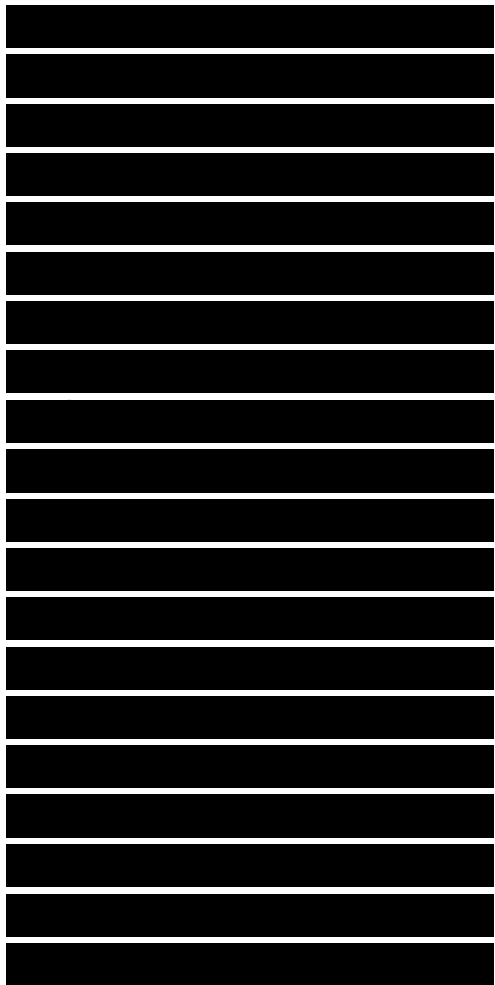
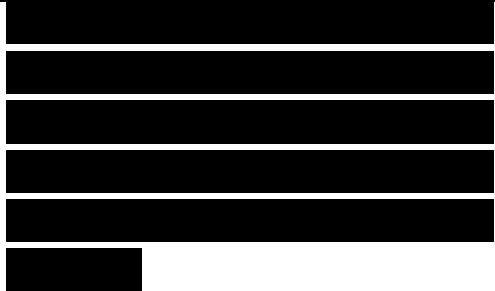
Because we are seldom interested in measurements made only at a single frequency, all contemporary network analyzers are designed to interface with controllable stepped-frequency signal sources, either internal or external. And because the general user is as interested in time-domain circuit properties as in the frequency response of a device, most display network analyzers are equipped with firmware that can transform test data back and forth between the two domains in real time (within one to six blinks of the eye). Any of several plug-in test sets are offered that expedite specific kinds of measurement, such as the reflection and transmission characteristics of two-port devices or their scattering matrices (S- parameters). Display options include Smith-chart representations and circuit gain or loss (amplitude) and phase, the latter in either rectangular or polar coordinates. Sets of precision devices (short circuits, open circuits, matched loads) are available in kits for calibration purposes.



The basic two-port representation now favored for materials testing is the S-parameter configuration shown in Figure 9.12. We encountered this configuration two-port network

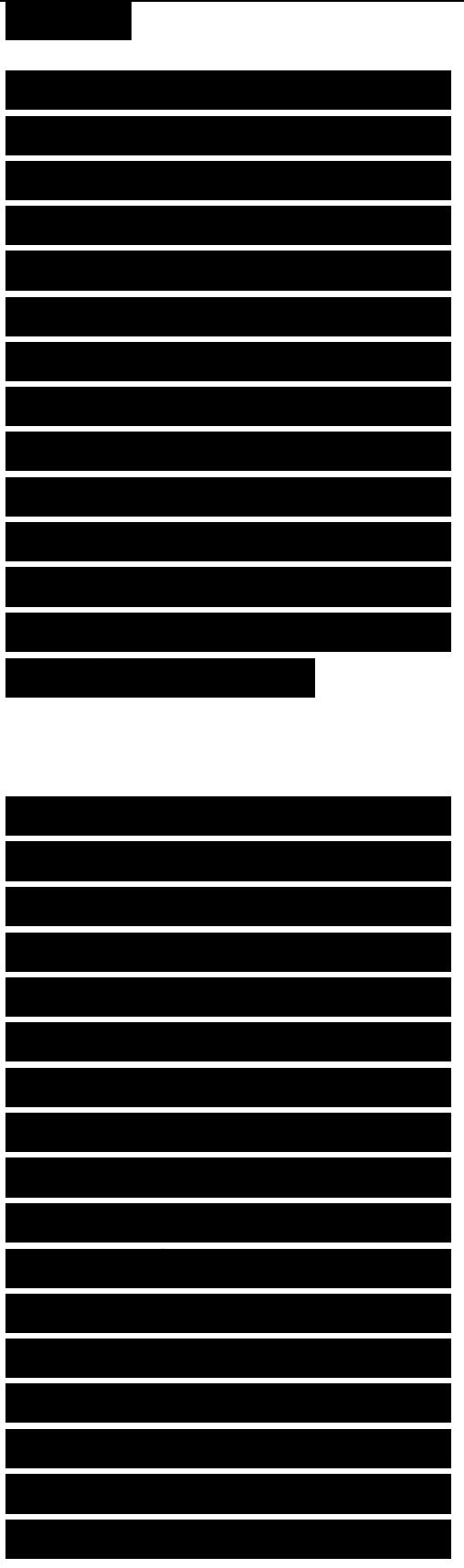
Figure 9.12. Four complex numbers characterize the scattering-matrix representation of two-port networks. It is not necessary to measure all four to determine the electromagnetic properties of passive absorbing materials.

in (8.24) and in Figure 8.4, in which the impedances of the input and output lines are both assumed matched. By “matched” we mean that the impedance Z_{01} of the input line has been carefully designed to “match” the impedance of the source, and that the impedance Z_{02} of the output line is similarly “matched” to the impedance of the load or detector terminating the output of the device. If these conditions can be maintained for all our test frequencies when the device (our test sample in its sample holder) is being measured, we may extract the desired electromagnetic parameters of our test material.



The complete characterization of the scattering matrix of an unknown device demands the measurement of no fewer than eight quantities: the amplitude and phase (or the real and imaginary parts) of the four scattering-matrix parameters. If the device is passive and reciprocal, however, as is the case for the materials we seek to measure, it can be shown that $S_{12} = S_{21}$ and $S_{11} = S_{22}$. Therefore, we need measure only two complex parameters (S_{11} and S_{21}) to characterize the material.

The basic measurement system is diagrammed in Figure 9.13. The slotted section described earlier is replaced in this system by a pair of directional couplers, one to sample the incident wave and one to sample the reflected wave, both of which may be routed to a detector and amplifiers (not shown) for measurement, amplification, and display. Although we may assemble these components on the test bench and perform the measurements manually, the manufacturers of some contemporary test equipment have developed systems in which most of the components are conveniently packaged into



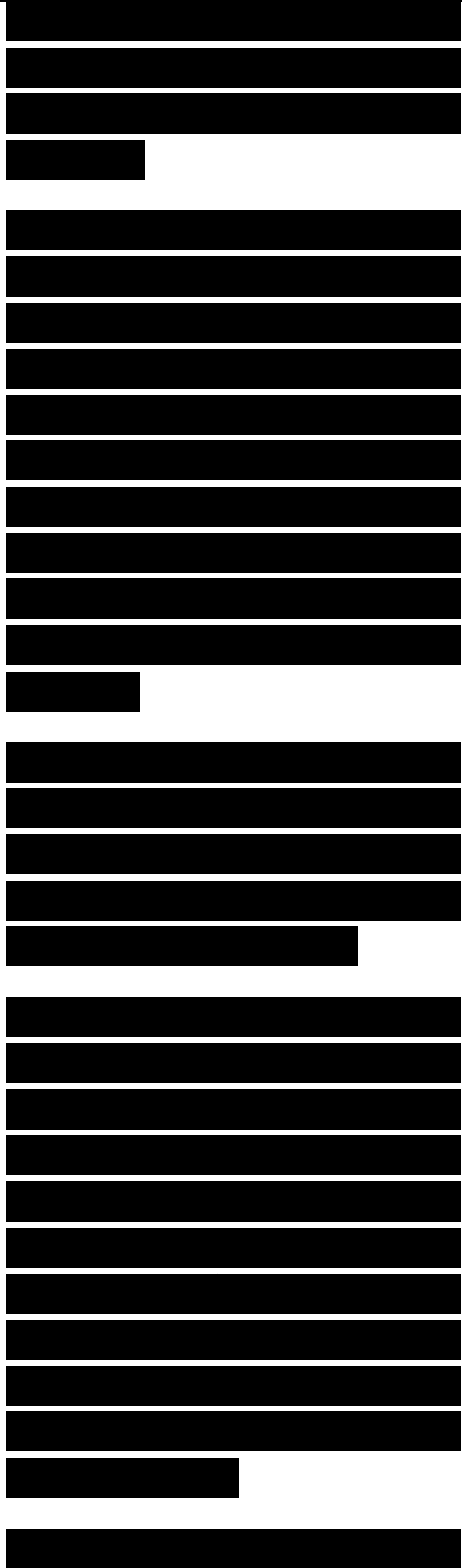
one or two units, as suggested in Figure 9.14.

In the more sophisticated designs, an internal signal source is controlled by a computer or microprocessor in the network analyzer itself, and a front-panel screen can display the measured data in any of several formats. The S-parameter test set contains the couplers and other devices needed to automate the process.

Figure 9.14. The S-parameter test set contains directional couplers and switching networks that simplify the operations required in the measurement of the scattering.

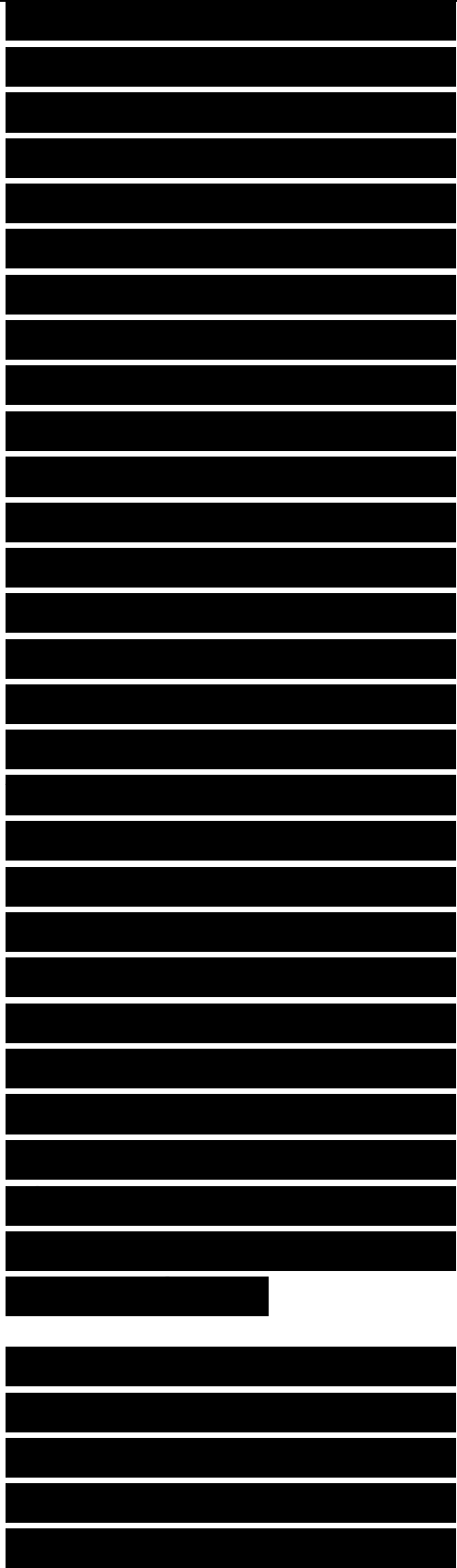
The test set has a pair of ports to which the test device is connected by means of cables or rigid coaxial lines, and some manufacturers even offer sets of “flexible arms” fitted with rotary joints to simplify making the connections. Precision calibration kits are also available to improve the accuracy of the measurements.

Indeed, calibration is essential



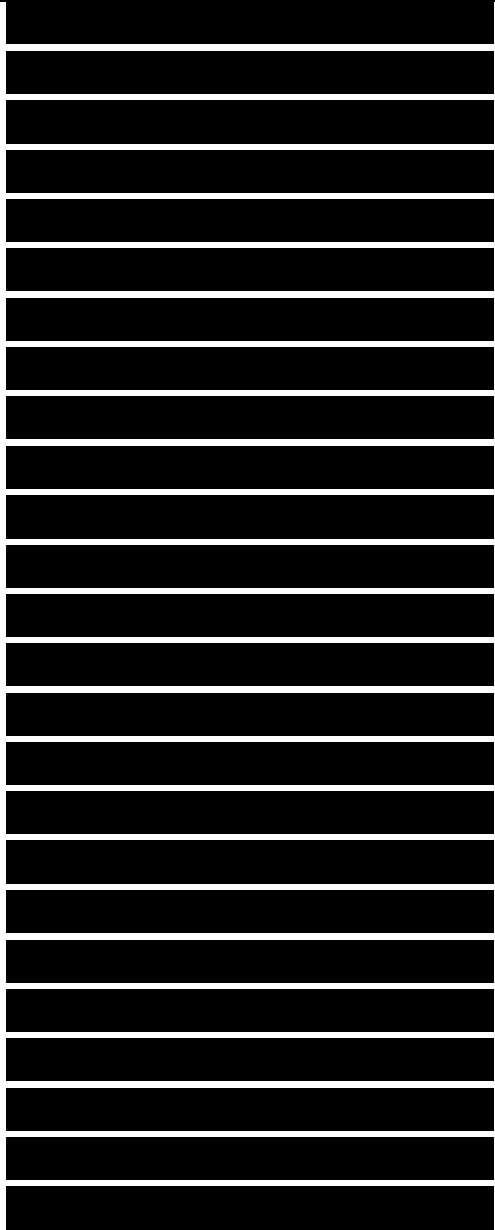
in the measurement of the scattering matrix because of undesired, but unavoidable, contamination of the desired quantities by others. A complete calibration sequence demands a characterization of the characteristics of ports 1 and 2 of the test device by separately terminating the input and output lines to the two ports, respectively, with a short circuit, an open circuit and a matched load. This results in no fewer than six numbers (three per port) that are stored in internal memory for each frequency used in the measurements. A pair of “through” calibrations are also performed, the first with the ends of the two lines from the test set connected together (bypassing the sample holder), and the second with them connected to the input and output ports of the empty sample holder. The sample is then inserted in the sample holder for the final set of measurements.

The purpose of the calibration is to determine several undesired parameters that may be removed or suppressed from the test sample data by subsequent mathematical operations. When properly



calibrated (measured) for each frequency in the data set, they include the effects of the directivity of and reflection from the couplers, reflections due to mismatches in the input and output test lines, and direct coupling of signals between the input and output ports of the device along external bypass routes. Although the microprocessor in the commercial network analyzer is designed to account for these sources of error, it is seldom aware of what we actually need: a comparison of scattering matrices measured with and without a test sample inserted in the sample holder. Nevertheless, it can store the calibrated measurements for the two cases and fetch them from memory when instructed to do so by software we ourselves design to make that comparison.

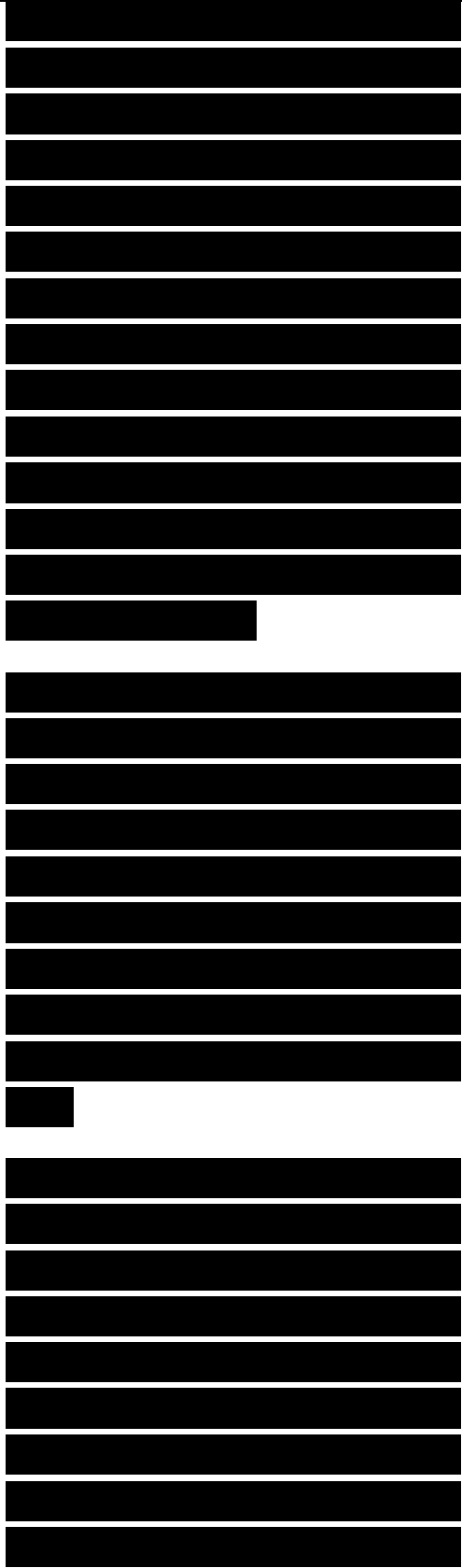
To extract the relative permittivity and permeability of our sample from these two sets of measurements, we use the concept illustrated in Figure 9.15 and the coefficient-stepping procedure detailed in Chapter 8. We represent our sample holder as the central section of transmission line



defined by the planes $z = 0$ and $z = t$ sandwiched between the input and output lines, whose characteristic impedance Z_0 and propagation constant k_0 also characterize the empty sample holder. We represent waves propagating in the forward direction (toward the sample) by A_1 , A_2 , and A_3 , and those traveling back to the source by B_1 , B_2 , and B_3 , all of which may be complex.

Invoking the definition of the scattering matrix in Chapter 8, we form the ratios B_3/A_3 and A_1/A_3 for the condition $B_1 = 0$ for the two cases (with and without the test sample in the sample holder). A comparison of the measured data for the two cases allows us to express the two scattering matrix elements as

Figure 9.15. The sample holder is represented as a section of TEM transmission line of length t , characteristic impedance Z_0 , and propagation constant k_0 sandwiched between a pair of lines whose characteristic impedances and propagation constants are Z_1 and k_1 and Z_2 and k_2 . Forward- and backward-traveling waves are characterized by coefficients A_1 , A_2 , A_3 , B_1 , B_2 , and B_3 .



and B.

and where $w = \exp(i\omega t)$ as before. The unknowns to be determined in (9.16) and (9.17) are u and w , with Su and $S21$ being the known (measured) quantities.

One solution is to solve (9.16) for w^2 and insert that value into (9.17), generating a quadratic equation for u in terms of known (measured) quantities. We therefore obtain the two equations

Equation (9.20) admits to two principal solutions for u :

$$u = -Q \pm (Q^2 - 1)^{1/2} \quad (9.23)$$

which we must compute using complex arithmetic, as Q is complex. The negative option in (9.21) happens to be the one we need, from which we may calculate a number U :

Note that, by virtue of (9.18), U is none other than yr expressed in terms of measured quantities:

$$VV)Ur = U \quad (9.25)$$

When we insert the now-known value of u into (9.20), and we generate another known number, call it W , also expressed in terms of measured quantities:

$$W = \frac{1 - f}{u - S_{i1}} \quad (9.26)$$

Therefore,

$$\frac{1 - f}{u - S_{i1}} = \frac{1 - f}{u - S_{i1}} \quad (9.27)$$

As in the short-circuit and open-circuit measurements discussed previously, we form the product and the ratio of (9.25) and (9.27) to extract the material properties:

$$\frac{1 - f}{u - S_{i1}} = \frac{1 - f}{u - S_{i1}} \quad (9.28)$$

$$\frac{1 - f}{u - S_{i1}} = \frac{1 - f}{u - S_{i1}} \quad (9.29)$$

This solution suffers the same ambiguity noted earlier, and if the sample is electrically thicker than $A/2$, it may require additional measurements to resolve it.

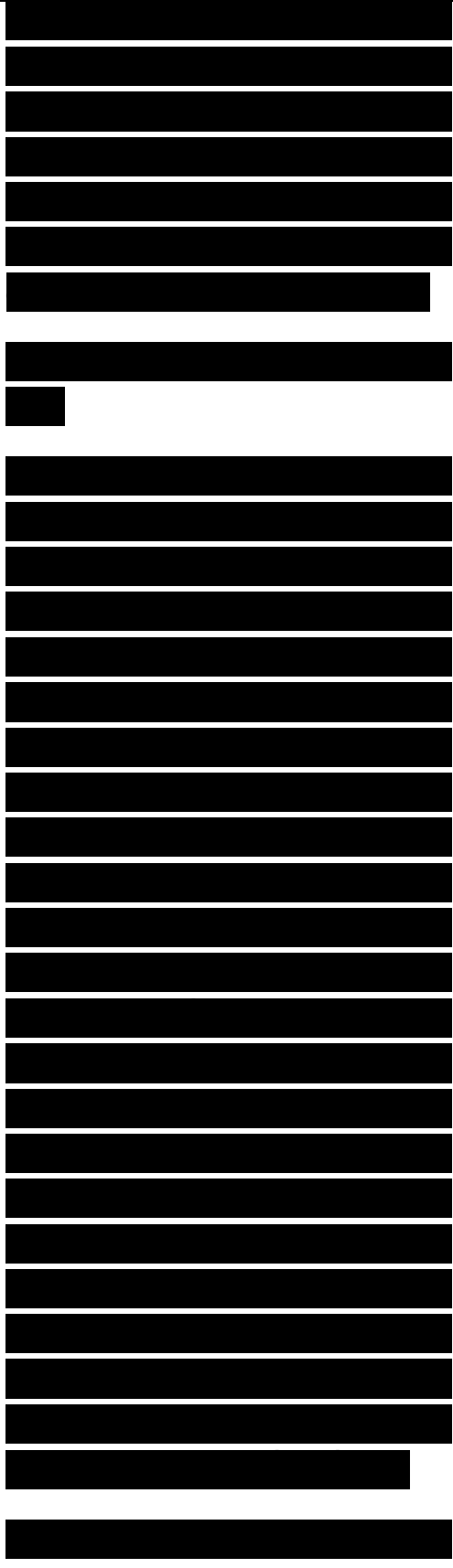
It is not necessary to measure both S_{11} and S_{21} if the sample material is nonmagnetic, in which case only the unknown complex permittivity appears in the right sides of (9.16) and (9.17), and the left side of either contains a single, measured complex quantity. As in the open- and short-circuit measurements discussed earlier, this results in a transcendental equation that may be solved with easily

applied mathematical procedures. If the attenuation through the material is not great, we usually rely on measurements of S_{21} to effect the solution because of the greater accuracy with which it can be measured in comparison to S_{11} .

9.3.3 Time-Domain Reflectometry

Although we may transform back and forth between the time and frequency domains when we use the ubiquitous network analyzer to collect our test data, the basic test signals are generated and detected in the frequency domain. We rely on the instrument's firmware to perform these forward and backward transformations digitally. It is also possible to make the basic measurements in the time domain, in which case the test instrument is called a time-domain reflectometer. Although time-domain reflectometry has fallen out of favor for materials testing, the instrument is of interest in its own right. One example is the test system described by Nicolson and Ross [3].

A diagram of the basic

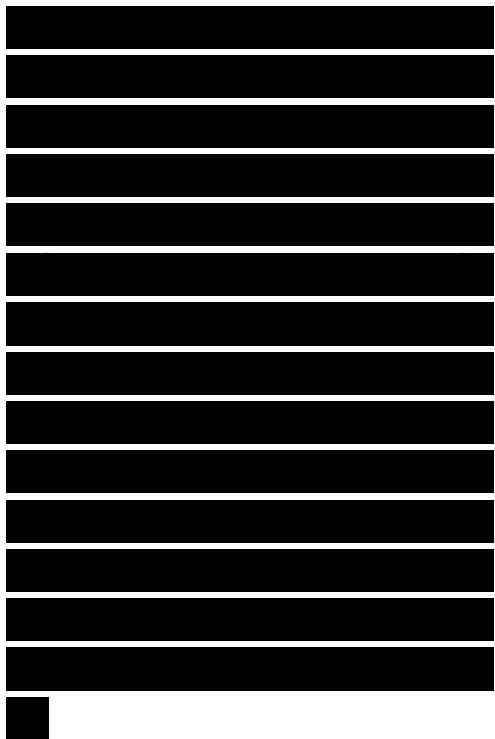
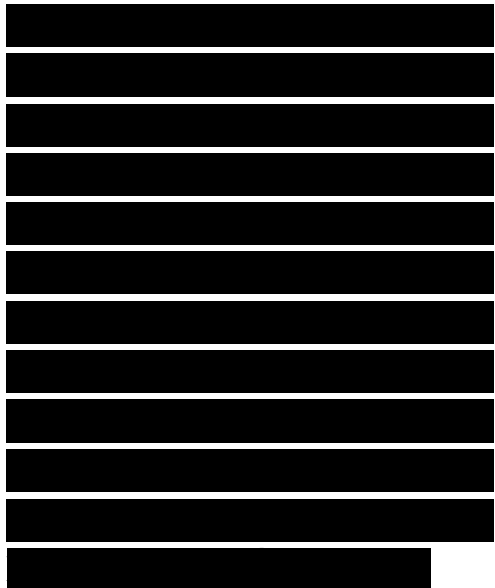


instrument is shown in Figure 9.16. It relies on a pulse generator for the signal source, whose ideal output is a unit step function,

Figure 9.16. Basic elements of a time-domain reflectometer. The pulse generator emits pulses with fast rise times, and a sampling oscilloscope is used to collect and record the data. The specified separations between its components (not to scale in the diagram) help suppress the effects of undesired system reflections.

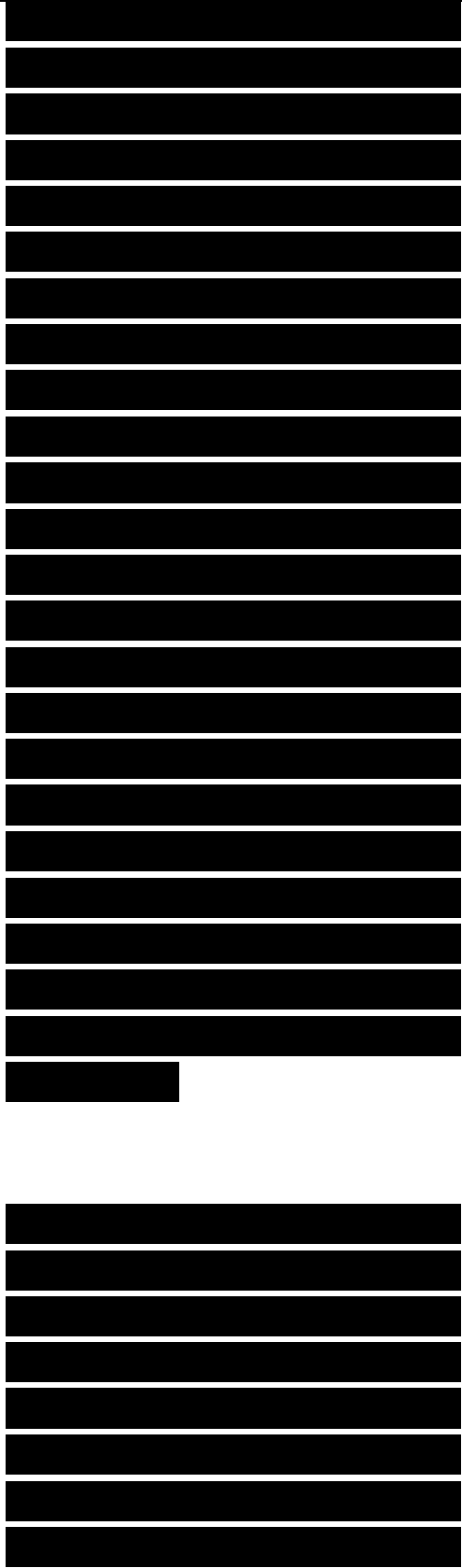
and on a sampling oscilloscope to detect and record the test data. To minimize the effects of undesired system reflections, the separations between the source and the oscilloscope, the oscilloscope and the sample, and the sample and the short circuit should be selected as shown in the figure. The ideal step function was approximated in this system by a relatively long, rectangular pulse that attained a steady voltage of 0.12 V in a rise time of 30 ps.

The measurement method hinges on the sampling of three



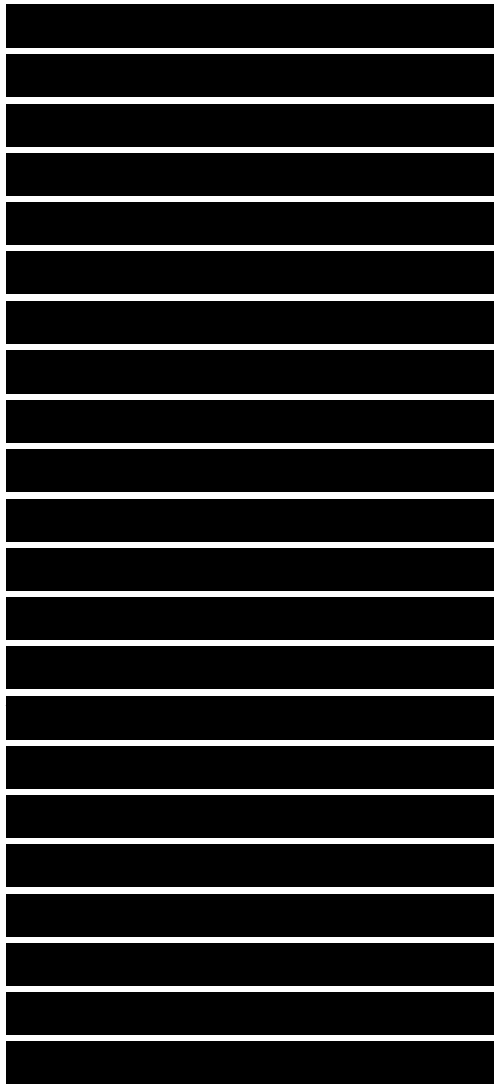
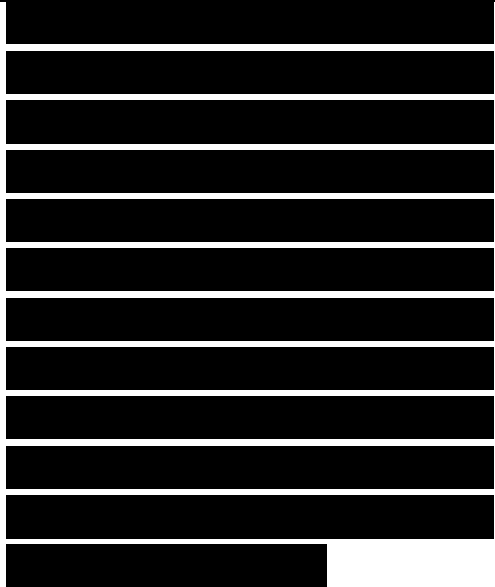
different signals at three different times. The pulse emitted by the generator travels through the oscilloscope sampling head, constituting a sample of the incident waveform against which the remaining two signal samples must be compared. The second signal is a combination of reflections from the front and rear faces of the test sample, which is assumed electrically thin enough that the two reflected pulses cannot be distinguished from one another when sampled. Although they travel back toward the pulse generator in the opposite direction taken by the incident pulse, the oscilloscope sampling head neither knows nor cares which way they travel. The third signal sampled by the oscilloscope is the reflection of the pulse from the short circuit behind the test sample, which therefore passes through the sample twice, once each in opposite directions.

The second signal constitutes the sum of the front and rear face reflections, which is a signal proportional to S_n . Because the third signal traverses the sample twice, and because $S_n = S_{21}$ by reciprocity, it is proportional to S_{21} . The constant of proportionality in both cases is



a system constant depending on many parameters, all of which can be accounted for when we normalize the second two signals with respect to the first (incident) signal in our processing. This processing is performed digitally after the waveforms are digitized and recorded by a computer not shown in Figure 9.16.

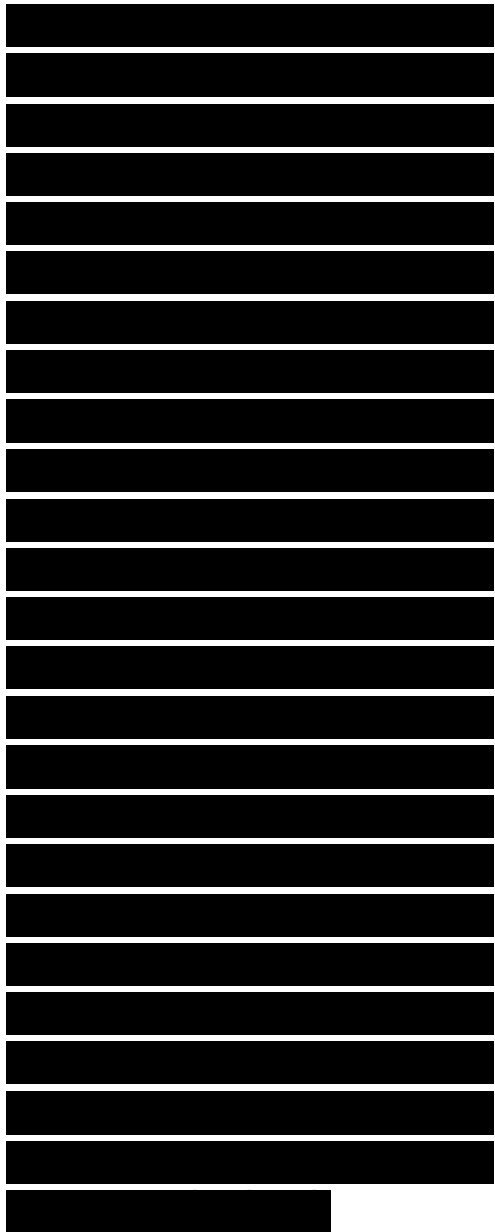
In principal, two sets of waveforms should be digitized and recorded. The first set should be a pair of calibration waveforms collected first with a short circuit installed at the position normally occupied by the front face of the sample, and then with the short circuit installed a distance behind the rear face of the sample. Because of the separation in the time of arrival of these two calibration waveforms at the sampling head, the second must be measured at a time delayed from the first. Except for this time delay, the two waveforms are sensibly identical, of course, and only the first need be measured in practice, because the time delay can be calculated from the known or measurable locations of the short circuit in the system. The sample may



then be installed in the sample holder and the second set of waveforms collected.

These digitized, calibrated data may then be transformed from the time domain to the frequency domain, just as in the case of more familiar measurements made with the network analyzer. The first set of normalized data is the frequency-dependent scattering matrix element $S_{n(i)}$. The phase of each datum in the second normalized set must be shifted by $2kd$ (twice the electrical thickness of the sample in free-space wavelengths), thereby yielding the square of $S_{1i}(\omega)$, from which $S_{21}(\omega)$ may be extracted by means of complex arithmetic. The measurements therefore provide the left sides of (9.16) and (9.17), which may be solved for the complex relative permeability and permittivity for each of the discrete frequencies generated by the FFT in the transformation of the data to the frequency domain.

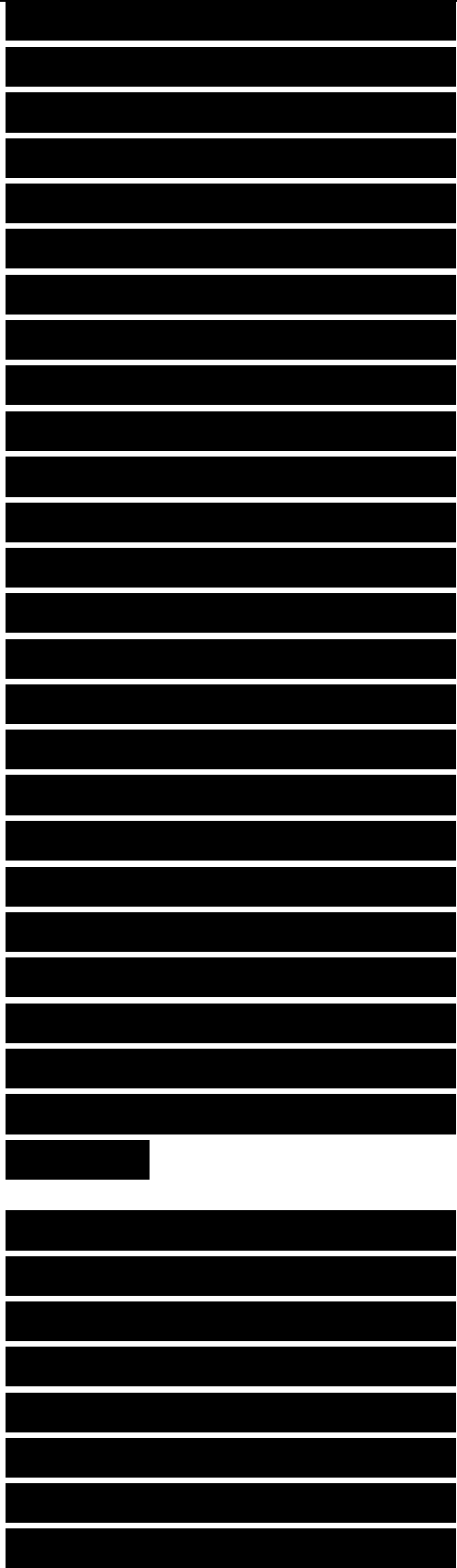
Figures 9.17 and 9.18 illustrate the results of measurements of a commercial magnetic absorbing material as obtained with a time-domain



reflectometer. It is doubtful that the true characteristics of the material actually behave as measured, particularly for the upper range of the frequency plots. As suggested below, the small cyclic variations are probably due to the narrowness of the time window over which the signal pulses were sampled.

In theory, the scattering matrix element $S_{n(o)}$ includes an infinity of multiple reflections between the front and rear faces of the test sample, and the sampling window should be wide enough to include the earliest (most significant) of them. If the sample losses are low and the sample is electrically long enough, we eliminate some of the reflections that are intrinsically part of the quantity defined as $S_n(w)$. The result of this exclusion is an interference “beat” between the reflections from the front and rear sample faces, producing the cyclic variations.

The period of the variation is about 425 MHz near a test frequency of 1 MHz, suggesting that the electrical thickness of the sample was about 13.9 in. This is the product of the physical sample thickness and the real part of the index of refraction, the latter of which may be



estimated from the measured characteristics near 1 GHz. When we divide the deduced electrical thickness by the real part of the index of refraction, we obtain a physical thickness of 3.0 in., which we suspect is very close to the length of the sample actually used for these particular tests.

If we assume that we must include at least the first reflection from the rear face of the sample in our time window, the window width should be no less than twice the electrical sample thickness divided by the speed of light, which amounts to 2.4 ns. Because the test window was about 2.5 ns wide for these tests, all higher order reflections were excluded from the measurement or at least greatly attenuated, and the first reflection itself was probably not adequately represented in the sampled time-domain pulse. The result is a contamination of the true material properties, as derived from the measured pulses, by the slight modulation seen in Figures 9.17 and 9.18 in the region up to about 5 GHz.

The period of these cyclic variations gradually increases

[REDACTED]

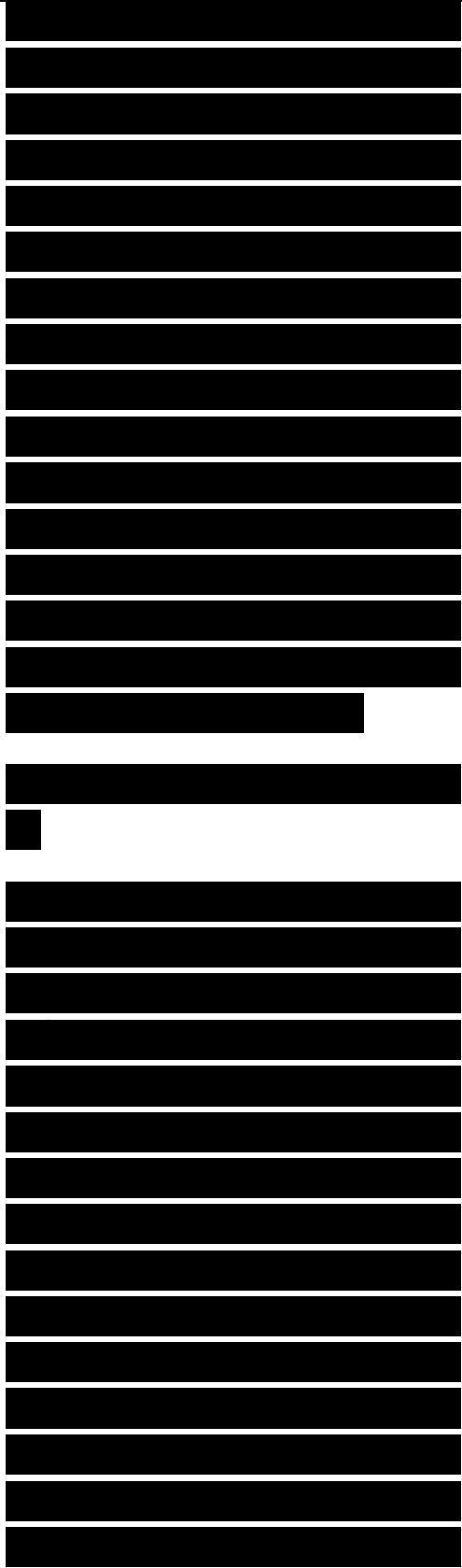
[REDACTED]

[REDACTED]

with increasing frequency, implying a reduction in the electrical thickness of the sample. As evidenced by the gradual decline of both the real and imaginary parts of the relative permeability with increasing frequency, this is indeed the case. Note that the amplitude of the modulation in the relative permittivity increases, particularly the imaginary part. Therefore, the accuracy of the test data above 5 GHz is suspect. It could probably be improved by expanding the width of the sampling window or reducing the thickness of the test sample or both.

9.4 FREE-SPACE METHODS

In contrast to the measurement of intrinsic material properties, the evaluation of absorbers for quality control or product development demands fewer measurements and less manipulation of test data and can often be accomplished with less sophisticated equipment. In the interest of economy, moreover, we would like the evaluation to be nondestructive so that we may retain the test panel in inventory for subsequent sale. And even if absorber samples can be sacrificed for the fab-doubtful that the true characteristics of



the material actually behave as measured, particularly for the upper range of the frequency plots. As suggested below, the small cyclic variations are probably due to the narrowness of the time window over which the signal pulses were sampled. In theory, the scattering matrix element $S_{n(o)}$ includes an infinity of multiple reflections between the front and rear faces of the test sample, and the sampling window should be wide enough to include the earliest (most significant) of them. If the sample losses are low and the sample is electrically long enough, we eliminate some of the reflections that are intrinsically part of the quantity defined as $S_n(w)$. The result of this exclusion is an interference “beat” between the reflections from the front and rear sample faces, producing the cyclic variations.

The period of the variation is about 425 MHz near a test frequency of 1 MHz, suggesting that the electrical thickness of the sample was about 13.9 in. This is the product of the physical sample thickness and the real part of the index of refraction, the latter of which may be estimated from the measured characteristics near 1 GHz.



When we divide the deduced electrical thickness by the real part of the index of refraction, we obtain a physical thickness of 3.0 in., which we suspect is very close to the length of the sample actually used for these particular tests.

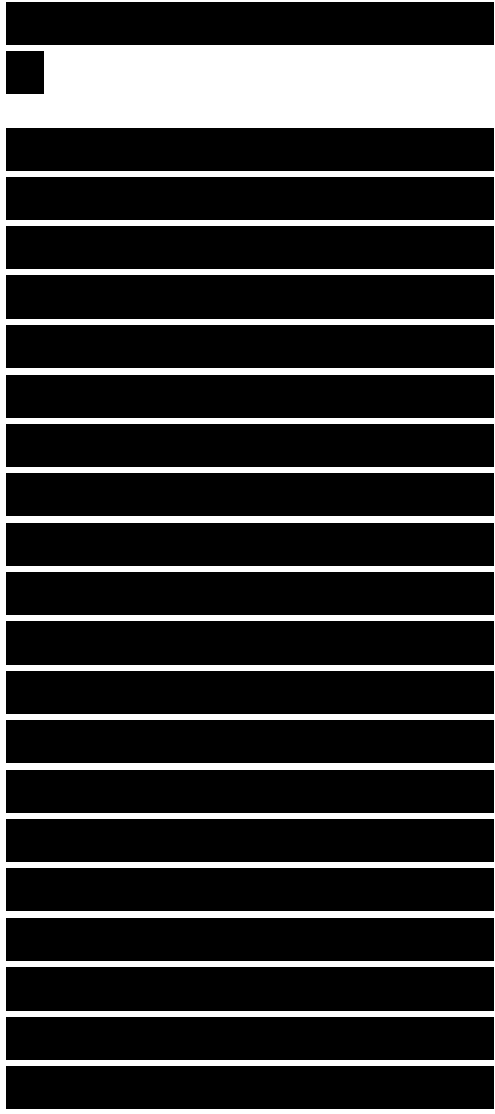
If we assume that we must include at least the first reflection from the rear face of the sample in our time window, the window width should be no less than twice the electrical sample thickness divided by the speed of light, which amounts to 2.4 ns. Because the test window was about 2.5 ns wide for these tests, all higher order reflections were excluded from the measurement or at least greatly attenuated, and the first reflection itself was probably not adequately represented in the sampled time-domain pulse. The result is a contamination of the true material properties, as derived from the measured pulses, by the slight modulation seen in Figures 9.17 and 9.18 in the region up to about 5 GHz.

The period of these cyclic variations gradually increases with increasing frequency, implying a reduction in the electrical thickness of the sample. As evidenced by the

gradual decline of both the real and imaginary parts of the relative permeability with increasing frequency, this is indeed the case. Note that the amplitude of the modulation in the relative permittivity increases, particularly the imaginary part. Therefore, the accuracy of the test data above 5 GHz is suspect. It could probably be improved by expanding the width of the sampling window or reducing the thickness of the test sample or both.

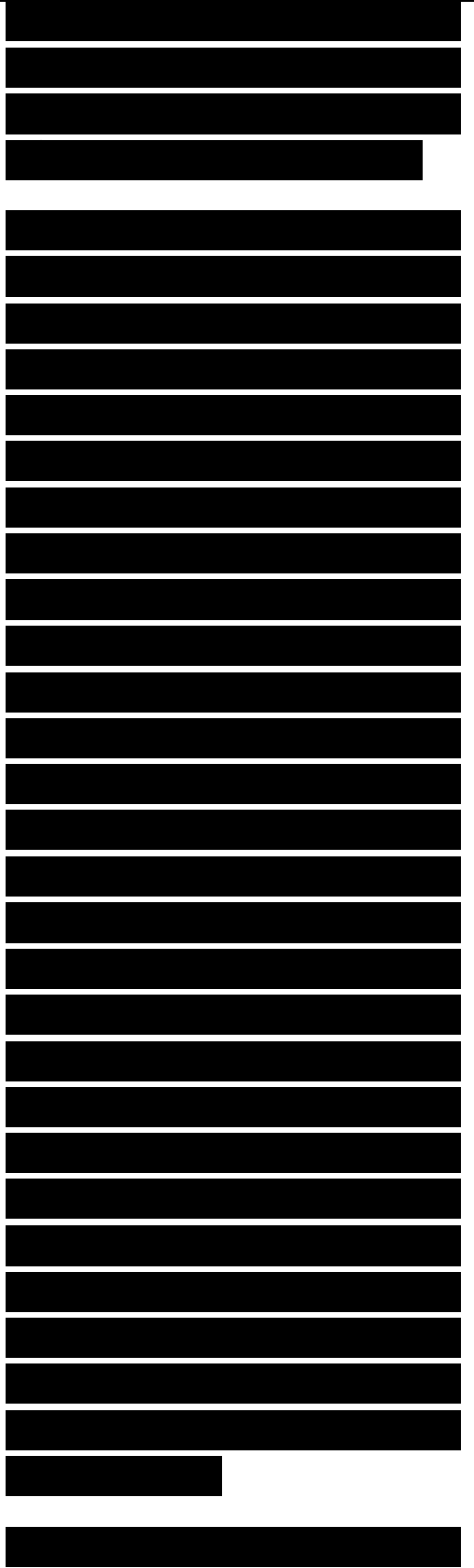
9.4 FREE-SPACE METHODS

In contrast to the measurement of intrinsic material properties, the evaluation of absorbers for quality control or product development demands fewer measurements and less manipulation of test data and can often be accomplished with less sophisticated equipment. In the interest of economy, moreover, we would like the evaluation to be nondestructive so that we may retain the test panel in inventory for subsequent sale. And even if absorber samples can be sacrificed for the fabrication of test specimens for transmission-line testing, the construction of most finished absorber products is ill-suited for insertion into small coaxial



lines or waveguides. Therefore, the relative simplicity of free-space testing is attractive.

We discuss two free-space methods in this section: the NRL arch method and a comparative RCS measurement. Although we label them free-space methods, the label refers only to the fact that the test panel is not installed in a waveguide or transmission line. In the case of the NRL arch, the test panel is placed within a few feet of a set of illuminating and receiving horns, and the framework that supports them is equally close by. The test panel is therefore well within the near fields of the antennas, and the test environment could hardly be called free space. Nevertheless, the arch method of absorber evaluation yields reliable results at low cost when operated with reasonable care. In the RCS method, by contrast, free-space conditions are closely simulated.



9.4.1 The NRL Arch

Despite the name, we believe the NRL arch method of absorber testing to have been developed at the Massachusetts Institute of Technology in the 1940s. An early prototype is believed to have been shipped to the Naval Research Laboratory for testing there, and we believe the arch design was implemented in other models pressed into use there. Whatever its origin, the arch is a model of simplicity. As shown in Figure 9.19, it is a vertical semicircular framework, often made of plywood, that allows a pair of small horns to be aimed at a test panel at a constant distance. The horns are mounted in carriages that can be clamped anywhere along the arch, making it possible to measure samples at virtually any desired bistatic angle.

monostatic radar: radar sử dụng

chung một ăng ten cho cả thu
lẫn phát

[REDACTED]

[REDACTED]

The two horns cannot be brought any closer than the width of one horn aperture, making pure monostatic measurements impossible. Nevertheless, the residual bistatic angle was small enough in most cases that the test results were very good indications of monostatic absorber performance. Sometimes it was necessary to slip a thin layer of absorbing material (not associated with the sample to be measured) edgewise between the two horns to suppress the direct coupling of energy from one to the other.

Early arches were not much more than 6 ft tall and were equipped with a short, flat, metal-topped pedestal at the center. The top of the pedestal was typically 2 ft square, a standard size for many absorber products; other common sizes were 1 ft x 1 ft and 1 ft x 3 ft. The metal plate provided the conducting backing necessary for the proper evaluation of the sample panel and was essential to the

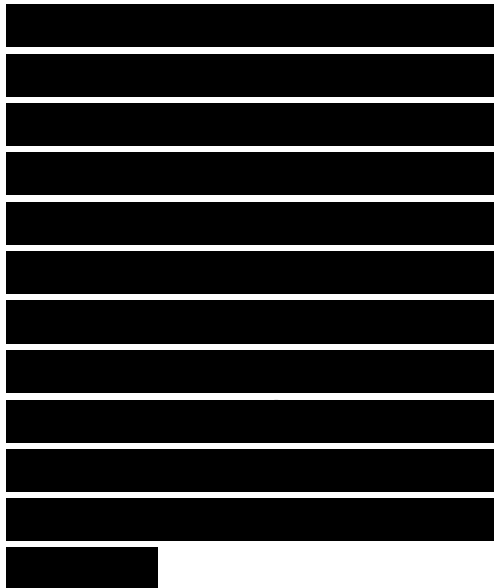
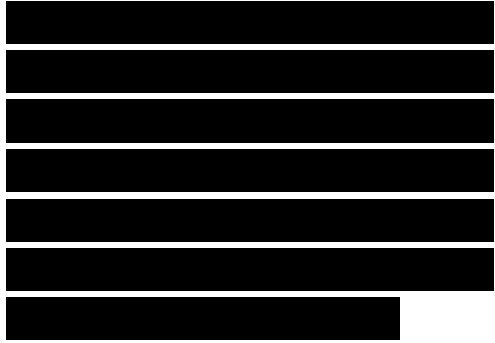
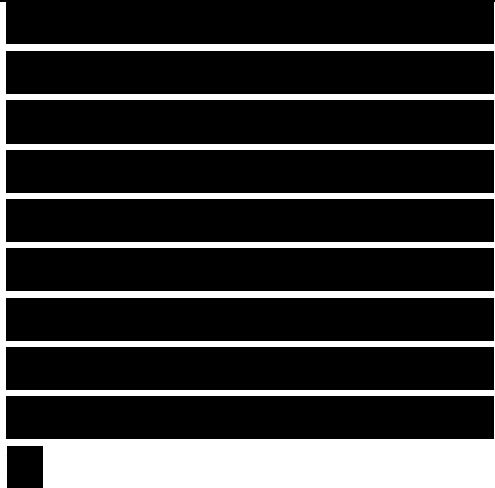
[REDACTED]

calibration of the system. Some arch users left the metal plate in place for both calibration and sample testing, but others elevated the plate, or installed an auxiliary plate, on a spacer for calibration. The thickness of this spacer was chosen to place the upper surface of the calibration plate at the same level that would be

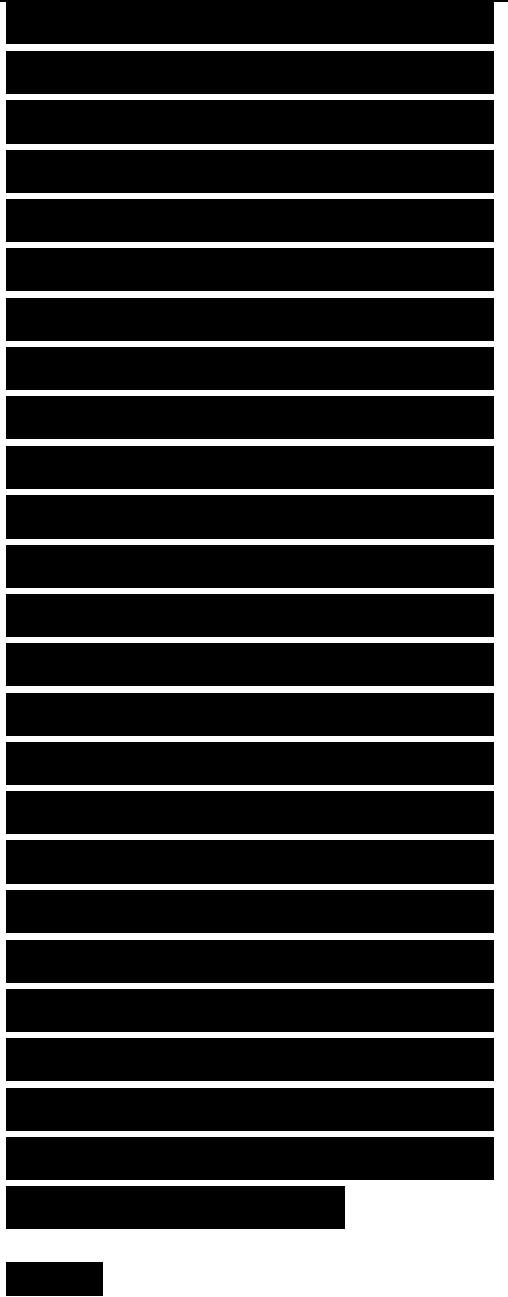
Figure 9.19. The classic NRL arch allows a pair of small antennas to be aimed at a test panel at a constant radius independent of the antenna position. The test panel is installed on a small pedestal at the center of the arch.

occupied by the upper surface of the absorber panel. The intent in the latter case was to establish a reference plane at the front face of the sample to be measured instead of the rear face. Although some arch users felt the spacer increased the accuracy of the measurement, it is doubtful that it made much difference, especially when the instrumentation horns were both moved to the top of the arch.

The electronic equipment needed for arch testing can be



as simple or as sophisticated as the user can afford. We have shown a very simple system in Figure 9.19, consisting of an audio-modulated RF signal generator feeding the transmitting horn through a variable attenuator, with the receiving horn feeding a crystal detector followed by an audio amplifier to boost the detected signal to measurable levels. The output signal is then rectified and displayed on a panel meter calibrated in decibels. The RF power requirements of the system are modest because the total transmission path is very short and the signals are strong, even when attenuated by the absorber under test. Moreover, the variable attenuator can be used to limit the dynamic range of the signals to be measured. Two measurement options were available, depending on the dynamic range of the detector.



If the received signals vary in amplitude by more than the nominal 30 dB dynamic range of the crystal detector, the variable attenuator could be used in a substitution method. The first step of the measurement process is to adjust the attenuator and the receiver gain settings to register a "comfortable" meter deflection with only the metal plate on the support pedestal. Once established, these settings need not be changed unless the user suspects that the system power level or receiver sensitivity has drifted (changed). The second step is to install the test panel on the metal plate and adjust the attenuator to restore original output meter deflection. The difference between the two attenuator settings then directly yields the absorption of the test panel. This step is repeated for all the samples in our pile of panels to be tested. If performance data are desired for other frequencies, the frequency of the RF signal generator is changed, the system recalibrated, and the measurements repeated. If performance data are desired for other bistatic angles of incidence and reflection, the complete sequence is repeated for those angles.

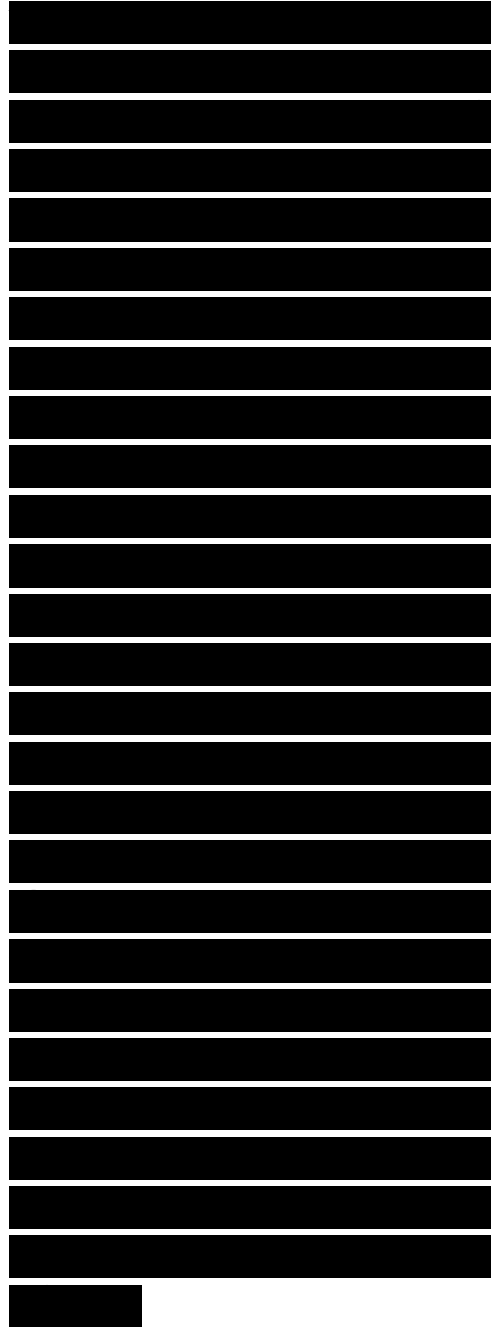
Nếu các tín hiệu nhận được có biên độ thay đổi nhiều hơn phạm vi hoạt động danh định 30 dB của detector tinh thể, chúng ta có thể dùng bộ suy hao biến thiên như một phương pháp thay thế. Bước đầu tiên của quá trình đo là điều chỉnh bộ suy hao và thiết lập độ lợi của bộ thu để kích hoạt độ lệch đồng hồ "comfortable" chỉ với bảng kim loại trên bệ đỡ. Một khi đã ấn định, những thiết lập này không thay đổi nếu người dùng không phát hiện mức công suất hệ thống hoặc độ nhạy bộ thu đã dịch chuyển (thay đổi). Bước thứ hai là cài đặt bản kiểm tra trên tấm kim loại và điều chỉnh bộ suy hao để phục hồi độ lệch của đồng hồ đầu ra ban đầu. Sự khác biệt giữa hai thiết lập của bộ suy hao sẽ cho ta biết sự hấp thụ của bảng kiểm tra. Bước này được lặp lại cho tất cả các mẫu trong hàng loạt tấm được kiểm tra. Nếu cần dữ liệu hiệu suất cho tất cả các tần số khác, tần số của máy phát tín hiệu RF được thay đổi, hệ thống được hiệu chuẩn lại, và các phép đo được lặp lại. Nếu cần dữ liệu hiệu suất cho các góc bistatic tới và phản xạ khác, chúng ta lặp lại

toàn bộ trình tự cho những góc đó.

Comfortable: thoải mái, đầy đủ

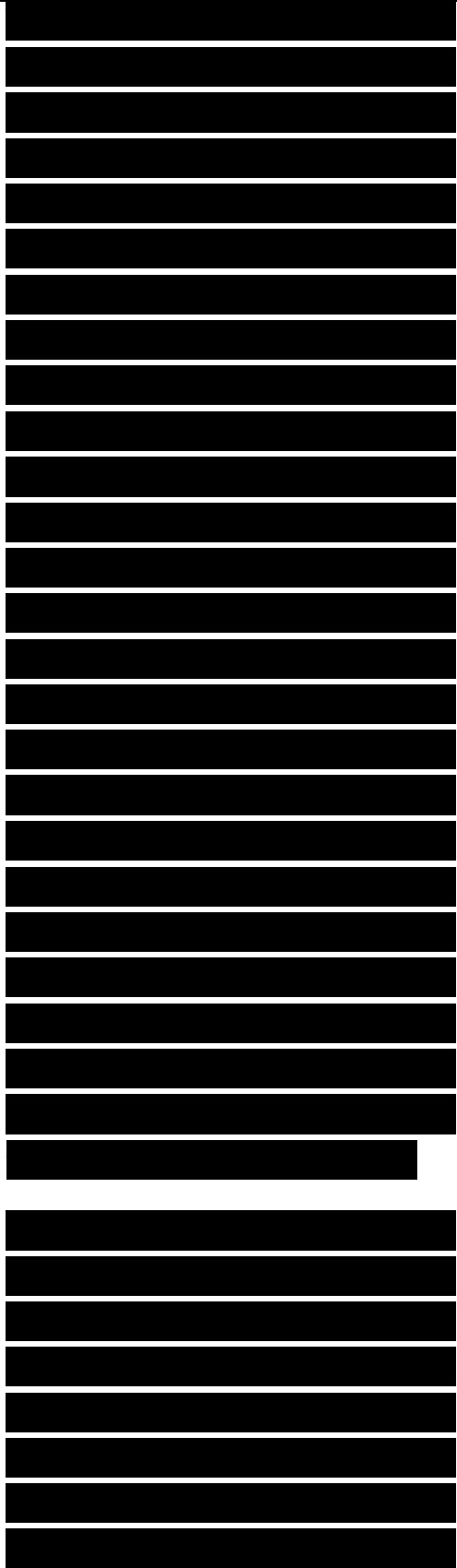
If the variation in the amplitude of the received signal is less than the dynamic range of the crystal detector, the measurements can be made without adjusting the variable attenuator. We must adjust the attenuator in the first (calibration) step as discussed previously, but once set for a “comfortable” meter deflection of the receiver, it need not be changed. That setting is chosen to place the calibration signal (for the metal plate alone) near the upper end of the dynamic range of the system and to keep the attenuated test panel signals above the lower end of the dynamic range. Once the calibration level has been established, we note the difference in meter deflections instead of the attenuator settings needed to restore the meter deflection for each test panel.

The ubiquitous network analyzer now makes such measurements child’s play. The principle of the measurement is



the same, but with this more sophisticated test device, we may collect the data for all the frequencies demanded in our test matrix with only one insertion of the test panel. The calibration procedure is the same as before (the collection of no-sample, metal-plate data) but we can do this in a single sweep of the required test spectrum. We save these calibration data digitally, and when we repeat the frequency sweeps with our test panel in place, we may recall those data and perform a simple subtraction (in decibels) to obtain the test panel performance. The dynamic range of the network analyzer is usually adequate for even the best of absorbing materials, and we may even elect to include phase information, for whatever it may be worth.

An example of swept-frequency absorber measurements made with the NRL arch method is shown in Figure 9.20. The arch in this case was a horizontal one (the arch parallel to the floor), and the test sample was a Salisbury screen tuned to about 6 GHz.



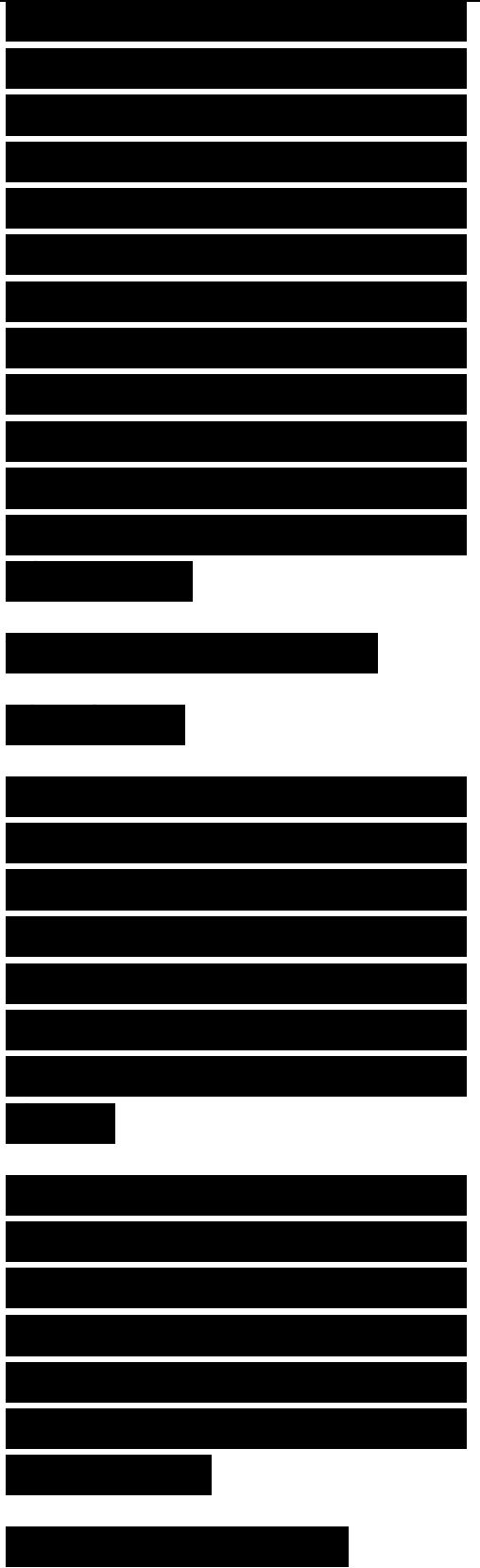
In this inverted form of display, the ordinate (signal attenuation in decibels) becomes more negative toward the top of the diagram. The frequency was swept from 2 to 18 GHz, and the ordinate runs from 0 at the bottom of the chart to -30 dB at the top. Thus, the peak near 6.5 GHz is actually a null in the response, having value of -24 dB. Ordinary horns cannot service this decade-

Frequency, GHz

Figure 9.20. This measurement of a Salisbury screen was made on a horizontal arch operated by the McDonnell Aircraft Company in St. Louis. In this inverted display, better performance is indicated by a higher position on the curve.

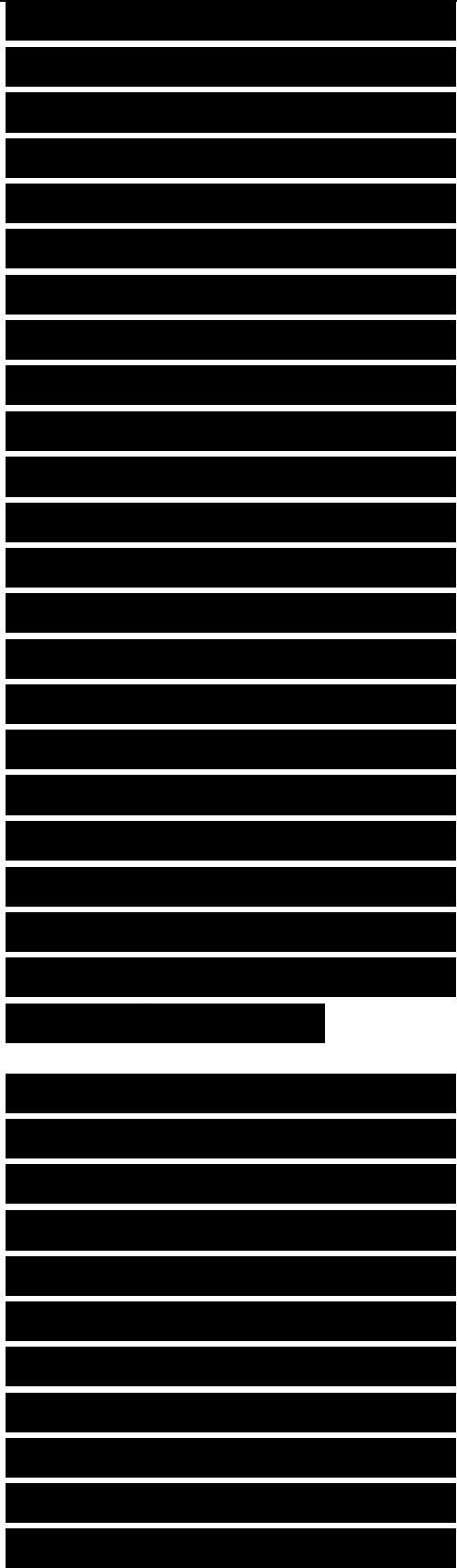
wide frequency coverage and must be replaced with more suitable (broadband) antennas. Even though the beamwidths of such antennas vary with frequency, the calibration process eliminates this variation from the measurement.

9.4.2 The RCS Method



Because the arch antennas are situated at best a few feet from the test sample, the phase fronts incident on it are spherical. If we hope to evaluate absorber samples under the more realistic conditions in which they will be used, we might prefer the flatter phase fronts available in compact ranges or conventional RCS ranges. To do so, we simply fasten the test panel to a sturdy flat plate, install the plate on a rotating support fixture, and record the RCS pattern of the ensemble, as suggested in Figure 9.21. In the case illustrated, a slot has been cut in the top of a plastic foam support column as a way to hold the sample upright and perpendicular to the line of sight to the radar.

This method of mounting the sample is easy to implement, and it exposes both the absorber-covered front face and the bare rear face of the backing plate to the radar once in every revolution of the support column. As such, the measurement is self-calibrating, because the specular echo seen from the back side becomes the



reference by which the specular echo from the front side may be compared. Figures 9.22 and 9.23 illustrate this fact.

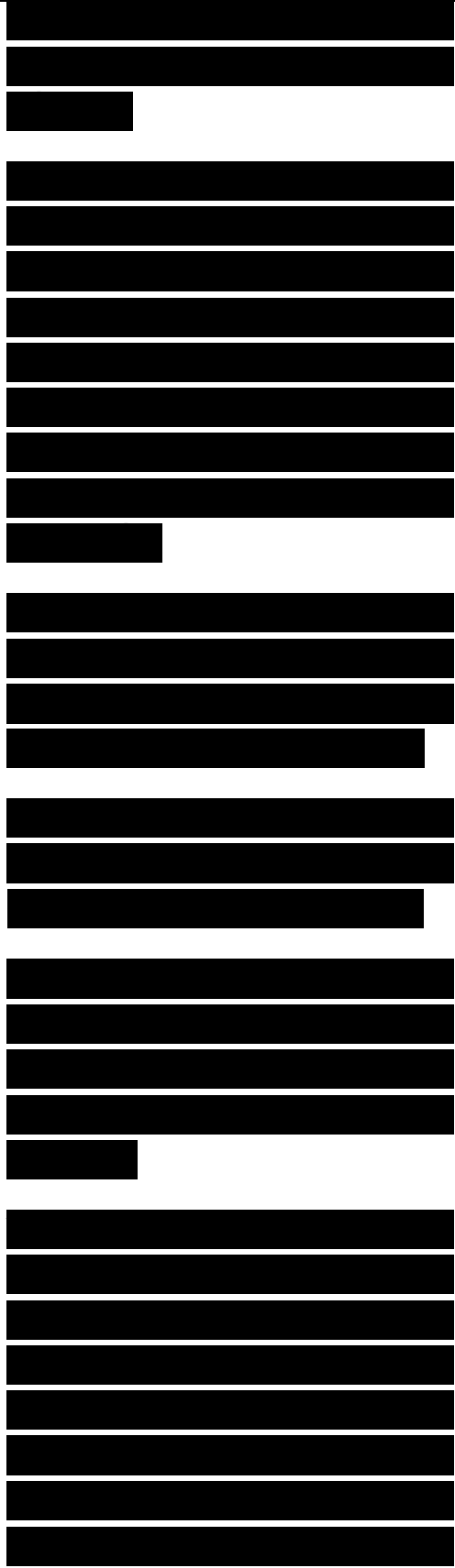
The metal plate in both cases was 6 in. square, which, at the test frequency of 10 GHz, amounts to about 5.1 λ . The patterns cover a full 360° of rotation, with edge-on incidence being at the center of the patterns and specular incidence lying

Figure 9.21. The RCS pattern of a metal-backed absorber panel may be measured when installed on a simple foam support fixture.

Figure 9.22. RCS pattern of a 6 in. square plate measured at 10 GHz with vertical polarization.

90° to either side. The amplitudes of the two specular echoes in Figure 9.22 are registered within 0.5 dB of each other.

As shown in Figure 9.23, the specular echo on the right is suppressed by a panel of absorber mounted on that face of the plate, and we see that the suppression is very nearly 20 dB. Note that the presence of the absorber does not change

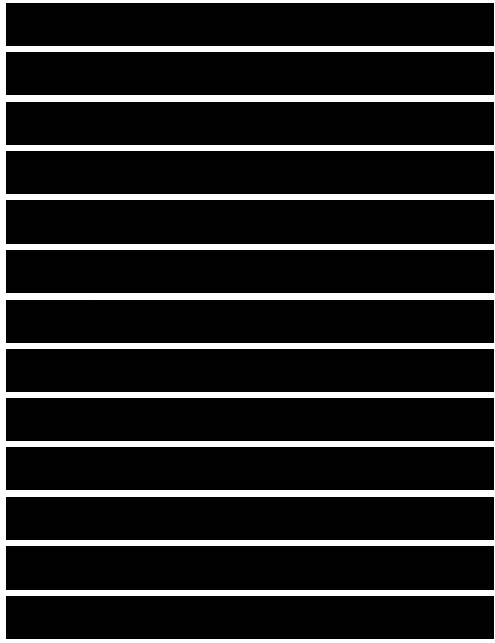
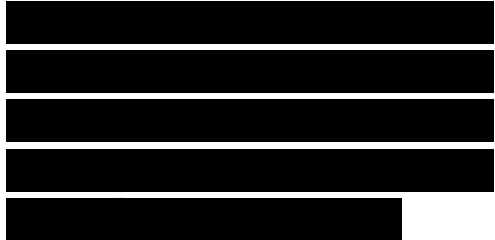
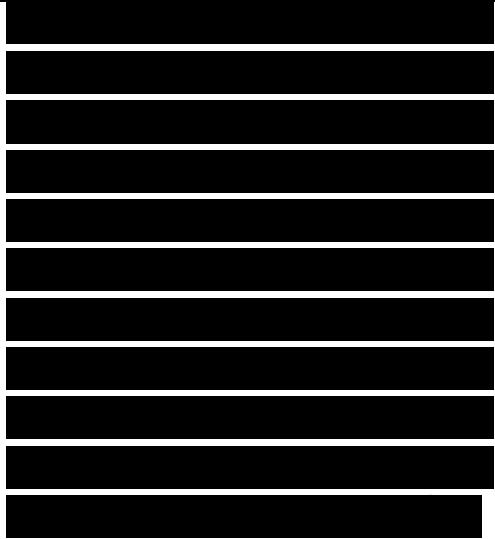


the amplitude of the specular echo from the bare rear side of the plate (left side of the pattern); indeed, we would be disturbed if it had. Therefore, we need not measure the plate twice (once with and once without the absorber installed), as the echo from the back side can be used to gauge the suppression of the echo from

Figure 9.23. RCS pattern of the plate of Figure 9.22 with a panel of Emerson & Cuming AN-75 absorber attached to one side.

the front. Moreover, because a comparison of the the two specular amplitudes is sufficient, we need not even calibrate the absolute amplitude of the RCS pattern.

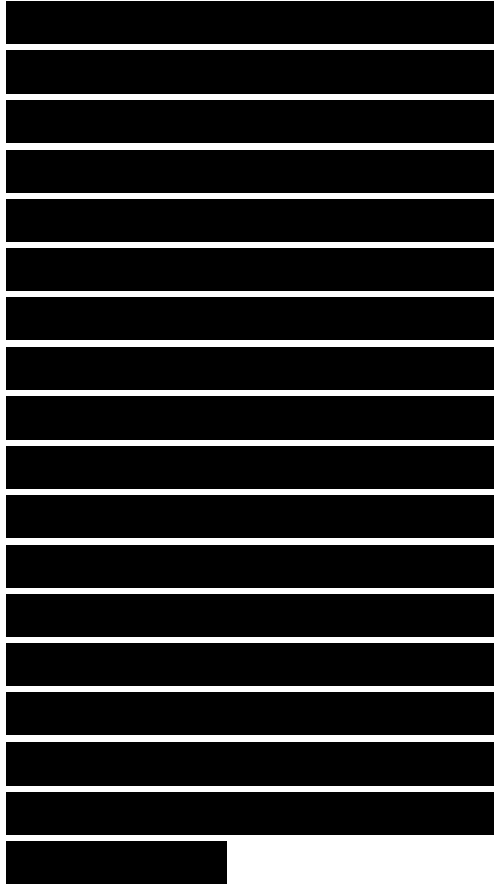
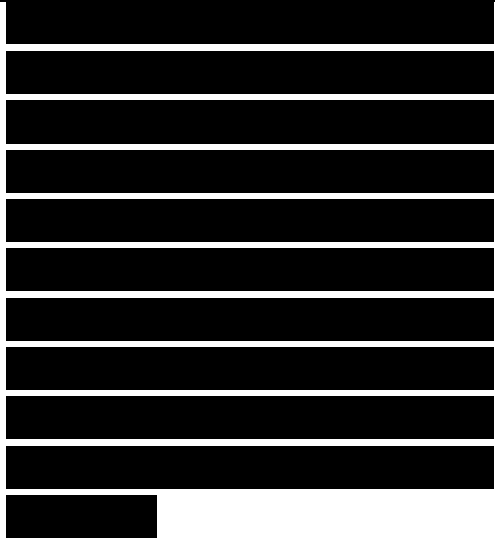
At one time we would have had to dismount the test plate and absorber from the support column if we needed to repeat the measurements at another frequency, but this is no longer necessary on most contemporary test ranges. The phase- locked, voltage-controlled, microprocessor-driven, computer-addressable, frequency-stepped RF signal generator has made it possible to measure RCS patterns over



dozens, and sometimes thousands, of frequencies within a single rotation of the test target. With such capability we may collect dozens of patterns like those in Figure 9.23, and thus assess the test material over a range of frequencies matching, and in some cases exceeding, the frequency range used to collect the data in Figure 9.20.

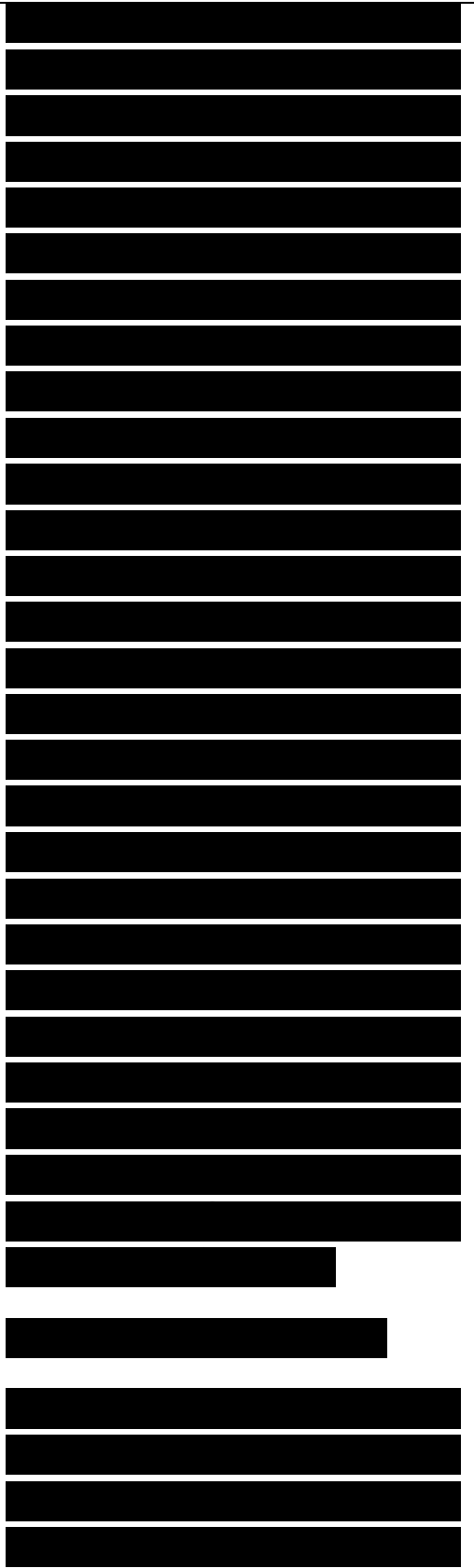
We must observe some precautions in making these kinds of measurements, however. First, the test specimen cannot be too small, lest edge effects contaminate the absorption we hope to characterize. A good rule of thumb is to cut the sample and test plate to be at least 3 A, and preferably 5 A, along a side at the lowest frequency to be used in the measurements. This becomes particularly important for very high-performance materials, for which the surface-effect absorption may approach the levels of edge effects.

Nearly as important is the need to limit the size of the plate to minimize the error of the



measurement due to misalignment of the specular peaks of the scattering pattern. The echo near in the specular region varies with the square of $[\sin(\theta) \sin \theta] / kh \sin \theta$, where θ is the angle from broadside incidence and h is the plate dimension measured in the plane in which θ is measured. The echo strength decays by 3 dB when the argument $kh \sin \theta$ (which we may approximate by $kh\theta$ for the plates of interest) attains a value of 1.39 rad, or when $kh = 1.39/\theta$ rad. It is difficult to maintain target và các cộng sự alignments any closer than 0.5° , and if we use this as a typical value for θ , we find that h should not exceed 25λ . Because we are measuring the pattern of the absorber-covered plate when rotated about a nearly vertical axis, this assessment is of a small tilt of the plate out of the vertical plane.

The actual error due to a 0.5° tilt will not likely be 3 dB for a 25λ plate, because the specular lobes of the bare and absorber-



covered sides will probably be misaligned by the same amount. However, the pattern structure near the specular lobe from the absorber-covered side will likely be slightly different from that of the clean, metal side of the fixture, and a 0.5° misalignment could well result in an error of 1 dB (ignoring all other sources of error). Therefore, the test panel used in the RCS method of absorber evaluations should probably be at least 5 A along a side at the lowest frequency used in the measurements but no larger than 25 A at the highest frequency.

[REDACTED]

[REDACTED]

[REDACTED]

9.5 OTHER METHODS

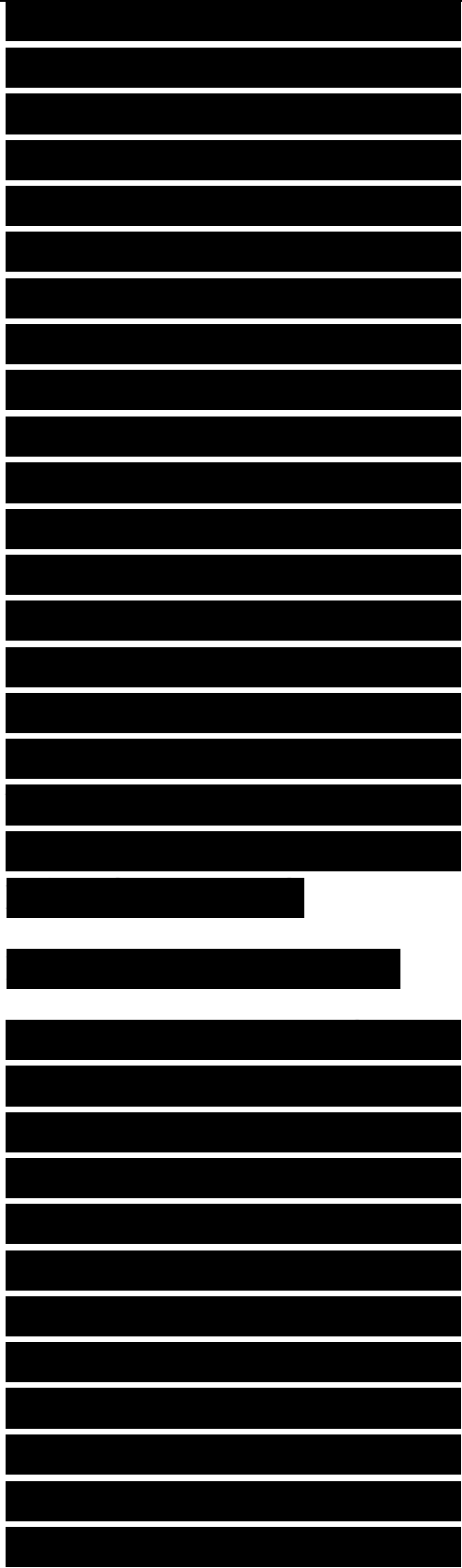
9.5.1 Large Waveguides

The NRL arch method of absorber testing is by far the most convenient and least costly of the free-space methods of evaluating absorber panels of modest thickness. The system is ill-suited for the measurement of pyramidal absorbers used to cover the walls of indoor anechoic chambers, however, especially those intended for frequencies below 1 GHz or so. Most commercial indoor chamber absorber panels are designed to

[REDACTED]

cover a 2 ft x 2 ft wall area, quite irrespective of the thickness of the material. Although thicknesses of a few inches might be accommodated in the arch test system, some of the pyramidal chamber absorbers are as thick as 12 ft, with the pyramid height exceeding the width of the base by a factor of 6. These thick materials are designed for chambers operated at frequencies as low as 100 MHz; and if an arch were to be built to test them it would have to be big enough to accommodate a collection of test samples covering an area as large as a barn door. An alternative to this gigantic, impractical arch is the large waveguide.

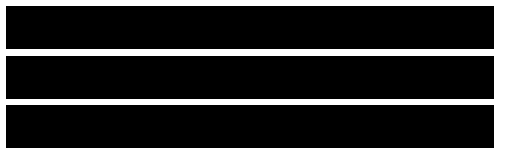
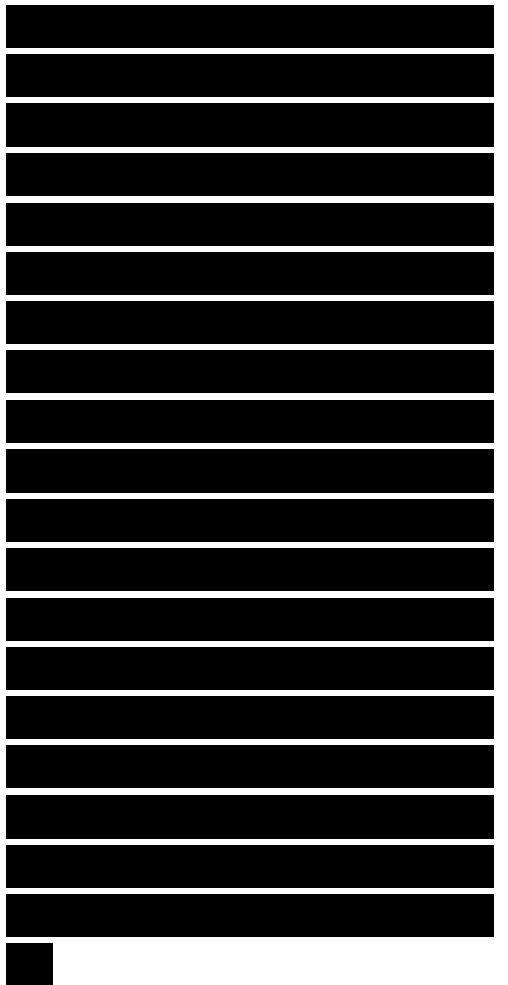
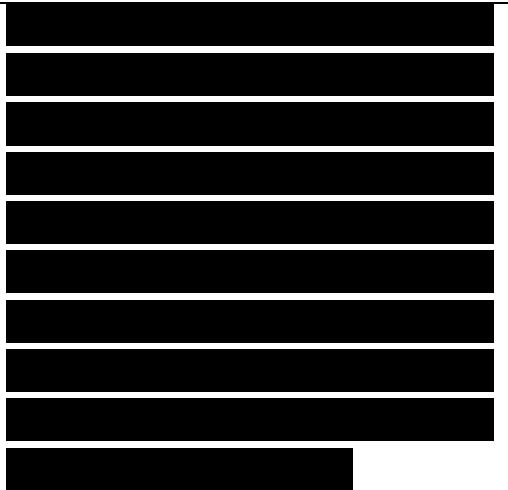
Although not necessarily much smaller than a scaled-up arch would be, the large waveguide makes it possible to test a much smaller collection of sample panels. The first waveguide built for such measurements was designed at the Sponge Products Division of the B. F. Goodrich Company, a major producer of carbon-loaded foam absorbers until the mid-1970s. Although the waveguide is a transmission line, it is used



only to measure the reflectivity of test samples, not the intrinsic electromagnetic properties of materials. A larger, more sophisticated version of the system was built by the Emerson & Cuming Company in 1981; a sketch of it appears in Figure 9.24.

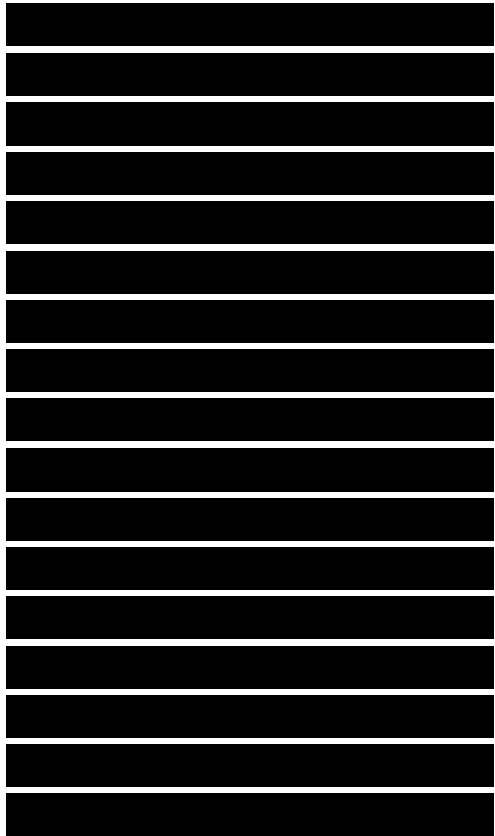
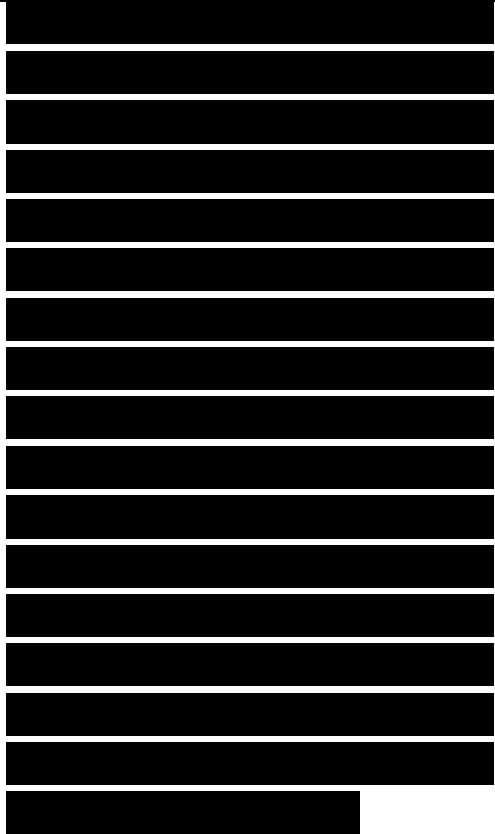
The waveguide is about 90 ft long and is excited by a broadband wave launcher at the instrumentation end, fitted with a 2 ft x 12 ft exit aperture at the other end, and a transition section between them that flares the guide out to the large dimension from the small one. The exit aperture is sized for six standard absorber panels affixed side by side to a large plate mounted on a rolling carriage. The carriage is withdrawn from the guide for the installation or removal of the test panels. Indicated, but not detailed in the figure, is a computer-driven data collection system we will describe in a moment.

The (earlier) B. F. Goodrich version of the large waveguide test fixture was equipped with a stationary probe inserted into



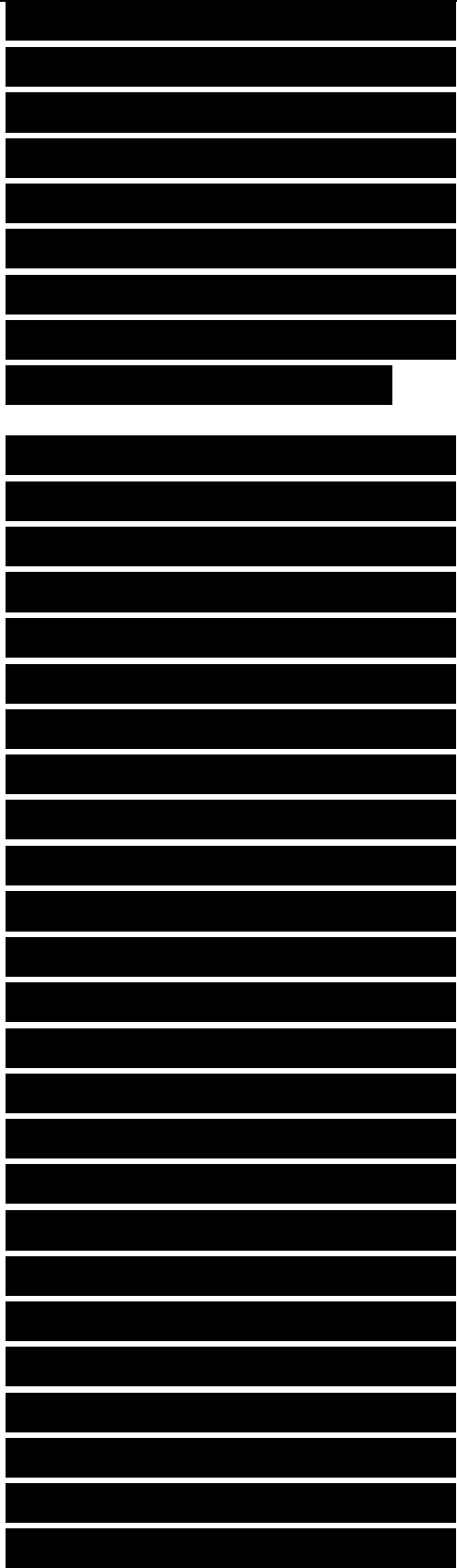
the guide at the instrumentation end to sample the standing wave pattern inside. We have already noted how the probe of a slotted section is moved back and forth to sample the pattern inside, but this was not the way the pattern was sampled in the Goodrich device. Bearing in mind that the standing wave is attached to the shorting plate at the end of the line, the plate and its six absorber panels can be rolled back and forth, thereby dragging the standing wave past the fixed probe, instead of moving the probe back and forth along a fixed standing wave.

Even though the measurement of the maximum and minimum voltages of this pattern does allow us to calculate a reflection coefficient, ideally that of the absorber-covered plate at the wide end of the waveguide, the stationary probe also responds to voltages due to stationary reflections in the waveguide. Thus the voltage maxima and minima we note from our probe readings are contaminated by contributions due to residual, if small, internal reflections. Indeed, the reflections from unavoidable discontinuities in the waveguide (due to practical



fabrication tolerances) might well be as strong as the sample reflections we hope to measure, particularly if the absorber is a very good one. Therefore, although the fixed-probe-sliding-load measurement technique is appealing, additional measurements are needed to account for the undesired reflections.

We can accomplish this by resorting once again to the use of swept-frequency instrumentation to excite the waveguide, and then transforming the measured data to the time domain. In its 1981 version of the B. F. Goodrich large-waveguide test system, Emerson & Cuming did just that. As shown in Figure 9.24, the swept-frequency source fed a fixed probe inserted into the guide, and the received signal was extracted from another probe installed further down the guide. The six test panels were installed on the shorting plate at the far end of the guide, as before, but were held in a fixed position once inserted into it. The computer-controlled system stepped the frequency from 100 to 450 MHz, and the probe signal was detected and stored for each frequency. The FFT was used to transform these signals to



the time domain, where unwanted reflections could be discerned from the sample reflections to be measured.

We seek to quantify and qualify the absorber product in the frequency domain, not the time domain, however, so further processing is necessary. To accomplish this, Emerson & Cuming engineers suppressed the unwanted reflections with a software filter and then transformed the filtered data back to the frequency domain. The result was the reflectivity of the set six panels displayed as a function of frequency, a great deal more information than could be collected in the earlier Goodrich version of the system.

Note that, because six panels were tested at once in both the Goodrich and Emerson & Cuming test fixtures, the measured values represented a composite performance figure integrated in some unknown way over the six test panels. If the test results revealed the

[REDACTED]

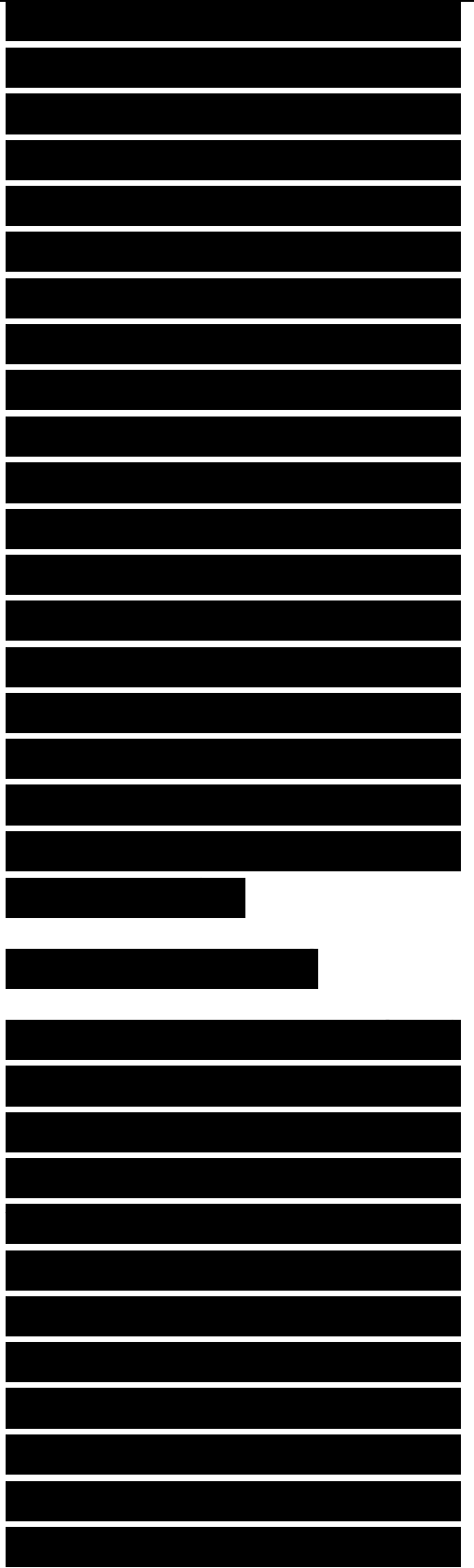
[REDACTED]

[REDACTED]

performance of a particular set to be unacceptable, the manufacturer could consign all six to the seconds pile, revise the advertised specifications of general product performance, or devise a method of isolating which of the six was responsible for the poor performance. The last would require retesting with some panels from the “bad” batch replaced by others drawn from a previously tested “good” batch. The large number of possible combinations involved in retesting, if performed, is one disadvantage of quality control based on samples of more than one unit of the product.

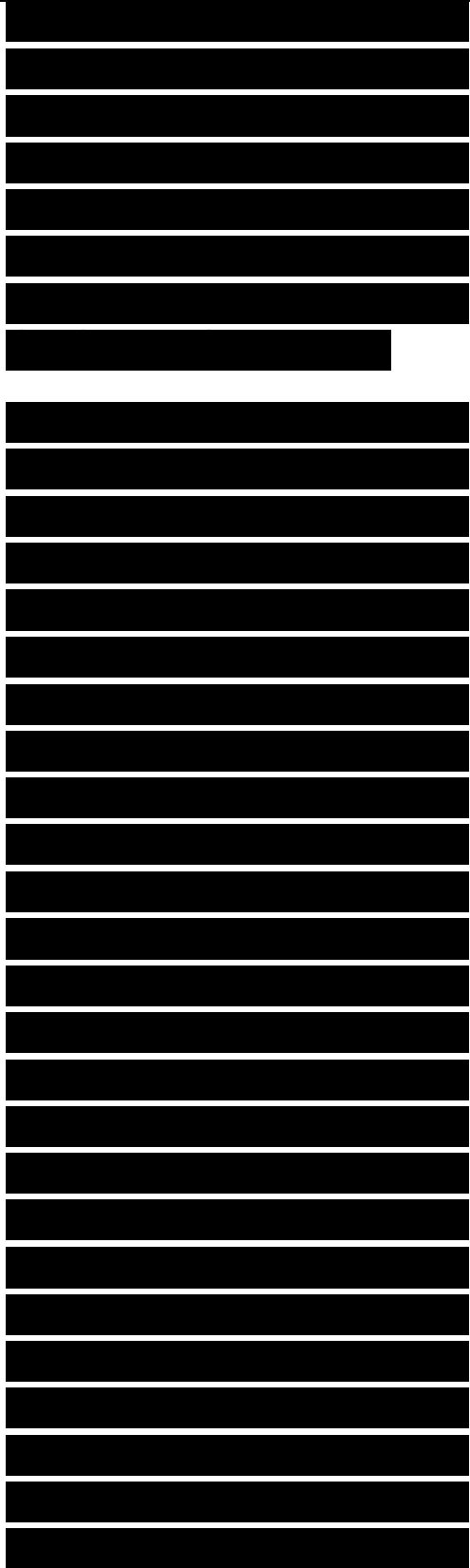
9.5.2 Interferometers

It is neither practical nor feasible to use transmission lines to measure the intrinsic properties of materials at short wavelengths. This is primarily because the transverse dimensions of the waveguide or coaxial line become so small that tolerances in the fabrication of sample holder and the test sample become too hard to maintain. In this case it is more practical to use cavities



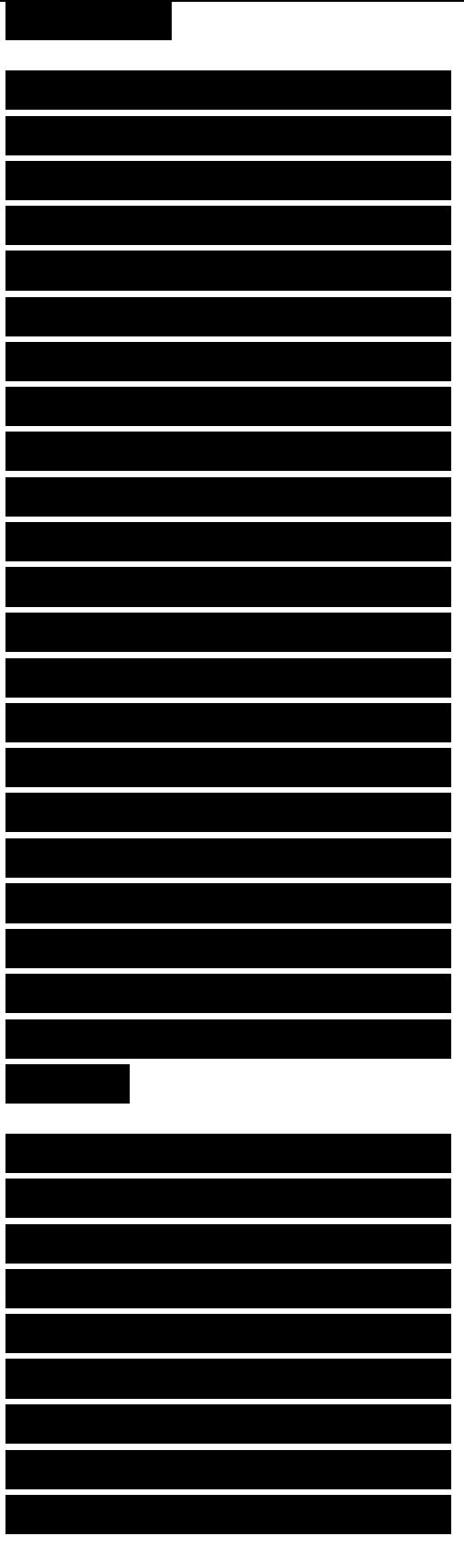
and interferometers, the latter representing an approximation of the former. The Fabry-Perot interferometer is an example drawn from optics and applied to millimeter wavelengths (very roughly, for frequencies between 30 and 100 GHz).

The Fabry-Perot interferometer is an optical device originally used to measure the wavelength of monochromatic light. In the microwave application, it is essentially a cavity without sidewalls [4]. A microwave cavity is a hollow metal box, excited by a small aperture, probe, or loop, that exhibits the resonant behavior of tuned circuits at lower frequencies. The resonant frequencies of the cavity are governed by the size and shape of the box, which need not be rectangular. These resonances are due to three-dimensional standing waves inside the box that can be supported only for discrete modes. The mode structure, and therefore the resonant frequencies, can be calculated fairly accurately for simple shapes, such as rectangular, cylindrical, and spherical cavities.



In addition to its resonant frequencies, a cavity may be characterized by its Q , which is the ratio of the energy stored in its electromagnetic fields to the ohmic energy lost, primarily by means of conduction currents in its less-than-perfectly-conducting walls. The Q and the resonant frequency are also governed by the characteristics and distribution of any material that may be placed in the cavity, and the intrinsic properties may be deduced from a comparison of the two values with and without a sample of material placed inside. For our discussion, we will assume the cavity to be a Fabry-Perot interferometer, for which the cavity side walls are missing and in which we may install thin slabs of material.

Consider first the optical Fabry-Perot interferometer built to measure the wavelength of light. As shown in Figure 9.25, it consists of a pair of partially silvered mirrors facing each other. They are illuminated by an extended source, shown at the left of the diagram, and the light passing

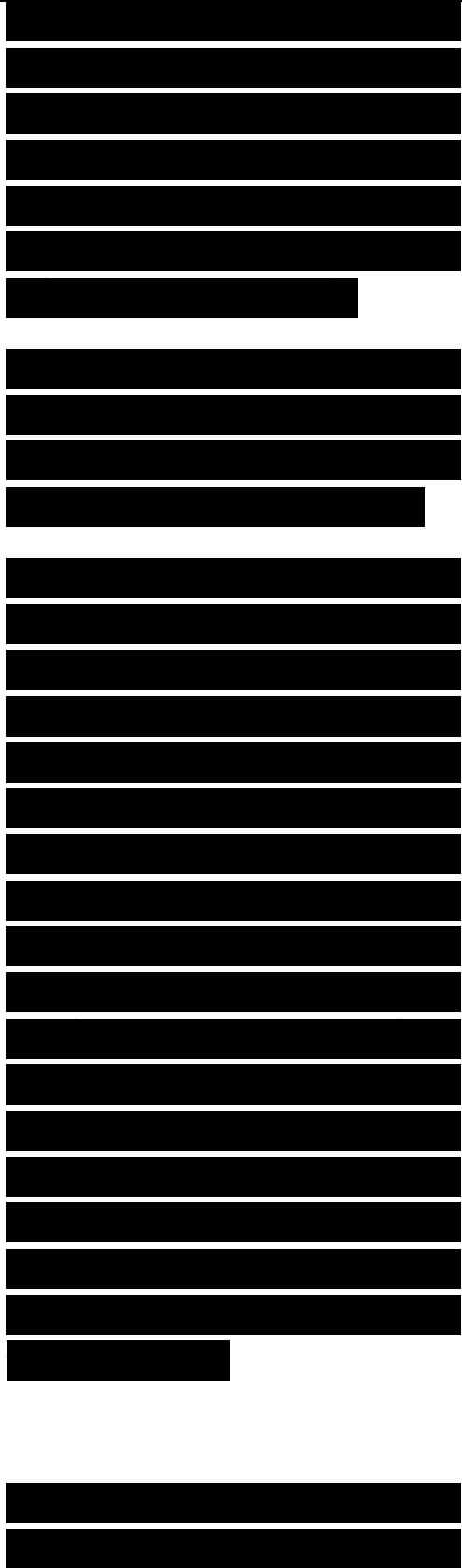


through them is focused on the observation screen shown at the right. Light passing through the nearest mirror is partly reflected by the second, which reflection is partly reflected by the first,

Figure 9.25. The optical Fabry-Perot interferometer generates a fringe pattern from which the wave-length of the light source may be deduced.

and so on, generating several reflections shown zigzagging between the pair, and several transmitted rays that are focused onto a single point on the observation screen. If the collimating lens is a body of revolution, that point lies on a ring centered on the lens axis. Other rays from other portions of the illumination source will find their way to this same ring, and when all arrive in phase, the ring will be brightened due to in-phase addition. At other points where they arrive out of phase, they will cancel, producing a darkened ring. The result is a fringe pattern consisting of a series of alternating bright and dark rings.

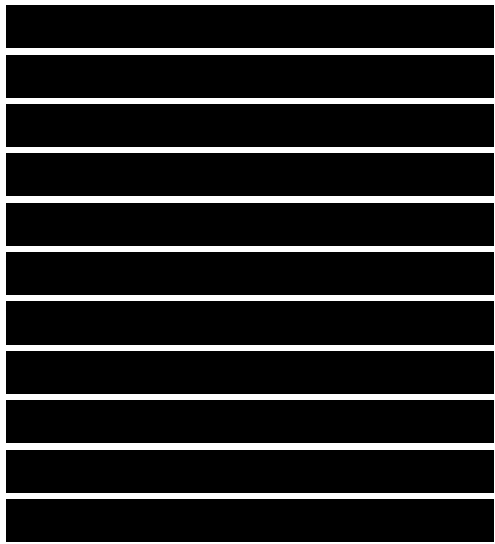
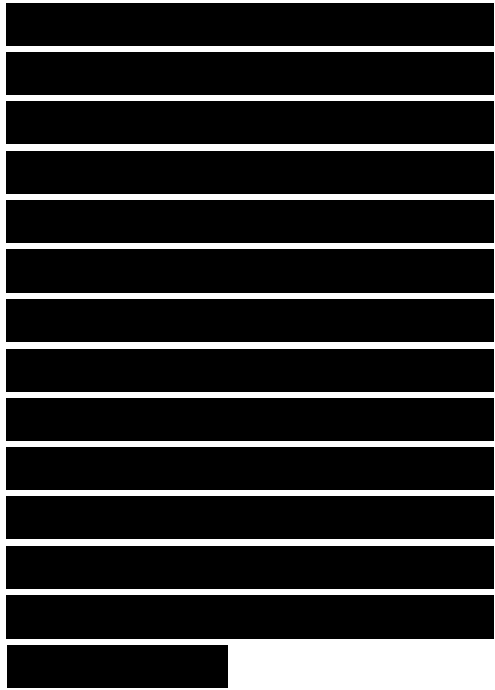
One of the mirrors is mounted



on a precision traversing carriage (not shown) so that the separation between the mirrors may be finely adjusted. Depending on the design, the distance between the mirrors may range from 0.1 to 10 cm. The radii of the bright rings involve the relationship

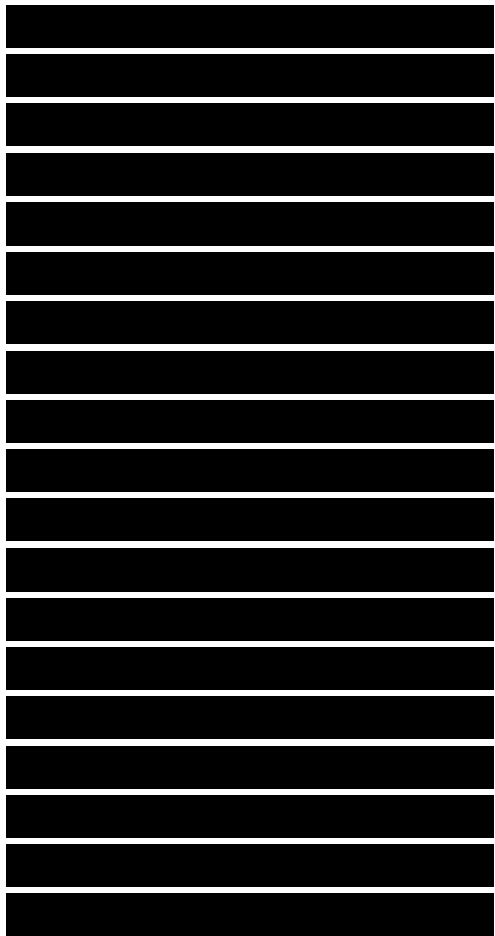
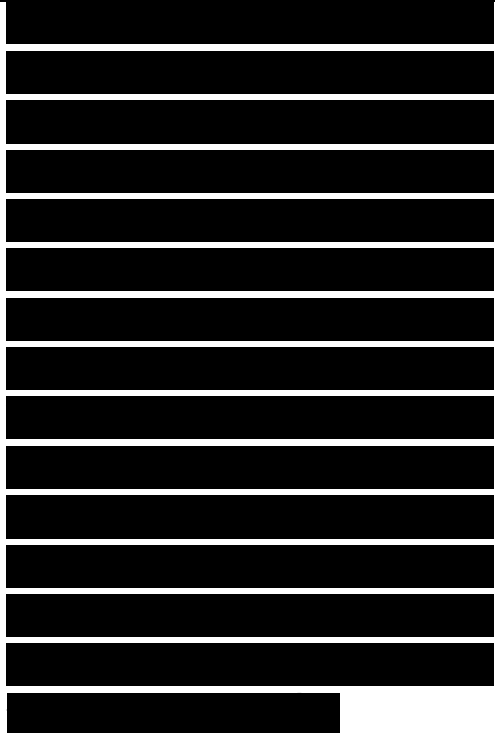
where d is the spacing between the plates and m is an integer. We may determine the wavelength of the light source by counting the number of fringes (rings) in a given pattern and then adjusting the plate spacing very slightly until a different number of fringes appears. We use the difference in the plate spacing, perhaps by counting the number of screw turns needed to move the plate, to deduce the wavelength of the light.

When applied to the measurement of test materials at millimeter wavelengths, the classic configuration of the Fabry-Perot interferometer must be modified to accommodate differences in instrumentation [5, 6]. The most obvious differences lie in the nature of the detector and the source. The detector in the optical case is an observation



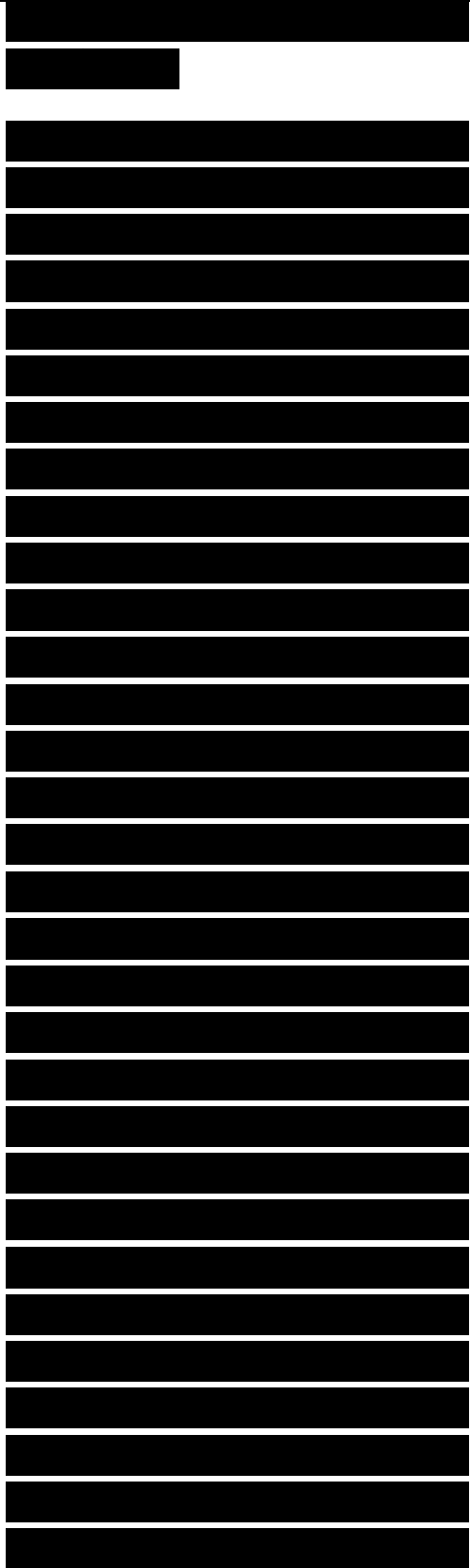
screen thousands of wavelengths in size, whereas we have small antennas only a few wavelengths in size at millimeter wavelengths. The electrical size of the sources used in the two regimes are similarly different, and we must use a small excitation source at millimeter wavelengths to inject energy into the resonant structure. The mirrors in that structure may even be concave to minimize the escape of energy from the system, and they are not likely to be partially silvered plates of glass.

The practical implementation of the interferometer at millimeter wavelengths is quite different from the optical version, yet the interference principle is exploited. An example of one application is illustrated in Figure 9.26, based on the description given by Balanis [7]. The partially silvered mirrors are simulated in the interferometer by perforated metal plates, which have the same effect. The holes in the plates admit a small amount of energy into the region between them, but permit relatively little of it to escape the sides of the enclosure. The RF signal is injected by means of a



means of measuring small displacements.

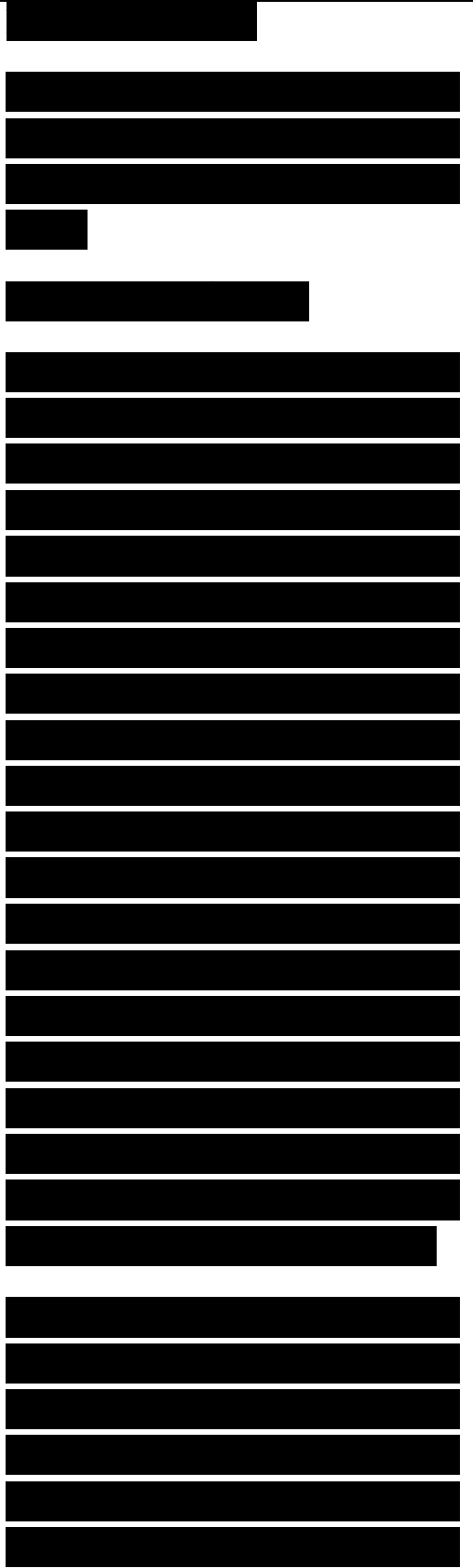
A slab of test material is then inserted between the plates more or less parallel to them, and the movable plate is again adjusted for a maximum detected signal. The signal strength and plate position are again recorded, from which the intrinsic material properties (complex dielectric constant) may be calculated, assuming that the thickness of the slab is known. Because only two calibrated quantities are measured, only two unknowns—generally the real and imaginary parts of the relative permittivity—can be determined. We encounter the same kind of ambiguity noted for transmission-line measurements: the plate displacements needed to restore resonance when the sample is inserted between the plates do not uniquely indicate the electrical sample thickness. The ambiguity can be resolved as it is in transmission-line tests: the measurements may be repeated for a slightly different test frequency or for a test sample slightly thinner or thicker than the first one.



9.5.3 The Admittance Tunnel

We have seen that thin sheets are used in the design and fabrication of absorbers in addition to one or more layers of bulk materials. Whether thin sheets are primarily resistive, as in the Salisbury screen and Jaumann absorbers, or whether they have significant reactive components, as in circuit analog designs, it is difficult to install them in waveguides for the measurement of their intrinsic properties. A more suitable test fixture is the admittance tunnel shown in Figure 9.27. It is an absorber-lined box that may be 8 to 12 ft long and 2 ft wide, and the test sheet is typically installed behind an absorber-shielded aperture.

In the configuration shown in the figure, the tunnel is arranged for measurements of the transmission coefficient of the sample (S21). A small antenna at one end of the box illuminates the test sheet and a



small receiving antenna at the other end picks up signals transmitted through it. In this configuration the test sheet is installed near the center of the tunnel, and the sheet properties are deduced from a comparison of the signals received with and without the test sample in place. The measured data are therefore of S_{21} , from which the sheet properties may be calculated. In another version of the tunnel (not shown), the receiving antenna is replaced with a metal plate that may be moved to and fro behind the sheet, and the reflection from the plate-backed sheet is measured. The testing and data reduction in that case are akin to those performed in the waveguide measurements discussed in Section 9.3.1.

In either configuration of the admittance tunnel, we seek to characterize the sheet by a complex admittance or impedance instead of a relative permeability and permittivity. For this purpose we find S_{21} a convenient parameter to measure with the simple instrumentation diagrammed in Figure 9.27. This is a nulling system absorber-lined box

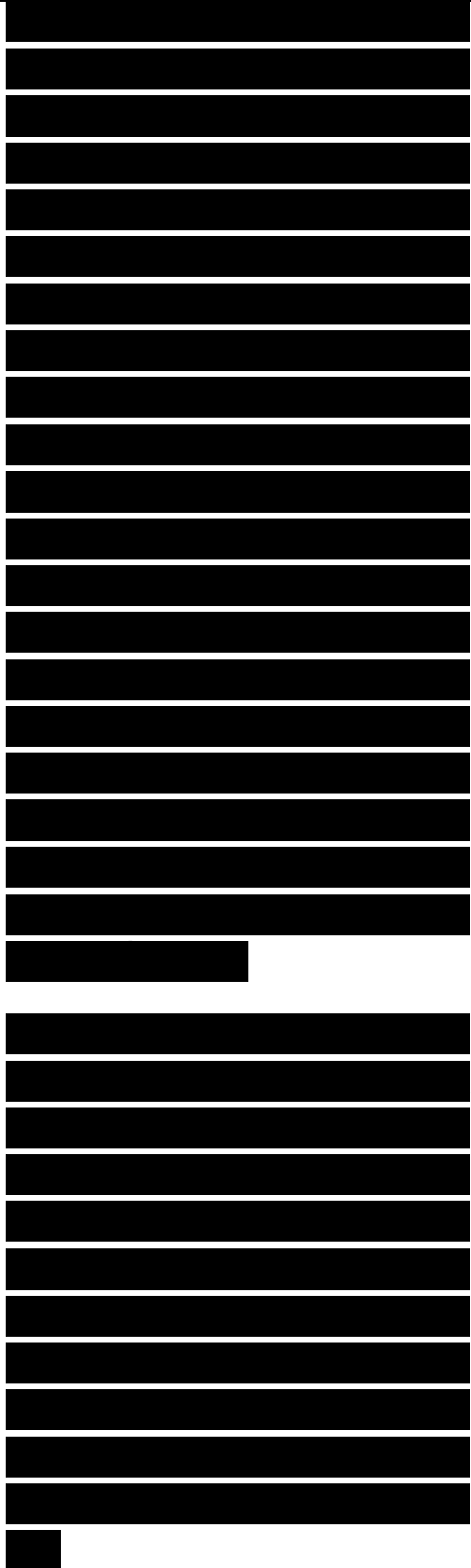
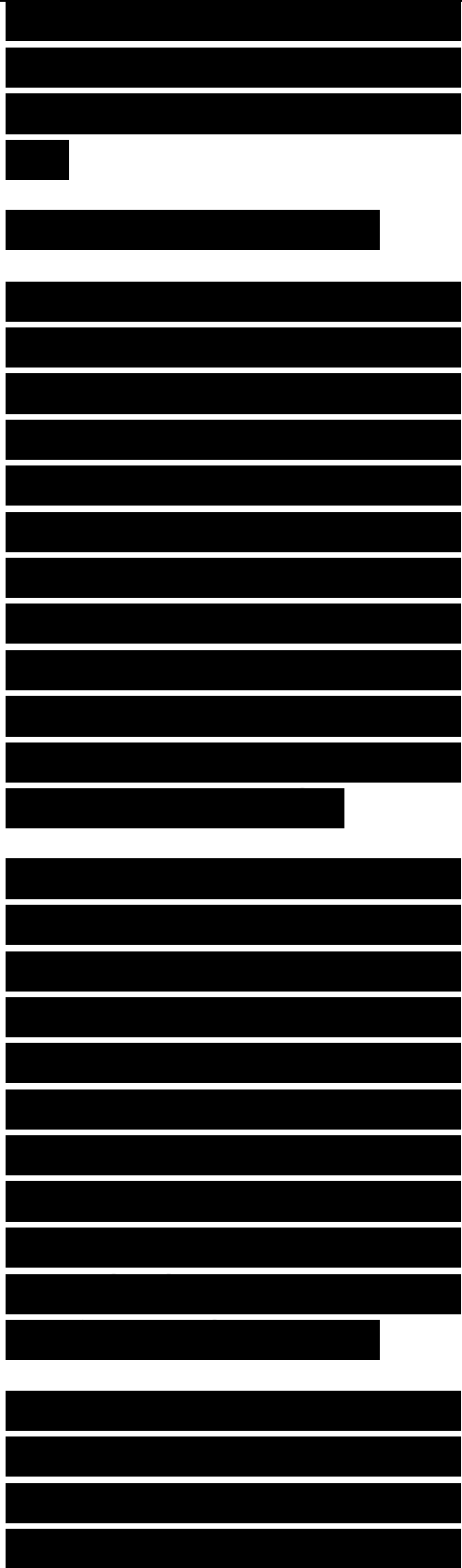


Figure 9.27. Schematic diagram of an admittance tunnel equipped with simple nulling instrumentation for measuring S_{21} .

in which the received signal and a sample of the received signal are compared in a hybrid tee. The sample signal is shifted in phase and adjusted in amplitude to cancel the received signal, both with and without the test sheet in place. The difference between the two phase shifter readings and the two attenuator settings is used to calculate S_{21} , from which we may calculate the complex sheet admittance or impedance.

Although the small, but nonzero, thickness of the test sheet may influence the signal transmitted through the sheet, that influence is contained implicitly in our definition of the sheet admittance. Because that admittance is assumed lumped in (confined to) a single plane in space, the scattering matrix element S_{21} may be written as

where Z_s is the sheet impedance and Y_s is the sheet admittance, one being the reciprocal of the other. Because



the sheet is tested in a good simulation of a free-space environment, Z_0 and Y_0 are the corresponding free-space values of impedance and admittance.

The left side of (9.31) is a complex number representing two values obtained from the measurements, and we may solve the expression for the impedance or admittance of the sheet in terms of the measured quantities. Because resistive sheets are common elements in absorber design, and because they are almost always characterized by a resistivity instead of a conductivity, we elect to use the impedance representation. Therefore, the normalized sheet impedance may be calculated from the test data as

$$Z_{sheet} = Z_0 \frac{1 - \Gamma}{1 + \Gamma} \quad (9.32)$$

Here it must be remembered that, in accordance with our $\exp(-j\omega t)$ time convention, positive values of the reactance X are capacitive and negative values are inductive.

The influence of these parameters on the observed values of S_{21} is charted in Figure 9.28 for a few selected values. Note that the higher values of impedance result in values of S_{21} that are clustered

[REDACTED]

[REDACTED]

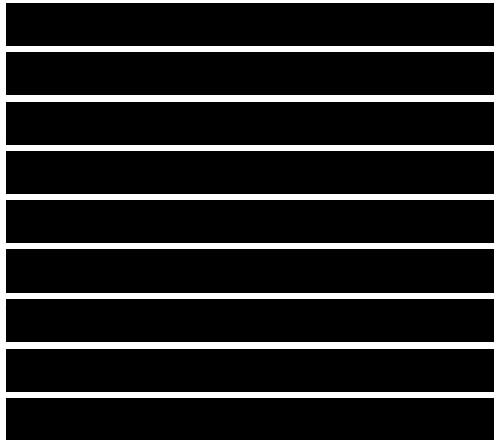
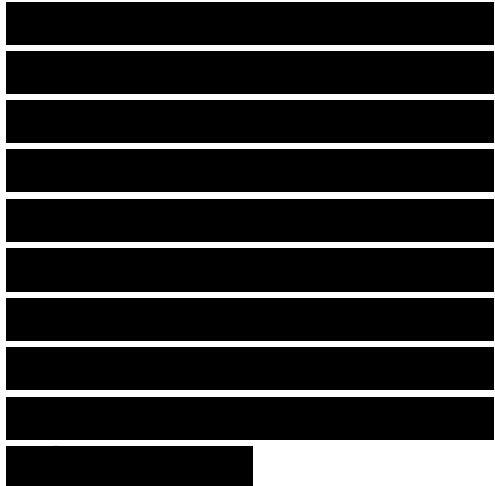
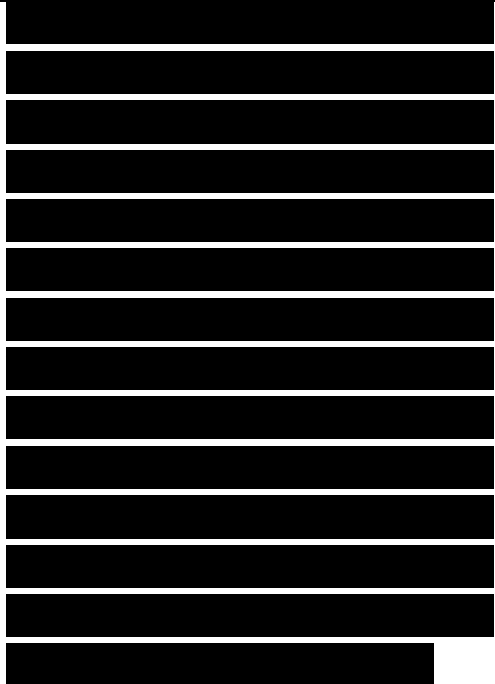
[REDACTED]

[REDACTED]

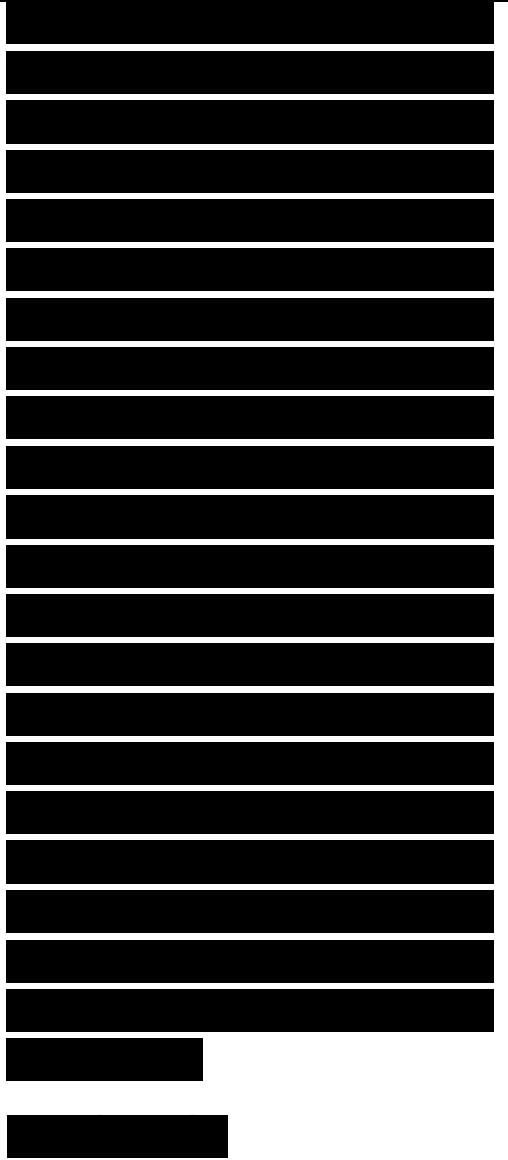
near the right side of the chart, where the transmission of energy through the chart approaches unity with little phase shift. The small attenuation and phase shift in this region of the chart may require the use of precision attenuators and phase shifters if accuracy is to be maintained. Modest impedances (in the central region of the chart) can be more accurately measured with standard-quality devices, and the phase shift always lies between

Figure 9.28. Variation in the phase and amplitude of S21 as influenced by the normalized sheet impedance. $\pm 90^\circ$. Very low impedances (not shown) may push S21 off the left side of the chart, but the 20 or 30 dB reduction in signal intensity is well within the capabilities of most test equipment.

Because the simple equipment diagrammed in Figure 9.27 demand a manual adjustment of the attenuator and phase shifter, the test data may be collected for only one frequency at a time. But, as in other testing described in this chapter, that simple instrumentation may be

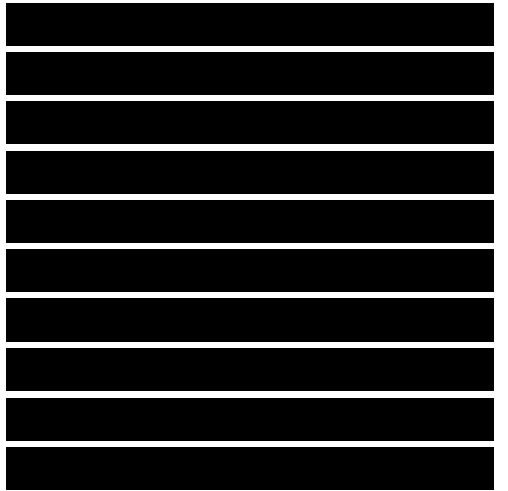


replaced by the more powerful microprocessor-driven network analyzer already discussed. We need only recognize that the terminals of the two antennas in this system can be regarded as the two ports of the device labeled sample holder in Figures 9.13 and 9.14. With broadband antennas and this more versatile instrumentation, we may measure the characteristics of thin impedance sheets in relatively short order. We note, finally, that no ambiguity is involved in this characterization. Even if the test sheet is not electrically thin, our electrical description of it—a lumped impedance or admittance—is uniquely related to the measured data.



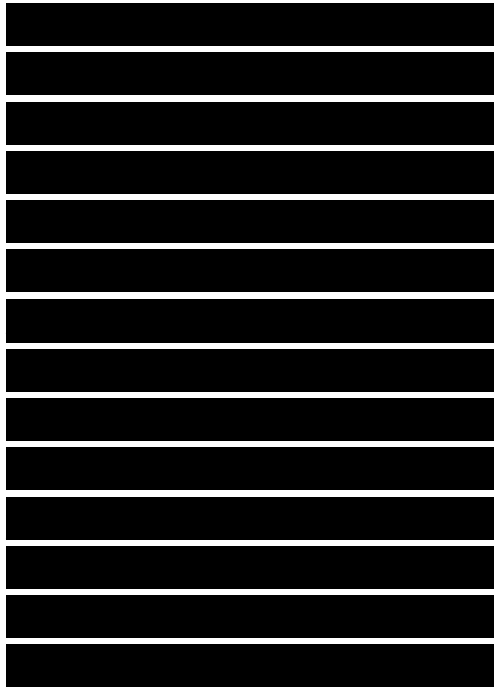
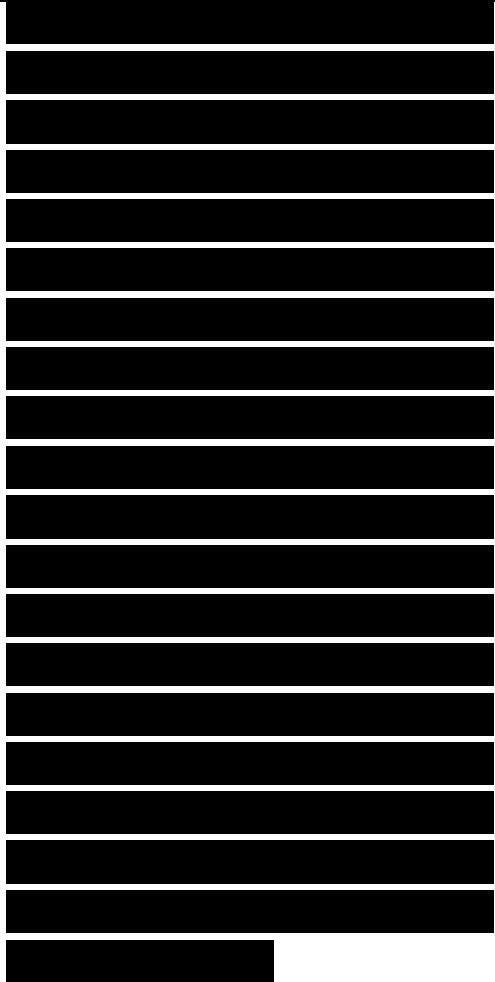
9.6 SUMMARY

The test and evaluation of absorbers and the materials we use in designing and constructing them depends on the information needed. To design absorbers, we need to know the intrinsic properties of the materials we hope to use, whether they already exist or we cook up new batches to test. The determination of those parameters generally requires



the use of enclosed test systems in the form of transmission lines, cavities or interferometers, or admittance tunnels. We emerge from such tests with characterizations of bulk permeability and permittivity or, in the case of thin sheets, the sheet admittance or impedance. We noted that sheet materials are not easily measured in transmission-line systems, and in the case of bulk materials, we must ensure that the sample is reasonably homogeneous throughout the small sample we insert in our sample holder.

We presented the basic theory for the measurement of small samples in transmission lines and how test data may be collected. We emphasized that unless the sample is electrically less than $A/2$ thick, as measured in the material, the test data are ambiguous. The ambiguity may be resolved if the measurements are repeated at a slightly different frequency or repeated with a second sample slightly thicker or thinner than the first. There is no ambiguity, on the other



hand, for thin sheets measured in an admittance tunnel, because we characterize sheets by an unambiguous impedance or admittance.

If nondestructive quality control of production panels is our objective, we need measure only the reflectivity of samples withdrawn from the production line. Because these panels are large, we would destroy them if we were to carve out small test specimens for transmission-line evaluation, and because such samples would not likely be homogeneous through the sample, we elect to use other methods of evaluation. Those methods, which rely on the classic NRL arch, measurements on an RCS test range, or on data collected in large waveguides, preserve the physical integrity of test panels and yield results averaged over large-scale inhomogeneities in the sample.

We illustrated some of these testing methods by using simple, inexpensive, single-frequency bench equipment, and although quite capable of yielding accurate results, they

[REDACTED]

[REDACTED]

[REDACTED]

are slow. Because convenience and speed are now as important as accuracy, experimenters have come to rely on frequency-swept, computer-controlled instrumentation. The network analyzer is particularly attractive for this application, and because some manufacturers even market what are known as S-parameter test sets, we included a brief description of how the elements of the scattering matrix of a two-port device can be measured.

Most network analyzers come equipped with firmware capable of transforming test data back and forth between the frequency and time domains and displaying the data in either. Coherent data are collected in the frequency domain and can typically be displayed on a panel screen in near real time in any of several formats. The basic temporal data collected by the time-domain reflectometer, on the other hand, must first be digitized and transformed to the frequency domain for display. Although both kinds of instrumentation yield essentially the same kind of information, the time-domain reflectometer has lost favor in

[REDACTED]

[REDACTED]

[REDACTED]

[REDACTED]. Mặc dù về cơ bản cả hai loại thiết bị đều cho ra cùng thông tin, phản xạ kế miền thời gian rất được ưu

<p>the materials evaluation community, not only because of the ease with which frequency-swept signals can be generated and controlled, but also because test-equipment manufacturers now employ large populations of digital engineers.</p>	<p>chuộng trong cộng đồng đánh giá vật liệu, không chỉ vì tín hiệu quét tần số được tạo ra và điều khiển dễ dàng mà còn do hiện nay những nhà sản xuất thiết bị kiểm tra sử dụng một số lượng lớn kỹ sư am hiểu về kỹ thuật số.</p> <p>checked</p>